REPORT DOCUMENTATION PAGE

Form Approved
OMB No 0704 0188

1. AGENCY USE ONLY (Leave blank)	2. REPORT DATE	3. REPORT TYPE AND DATES COVERED
	4 NOV 93	THESIS/DISSERTATION

4. TITLE AND SUBTITLE
NUMERICAL SIMULATIONS OF A MOUNTAIN THUNDERSTORM: A COMPARISON WITH DOPPLER RADAR OBSERVATIONS

5. FUNDING NUMBERS
1

6. AUTHOR(S)
MARK EDWIN RAFFENSBERGER

7. PERFORMING ORGANIZATION NAME(S) AND ADDRESS(ES)
AFIT Student Attending: THE FLORIDA STATE UNIVERSITY

8. PERFORMING ORGANIZATION REPORT NUMBER
AFIT/CI/CIA- 93-155

9. SPONSORING/MONITORING AGENCY NAME(S) AND ADDRESS(ES)
DEPARTMENT OF THE AIR FORCE
AFIT/CI
2950 P STREET
WRIGHT-PATTERSON AFB OH 45433-7765

10. SPONSORING/MONITORING AGENCY REPORT NUMBER

11. SUPPLEMENTARY NOTES

12a. DISTRIBUTION/AVAILABILITY STATEMENT
Approved for Public Release IAW 190-1
Distribution Unlimited
MICHAEL M. BRICKER, SMSgt, USAF
Chief Administration

12b. DISTRIBUTION CODE

13. ABSTRACT (Maximum 200 words)

14. SUBJECT TERMS	15. NUMBER OF PAGES 212
	16. PRICE CODE

17. SECURITY CLASSIFICATION OF REPORT	18. SECURITY CLASSIFICATION OF THIS PAGE	19. SECURITY CLASSIFICATION OF ABSTRACT	20. LIMITATION OF ABSTRACT

DEPARTMENT OF THE AIR FORCE
USAF ENVIRONMENTAL TECHNICAL APPLICATIONS CENTER (AWS)
SCOTT AIR FORCE BASE, ILLINOIS

From: USAFETAC/SYT (Capt Raffensberger, DSN 576-5412) 4 Nov 93
859 Buchanan St, Rm 403
Scott AFB IL 62225-5116

Subj: AFIT Program Completion (Our Telecon, 3 Nov 93)

To: AFIT/CIR (Maj Smith)

1. The purpose of this letter is to notify you that I have completed my AFIT-sponsored Master's Degree program at Florida State University. I have enclosed at Atch 1 a copy of my thesis entitled "Numerical Simulations of a Mountain Thunderstorm: A Comparison With Doppler Radar Observations." I have also enclosed at Atch 2 two copies of the abstract for the thesis.

2. I will arrange for Florida State University to forward an official transcript to you when the degree is posted (mid- to late-December).

3. Thank you for your assistance. If you require any additional information, please contact me at DSN 576-5412.

Mark E. Raffensberger

MARK E. RAFFENSBERGER, Capt, USAF

2 Atch
1. Thesis
2. Thesis Abstract (2 copies)

THE FLORIDA STATE UNIVERSITY

COLLEGE OF ARTS AND SCIENCES

NUMERICAL SIMULATIONS OF A MOUNTAIN THUNDERSTORM: A COMPARISON WITH DOPPLER RADAR OBSERVATIONS

BY

MARK EDWIN RAFFENSBERGER

A Thesis submitted to the
Department of Meteorology
in partial fulfillment of the
requirements for the degree of
Master of Science

Degree Awarded:

Fall Semester, 1993

The members of the Committee approve the thesis of Mark E. Raffensberger defended on October 28, 1993.

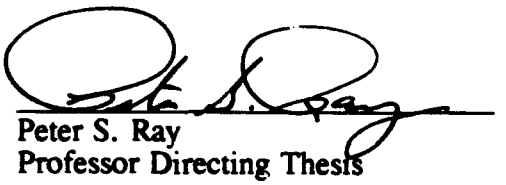

Peter S. Ray
Professor Directing Thesis

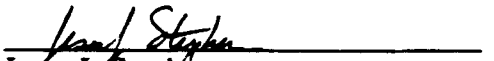

Jesse J. Stephens
Committee Member

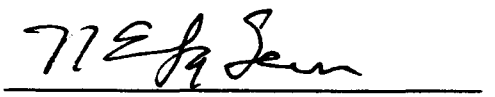

Noel E. LaSeur
Committee Member

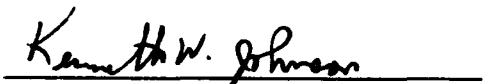

Kenneth W. Johnson
Committee Member

ACKNOWLEDGEMENTS

Many people have contributed their time, talent, and resources to help me complete this research. I extend my deep appreciation to Dr. Peter S. Ray, my advisor, for his many useful suggestions, valuable guidance, and tremendous encouragement and patience. I am most grateful to my committee members, Dr. Ken Johnson, Dr. J.J. Stephens, and Dr. Noel LaSeur for their careful reviews of this manuscript and for their many thoughtful comments and suggestions. I especially thank Dr. Ken Johnson for his unending patience and advice in helping me adapt to many new computer systems along the way. I also thank Dr. William Cotton, Dr. Greg Tripoli, Craig Tremback, and other members of Dr. Cotton's group for the advice and suggestions they provided on using their model. I offer many thanks to Mary Stephenson, Dr. B.J. Sohn, Dr. Mohan Ramamurthy, Steve Lang, Terry Given, Russ Treadon, and especially Dr. Ying Lin and Anna Nelson Smith, and the many others who helped me at FSU. I thank the United States Air Force for supporting my education through the Air Force Institute of Technology Civilian Institutions program and all my supervisors and coworkers at Air Weather Service who encouraged me to finish this work. To my parents, James and Loretta, I offer my deep thanks for instilling in me the desire to continue my education. To my daughters, Emily and Gretchen, I offer my appreciation for their patience while I spent countless nights and weekends in front of the computer and away from them. Finally, I offer my deepest gratitude to Donelle, my wife, for her all her loving support, sacrifice, encouragement, and good counsel without which I could not have succeeded.

TABLE OF CONTENTS

LIST OF TABLES

LIST OF FIGURES

LIST OF SYMBOLS AND ABBREVIATIONS

2-D	two-dimensional
3-D	three-dimensional
cm	centimeters
CSU	Colorado State University
dBZ	radar reflectivity expressed in decibels
Δz	vertical grid spacing
g kg^{-1}	grams per kilogram
hr	hours
km	kilometers
m	meters
m s^{-1}	meters per second
mb	millibars
min	minutes
MSL	Mean Sea Level
MST	Mountain Standard Time
NCAR	National Center for Atmospheric Research
N_{ic}	total concentration of pristine ice crystals
NOAA	National Oceanic and Atmospheric Administration
π	Exner function
p	pressure

θ	potential temperature
θ_{il}	liquid-ice potential temperature
ρ	density
r_a	aggregated snow flake mixing ratio
RAMS	Regional Atmospheric Modeling System
r_c	cloud water mixing ratio
r_g	graupel or hail mixing ratio
r_i	pristine ice crystal mixing ratio
r_r	rain water mixing ratio
r_t	total water mixing ratio
r_v	water vapor mixing ratio
s	seconds
T	temperature
t	time coordinate
TRIP	Thunderstorm Research International Project
u	x component of air motion
v	y component of air motion
w	z component of air motion
x	east-west coordinate coordinate
y	north-south coordinate
z	vertical coordinate

Numerical Simulations Of A Mountain Thunderstorm: A Comparison With Doppler Radar Observations

Mark Edwin Raffensberger, M.S.
The Florida State University, 1993
Major Professor: Peter Sawin Ray, Ph.D.

A two-dimensional, non-hydrostatic cloud model was used to isolate the processes and initial conditions most important in the initiation and development of a small mountain thunderstorm. Six numerical simulations were conducted--one control and five experiments. The control simulation was conducted with realistic initial conditions and physical processes. The simulation's accuracy was evaluated by comparison to multiple-Doppler radar analyses of a storm that occurred on 31 July, 1984 near Langmuir Laboratory, New Mexico and to a microphysical retrieval conducted for a different, but similar storm. The other five simulations were conducted to test the sensitivity of the simulated storms to the initial wind profile, the lack of solar heating, restriction to warm rain processes, and the initial moisture profile. Comparison of the evolution of the control's simulated storm with observations and with the microphysical retrieval show that the simulation accurately captured the major features observed by the radars and accurately depicted the microphysical evolution of the storm cells. The results of the numerical experiments showed the following conditions and

processes to be most important (in descending order) to the development and maintenance of the mountain storm: solar heating, ice phase microphysical processes, environmental wind profile, and low-level moisture profile. The environmental wind profile was the single most important factor in the convective initiation location.

NUMERICAL SIMULATIONS OF A MOUNTAIN THUNDERSTORM: A COMPARISON WITH DOPPLER RADAR OBSERVATIONS

Chapter 1

Introduction

Mountain thunderstorms have been studied extensively to determine the processes and conditions important to their initiation, development, and maintenance. Mountain thunderstorms play a major role in the economy of the western United States as they produce the bulk of summertime precipitation, and their lightning starts many of the region's forest fires. The extensive research into mountain thunderstorms has been prompted by the need to improve the understanding and prediction of the storms in order to improve precipitation, flash flood, lightning, and civilian and military aviation forecasts. In addition to their economic importance, the frequency of occurrence of mountain storms over the same general location makes them ideal subjects for intense scientific study.

Over the past 40 years, numerous descriptive models of mountain thunderstorms were developed based on observational studies which used photogrammetric techniques, instrumented aircraft, Doppler radars, and dense observational networks. Within the past 30 years, two- and three-dimensional numerical models have been developed which allow researchers to simulate mountain thunderstorms. These models permit "experimentation" with the storms by allowing the researcher to vary important physical processes and initial conditions in a way not permitted in nature.

The current research examines the initiation, development, and maintenance of a small mountain thunderstorm using numerical simulations and observationally-based information. The storm considered in this study occurred on 31 July 1984 during the Thunderstorm Research International Project (TRIP), a field experiment conducted near the Langmuir Laboratory in the Magdalena Mountains of central New Mexico during the summer of 1984. Four Doppler radars, two instrumented research aircraft, rawinsondes, and a surface network for measuring electrical fields were employed to collect storm data during TRIP.

This study employs the two-dimensional, non-hydrostatic cloud model configuration of the Colorado State University Regional Atmospheric Modeling System (RAMS) (Tripoli and Cotton, 1982, 1986; Cotton *et al.*, 1982, 1986; Tripoli, 1986) to simulate the 31 July 1984 storm. The study also uses multiple Doppler analyses performed following the technique of Ray *et al.* (1980) and described in detail by Lang (1991), as well as the three-dimensional microphysical retrievals performed by Lang (1991) for a similar storm that occurred on 3 August 1984.

This research has two primary goals: 1) to assess the validity of a RAMS simulation compared with observations from 31 July 1984, and 2) to use RAMS to conduct numerical simulation experiments to test the sensitivity of the simulated storms to different physical processes and initial conditions. A total of six simulations were conducted. The first simulation was the control and included all appropriate physical parameterizations and processes and was initialized with observationally-based base state atmospheric profiles. The results of the control simulation were compared with Doppler analyses and with Lang's (1991) retrieval to assess the validity of the simulation and its usefulness in studying the storm. The other five simulations were conducted to test the sensitivity of the simulated storms to the initial wind profile, the

lack of solar heating, restriction to warm rain processes, and the initial moisture profile. The results of the numerical experiments were compared with those of the control to determine the impact of the change imposed for each experiment.

The thesis is organized in the following manner. Chapter 2 provides an historical review of both observational and numerical mountain thunderstorm studies. Chapter 3 describes the observations of the 31 July 1984 storm and its environment. This chapter includes discussions of the data collection and analysis procedures and a detailed description of the evolution of the storm as observed by the Doppler radars. Chapter 4 describes the numerical model as it was configured for this study. Chapter 5 explains the experimental design chosen for this study. This chapter includes information on the construction of the base-state profiles used to initialize the simulations. Chapter 6 details the results of the control simulation and compares those results with the Doppler analyses, synthesized wind fields, and Lang's (1991) microphysical retrieval for the 3 August 1984 case. Chapter 7 describes the results of the experiments conducted to test the sensitivity of the simulated storms to the initial wind profile. Chapter 8 presents the results of the experiments conducted to test the sensitivity of the simulated storms to diabatic heating effects; namely elimination of solar heating and restriction to warm rain processes. Chapter 9 describes the results of the experiment conducted to test the sensitivity of the simulated storms to the initial moisture profile. Finally, Chapter 10 summarizes with the conclusions.

Chapter 2

Historical Review Of Mountain Thunderstorm Studies

2.1 Observational Studies

Mountain thunderstorms are believed to result from thermally driven mountain-valley circulations (Defant, 1951). Solar heating of the mountain slopes causes the adjacent air to become warmer than free air at the same elevation. The consequent buoyant rise of the warmer air to the condensation level produces clouds (Raymond and Wilkening, 1980). At this point the effects of latent-heat release mask the original circulation and may soon become the dominant mechanism for cloud and storm maintenance.

Banta and Schaaf (1987) presented several other mechanisms thought to be responsible for the production of thunderstorms in the mountains, the first of which was orographic lifting. Orographic lifting involves the mechanical lifting of air as it approaches a barrier. Wake effects were the second mechanism. They include wake turbulence, gravity waves and confluence generated by flow around a mountain. Other mechanisms described include: leeside convergence (discussed below), flow into convergent valleys, and other mechanisms not dependent on topography (e.g., fronts, local gradients of moisture, etc.)

Environmental conditions may play an important role in determining which of the above processes, if any, dominate the development of mountain convection. Among the environmental conditions to be considered are ambient wind, temperature, and humidity profiles and surface characteristics such as vegetation, soil type, and soil

moisture. Many observational and numerical studies have been conducted to document the nature of mountain convection and to determine the processes and conditions important to its initiation and maintenance. In order to concentrate on the thermally driven circulations leading to convection, most of these studies focused on conditions of light winds and strong solar heating. A review of some of these studies is given below beginning with observational studies and followed by numerical studies.

Several of the early observational studies were not motivated purely by an interest in mountain convection, but rather were designed to settle a long-standing debate over the actual nature of convection. The "bubble theory" (Scorer and Ludlam, 1953; Scorer, 1958) held that convection consisted of a series of short impulses, or bubbles, of buoyant air rising from the surface with mixing occurring mainly at the tops of the bubbles. The "jet theory", on the other hand, held that convection could be thought of as a jet, or plume, of buoyant air with a continuous source of buoyant air entering through the bottom and entrainment occurring at the sides. The observation that cumulus clouds have flat bases was difficult to explain with the bubble theory. To solve this problem, Turner (1962) proposed that convection be viewed instead as a "starting plume" which consisted of a plume of buoyant air capped by a rising thermal. By linking the jet and bubble theories, this theory allowed for a continuous source of buoyant air through the bottom, which could explain the existence of flat cloud bases. Because mountain convection was known to occur frequently over the same location, it soon became a "natural laboratory" for testing these theories. The information from these studies showed that the topic of mountain convection itself was one worthy of further research.

Braham and Draginis (1960) used an instrumented aircraft to measure temperature and humidity over the Santa Catalina Mountains near Tucson. They found that by

mid-morning a "convective core" measuring about 1-4 km in diameter had formed over, or slightly downwind of the peaks. In contrast to the relatively dry and moderately stable environment, the core was characterized by an excess of water vapor mixing ratio and a nearly dry adiabatic lapse rate. Excesses of temperature and virtual temperature also were noted in the lower portion of the core. Although no wind measurements were collected, negative mixing ratio anomalies and positive potential temperature anomalies surrounding the core at higher elevations implied that downdrafts as well as updrafts were integral parts of the observed convective system.

Anderson (1960) studied congestus clouds in Arizona with photogrammetric techniques. The study showed that as the clouds grew, they pulsated with a frequency of about 10 minutes. Anderson attributed these pulsations to the buoyancy-restoring force of statically stable air and proposed a model in which pulsating flow was superimposed on a slowly increasing, large-scale updraft.

Glass and Carlson (1963) used photogrammetric techniques to study small cumulus clouds over the San Francisco Peaks near Flagstaff. They found that many of the clouds in their study seemed to fit the bubble theory of convection. The clouds in this study typically measured 1 km or less in diameter. Todd (1964) combined aircraft observations with time-lapse cloud photography to trace the continuity of individual updrafts over the San Francisco Peaks. His study was different from those above in that it followed the convective development through to the precipitation stage. He found that many updrafts lasted from 7 to 18 minutes and that individual updrafts had maximum velocities two to three times greater than the maximum rate of rise of the convective tower tops. Todd used these observations to suggest that the clouds he studied followed the "starting plume" theory of Turner (1962). The non-precipitating

clouds in this study also typically measured less than 1 km in diameter, and the precipitating clouds measured from 1 to 3 km in diameter.

In another photogrammetric study, Orville (1965b) studied convection over the Santa Catalinas when the low-level wind speeds were between 5 and 10 m s^{-1}. He found that the location of convective initiation strongly depended on the direction of the environmental wind. Orville speculated that this dependency resulted from the translation of the updrafts by the environmental wind.

In their study of dry mountain convection, Raymond and Wilkening (1980) used an instrumented aircraft to collect temperature, humidity and wind data over the San Mateo Mountains near Socorro, New Mexico. By carefully analyzing and filtering the data, the authors isolated two important scales of motion. Superimposed on the ambient flow was a heat-island circulation, convergent in the lower levels and divergent aloft, which measured approximately 20 km in diameter. The strength of this mesoscale flow averaged over its area ranged from about one meter per second in the vertical wind to a few meters per second in the horizontal. The authors compared this feature to the "convective core" discussed earlier by Braham and Draginis (1960). Embedded within the convective core were numerous convective eddies with horizontal wavelengths of 3-4 km and vertical velocities measuring about 5 m s^{-1}. The eddies were responsible for most of the heat and moisture fluxes over the mountain. The authors felt that the eddies and the mesoscale circulation coexisted in a "symbiotic relationship": the heat carried aloft by the eddies drove the mesoscale circulation, and the mesoscale circulation carried the heat out of the region, thus preserving a favorable lapse rate for the eddies.

In a follow-up study of moist convection Raymond and Wilkening (1982) showed that moisture negligibly affected the low-level convergence during the early stages of

convection. They found that the dry-convective pattern of convergence below the peaks and divergence above persisted through the cumulus stages of development and into the early cumulonimbus stage. They found only a single storm that developed its own low-level flow pattern. The authors presented a schematic diagram of the estimated mass budget of a typical mountain thunderstorm. It depicted a convergent flow below the peaks, which supported both the mesoscale upcurrent and a divergent flow which extended from above the peaks to about half the height of the cloud.

In a paper describing the evolution of the daytime boundary-layer over mountainous terrain, Banta (1984) documented the existence of a "leeside convergence zone". He showed that as the mountain surface heated during the morning, a shallow upslope flow developed near the slope beneath the nocturnal inversion cold pool. At elevations above the cold pool the winds were convectively mixed. On the lee side of the mountain these two flows opposed each other and thus created a convergence zone. Banta felt that this leeside convergence zone might explain the slight displacement downwind from the peaks of the convective elements observed by Braham and Draginis (1960), Glass and Carlson (1963), and Orville (1965b).

Recently several investigators (Barker and Banta, 1985; Banta and Schaaf, 1987; Schaaf *et al.*, 1988) have used geostationary satellite imagery to trace mountain convection back to its initiation location. The authors found that certain topographical features act as preferred storm initiation locations or "genesis zones". When they stratified the initiation locations by the direction of the ridge top wind, the authors found that the wind direction strongly affected the ability of a particular topographic feature to act as an initiation point. All three of these studies showed the same tendency toward leeside development that appeared in earlier studies.

Raymond and Wilkening (1985) used budget residual techniques to study thunderstorms and cumulus congestus clouds near Socorro, New Mexico. As part of the study the authors compiled a composite thermodynamic sounding for thunderstorm and congestus cases and found the congestus sounding to be much drier at mid-levels than the thunderstorm sounding. The authors also found that the peak vertical mass flux for thunderstorms was only slightly greater than that for congestus clouds. They felt this ruled out a significant feedback between latent heat release and the generation of low-level convergence. This implied that the low-level forcing for both cases was about the same. They also found that for thunderstorms the vertical mass flux near 700 mb was only about half that found in congestus clouds. This difference was attributed to the thunderstorm downdraft, which was estimated to be about one-half the updraft strength.

Toth and Johnson (1985) used wind data collected from a dense surface mesonetwork to study surface flow characteristics over the Front Range in northeast Colorado. The observations showed the evolution of upslope flow during the morning hours with a convergent region just to the lee of the ridges. In late afternoon, a downslope flow began in the high elevations. The confluence zone between the downslope and the upslope regimes gradually moved eastward onto the plains. The authors found that this propagating confluence line coincided with a maximum radar echo frequency in the late afternoon over the western plains.

Ziegler *et al.* (1986) used Doppler radars in their study of a thunderstorm near Socorro. They found vertical extensions in the radar reflectivity field that occurred with a period of about 12 min. These upward extensions were suggestive of pulses in the vertical velocity field similar to those observed by Anderson (1960). The maximum updrafts inferred from the Doppler velocities were between 15 and 20 m s^{-1}.

Additionally, the inferred flow field reported in this study supported the convergent below/divergent aloft flow field reported by Raymond and Wilkening (1980).

McCutchan and Fox (1986) used automatic surface weather stations to collect wind, temperature, and humidity data at various aspects and elevations on an isolated conical mountain in New Mexico. The station positions allowed the authors to use analysis of variance techniques to study the effects of elevation and aspect on the measured variables. The data were divided into two groups of wind speeds at the peak: light (less than 5 m s^{-1}) and strong (greater than or equal to 5 m s^{-1}). Analysis of variance tests showed that for daytime cases in both groups: 1) the effect of aspect on the u and v wind components was significant, and 2) the effects of both elevation and aspect were significant on the potential temperature. Of the four case studies presented, the two daytime cases are of interest here. The first case illustrated a typical "light wind" situation. The observations were marked by a pronounced upslope flow at all stations. The lapse rate indicated neutral to slightly stable air over the southern slopes and significant instability over the northern slopes. Temperature observations very near the surface on the southwest slope indicated a very strong positive heat flux on that day. The second case illustrated a typical "strong wind" situation. The strong ambient flow dominated the observations at all stations. The authors found they were able to recover an upslope flow similar to the light wind case by subtracting a fraction of the mountain-top wind from the wind velocities everywhere. This implies that the strong ambient winds simply masked the weaker thermally-driven upslope flow. The lapse rates in this case indicated nearly neutral conditions everywhere. The near-surface temperatures on the southwest slope indicated a much smaller heat flux in this case than in the light wind case. The authors speculated that the strong winds pre-

vented the buildup of sufficient near-surface temperature gradients to produce the positive heat flux magnitude found in the light wind case.

2.2 Numerical Modeling Studies

Many numerical models have been used to simulate mountain convection and to improve our understanding of some of the above observations. Early numerical studies were almost exclusively two-dimensional and contained only crude, if any, parameterizations of subgrid-scale processes, such as turbulence and cloud microphysics. Later models expanded to three dimensions and included more sophisticated treatments of subgrid-scale processes. A brief summary of some of these studies is given below.

Orville (1964) developed a two-dimensional model based on the equations of Ogura (1962) to study mountain upslope winds. In this study Orville simulated the development of an upslope circulation, the center of which moved from the lower slope of the mountain to well above the peak. Several elements of the simulated wind field matched those described by Defant (1951). The thermal fields from this simulation also showed some similarities to those described by Braham and Draginis (1960).

In a later paper, Orville (1965a) reported the results of simulations that included the effects of moisture in his two-dimensional model. Comparison of these results with those from the "dry" simulations (Orville, 1964) showed that moisture effects caused the upslope flow to develop 10 to 20 percent faster than in the dry model. Again, the model showed some qualitative agreement with the observations of Braham and Draginis (1960). Other simulations in this study were compared to the photogrammetric observations reported by Orville (1965b). The simulations produced clouds in a reasonable time scale and at reasonable elevations. Orville pointed out, however, that neither the fields of moisture and temperature nor the time scale of

cloud growth were realistic. One simulation in this study produced a pulsation reminiscent of those observed by Todd (1964) and Anderson (1960).

Orville (1968) extended his previous studies to include the effects of ambient winds on the initiation and development of simulated mountain cumulus clouds. In general, he found that vertical wind shear enhanced cloud initiation but damped further cloud development. In addition the simulations showed that the clouds formed downwind of the peak as they had in most of the observational studies. Orville also discussed the simulation of a mountain wave and its associated cloud development. He found that in this situation, the damming effect of the mountain and heating of the upwind slope acted together to produce a wave in the upwind airflow. When small perturbations of moisture and potential temperature reached this wave, they were amplified and advected over the top of the mountain into air moistened by the large downwind circulation. At this point, the amplified perturbations initiated clouds. Orville felt this method could explain the pulsations observed in stationary clouds that form in the downwind circulation.

Liu and Orville (1969) added the effects of precipitation and cloud shadows to Orville's model. The precipitation processes were parameterized following Srivastava (1967) and Kessler (1969), and the cloud shadow effects were simulated by decreasing the temperature and water vapor changes at the ground points directly below the cloud. Comparison of precipitating and non-precipitating clouds showed the effect of the precipitation processes to be negligible during early development. During later stages of development, however, evaporation below the cloud in the precipitating case generated a downdraft that tended to shorten the cloud's lifetime. The shadow effects caused both the clouds to move out of the grid faster and subsequent clouds to be smaller.

Gal-Chen and Somerville (1975a) developed a terrain-following coordinate system for use in simulations with irregular lower boundary conditions. This coordinate transformation greatly simplified the lower boundary conditions but only slightly complicated the basic model equations. The complications take the form of terrain-dependent transformation coefficients, which must be included in some terms of the model equations. Details of this coordinate transformation will be discussed further in Chapter 4. Gal-Chen and Somerville (1975b) used a two-dimensional model based on the Navier-Stokes equations to test their new coordinate transformation. They simulated upslope mountain winds and found their results to be similar to Orville's (1964) observations.

In the late 1970's numerous three-dimensional, non-hydrostatic models were developed (see for example Tapp and White, 1976; Clark, 1977; Schlesinger, 1975, 1978; Cotton and Tripoli, 1978; Klemp and Wilhelmson, 1978a,b). Since that time these models have been used mainly to study severe storms. In these studies the convection was usually started by the imposition of a temperature and/or a moisture perturbation on an initially horizontally homogenous environment. Only a few investigators have used three-dimensional models to study mountain convection. These studies will be summarized next.

Clark and Gall (1982) used a three-dimensional model to simulate the airflow over mountainous terrain. One part of their study attempted to simulate the case of dry convection over Mount Withington in New Mexico presented by Raymond and Wilkening (1980). A prominent feature of the simulations was the development of strong longitudinal rolls after sunrise. This longitudinal development did not compare well with the more cellular development found in the observations. The authors attributed this difference to the crude surface layer parameterization used in the model, to the

difficulty in choosing low level winds, and to poor horizontal grid resolution. The simulated flow field also failed to show the low-level convergence and higher level divergence described by Raymond and Wilkening.

Smolarkiewicz and Clark (1985) developed a surface boundary layer model which used single-level surface mesonetwork data to calculate surface fluxes of momentum, heat, and moisture. These fluxes were then used in a three-dimensional model to simulate the evolution of a field of cumulus clouds over complex terrain in western Montana. The simulated cloud field qualitatively agreed quite well with photographs and other observations of the actual clouds. Sensitivity experiments showed that during the early stages of cloud development, the dynamical effects of flow over the terrain and the thermodynamical effects of soil type and vegetation played equal roles in the rate of development of the cloud field. During the later stages of development, the thermodynamical effects primarily influenced the local properties of the cloud field. The authors found that the gross characteristics of the cloud field were mostly determined by the topography rather than the thermodynamics of the surface layer.

Banta (1983, 1986) used a two-dimensional version of the Cotton-Tripoli model to study the boundary layer evolution over mountainous terrain. His numerical experiments showed the importance of the inversion layer and the ridgetop winds to the formation and duration of the upslope flow. He found that the duration of the upslope flow was inversely proportional to the strength of the ridgetop winds. This finding implied that the leeside convergence effect discussed earlier is less effective when the upper-level winds are strong.

Chapter 3

Observations Of The 31 July 1984 Storm And Its Environment

This chapter describes the observed initiation and evolution of a mountain thunderstorm over the Magdalena Mountains near Socorro, New Mexico on 31 July 1984. Section 3.1 describes the general nature of central New Mexico mountain storms. Section 3.2 describes the field experiment facilities, and the data collection and analysis methods used to acquire and analyze the data used in this research. The local terrain in the field experiment area also is described in this section. Finally, section 3.3 details the 31 July 1984 storm history as observed by the Doppler radars.

3.1 New Mexico Mountain Thunderstorms

The small, isolated summer thunderstorms that frequently develop over the Magdalena Mountains and other nearby mountain ranges of New Mexico have been studied extensively for at least the past 15 years (see for example Winn *et al.*, 1974; Raymond and Wilkening, 1980, 1982, 1985; Dye *et al.*, 1987; and Lang, 1991). The storms usually occur under conditions of weak environmental winds and wind shear (Raymond and Wilkening, 1985), and so generally are thought to develop primarily as a result of the thermally driven mountain-valley circulations described in Chapter 2 (Raymond and Wilkening, 1980, 1982; and Dye *et al.*, 1987). Orographic lifting and flow into convergent valleys resulting from the weak environmental winds may play a secondary role in storm development and a more important role in determining the location of development (see, for example Barker and Banta, 1985; Banta and Schaaf, 1987; and Schaaf *et al.*, 1988). Initial cloud development is often restricted by weak

stable layers which are eroded slowly by the convective action until small thunderstorms develop with tops ranging from 9 to 14 km MSL (Dye *et al.*, 1987). As a result of the weak environmental winds, the storm movements are small, making the Magdalena Mountain range and surrounding ranges ideal locations for thunderstorm studies.

3.2 Data Collection And Analysis

As part of the Thunderstorm Research International Project (TRIP), a field experiment was conducted near the Langmuir Laboratory (elevation 3255 m MSL) in the Magdalena Mountains of central New Mexico during the summer of 1984. During the field experiment, 22 storms occurred on 19 different days from 14 July to 24 August (Dye *et al.*, 1987). This study uses primarily the data collected on 31 July 1984. The numerical simulations conducted for this study were initialized with rawinsonde and Doppler radar-derived wind data from the 31 July case. The simulations were then compared with the 31 July Doppler radar observations and with Lang's (1991) study of the microphysical evolution of the 3 August storm.

3.2.1 Facilities

Four Doppler radars, two instrumented research aircraft, rawinsondes, and a surface network for measuring electrical fields were employed to collect storm data over the Magdalena Mountains during the TRIP experiment. Rawinsonde observations were collected from a site (elevation 3223 m MSL) in the mountains near the Langmuir Laboratory and from the Socorro Airport (elevation 1456 m MSL) in the valley during the mornings and early afternoons throughout the experiment. The radar network (Fig. 1) consisted of two National Center for Atmospheric Research (NCAR) 5-cm radars, CP-3 and CP-4, and two National Oceanic and Atmospheric Administration (NOAA) 3-cm radars, NOAA-C and NOAA-D. Lang (1991) and Dye *et al.*

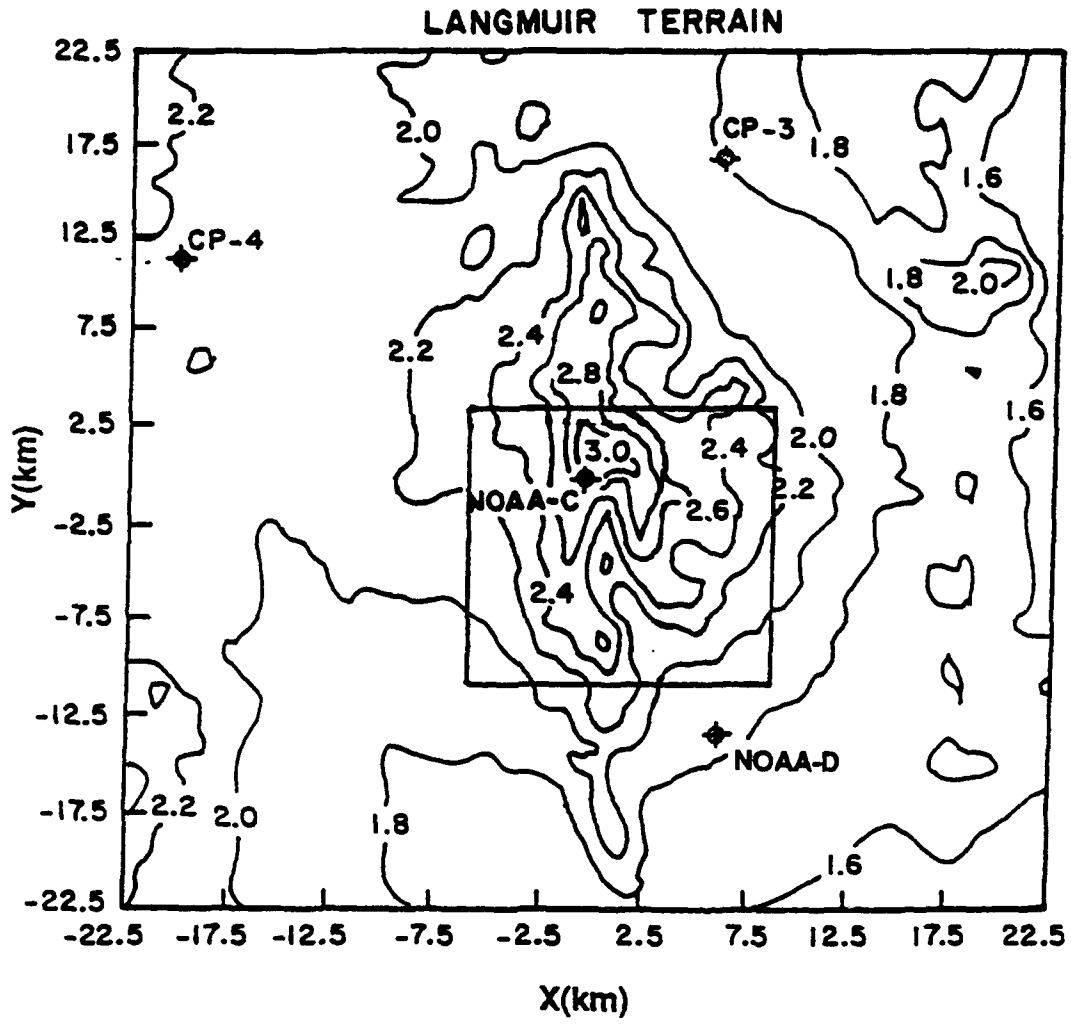

Fig. 1. Radar network and topographical view of terrain features near Langmuir Laboratory. Terrain elevation is relative to mean sea level in kilometers and contour intervals are every 0.2 km. The horizontal and vertical axes are labeled in kilometers. The origin (0,0) is located at Langmuir Laboratory. A sample radar analysis domain is shown for reference.

(1987) described in detail the location and characteristics of the Doppler radars. Depending on storm development, the radars collected data from mid-morning into the afternoon throughout the experiment.

3.2.2 Rawinsonde Observations

Two thermodynamic soundings were collected from rawinsondes launched on the morning of 31 July 1984. The first sonde was launched at 0719 MST from the Socorro airport located in the valley several miles east of the Magdalena Mountains. The second was launched at 0945 MST from the balloon hangar near the Langmuir Laboratory. This sounding coincided with the onset of early convective development as observed by the NCAR CP-4 radar.

Figures 2 and 3 show the airport and Langmuir thermodynamic soundings, respectively. Both soundings exhibit essentially the same characteristics. The soundings show a conditionally unstable atmosphere with a mixed layer extending from the surface to 550 mb (500 mb in the Langmuir sounding). The mixed layer was relatively moist throughout with a very moist layer 30-40 mb deep near its top. The mixed layer and the associated moist layer aloft were capped by an inversion approximately 50-100 mb deep. Below 300 mb, the Langmuir Laboratory sounding tended to be more moist and slightly cooler than the airport sounding. The thermodynamic structure observed in both 31 July 1984 soundings was very similar to that reported by Lang (1991) for the 3 August 1984 case and by Raymond and Wilkening (1985) for their "composite thunderstorm sounding". The observed thermodynamic profiles were combined and smoothed as described in Section 5.2.1 to initialize the numerical simulations.

The wind data (not shown) from both the airport and Langmuir rawinsondes are very noisy and dissimilar due to problems with the rawinsonde tracking equipment

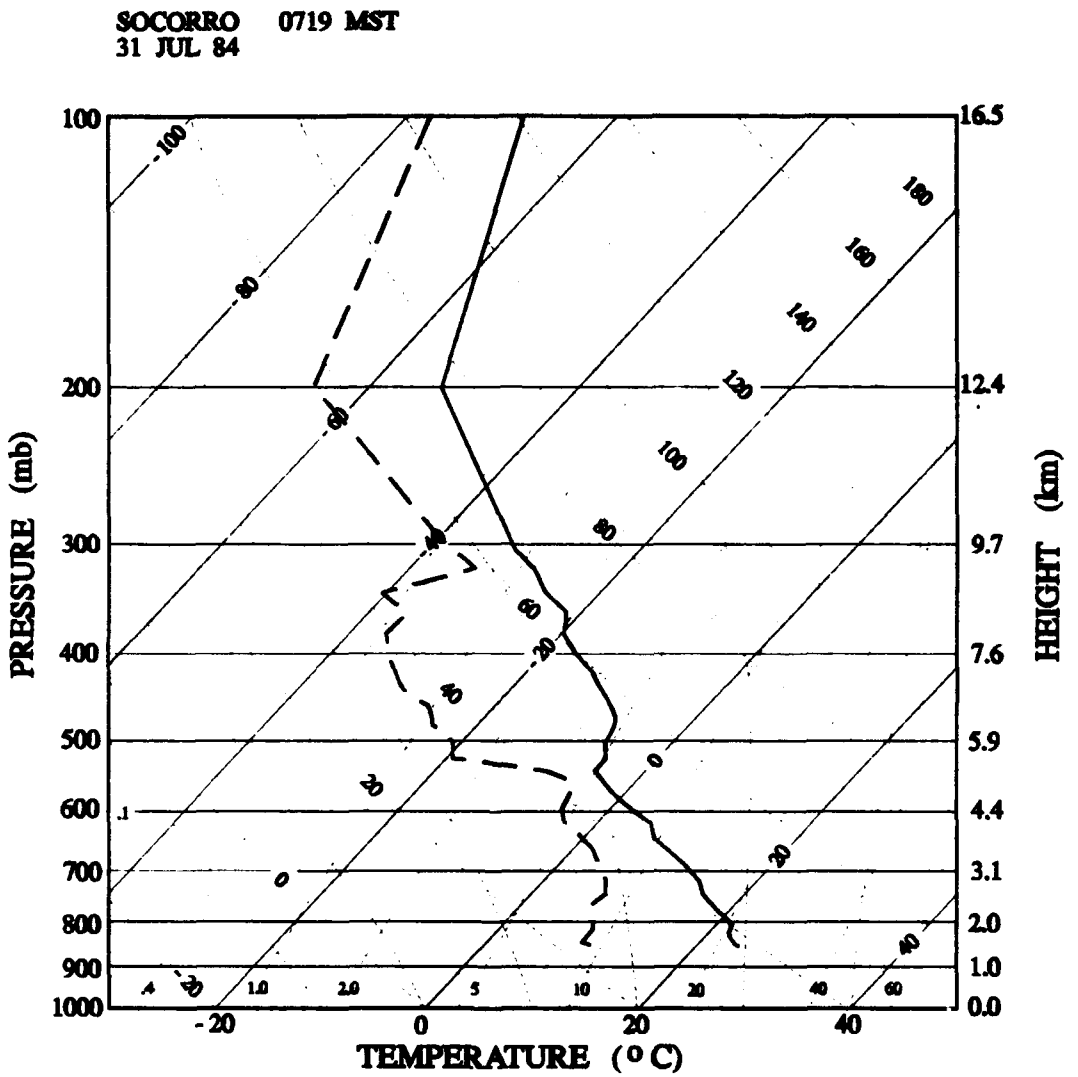

Fig. 2. Skew T, log P plot of the 0719 MST 31 July 1984 Socorro Airport thermodynamic sounding. Solid skewed lines are temperatures in degrees Celsius; dashed skewed lines are mixing ratios in grams per kilogram; curved dashed lines are dry adiabats in degrees Celsius; solid horizontal lines are pressures in millibars. Heavy solid and dashed lines represent sensible and dewpoint temperature profiles, respectively.

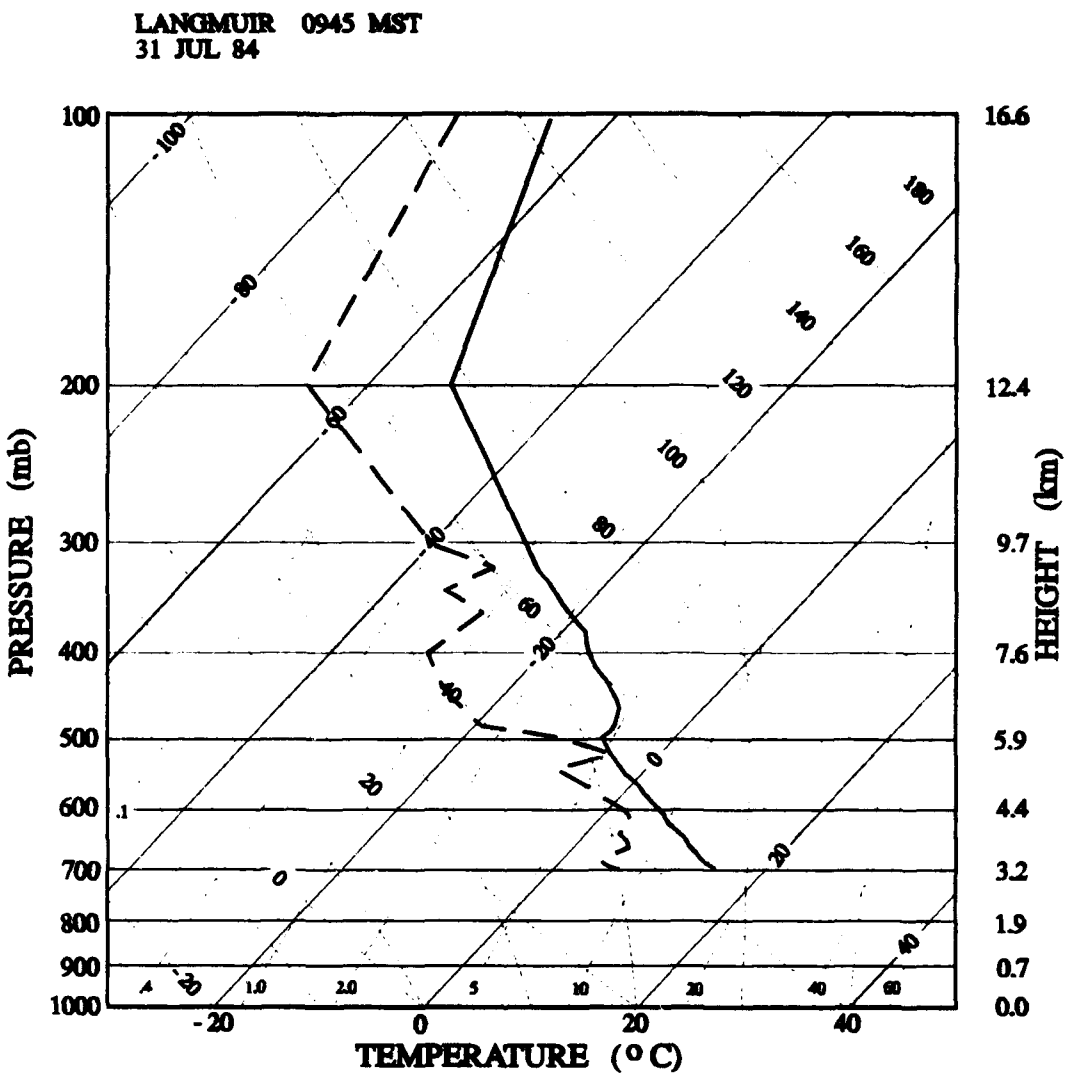

Fig. 3. As in Fig. 2, 0945 MST 31 July 1984 Langmuir Laboratory thermodynamic sounding.

(Winn, personal communication, 1987; Lang, 1991). The tracking problem persisted throughout the field experiment.

To overcome the problems with the rawinsonde wind data, alternative wind profiles for heights above the mountain top were constructed from the synthesized Doppler radar wind data (see Section 3.2.4). The only wind information available (other than rawinsonde) for below the height of the mountain top was an estimated profile provided by a TRIP scientist who participated in the observational phase of the experiment (Ziegler, personal communication, 1986). The profile was estimated by using Doppler radar wind data above the mountain top and extending the profile down to the valley floor using an Ekman spiral approximation. Figure 4 shows this profile. These alternative Doppler-derived and estimated wind profiles were combined and smoothed as described in Section 5.2.2 to initialize the numerical simulations.

3.2.3 Doppler Radar Observations And Analyses

All four Doppler radars in the network surrounding Langmuir Laboratory were operational on 31 July 1984. The radars collected radial velocity and reflectivity data intermittently between 0946 and 1058 MST, and collected data regularly between 1058 and 1219 MST with one break between 1119 and 1134 MST. The radial velocity data were used to synthesize three-dimensional wind fields at the same analysis times as the reflectivity analyses. The wind and reflectivity analyses then were used to investigate the 31 July 1984 storm development and to evaluate the numerical simulations of the storm development.

The multiple-Doppler wind analyses used in this study were performed by Lang (personal communication, 1992) and follow exactly his implementation of Ray *et al.*'s (1980) iterative method (Lang, 1991) for the 3 August case. The method determines the wind components at each analysis grid point by solving the set of equations con-

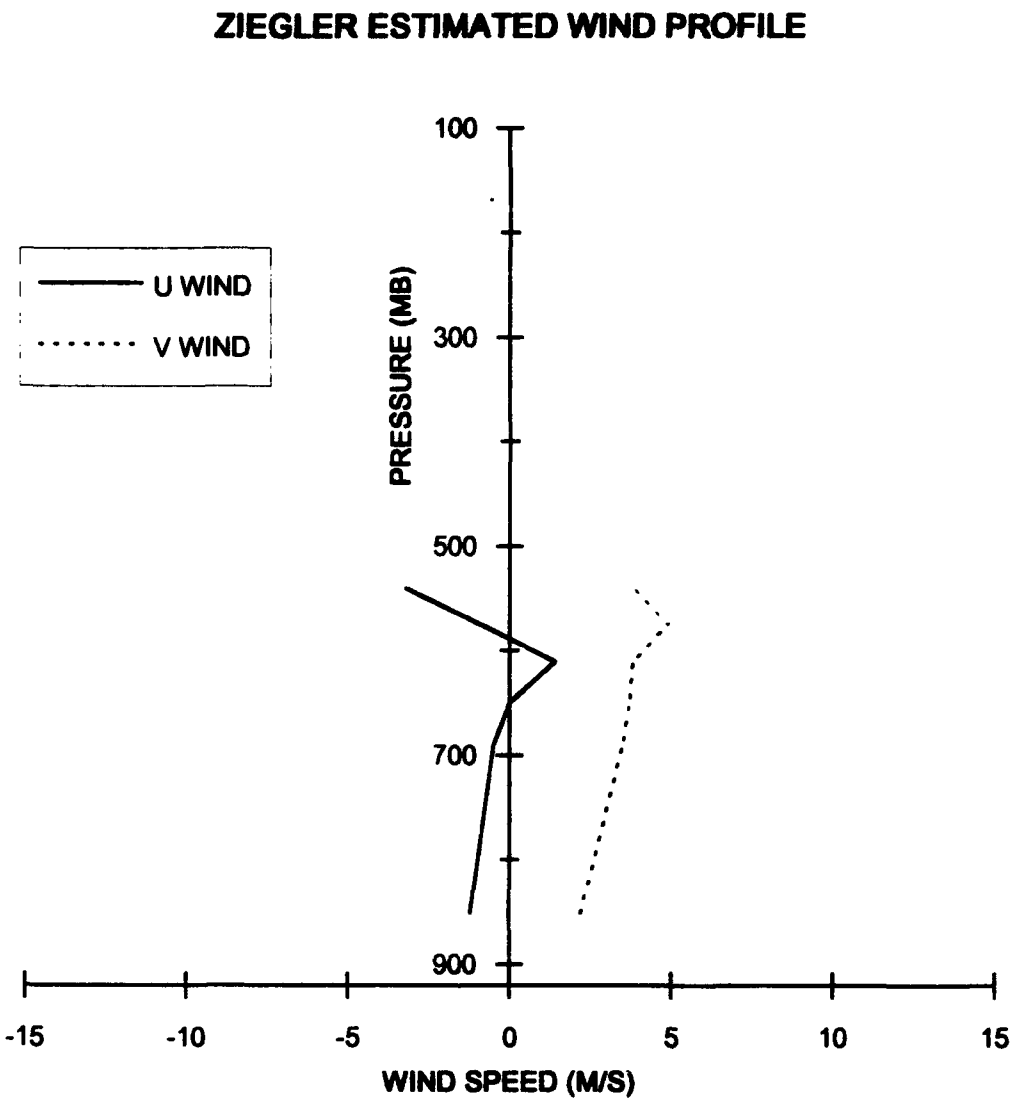

Fig. 4. Vertical profiles of estimated u (solid curve) and v (dashed curve) wind components from Ziegler, personal communication (1986). The horizontal axis is wind speed in meters per second, and pressure in millibars is along the vertical axis.

sisting of the overdetermined solutions for the u and v wind components (derived by using the radial velocity relationship for each radar), Joss and Waldvogel's (1970) particle terminal velocity relationship, and the anelastic continuity equation. The iteration first solves the u and v equations using a first guess for w, which is the previously calculated w for the layer immediately above the analysis grid point. At the top of the analysis grid, this value is a specified kinematic upper boundary condition for w. The continuity equation is next integrated downward to give a value for w at the bottom of the analysis grid box. A mean grid box w is calculated using the new values of w at the top and bottom of the grid box, and u and v are recalculated. The iteration continues until the solution converges. As in Lang's (1991) 3 August analysis, a vertical velocity of 2.0 m s^{-1} was imposed as the upper boundary condition over the entire analysis domain. Unlike the 3 August analysis which only used radial velocity data from three radars, the wind analyses for the 31 July case incorporated radial velocity data from all four radars. Lang (1991) showed Doppler-derived vertical velocities for the 3 August case compared favorably with observed vertical velocities collected from an instrumented aircraft.

The Doppler radar reflectivity and wind analyses were performed at 3-minute intervals starting at 0946 MST. As in Lang's (1991) 3 August analysis, the 31 July wind analysis was performed on a three-dimensional grid with 30 gridpoints on each side and 20 points in the vertical. The grid spacing was one-half kilometer in all directions. During the period of greatest storm development, the grid was centered on Langmuir Laboratory. At several times early in the analysis period, the analysis grid was centered south of Langmuir Laboratory to capture early convective development in that area. Throughout the entire analysis period, the lowest analysis level was 3.3 km MSL, putting it very near the elevation of the mountain tops near Langmuir.

This study follows Lang (1991) and takes the analyzed reflectivities directly from the NCAR CP-4 observations. As with the 3 August 1984 case (Lang, 1991), the CP-4 radar, located on the plain approximately 22 km to the northwest of Langmuir, afforded the best view of the 31 July 1984 storm development. Additionally, as noted by Lang (1991), the 5-cm wavelength CP-4 was less likely to be attenuated than the 3-cm NOAA radars.

3.2.4 Doppler-Derived Environmental Wind Profiles

Section 3.2.2 described the problems associated with both rawinsonde wind profiles collected on 31 July 1984. To avoid these problems and still achieve an observation-based estimate of the pre-storm environmental wind field, a scheme was developed to estimate the wind profile using Doppler radar data.

The Doppler-derived wind profiles were constructed with a scheme which uses the observed Doppler radar reflectivity and synthesized wind data described in Section 3.2.3. An inherent problem with using Doppler wind data to estimate pre-storm environmental winds is that the data are available only after convection develops enough to produce a radar echo. Thus, the Doppler-derived wind profile may be strongly influenced by convective circulations and may not necessarily represent the pre-storm wind profile. However, by assuming the wind field near the storm boundary is not significantly affected by the storm circulations, the pre-storm wind profile may be reasonably estimated by using only the wind information from the outer boundary of the radar echo. The scheme used in this study follows this approach.

As described in Section 3.2.3, Doppler radar reflectivity and synthesized wind data were available from 0946 through 1219 MST 31 July 1984. The data were available above the mountain top (approximately 3.3 km) on horizontal cross-sections spaced 0.5 km apart vertically. Very little wind data could be synthesized for the

times between 1019 and 1116 MST. For the purpose of creating environmental wind profiles, the radar reflectivity and synthesized wind data were divided into two sections; the first section included data collected between 0946 and 1019 MST, and the second section included data collected between 1116 and 1216 MST. For simplicity, the "cloud boundary" was defined as any region with a radar reflectivity of less than 15 dBZ. For each radar analysis time, the mean wind within the cloud boundary was computed at each horizontal level. Figures 5 and 6 show the resulting Doppler-derived wind profiles after interpolation to pressure levels for the data periods beginning at 0946 MST and 1116 MST, respectively. These profiles were combined as described in Section 5.2.2 to construct the base-state wind profiles used to initialize the numerical simulations.

3.2.5 Local Terrain

Langmuir Laboratory is located on South Baldy Peak at an elevation of 3255 m in the center of the Magdalena Mountains. Two ridges extend south and southeast (denoted R1 and R2 respectively) from South Baldy Peak. A valley (denoted V1) separates R1 and R2. Two minor ridges extend eastward from R2, one to the southeast (denoted R3) and the other to the northeast (denoted R4). A small valley (denoted V2) separates R2 and R3. A minor valley (denoted V3) separates R3 from R4. Finally, a deep valley (denoted V4) separates R4 from the main ridge that contains South Baldy Peak. Figure 7 shows the above features on a topographic map of the terrain surrounding Langmuir Laboratory.

3.3 31 July 1984 Storm History: Radar Observations

This section provides a description of the 31 July 1984 storm development using the Doppler radar reflectivity and synthesized wind analyses described in previous sections. The detailed analyses which follow track the storm development from weak

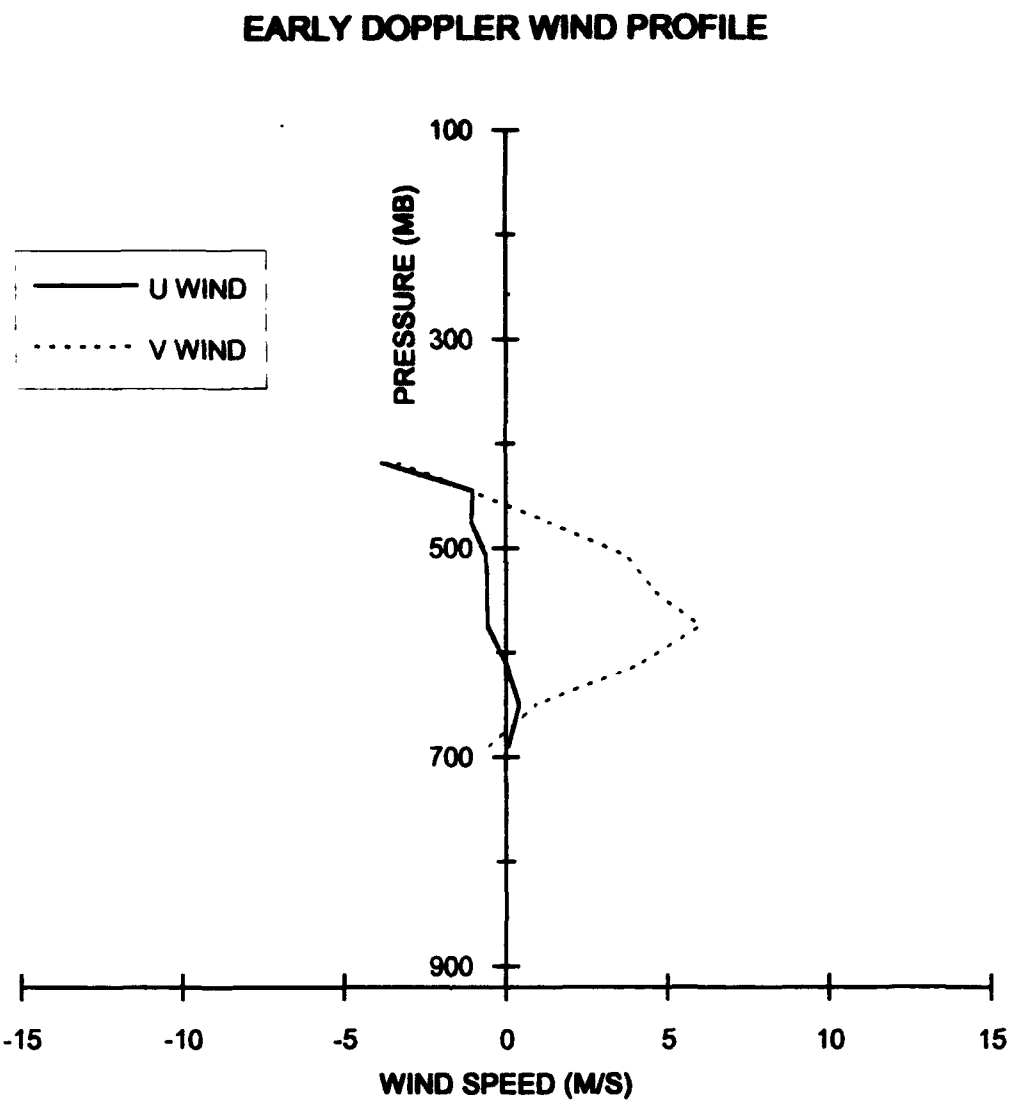

Fig. 5. Vertical profile of Doppler-derived u (solid curve) and v (dashed curve) wind components calculated as described in text using Doppler-derived wind data from the period between 0946 and 1019 MST. Axes labeled as in Fig. 4.

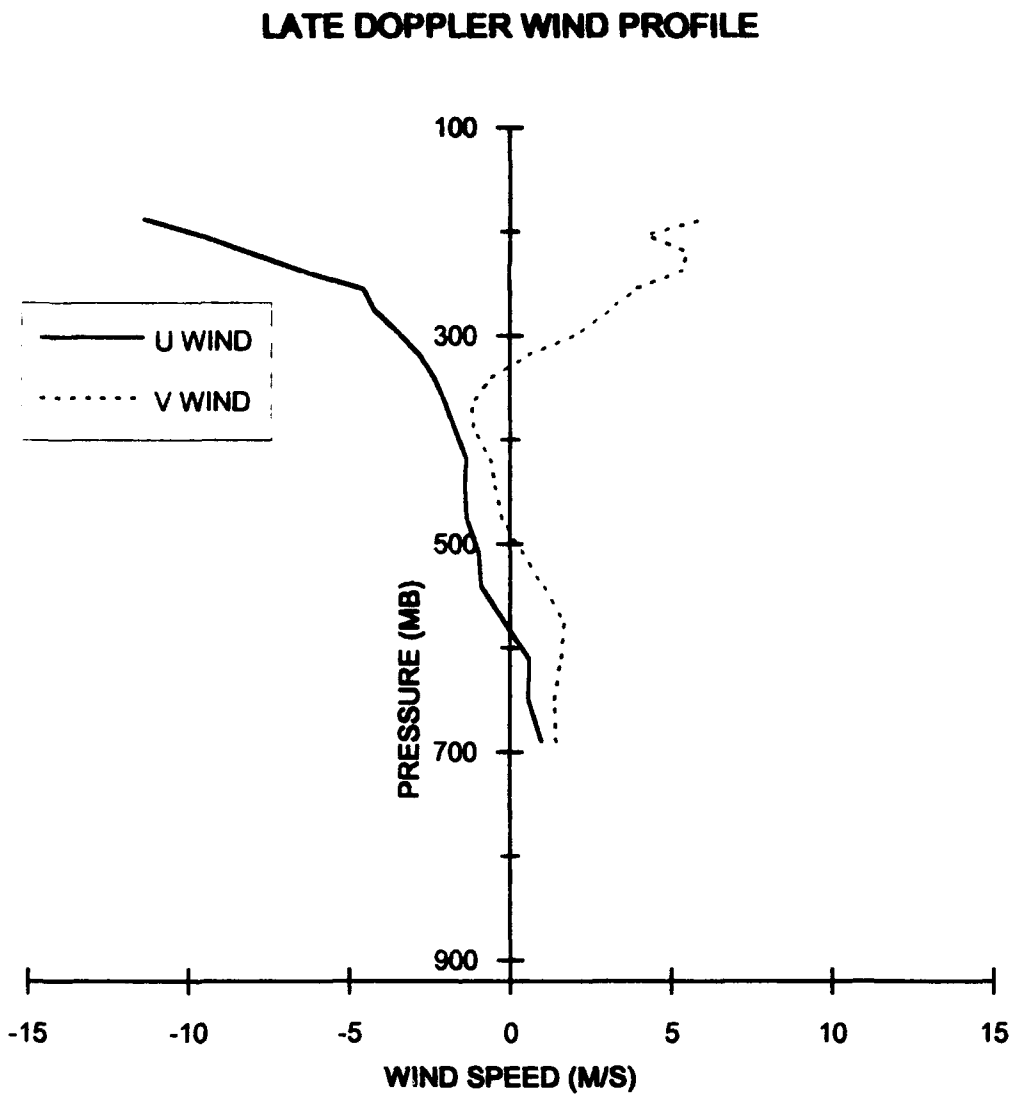

Fig. 6. Vertical profile of Doppler-derived u (solid curve) and v (dashed curve) wind components calculated as described in text using Doppler-derived wind data from the period between 1116 and 1216 MST. Axes labeled as in Fig. 4.

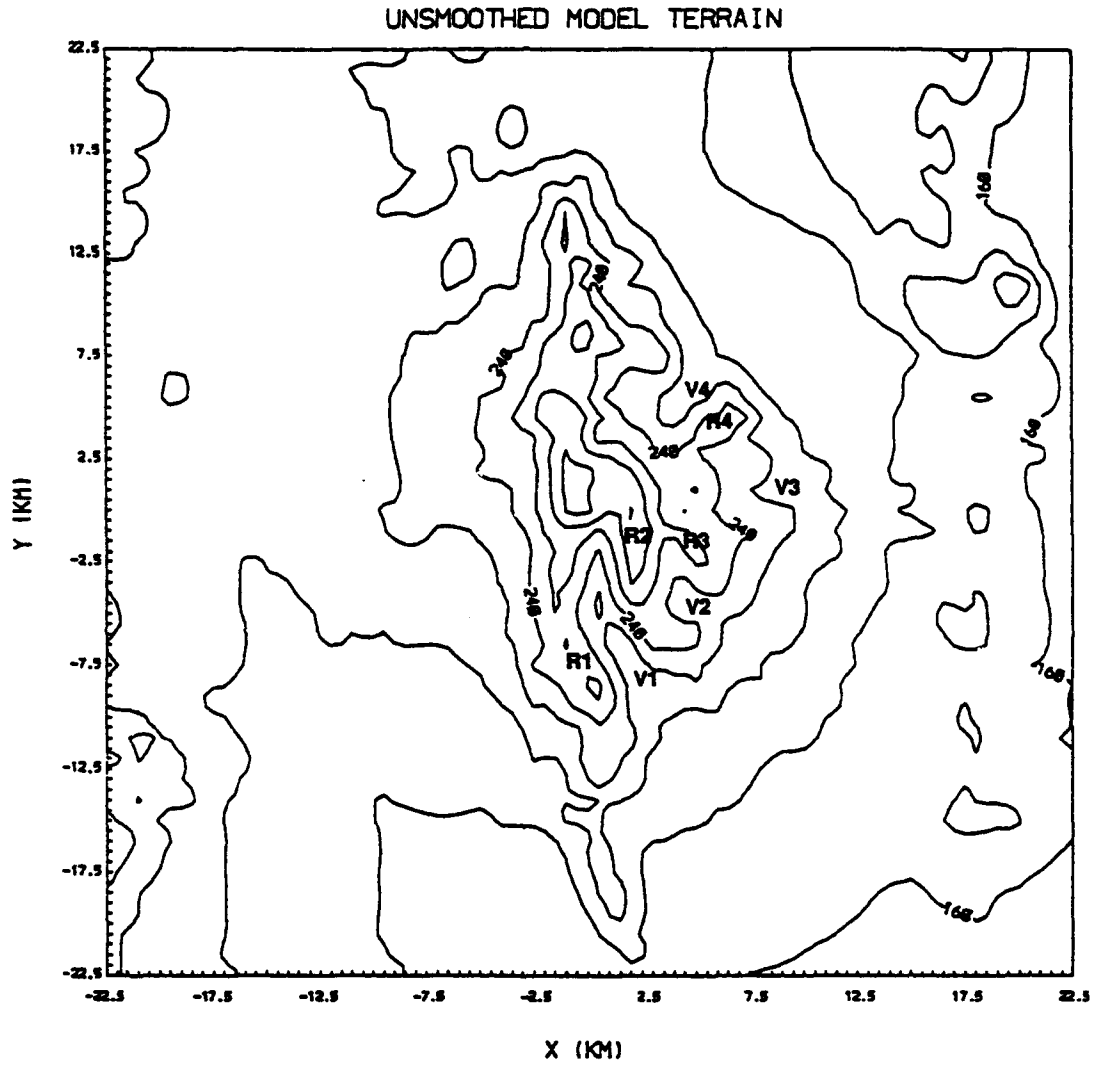

Fig. 7. Topographical view of terrain features near Langmuir Laboratory. Terrain elevation is relative to sea level in dekameters and contour intervals are every 20 dekameters. The horizontal and vertical axes are labeled in kilometers. The origin (0,0) is located at Langmuir Laboratory. Valleys and ridges are labeled as described in text.

initial activity in the mid-morning hours to full development shortly before noon to gradual decay shortly after noon. All (x,y) coordinate references are in kilometers and based on a coordinate system with its origin at Langmuir Laboratory.

3.3.1 Pre-Storm Development

The NCAR CP-4 radar first detected an echo at 0946 MST over the eastern slope of the main ridge approximately 1.5 km north of Langmuir Laboratory. The first echo extended vertically to only 6.3 km MSL. The radar detected several shallow, weak, short-lived showers between 0946 and 1110 MST. During this period one shallow shower persisted north of Langmuir Laboratory. The shower's radar returns rarely exceeded 40 dBZ and never extended above 6.3 km MSL. Although these early showers never developed into thunderstorms, they served to moisten the low-level environment for later storm development.

3.3.2 Storm Initiation And Early Development

By 1116 MST the CP-4 radar detected an organized cell (denoted hereafter as C1) (-1.0, -4.5) with returns of approximately 20 dBZ over and east of R1 south of Langmuir Laboratory. C1 was the first in a series of cells that developed and combined to form a multi-cellular storm. For the purposes of this study a cell is defined, as in Lang's (1991) analysis, as any relative reflectivity and/or updraft maximum that exhibits vertical continuity. The radar also detected weak returns over R2 southeast of the Laboratory. The radar returns at elevation 3.3 km MSL located along the main ridge just to the north of Langmuir Laboratory appear to be ground clutter and persisted through most of the remaining analysis times. By 1119 MST, C1's radar returns (-1.0, -4.5) reached 30 dBZ, and 20 dBZ echoes extended to 7.3 km MSL. The activity over R2 southeast of Langmuir continued to develop slowly (Fig. 8).

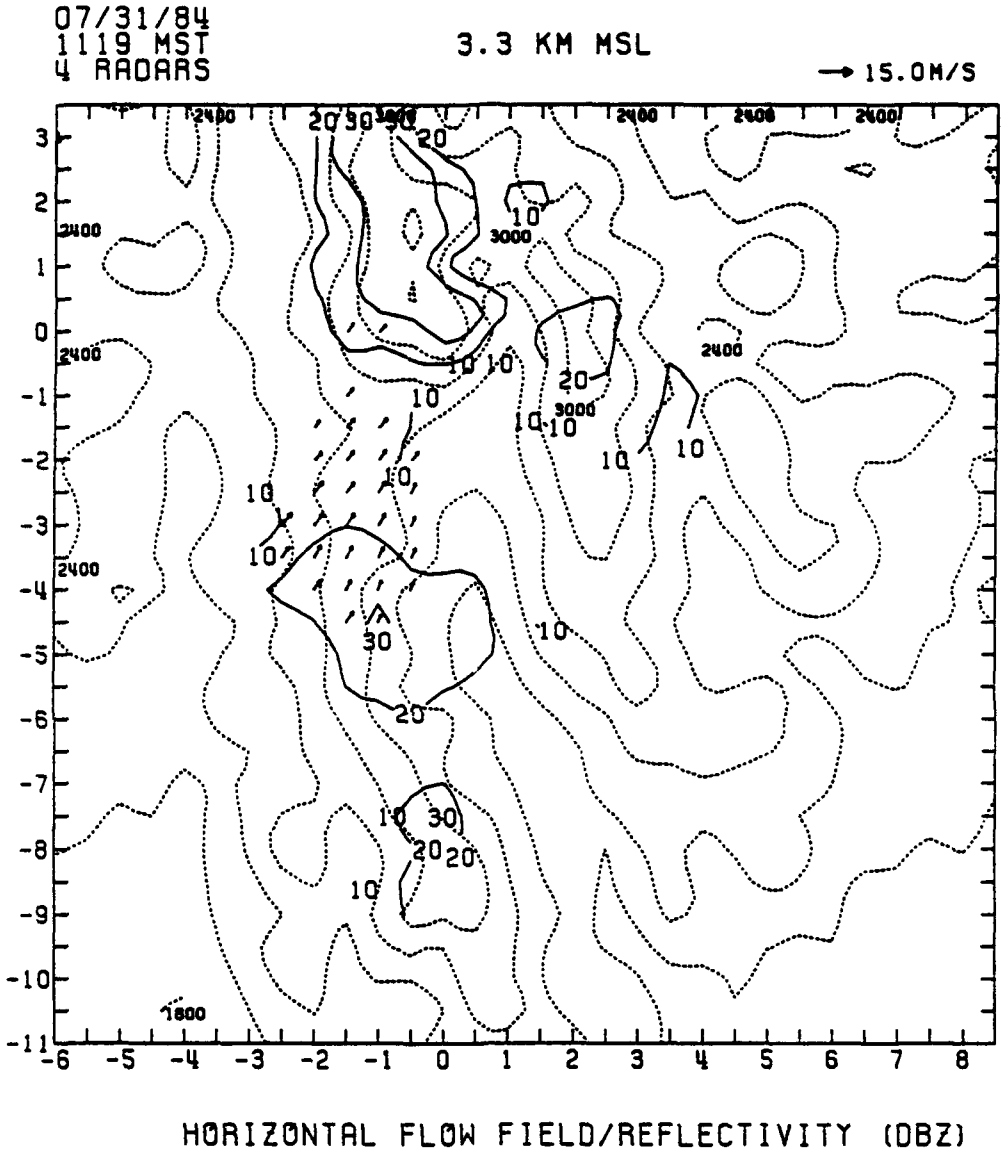

Fig. 8. Horizontal cross-section of observed radar reflectivities in dBZ and vector velocities at an altitude of 3.3 km relative to mean sea level at 1119 MST 31 July 1984. Reflectivities (solid contours) are contoured every 10 dBZ. Vector velocities are ground-relative with a vector length of one grid interval (0.5 km) equal to 15 m s^{-1}. Terrain elevations (dashed contours) are relative to sea level in meters, and contour intervals are every 200 meters. The origin is at Langmuir Laboratory, and the axes are labeled in kilometers.

At the next available analysis time, 1134 MST, the radar detected two well-defined cells over the ridges: C1 (0.0, -5.0) over R1 south of Langmuir; and a new cell (denoted hereafter as C2) (2.5, -1.0) over R2 approximately 3 km east-southeast of Langmuir. C1's radar reflectivities exceeded 40 dBZ and C2's exceeded 45 dBZ. C1's 20 dBZ returns extended to 9.3 km MSL, while C2's extended to 10.0 km. The horizontal wind analysis at 3.3 km MSL showed significant upslope flow on the western side of R1 along with upslope flow through V1. The two flows converged very near the location of C1. Additionally, upslope flow on the eastern side of R2 converged with the V1 flow in the vicinity of C2. Above 6.3 km MSL, the horizontal wind analysis also showed strong divergent flow over C1 and weak divergence over C2 (Fig. 9). C1 contained a 1.5 km-wide updraft located on the southeastern edge of the cell and an approximately 1.0 km-wide downdraft located just to the north of the updraft. The updraft exceeded 9.0 m s^{-1} between 3.3 and 6.3 km MSL with a maximum updraft of 12.0 m s^{-1} located at 5.3 km MSL. The updraft diminished rapidly above 7.3 km MSL. The downdraft averaged approximately 3.0 m s^{-1} between 3.3 and 4.3 km MSL. C2 also contained a 1.5 km-wide updraft located on the southeastern edge of the cell and an approximately 1.0 km-wide downdraft located north of the updraft. The updraft exceeded 9.0 m s^{-1} between 5.3 and 7.3 km MSL and remained identifiable up to 10.3 km MSL. Like C1's downdraft, C2's extended between 3.3 and 4.3 km MSL.

3.3.3 Mature Storm Development

By 1137 MST, both C1's and C2's maximum reflectivities exceeded 50 dBZ at 3.3 km MSL. The CP-4 radar again detected 20 dBZ returns up to 9.3 km MSL from C1 (0.0, -4.5) and to 10.0 km MSL from C2 (2.5, -1.5). The horizontal wind analysis at 3.3 km MSL showed little change from the 1134 MST analysis. The strong di-

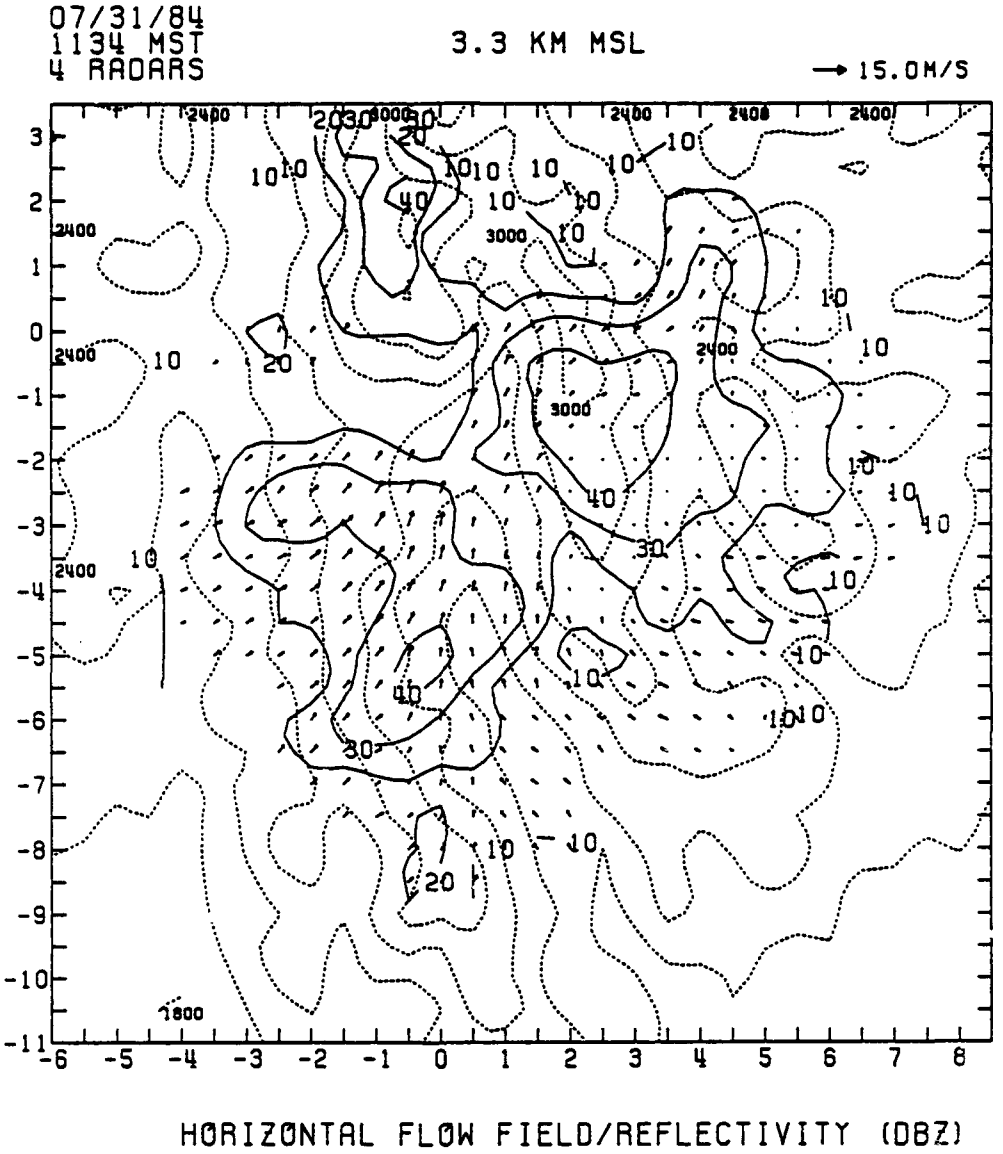

Fig. 9a. Horizontal cross-section of observed radar reflectivities and vector velocities as in Fig. 8, except at 1134 MST and at 3.3 km MSL.

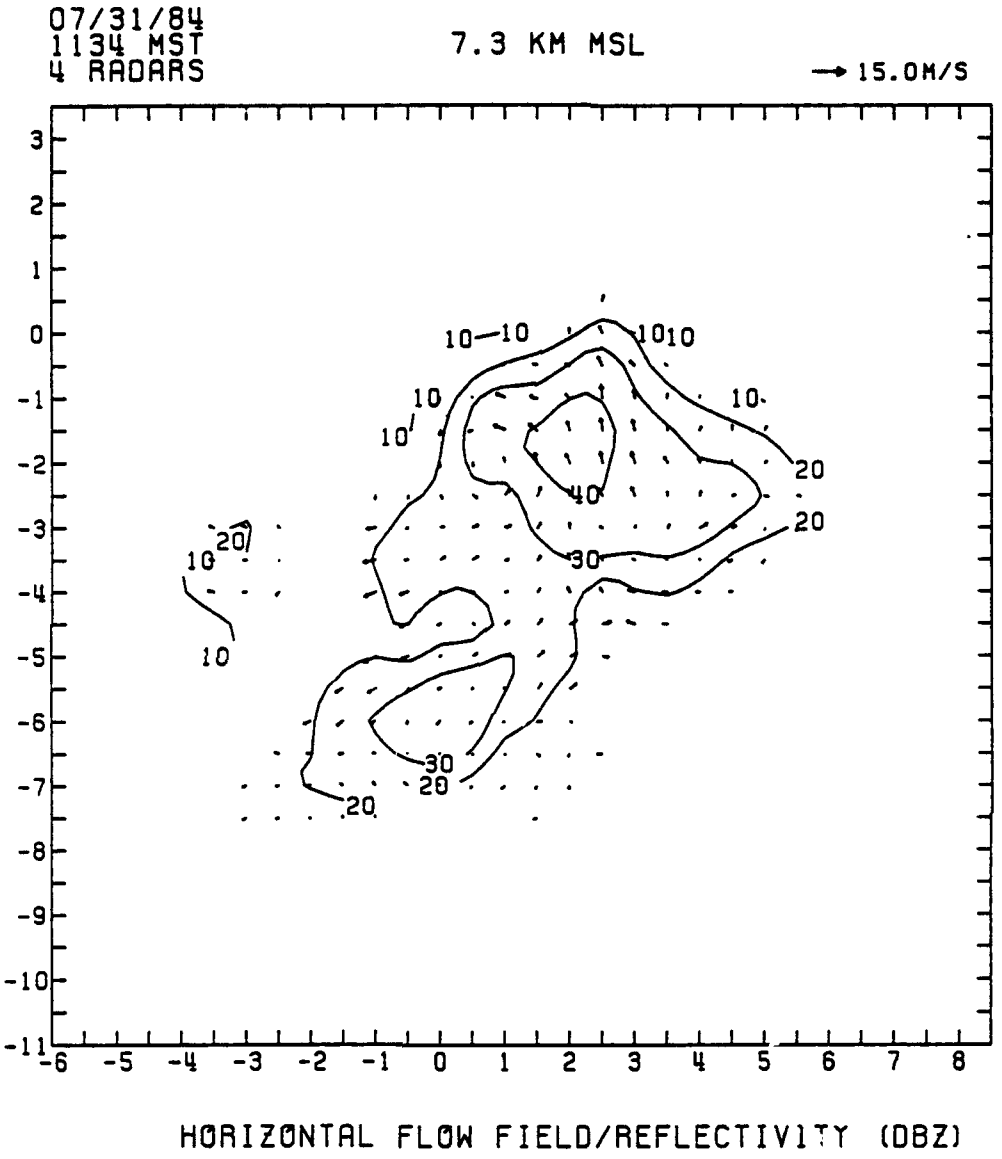

Fig. 9b. As in Fig. 8, horizontal cross-section of observed radar reflectivities and vector velocities for 1134 MST and at 7.3 km MSL.

vergence above 6.3 km MSL continued over C1 while virtually non-divergent flow existed over C2. C1's updraft expanded to a width of approximately 3.0 km. The enlarged updraft contained two areas of maximum vertical velocities at low levels which merged into a single updraft at 6.3 km. C1's updraft exceeded 9.0 m s^{-1} between 4.3 and 7.3 km MSL with a maximum of 12.0 m s^{-1} between 5.3 and 6.3 km MSL. C1's downdraft became extremely weak (less than 3.0 m s^{-1}). C2's updraft began to weaken considerably from the bottom with vertical velocities exceeding 9.0 m s^{-1} only between 7.3 and 8.3 km MSL. C2's downdraft became much stronger than at 1134 MST, exceeding 3.0 m s^{-1} between 3.3 and 6.3 km MSL with a maximum of 6.0 m s^{-1} at 3.3 km MSL. Strong divergent flow near 7.0 km MSL over C1 contributed to the weakening of C2's updraft.

The trend of C1 strengthening and C2 weakening continued at 1140 MST. The radar continued to detect maximum returns of 50 dBZ from both cells, but C1's strongest returns (-0.25, -4.75) extended higher (to 4.3 km MSL) than at the previous time. C1's double-maxima updraft continued with the northern branch strengthening to 15.0 m s^{-1} between 5.3 and 6.3 km MSL while the southern branch remained at about 9.0 m s^{-1}. The two branches merged near 8.3 km MSL. Meanwhile, C2's (2.25, -0.75) updraft weakened to about 6.0 m s^{-1}. Both cells contained weak downdrafts at this analysis time. C1's downdraft remained less than 3.0 m s^{-1}, while C2's decreased to about 3.0 m s^{-1} between 3.3 and 4.3 km MSL. The vertical cross-section shown in Figure 10 again shows strong divergent flow near 7.0 km MSL over C1 undercutting the remnants of C2's updraft.

By 1143 MST, both cells had weakened from their previous strengths. C1's maximum reflectivity (-0.25, -4.0) decreased to 45 dBZ and C2's (2.25, -1.75) decreased to 40 dBZ. The horizontal flow at 3.3 km MSL remained virtually un-

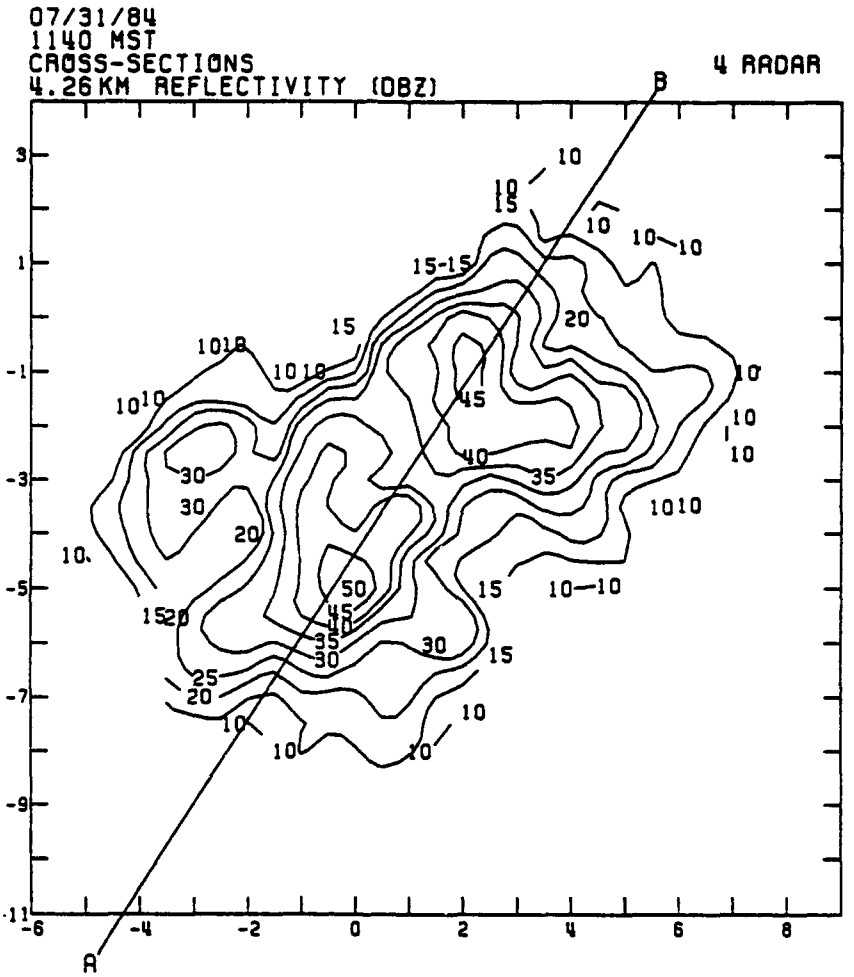

Fig. 10a. Horizontal cross-section of observed radar reflectivities in dBZ at an altitude of 4.3 km relative to mean sea level at 1140 MST 31 July 1984. Reflectivities are contoured every 5 dBZ. The origin is at Langmuir Laboratory. The axes are labeled in kilometers. Line AB shows the location of the vertical cross-section in Fig. 10b.

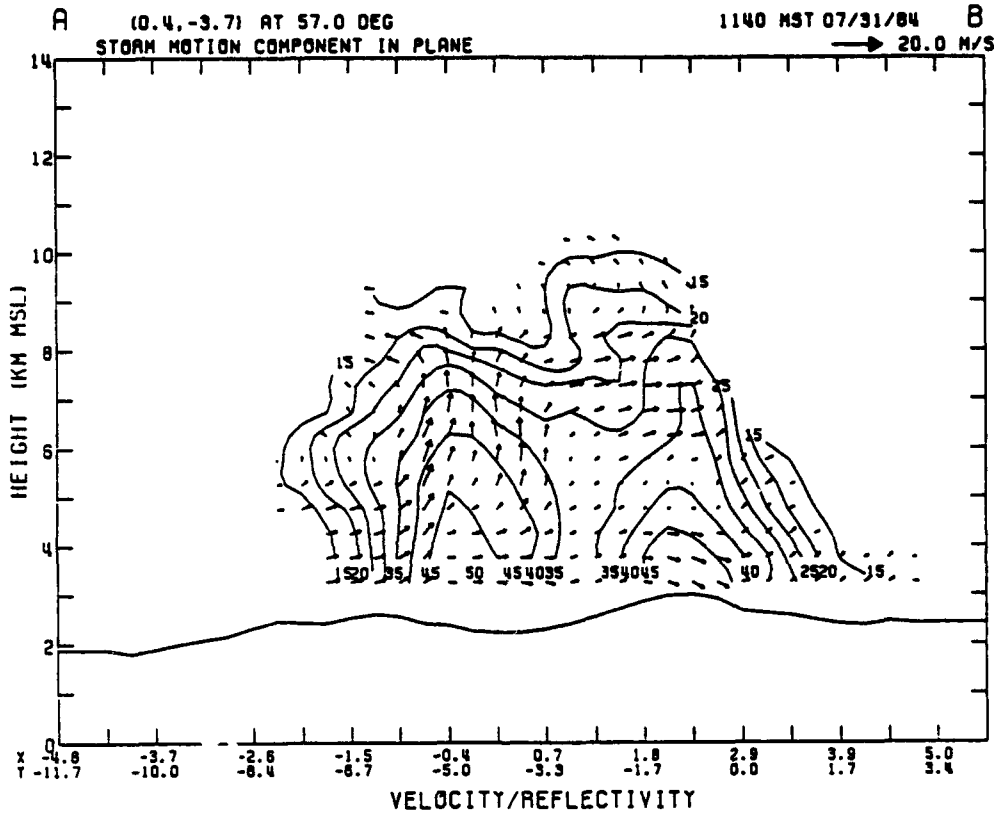

Fig. 10b. Vertical cross-section of observed radar reflectivities in dBZ and vector velocities at 1140 MST 31 July 1984. Reflectivities are contoured every 5 dBZ. Vector velocities are ground-relative with the vector length shown in upper right-hand corner of figure equal to 20 m s^{-1}. Cross-section location AB is shown in Fig. 10a.

changed from previous times. The horizontal wind analyses between 4.3 and 5.3 km MSL, however, showed that the circulation induced by C1 significantly diminished the southwesterly flow into C2 found in earlier analyses at these levels. C1's updraft remained split with the northern branch dominant with vertical velocities exceeding 12.0 m s^{-1} at 7.3 km MSL. The southern branch contained vertical velocities as strong as 9.0 m s^{-1}. C1 again developed an identifiable downdraft of about 3.0 m s^{-1} between 3.3 and 4.3 km MSL. C2's updraft became very weak (approximately 3.0 m s^{-1}) and narrow (approximately 0.5 km wide). C2's downdraft remained at about 3.0 m s^{-1} at 3.3 km MSL.

At 1146 MST both cells began to show some signs of regeneration. The reflectivities from both cells remained about the same as at 1143 MST. The horizontal wind analysis shows continued strong low-level convergence near the location of C1 (0.0, -3.5) and increased low-level convergence in the vicinity of C2 (2.25, -1.25). Strong upper-level divergence continued over C1 (Fig. 11). The split updraft continued in C1 with the northern branch remaining dominant. A new updraft formed at this time on the eastern edge of C1 (over the western slopes of R2). This updraft was approximately 1.0 km wide and reached a maximum strength of 9.0 m s^{-1} before merging with the other two branches of C1's updraft at 8.3 km. C2's updraft remained very narrow, but increased in strength to over 9.0 m s^{-1} between 6.3 and 8.3 km MSL with a maximum of 12.0 m s^{-1} at 7.3 km MSL. C1's downdraft remained 3.0 m s^{-1}, but increased in vertical extent to 5.3 km MSL. C2's downdraft remained unchanged from the previous analysis time (Fig. 12).

The regeneration trend of C1 (0.0, -4.25) continued at 1149 MST as its maximum reflectivity increased to 50 dBZ. C2's (3.0, -1.75) maximum reflectivity remained steady at 40 dBZ, but extended in height to 7.3 km MSL from the previously ob-

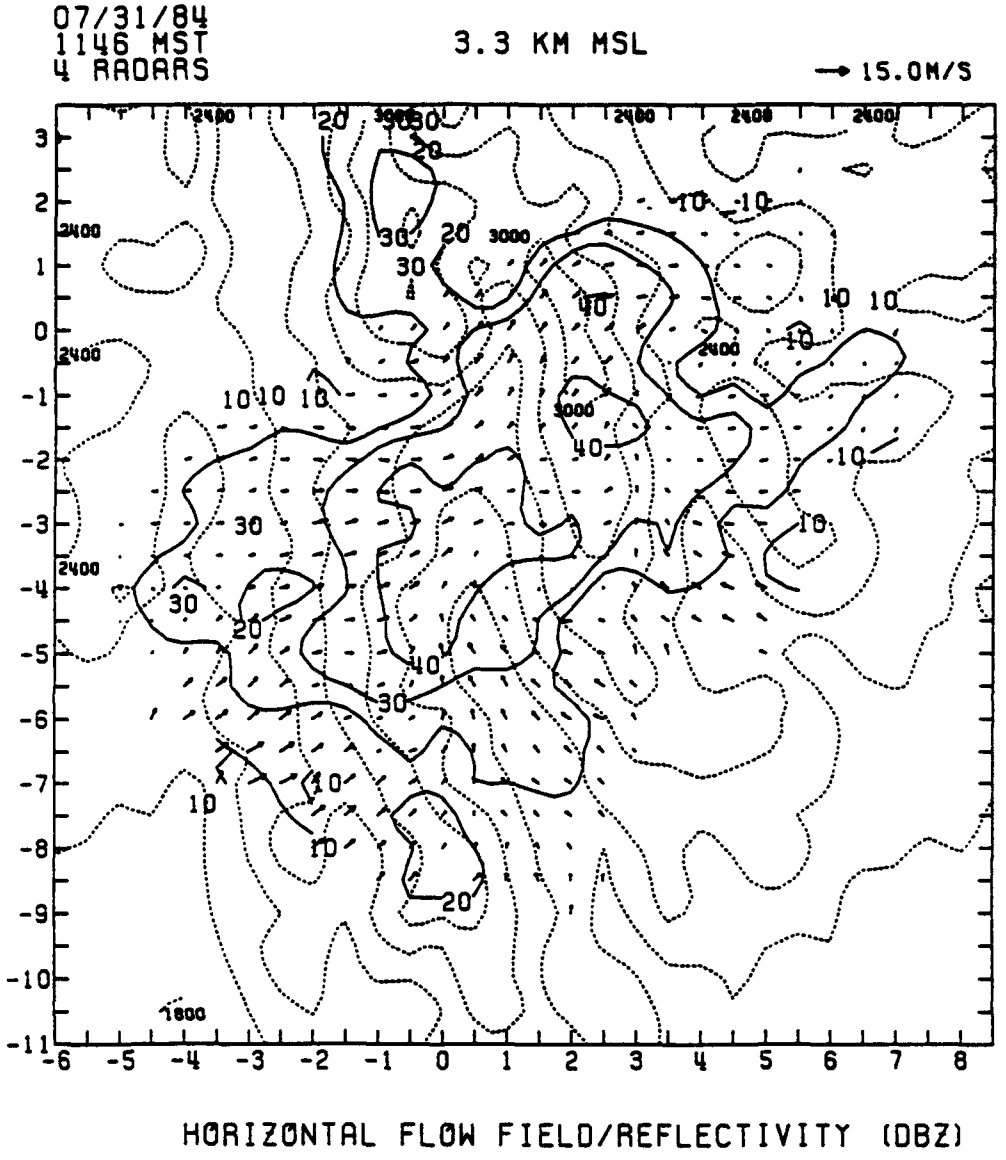

Fig. 11a. Horizontal cross-section of observed radar reflectivities and vector velocities as in Fig. 8, except at 1146 MST and at 3.3 km MSL.

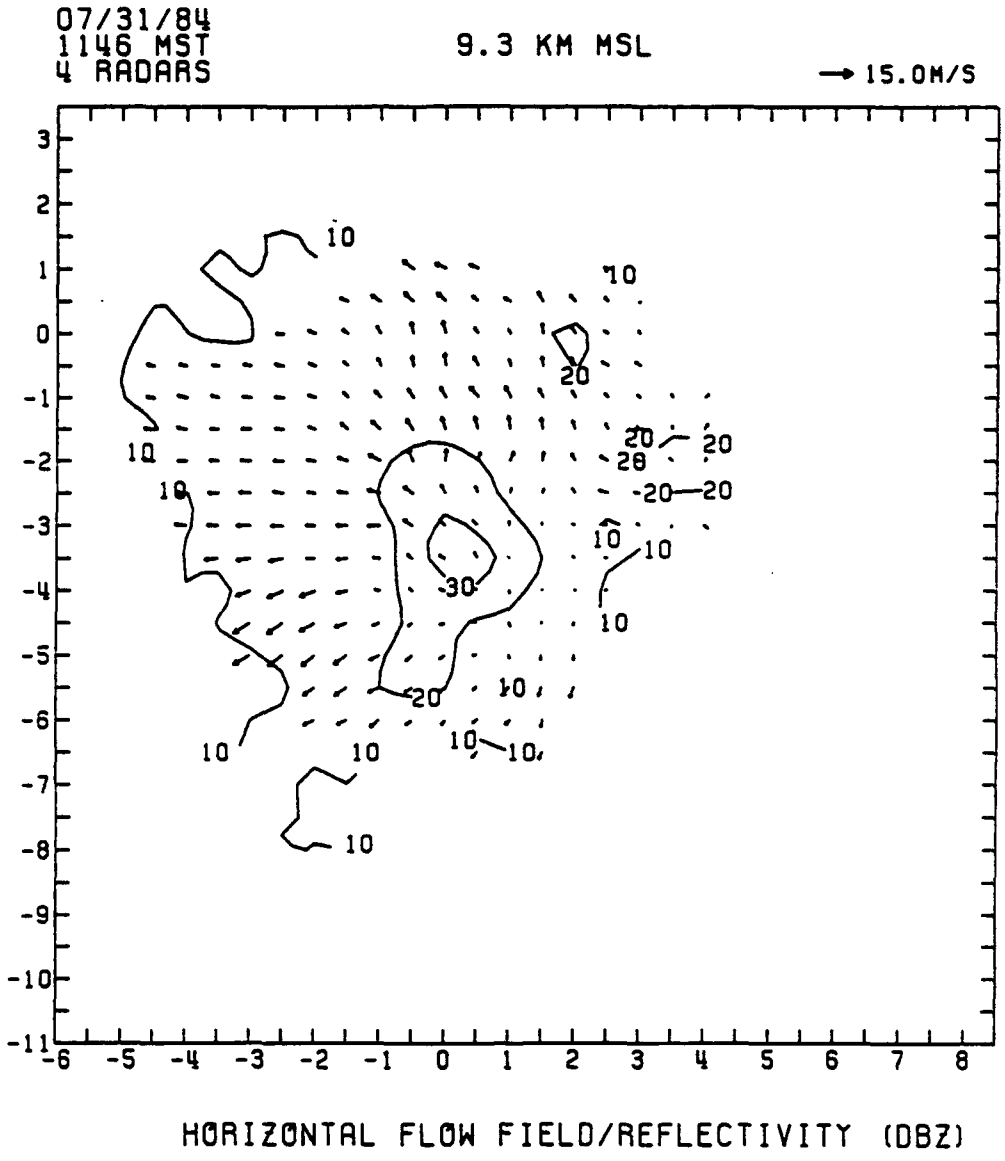

Fig. 11b. As in Fig. 8, horizontal cross-section of observed radar reflectivities and vector velocities for 1146 MST and at 9.3 km MSL.

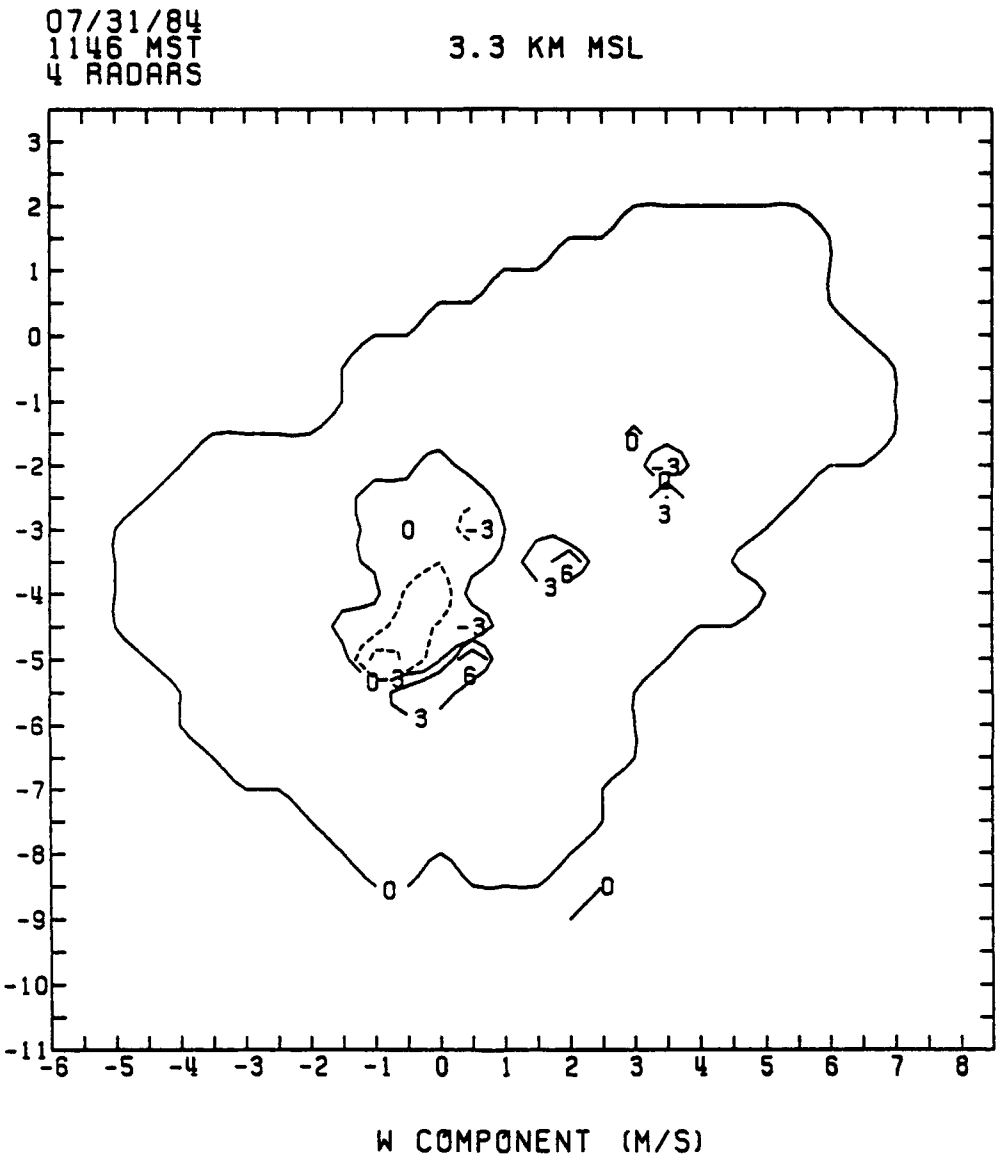

Fig. 12a. Horizontal cross-section of observed vertical velocities at an altitude of 3.3 km relative to mean sea level at 1146 MST 31 July 1984. Velocities are contoured every 3.0 m s^{-1} starting at 0 m s^{-1}. Solid contours denote upward vertical velocities (positive w). and dashed contours denote downward vertical velocities (negative w). Origin and axes are as in Fig. 8.

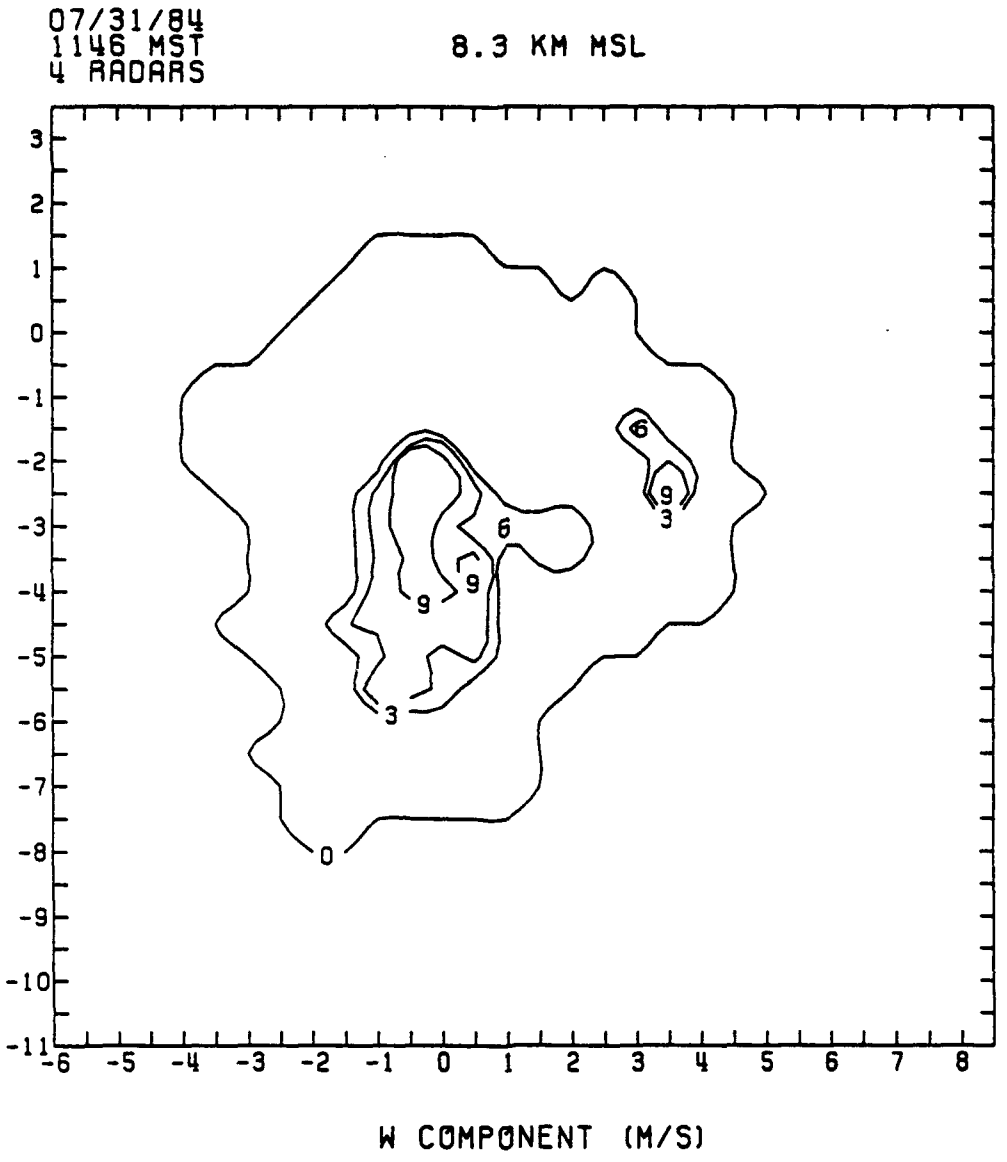

Fig. 12b. Horizontal cross-section of observed vertical velocities at 1146 MST 31 July 1984 as in Fig. 12a except at 8.3 km MSL.

served 3.3 km MSL. Low-level convergence continued in the vicinity of C1 and C2, while strong divergence continued over C1. The reflectivity analysis also shows the development of a new cell (-0.5, -7.5) (denoted hereafter as C3) as an elongation in the reflectivity contours along R1's ridge axis (Fig. 13). C1's updraft remained split at this time. The new updraft noted on the eastern edge of cell C1 at 1146 MST dominated C1 with a maximum vertical velocity of 18.0 m s^{-1} at 6.3 km MSL (1.25, -4.0). C1's southern updraft remained relatively strong with a maximum updraft of 12.0 m s^{-1} (0.0, -5.5). The two updrafts merged with each other and with the remnants of the older third updraft at 8.3 km MSL. C2's updraft (3.25, -2.5) remained relatively weak, barely reaching 9.0 m s^{-1} at 8.3 km MSL. C3 contained no distinguishable updrafts or downdrafts at this time. The downdrafts from both C1 and C2 combined to form a broad area of downward motion covering approximately 12 km^2 below 4.3 km MSL northwest of the updrafts. The downdrafts reached a maximum strength of 6.0 m s^{-1} (Fig. 14).

By 1152 MST, C1 (-0.25, -4.0) had drifted slowly northward. C2 lost its identity after slowly weakening and being absorbed by the northward-moving C1. C1 remained strong with its maximum reflectivity exceeding 50 dBZ. C3 (-0.25, -6.5) showed further signs of development with its maximum reflectivity exceeding 30 dBZ between 3.3 and 8.3 km MSL. The horizontal wind analysis continued to show strong convergence over both R1 and R2, especially at 4.3 km MSL. Strong divergence existed above both C1 and C3 at and above 8.3 km MSL. C1 continued with a very complex updraft structure below 8.3 km MSL. Several small updrafts formed at this time below 8.3 km MSL, especially along the southeastern edge of the cell. These were likely caused by the convergence of the downdraft air as it spilled down the valleys and the southeasterly flow up the valleys ahead of the storm. The updrafts

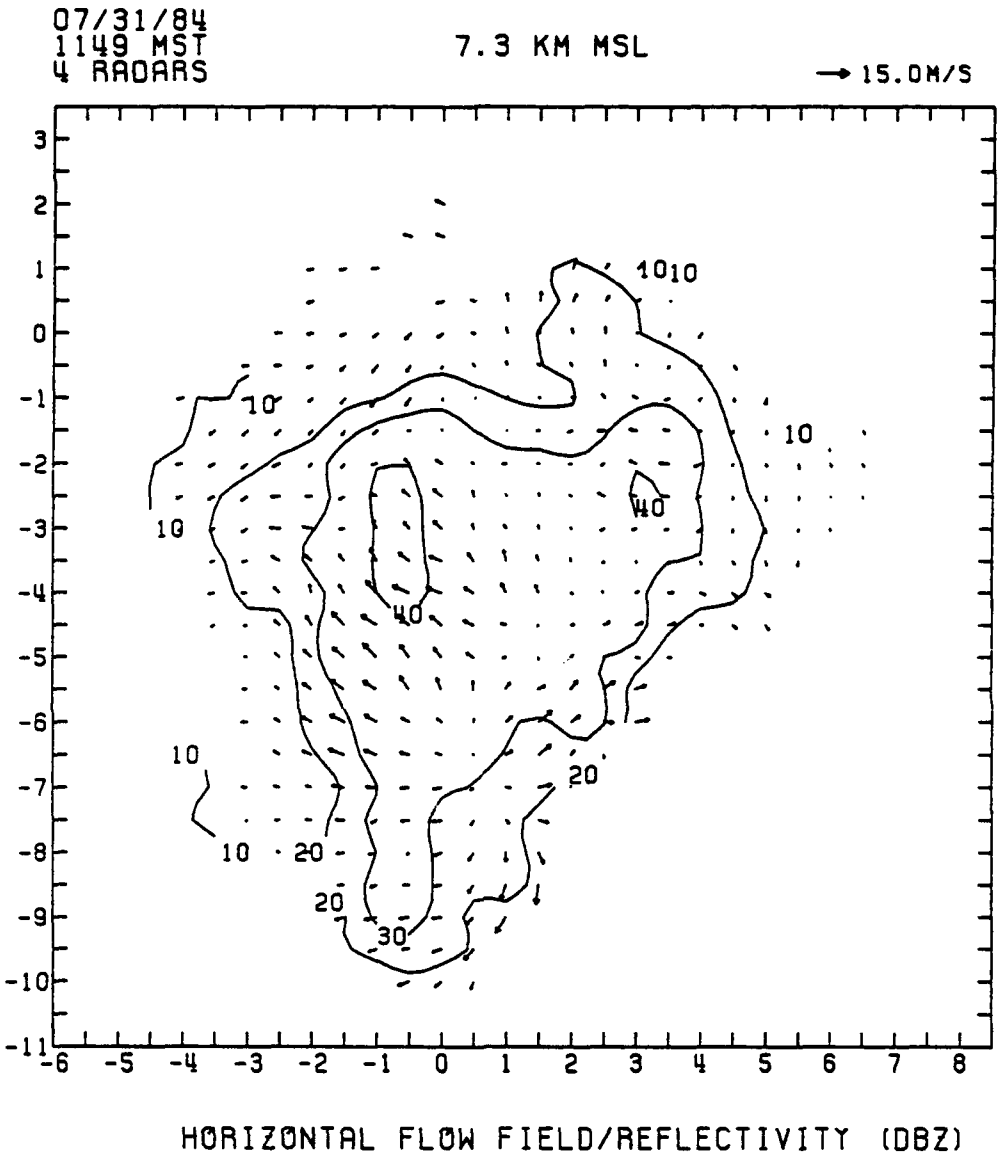

Fig. 13. As in Fig. 8, horizontal cross-section of observed radar reflectivities and vector velocities for 1149 MST and at 7.3 km MSL.

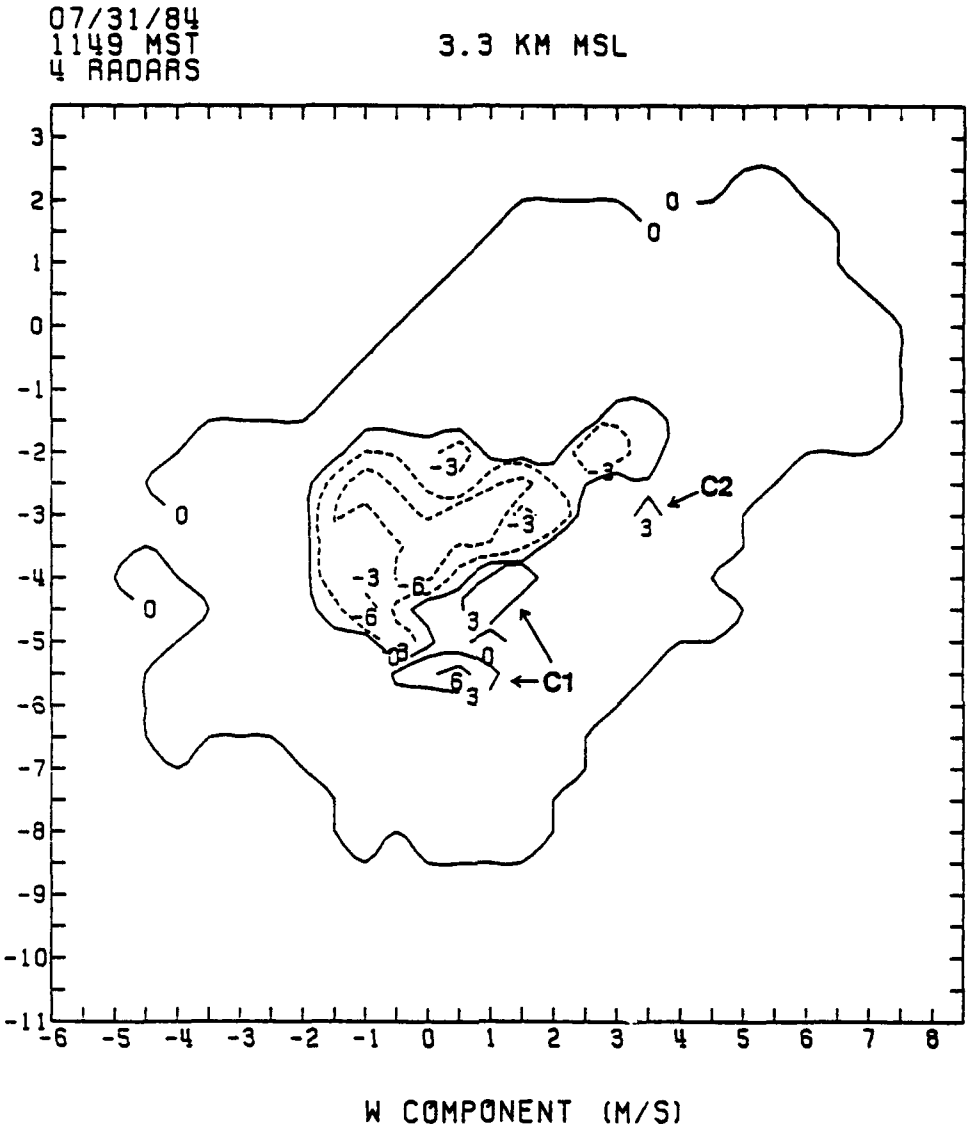

Fig. 14a. Horizontal cross-section of observed vertical velocities as in Fig. 12a, except at 1149 MST and at 3.3 km MSL. Labels indicate locations of updrafts associated with cells C1 and C2.

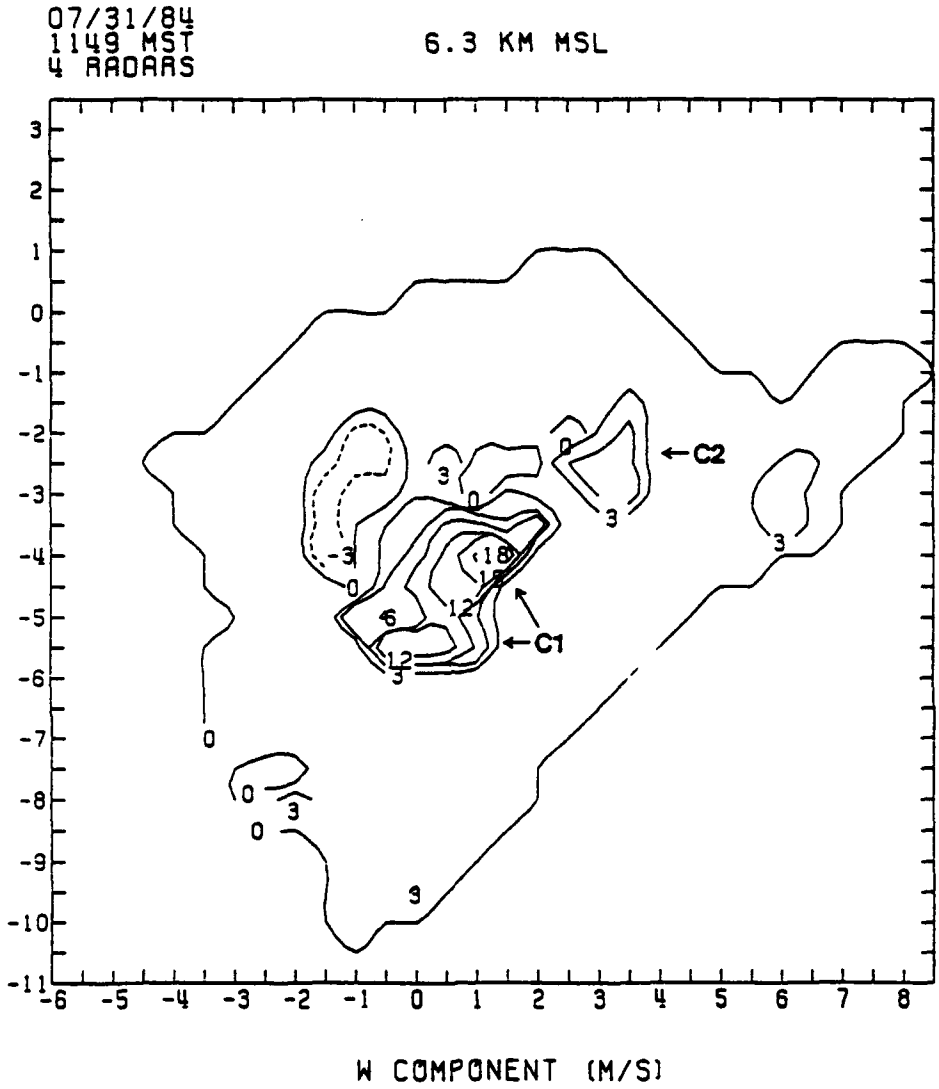

Fig. 14b. As in Fig. 12a, horizontal cross-section of observed vertical velocities for 1149 MST and at 6.3 km MSL. Labels indicate locations of updrafts associated with cells C1 and C2.

combined to form the main C1 updraft with a maximum strength of 12.0 m s^{-1}. C3's narrow updraft (approximately 0.5 km wide) strengthened markedly from the previous analysis to a maximum strength of 15.0 m s^{-1}. C1's downdraft continued to cover a broad area with a maximum strength of 6.0 m s^{-1}. The vertical cross-sections shown in Figure 15 show that C1 had a significant backward tilt. As a result, the precipitation and the precipitation-induced downdraft occurred north and west of the updraft so that they did not interfere with it. Similar storm structures and circulations have been observed in some long-lived severe storms (see e.g., Browning *et al.*, 1976).

Poor data quality at 1155 MST prevented an analysis for that time. At 1158 MST, C1 (0.5, -3.5) reached its peak intensity, and C3 (-0.5, -6.5) increased in strength slightly. C1's area of 50 dBZ reflectivities grew substantially from 1152 MST, and C3's reflectivities increased to 40 dBZ. A new cell (5.0, -3.5) (denoted hereafter as C4) developed at this time over R3 (Fig. 16). The maximum reflectivity from C4 reached 40 dBZ at 7.3 km MSL. Strong low-level convergence continued over both R1 and R2. The horizontal wind analysis showed strong divergence over C1 between 10.3 and 12.3 km MSL and over C3 and C4 at 8.3 km MSL. C1's multiple updrafts continued, but weakened considerably at low levels. The analysis showed updrafts greater than 9.0 m s^{-1} only above 8.3 km MSL with maximum updrafts of 12.0 m s^{-1}. The updrafts merged at 11.3 km MSL. The downdraft associated with C1 became very broad and strong by this time, exceeding 12.0 m s^{-1} at 3.3 km MSL. The downdraft impacted the surface very near the top of V1. The analysis also showed a strong updraft (maximum strength 18.0 m s^{-1}) associated with C3 located directly over R1. The vertical cross-sections shown in Figure 17 show the strong interrelationships between the circulations of all three cells. For example, the

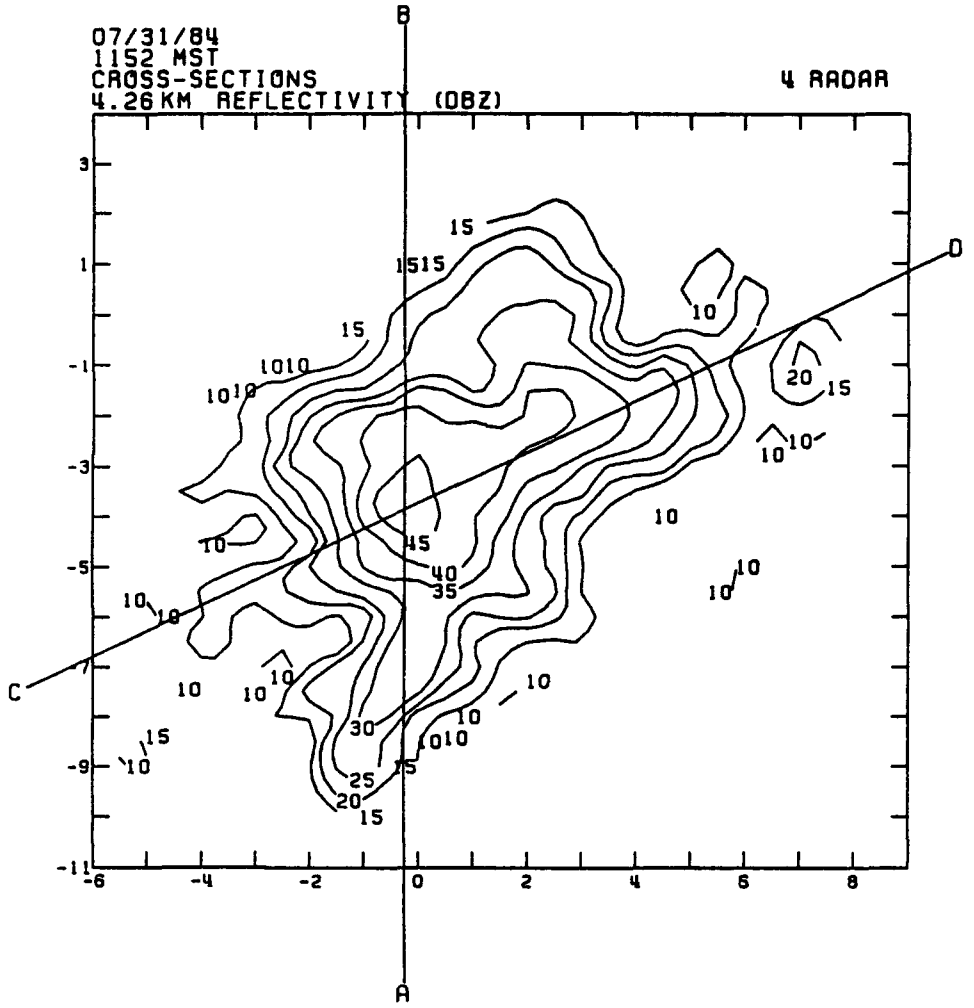

Fig. 15a. Horizontal cross-section of observed radar reflectivities as in Fig. 10a. except at 1152 MST and 4.3 km MSL. Lines AB and CD show locations of vertical cross-sections in Figs. 15b and 15c, respectively.

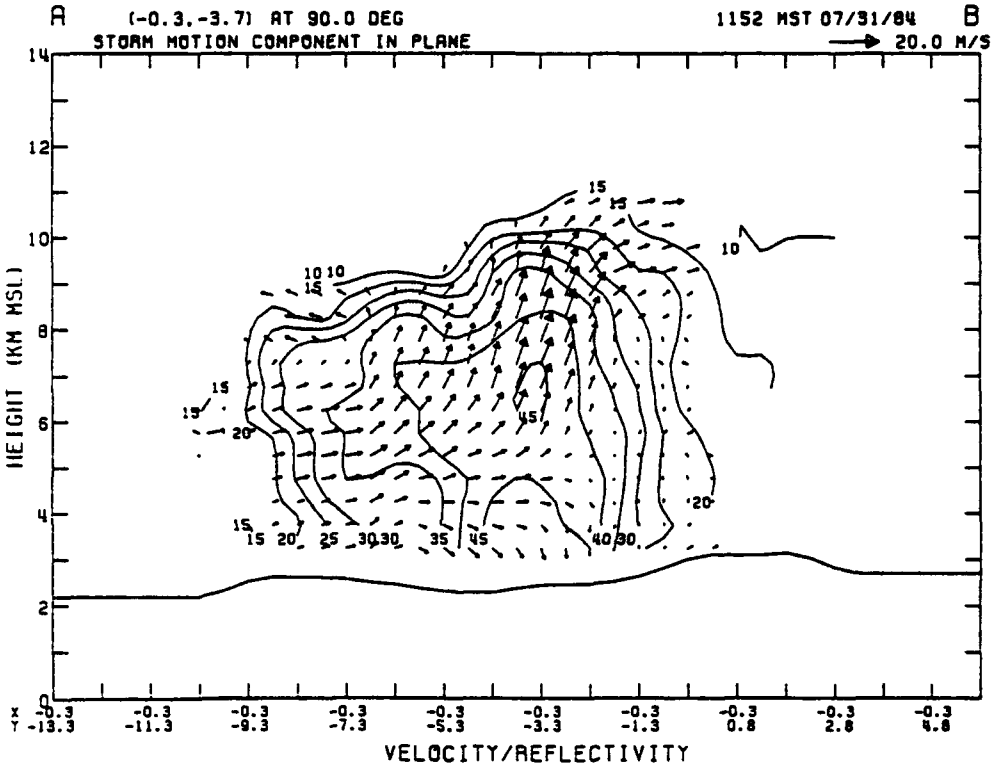

Fig. 15b. As in Fig. 10b, vertical cross-section of observed radar reflectivities and vector velocities at 1152 MST. Cross-section location AB is shown in Fig. 15a.

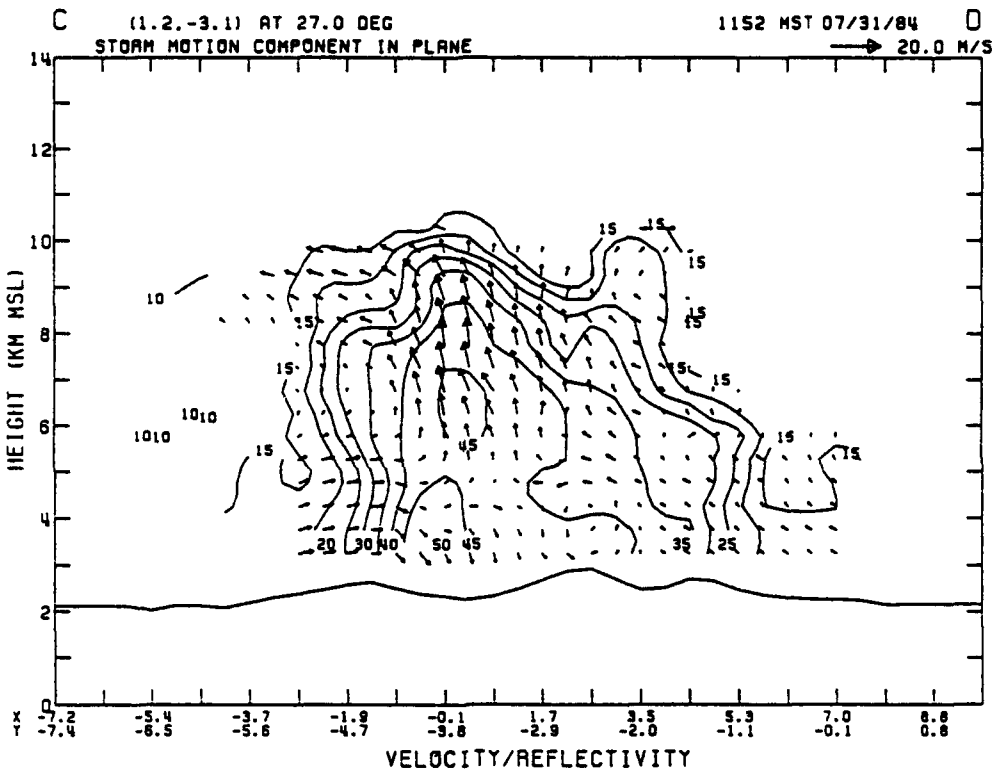

Fig. 15c. As in Fig. 10b, vertical cross-section of observed radar reflectivities and vector velocities at 1152 MST. Cross-section location CD is shown in Fig. 15a.

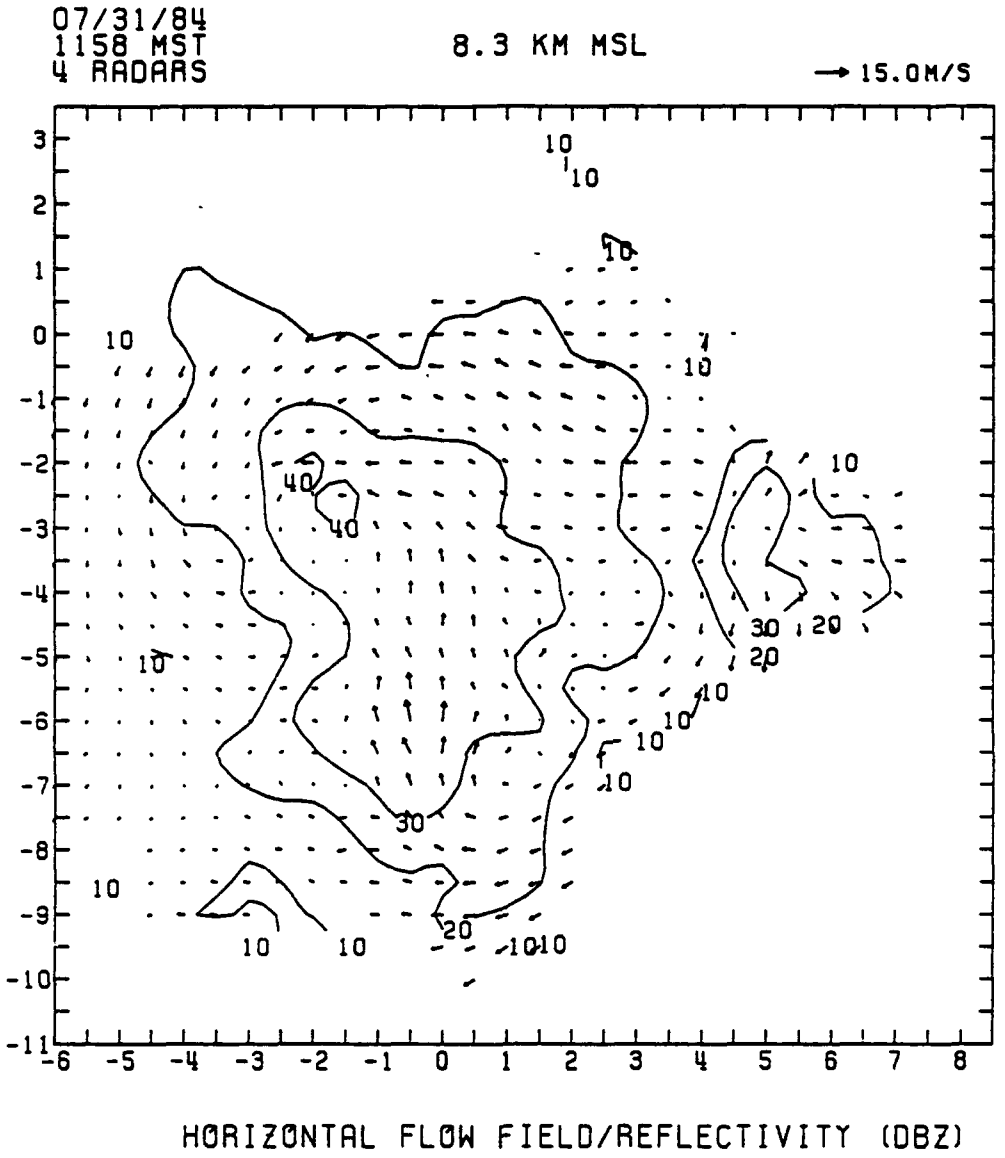

Fig. 16. Horizontal cross-section of observed radar reflectivities and vector velocities as in Fig. 8, except at 1158 MST and at 8.3 km MSL.

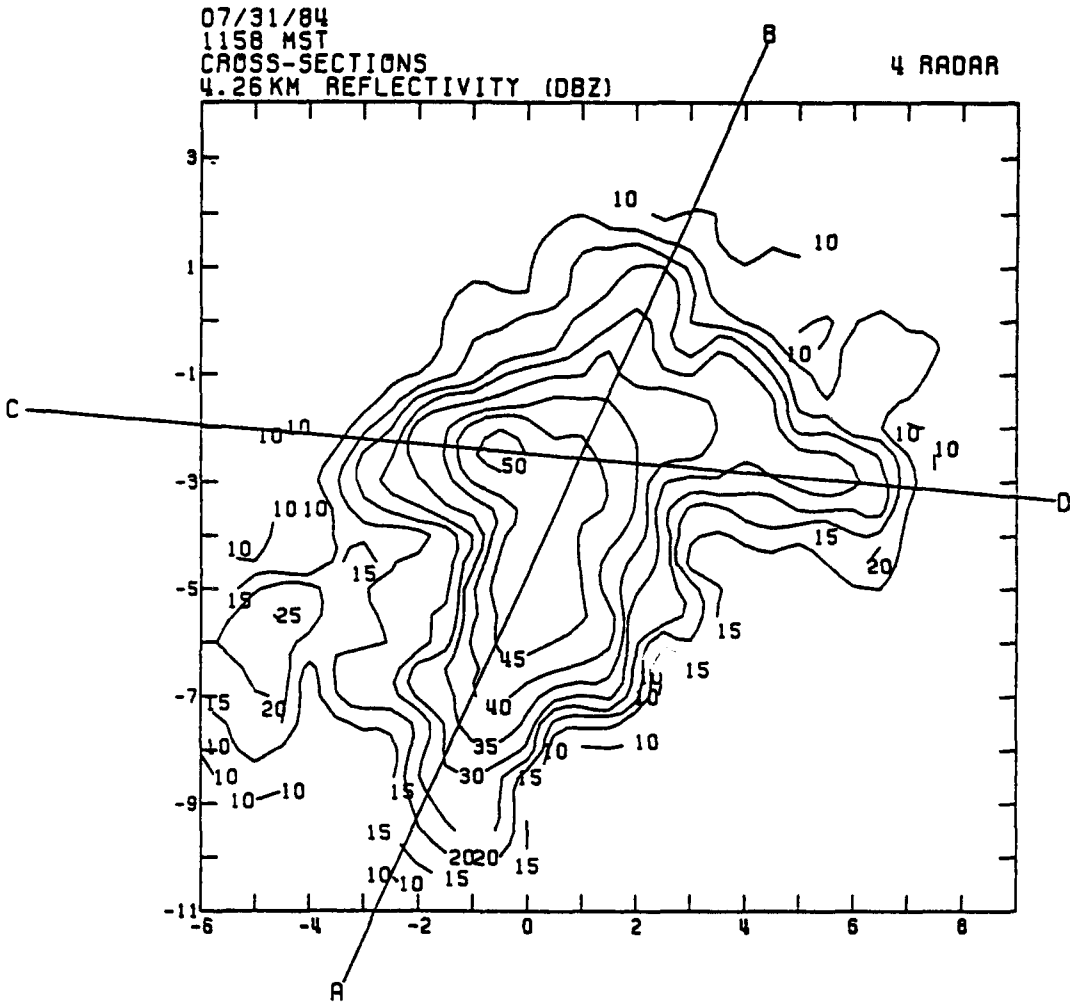

Fig. 17a. As in Fig. 10a, horizontal cross-section of observed radar reflectivities at 1158 MST and 4.3 km MSL. Lines AB and CD show locations of vertical cross-sections in Figs. 17b and 17c, respectively.

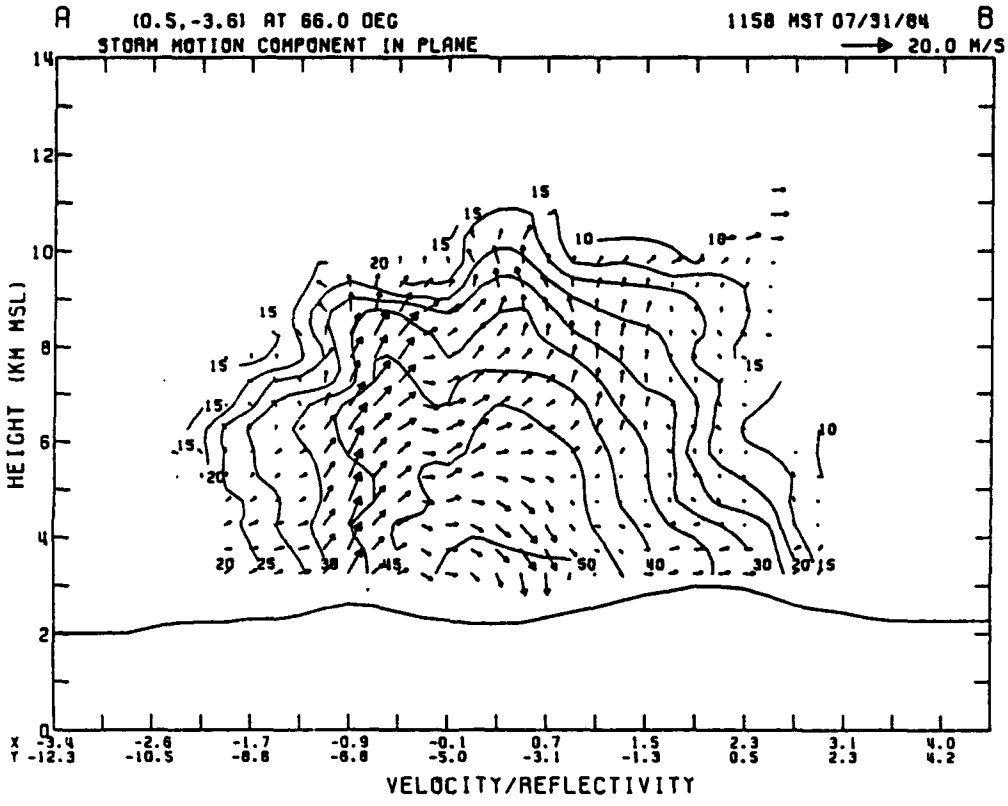

Fig. 17b. Vertical cross-section of observed radar reflectivities and vector velocities as in Fig. 10b, except at 1158 MST. Cross-section location AB is shown in Fig. 17a.

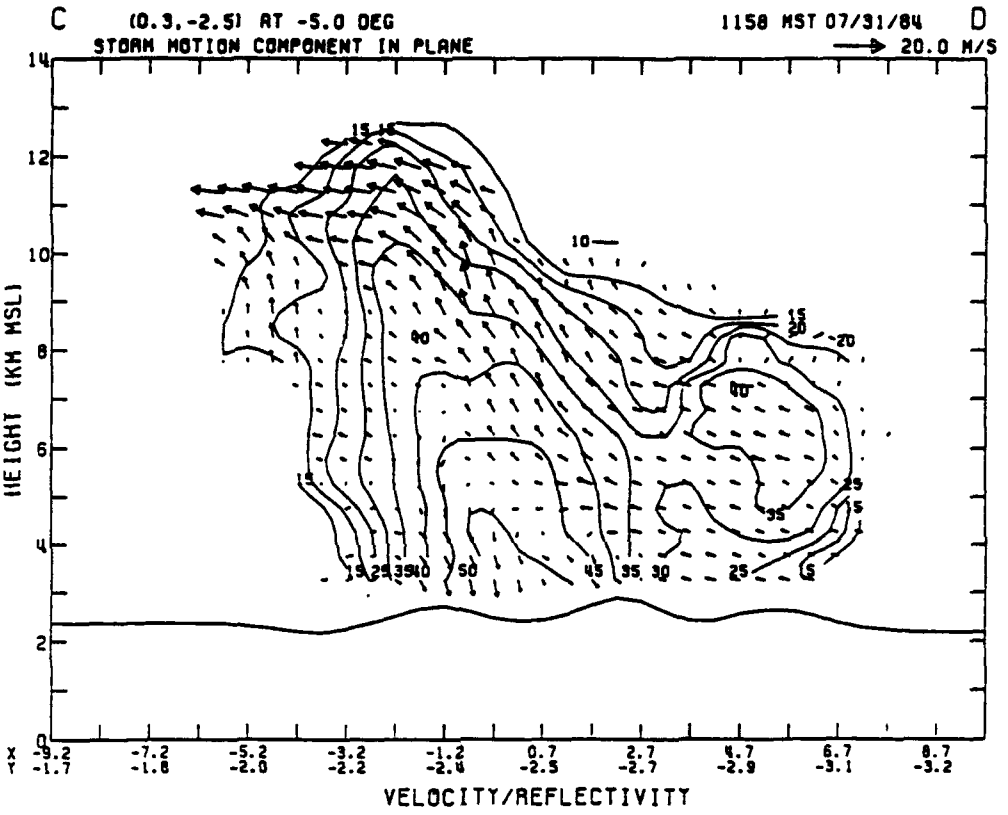

Fig. 17c. Vertical cross-section of observed radar reflectivities and vector velocities as in Fig. 10b, except at 1158 MST. Cross-section location CD is shown in Fig. 17a.

outflow at the top of C3, the newer cell, feeds directly into the much higher updraft in the older cell, C1. Additionally, the flow through C4 feeds directly into C1's updraft.

3.3.4 Storm Decay

The 1201 MST analysis suffered from a lack of data over most of the southern half of the analysis grid. The available data showed C1 (0.5, -3.0) began a slight weakening trend at this time. The maximum reflectivities observed from C1 decreased to 40 dBZ. C3 (-0.5, -6.5) moved slightly northward and weakened slightly, but radar still detected 45 dBZ returns. The actual amount of weakening is questionable due to the lack of data. C4 (5.0, -3.0) continued to strengthen with 40 dBZ returns detected between 6.0 and 8.3 km MSL. The horizontal wind analysis showed strong mid-level divergence southeast of the storm area over the eastern slope of R1. Additionally, the analysis showed strong upper-level divergence over both C1 and C3. The updrafts in both C1 and C3 weakened at this time: C1 to a maximum strength of 9.0 m s^{-1}, C3 to a maximum of 12.0 m s^{-1}. C4's updraft intensified rapidly to 12.0 m s^{-1}. C1's downdraft remained broad and strong with a maximum strength of 12.0 m s^{-1} at 3.3 km MSL. The missing data prevented analysis of C3's downdrafts. C4's rapid intensification led to the development of a narrow, but strong downdraft (9.0 m s^{-1}).

The reflectivity analysis at 1204 MST showed only minor changes in C1 (0.5, -2.5) and C3 (0.0, -5.5) from the 1201 analysis. By 1204, C4 (3.5, -2.5) had drifted northwestward to the location where C2 had previously dissipated, and its area of 40 dBZ returns extended downward to 3.3 km MSL. The radar detected 30 dBZ returns between 4.3 and 7.3 km MSL from a new cell (-4.0, -5.0) (denoted hereafter as C5) just west of R1 (Fig. 18). The horizontal wind analysis showed a weakening of the

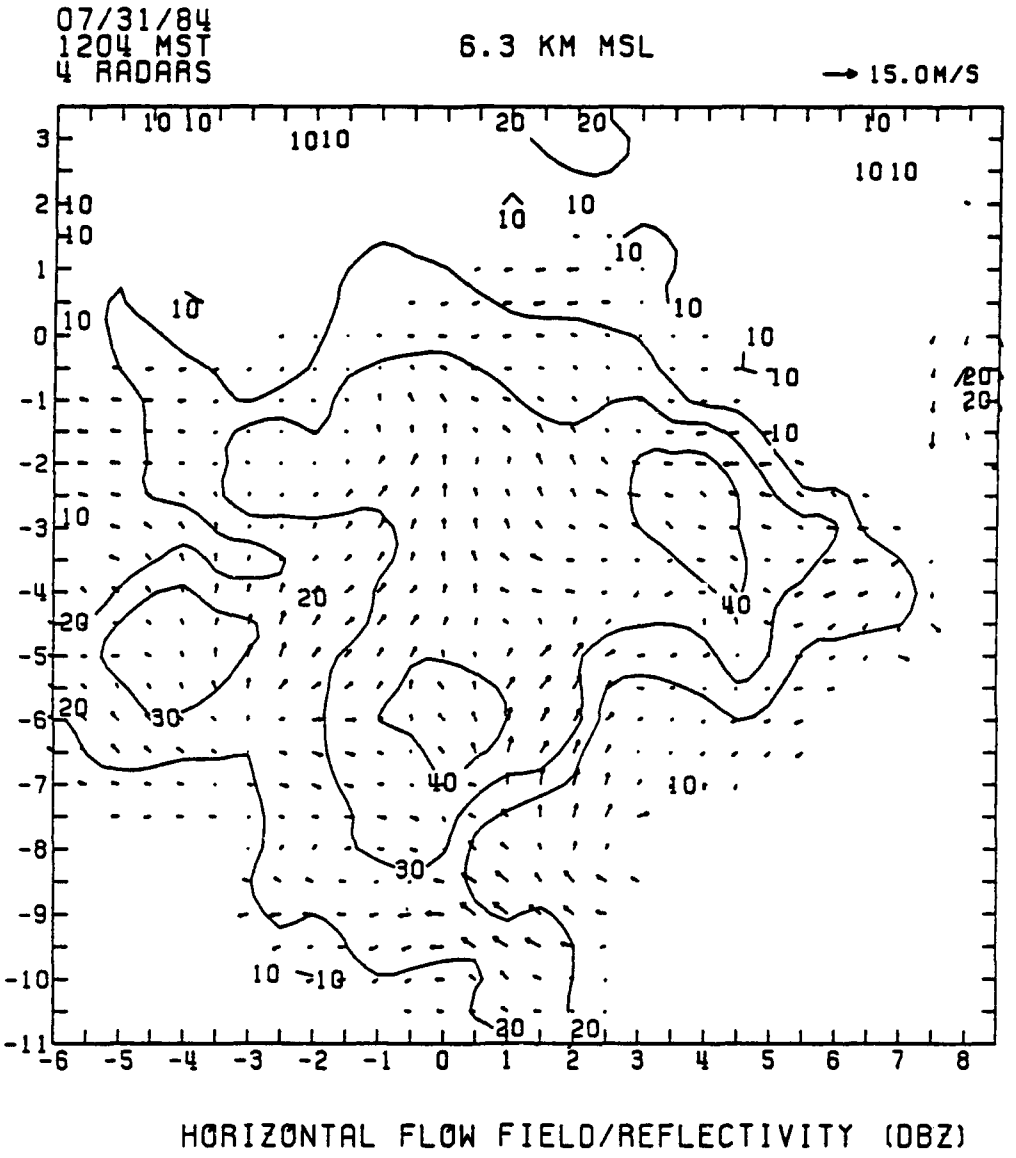

Fig. 18. As in Fig. 8, horizontal cross-section of observed radar reflectivities and vector velocities for 1204 MST and at 6.3 km MSL.

channelling effect in V1 with a slight increase in the convergent channelling in V2. Moderate low-level convergence existed in the region between C1 and C4 directly over the southern tip of R2. The mid-level divergence continued over the eastern slopes of R1 and a new divergence area formed over the western slopes of R1 in the vicinity of C5. The strongest upper-level divergence existed over C4. The vertical velocity analysis for 1204 MST showed a slight increase in updraft strength in C1, C3, and C4. The analysis showed no distinct updraft regions associated with C5. The downdrafts in C1 and C4 weakened to 6.0 m s^{-1} and covered a slightly smaller area than earlier. The analysis showed a well-established (6.0 m s^{-1}) downdraft associated with C3. The vertical cross-section (Fig. 19) shows the strong development of C4 and that its circulation continued to feed into C1's circulation.

The reflectivity analysis at 1207 MST showed very few changes from the 1204 and 1201 MST analyses. By this time both C1 (0.5, -2.5) and C3 (0.0, -5.5) had drifted slowly northward. Radar detected several new echoes developing over the eastern slopes of R3. These appear to have developed as a result of the strong upslope flow into C4 (3.5, -2.5). The horizontal wind analysis showed continued strong low- and mid-level convergence in the vicinity of C1. The analysis showed strong upper-level divergence over both C3 and C4. C1's updraft remained at about the same strength as at 1201, while C3's weakened slightly. C4's updraft weakened considerably to a strength of 6.0 m s^{-1}. C5's (-3.75, -4.75) updraft became more organized, reaching a strength of 6.0 m s^{-1}. All four active cells showed organized downdrafts at this time with C1's and C3's increasing in strength again to over 9.0 m s^{-1}. The vertical velocity analyses showed that by this time the updrafts existed mainly at mid- and upper-levels.

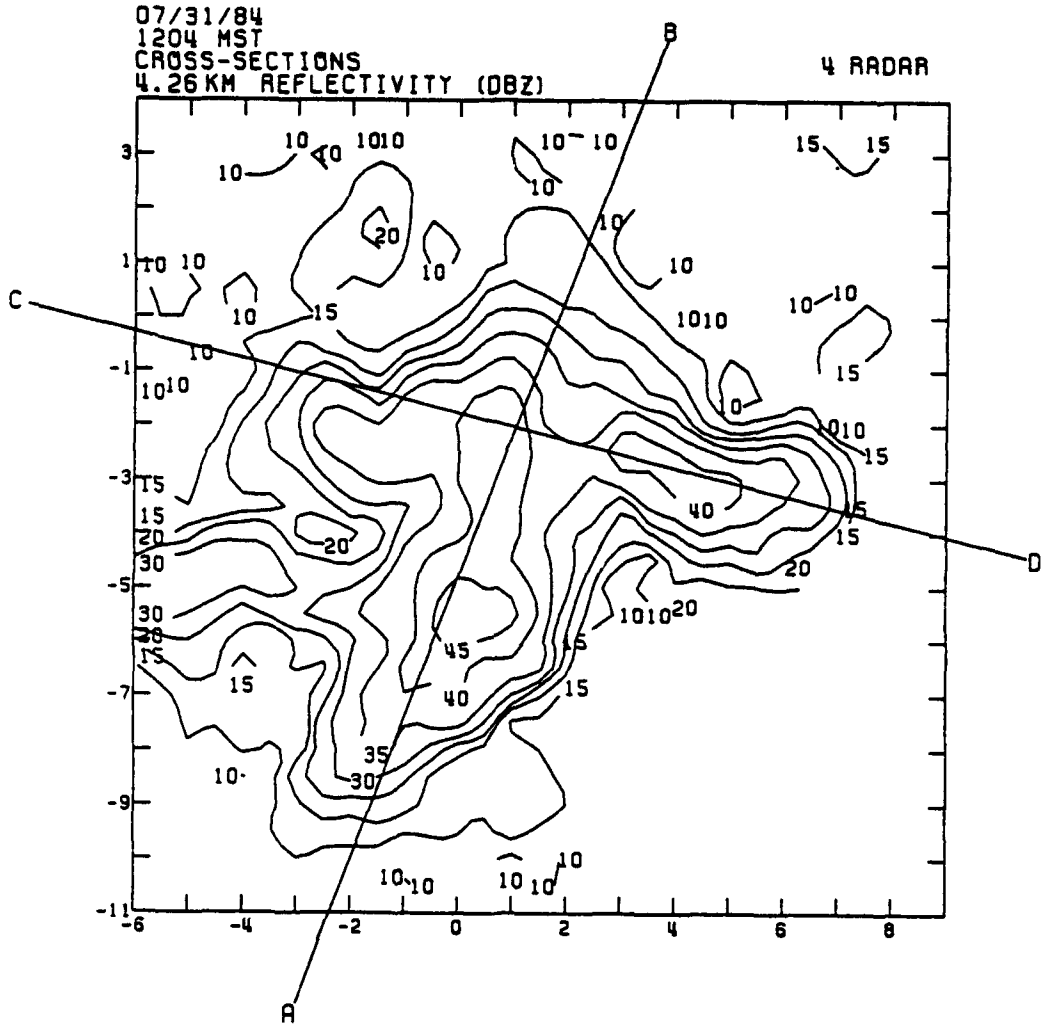

Fig. 19a. As in Fig. 10a, horizontal cross-section of observed radar reflectivities at 1204 MST and 4.3 km MSL. Line CD shows location of vertical cross-section in Fig. 19b. Line AB was not used.

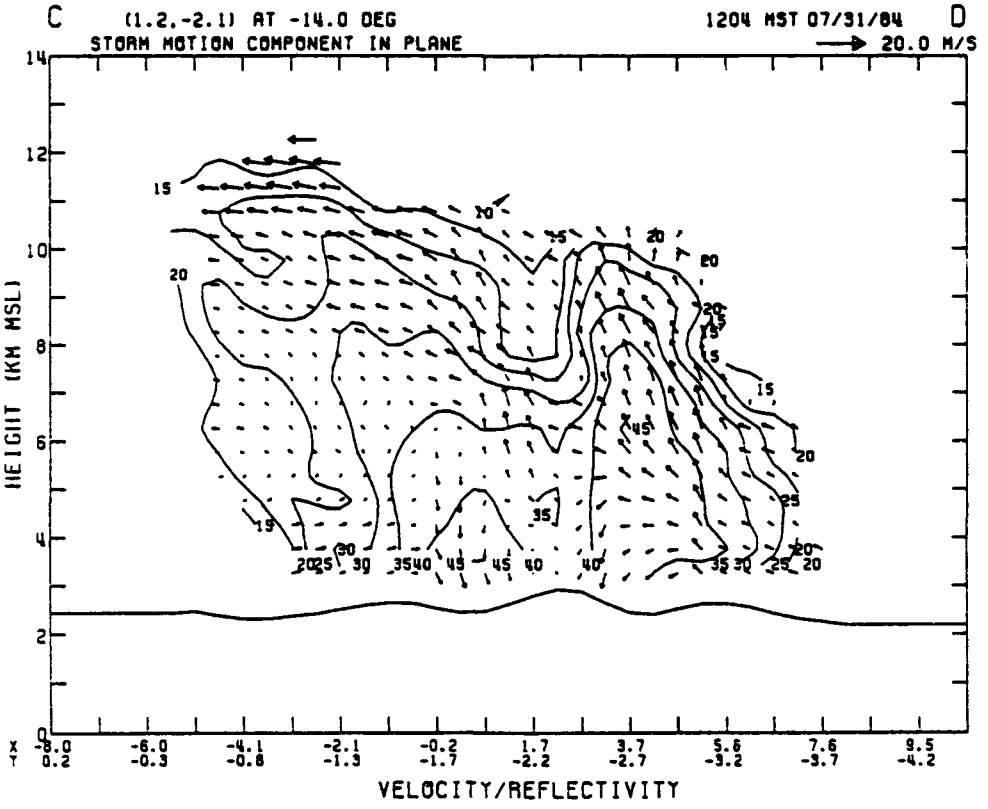

Fig. 19b. Vertical cross-section of observed radar reflectivities and vector velocities as in Fig. 10b, except at 1204 MST. Cross-section location CD is shown in Fig. 19a.

By 1210 MST, the defining reflectivity contours of C1 (0.5, -2.0) and C3 (0.5, -4.5) had merged. Radar returns from C4 (3.0, -2.5) weakened slightly while those from C5 (-3.5, -4.0) increased in strength to 40 dBZ at 3.3 km MSL. The weak development over R3 continued while several new cells formed in the extreme northeastern corner of the analysis area. The horizontal wind analysis showed strong low-level convergence over the western slopes of R2 and over the northern end of V2. Strong upper-level divergence also existed over these same regions. C1's updraft remained as its onl distinguishing feature at 1210 MST. At this time, it still maintained a strength of 9.0 m s^{-1}. C3's updraft remained about the same strength as at 1207 MST, but C4's updraft strengthened again to 9.0 m s^{-1}, and C5's updraft reached 9.0 m s^{-1} for the first time. At this analysis time, C1's downdraft had decreased significantly to less than 3.0 m s^{-1}. C3, C4, and C5 all contained maximum downdrafts of 6.0 m s^{-1}.

By 1213 MST, C3 (0.5, -3.5) had overtaken all remnants of C1 and most of the remnants of C4 (2.5, -2.0). C3's maximum reflectivity increased to over 50 dBZ at 3.3 km MSL at approximately the midpoint between the previous locations of C3, C1, and C4. C4 appeared in the reflectivity analysis as only a bulge in the 40 dBZ contour at 3.3 km MSL. C5's (-3.0, -4.0) maximum reflectivity remained about 40 dBZ, however the maximum expanded in vertical extent to 5.3 km MSL. A new cell (2.0, -7.0) (denoted hereafter as C6) developed along the southeastern edge of C3 almost directly over the center of V1. This cell was best defined in the reflectivity analyses at 6.3 and 7.3 km MSL (Fig. 20). The horizontal wind analysis showed weak low-level flow over the northern half of the analysis domain, but a relatively strong southwesterly flow over the southern half. The analysis showed very little low-level convergence. Some upper-level divergence still existed over C3 and C6.

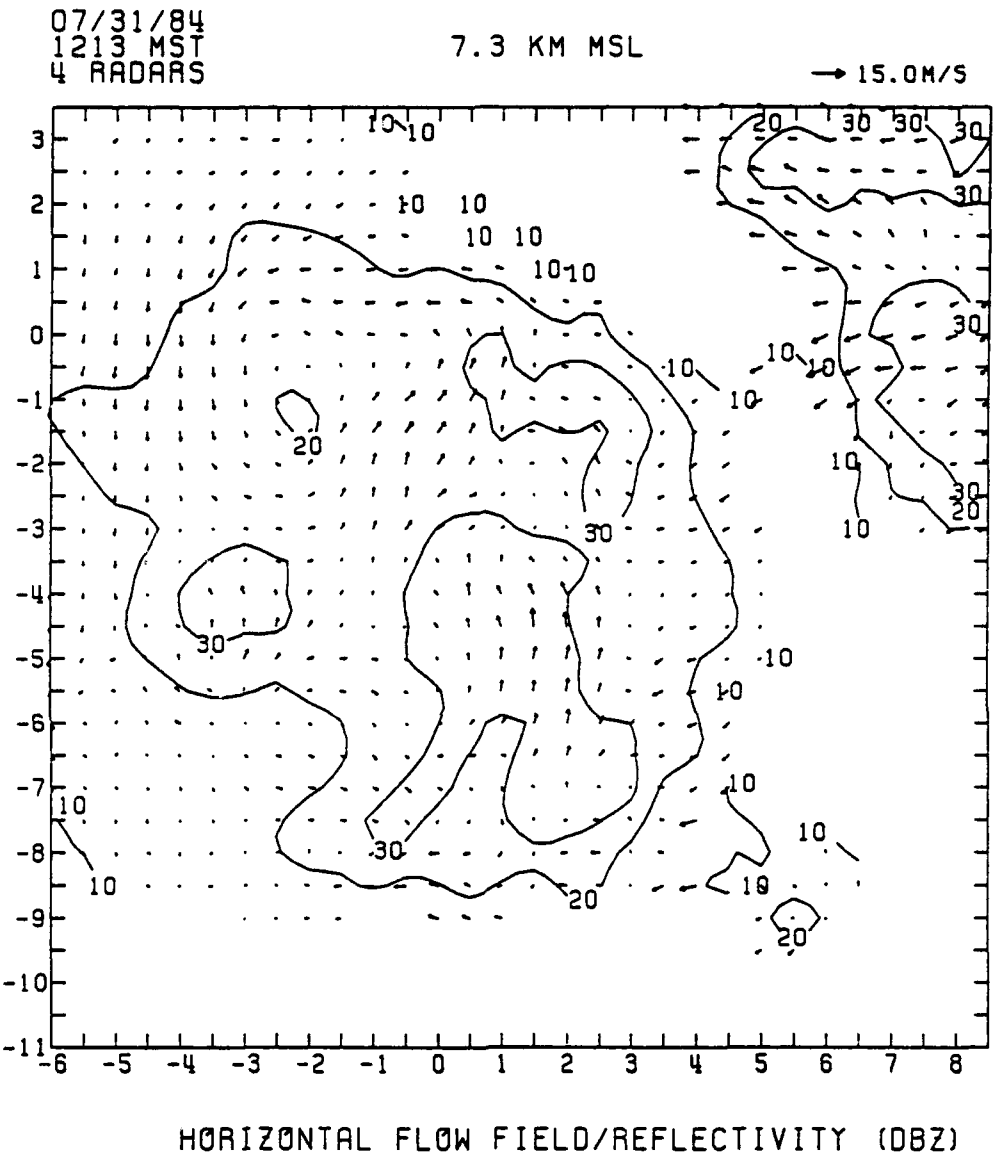

Fig. 20. Horizontal cross-section of observed radar reflectivities and vector velocities as in Fig. 8, except at 1213 MST and at 7.3 km MSL.

C3's updraft continued with a maximum strength of 9.0 m s^{-1} between 5.3 and 9.3 km MSL while C4's updraft became indistinguishable at this time. C5's updraft continued to strengthen, reaching a maximum strength of 12.0 m s^{-1}. By 1213 MST, C6's updraft had already reached 9.0 m s^{-1} between 5.3 and 6.3 km MSL. The area covered by C3's downdraft continued to shrink, although the downdraft's maximum strength continued at 6.0 m s^{-1}. The weak downdraft (3.0 m s^{-1}) remained as the only structure that distinguished C4 from C3 at 1213 MST. C5's downdraft increased in strength to 6.0 m s^{-1}.

At 1216 MST, C3 (0.5, -4.0) had absorbed the final remnants of C4. C3 continued with a maximum reflectivity of 40 dBZ. C5 (-3.0, -4.0) maintained its previous strength, while C6 (2.0, -7.0) strengthened rapidly, with its 40 dBZ maximum reflectivities extending down to the lowest analysis level of 3.3 km MSL. A weak new cell (5.5, -2.0) (denoted hereafter as C7) developed at this time over R3. The horizontal wind analysis at this time again showed very weak flow over the northern half of the analysis domain with a relatively strong southerly to southwesterly flow over the southern half. Some weak low-level convergence existed just east of C6. The vertical velocity analysis showed that by this time most of the vertical motion had weakened considerably. Only C6's updraft exceeded 9.0 m s^{-1}. Downdrafts of 6.0 m s^{-1} existed only in C3 and C5 by this time.

3.3.5 Summary

The previous subsections provide a detailed description of the initiation and evolution of the 31 July 1984 storms as observed by the Doppler radars. These observations provide some insight into the general nature of the storms.

Early cell development occurred directly over or slightly east of the ridge lines. These observations are consistent with the theory that the New Mexico storms evolve

mainly as a result of thermally driven mountain-valley circulations and are focused by local topographic features (see, for example, Barker and Banta, 1985; Banta and Schaaf, 1987; Schaaf *et al.*, 1988). The weak low-level southeasterly flow into the convergent valleys, V1 and V2, produced areas of upslope and convergent flow at the northwestern (upslope) end of those valleys. The upslope flow and convergence focused the areas of convective initiation over the ridges nearest the ends of V1 and V2 as described by Banta and Schaaf (1987).

After the first cells had developed, the mountain-valley circulation and the convergent flows continued to help focus the location of new cell initiation. However, circulations from the existing cells also began to affect the location of cell initiation. For example, at 1152 MST, several short-lived cells developed along the outflow boundaries from C1 and C3. In some cases the low-level flow induced by the existing cells enhanced or created upslope and/or convergent flows which in turn helped focus new cell development.

The storm observed near Langmuir Laboratory on 31 July 1984 generally had a lifetime of approximately 1.0 to 1.5 hr. The storm contained several cells with lifetimes of from 20 to 60 min. Many of the cells exhibited periodic intensification and weakening with a period of 6 to 12 min. For example, both C1 and C2 underwent at least two cycles of intensification/weakening during the analysis period (C1 from 1134 to 1143 MST and 1146 to 1210 MST; C2 from before 1134 to 1143 MST and 1146 to 1152 MST). This periodic activity resembles closely the updraft pulsations suggested by Ziegler *et al.* (1986). Radar returns from the strongest cells exceeded 50 dBZ several times, but maximum returns from most cells ranged from 30 to 40 dBZ. Most of the cells never extended higher than 10.0 km MSL, however, the stronger

cells, C1 and C4, frequently extended above 10.0 km and in some cases to over 12.0 km MSL.

Most cells contained single updrafts approximately 2.0 km wide with maximum vertical velocities of 12.0 m s^{-1} or less. C1 frequently contained multiple low-level updrafts which merged into a single updraft at mid-levels. The strongest observed updrafts of 18.0 m s^{-1} occurred in C1 and C3. In the early stages of cell development, the downdrafts were only about 1.5 km wide with maximum vertical velocities of 3.0 m s^{-1} or less. As the cells matured, however, the downdrafts expanded in areal coverage and increased in strength with maximum vertical velocities frequently exceeding 6.0 m s^{-1} and with an absolute maximum of 12.0 m s^{-1}. In at least one cell, C1, during the cell's mature stage, the interaction between the updraft and the downdraft appeared to be symbiotic in a manner similar to that often observed in long-lived severe storms. As discussed in a previous section, the updraft tilted northwestward (or backward relative to the low-level storm inflow). The precipitation and its associated downdraft were located behind and below the updraft (relative to the low-level inflow) and thus did not interfere with the inflow or the updraft. Several other cells contained tilted updrafts, but to a lesser extent than C1. As the cells entered the decay stage, the updrafts became nearly vertical so that the precipitation and the downdraft interfered considerably with the updraft.

The Doppler radar observations and the associated wind analyses reveal a strong interrelationship between all the cells in the analysis domain. In the mature stage, the outflow from downdrafts appeared in some cases to enhance low-level convergence that either focused the development of new cells or helped sustain existing cells. In several instances the updrafts of two or more cells merged into one updraft at upper-levels. Often the updraft of a newer cell developed in the low- to mid-levels and fed

into a higher-level updraft associated with an older cell. Additionally, the divergent flow located near the top of a strong cell often cut off the updraft of a weaker neighboring cell. The periodic intensification noted above frequently appeared to alternate among the cells. For example, during C1's first period of intensification, C2 was weakening. This certainly did not occur without exception, but the trend was readily apparent. Finally, the observations showed several cases where older or weaker cells were overtaken and absorbed by newer and/or stronger cells.

Chapter 4

The Numerical Model

This chapter describes the numerical model chosen for this study. Section 4.1 describes the criteria used to select the numerical model. Section 4.2 discusses the model's ability to simulate mountain thunderstorms. In section 4.3 the model selected for this study is briefly described. Sections 4.4 and 4.5 describe the model's vertical and horizontal grid structures, respectively, and section 4.6 describes the topography used in the numerical simulations. Finally, the model initialization procedure is discussed in section 4.7.

4.1 Model Selection

Before conducting any numerical study, a numerical model must be selected. Choosing a model is extremely important and should be deliberate and well-planned. Essential criteria must be defined and used in the selection process. Flexibility, applicability, and availability must also be considered. If existing models do not meet the needs of the study, then a new model must be developed.

To study the type of mountain thunderstorms of interest here, it was necessary to choose a model with fully compressible, non-hydrostatic equations of motion; the option of conducting two- or three-dimensional simulations; a terrain-following coordinate system; a surface layer parameterization and a soil model which interact with realistic long- and short-wave radiation parameterizations; and a cloud microphysical parameterization which includes the ice phase. Additionally, the model needed to be compatible with locally available computer software and hardware. The Colorado

State University (CSU) Regional Atmospheric Modeling System (RAMS) was chosen for this study. RAMS was chosen over other potential models because it met all of the above criteria, because of its flexibility, its applicability to modeling mountain circulations and storms, and its availability.

4.2 Model Ability To Simulate Mountain Storms

Before undertaking any numerical study, it is essential to assess the model's ability to simulate the basic processes responsible for the phenomenon under study. This study is concerned with the initiation and development of mountain thunderstorms under conditions of strong solar heating and weak ambient flow. As discussed in Chapter 3, these processes are expected to include primarily thermodynamic processes and possibly dynamic processes such as orographic lifting and valley channeling. Only after verifying the model's skill with these processes can we use it with confidence to study the more complex phenomenon of mountain thunderstorms.

The simple, three-dimensional, no-wind simulation used by Klemp and Wilhelmson (1978a) to test their model also provided an excellent test for this model's skill with thermodynamic processes. In this test, simulated convection is initiated by inserting a warm, moist, symmetric perturbation in the lower part of an otherwise homogeneous atmosphere. Because this type of perturbation should yield an axisymmetric storm, this type of test can immediately reveal many coding errors. This was an important benefit in this case because RAMS was revised and recoded shortly before the start of this study. The results of this test did, in fact, reveal several coding errors. After these errors were corrected, the test results agreed very well with those reported by Klemp and Wilhelmson. Some minor differences were noted between the two tests. These could be attributed to the different physical parameterizations used by the two models. Tripoli (1986) tested the model's ability to simulate

simple gravity waves and reported good agreement between his simulations and those of Durran (1981).

In addition to these simple tests, the model has been used for simulations of more complex processes important to mountain convection. Banta (1983, 1986), Bader and McKee (1983, 1985), and Bader *et al.* (1987) used the cloud model portion of RAMS to study mountain upslope flow and boundary layer evolution. Cotton and Tripoli (1978), Tripoli and Cotton (1980, 1982, 1986), and Cotton *et al.* (1982) also used the cloud model portion of RAMS successfully in studies of cumulus and thunderstorm development. The simple Klemp-Wilhelmson tests described above, along with the successful complex simulations carried out by other investigators, indicate that the model is well-suited to simulate the initiation and development of mountain thunderstorms of interest in this study.

4.3 Model Description

As its name implies, the CSU RAMS is a modeling system, not a single model. RAMS is a combination of the Tripoli and Cotton (1982) non-hydrostatic cloud model and of two hydrostatic mesoscale models (Tremback *et al.*, 1985; Mahrer and Pielke, 1977). Because of this combination, RAMS is very flexible and allows the user to select from a wide variety of physical processes and numerical techniques.

This study employed the non-hydrostatic cloud model portion of RAMS. This section briefly describes the characteristics of the non-hydrostatic model and the various options employed in this study. The description here closely follows that given by Tripoli (1986).

The model formulation is a revised and slightly modified form of the CSU cloud/mesoscale model described by Tripoli and Cotton (1982) and Cotton *et al.* (1982, 1986). The model employs a non-hydrostatic, quasi-Boussinesq, fully com-

pressible set of primitive equations cast in two or three dimensions (Tripoli and Cotton, 1986; Tripoli, 1986). The current model formulation follows Klemp and Wilhelmson (1978a) and predicts the Exner function (π) and diagnoses density (Tripoli, 1986; Bader *et al.*, 1987).

The model uses time-dependent partial differential equations to predict the three wind components (u, v, w), the Exner function (π) , the liquid-ice potential temperature (θ_{il}) (Tripoli and Cotton, 1981), total water mixing ratio (r_t), mixing ratios of rain water (r_r), pristine ice crystals (r_i), graupel or hail (r_g), and aggregated snow flakes (r_a). The model also predicts the total concentration of pristine ice crystals (N_{ic}). This gives a total of eleven prognostic variables. The model uses a diagnostic procedure described by Tripoli and Cotton (1982) to diagnose potential temperature (θ), temperature (T), cloud water mixing ratio (r_c), water vapor mixing ratio (r_v), pressure (p), and density (ρ).

The model includes parameterizations for several important physical processes. Microphysical processes are treated by a generalized microphysical parameterization scheme described by Tripoli *et al.* (1988). Within this generalized framework it is possible to vary parameters to formulate the desired microphysical parameterization. The microphysical parameterizations chosen for this study are similar to those of Tripoli and Cotton (1980) for warm rain processes and Cotton *et al.* (1982, 1986) for ice phase processes. Long- and short-wave radiative tendencies on θ_{il} are computed following Chen and Cotton (1983). For the simulations conducted in this study, the radiative tendencies were updated at 120 s intervals starting at t = 900 s. Surface layer fluxes of heat, moisture, and momentum are parameterized following the methods of Louis (1979) and Manton and Cotton (1977). A surface roughness of 1.0 cm was prescribed for the surface layer parameterization. Soil temperature and soil mois-

ture are predicted by an underlying soil model described by McCumber and Pielke (1981) and modified by Tremback and Kessler (1985). The soil model included five levels located at the surface and 1, 4, 16, and 32 cm beneath the surface. Chapter 5 provides further details on the soil parameters prescribed for the simulations. Turbulent mixing above the surface layer is modeled using the eddy viscosity approach described by Lilly (1962). Mixing is enhanced in unstable regions as suggested by Hill (1974) and implemented by Tripoli (1986).

The predictive equations are solved on a staggered grid described by Tripoli and Cotton (1982) with a terrain-following vertical coordinate system similar to that of Gal-Chen and Sommerville (1975a, 1975b). The time-differencing scheme used here was described by Tripoli and Cotton (1982) and modified by Tripoli (1986). The time-split leapfrog scheme developed by Klemp and Wilhelmson (1978a) provides the basic time-differencing framework. In this scheme the terms responsible for sound wave propagation are integrated on a small time step while the non-acoustic terms are held fixed for several small time steps and updated on the larger leapfrog time step. For the small time step, the model employs a forward-backward differencing scheme for the horizontal terms and an implicit Crank-Nicholson scheme described by Durran (1981) and Tripoli and Cotton (1986) for the vertical terms. The physical parameterizations are all computed with a forward time-differencing scheme. The turbulent mixing parameterization uses a combined forward and Crank-Nicholson scheme suggested by Paegle *et al.* (1976). For this study, the acoustic terms were integrated using a 2.5 s small timestep, while the non-acoustic terms were integrated with a 5.0 s large timestep. All advective terms are computed with a fourth-order finite-differencing method.

Because RAMS is a limited area model, appropriate boundary conditions must be specified in order to determine unique solutions to the time dependent equations. For the top boundary condition a rigid upper lid similar to that employed by Klemp and Wilhelmson (1978a) was used. The bottom boundary condition assumed zero mean vertical fluxes at the surface with surface layer turbulent fluxes of momentum, heat, and water vapor diagnosed by the surface layer parameterization. The open lateral boundary conditions described by Klemp and Wilhelmson (1978a) were employed with a specified intrinsic gravity wave phase velocity of 30 m s^{-1}.

4.4 Horizontal Grid Structure

The horizontal grid structure for this study was chosen to maximize the horizontal resolution over a model domain large enough to accommodate the simulation of *mountain* convection while minimizing artificial model boundary effects on the simulated storms. Computational limitations dictated the choice of a medium-sized domain to allow for a desired high-resolution grid structure.

As discussed in Chapter 3, the storms of interest here developed over the Magdalena Mountains, a range that extends approximately 28 km in the north-south direction and approximately 20 km in the east-west direction. Most of the convection on 31 July 1984 developed and remained near the center of the range. A 33 km model domain centered on the Langmuir Laboratory was chosen for the simulations in this study. This domain was large enough to allow ample room for storm development near the domain center and also provided for "buffer" regions around the domain boundaries to minimize the boundary effects on the domain's interior.

A 500 m horizontal resolution was chosen for this study. This resolution was chosen based on three considerations. First, an accurate numerical simulation of the types of storms of interest here required a high-resolution grid to capture the cloud-

and sub-cloud-scale processes known to be important in mountain convection. Second, the extremely rough terrain in the model domain (see Section 4.6) necessitated a high-resolution grid to capture the important terrain features and resultant effects on storm development. Finally, the desire for the highest resolution possible was necessarily tempered by the availability of computer resources. The 500 m grid structure provided a suitable compromise among the considerations above.

Several other studies have employed similar grid structures and domain sizes to simulate thunderstorm development in general and mountain convection in particular. For example, Klemp and Wilhelmson (1978a) employed a 24 km domain with 1000 m grid spacing to simulate a generic severe storm; Tripoli and Cotton (1980) used a 35.25 km domain with 750 m grid spacing to simulate a Florida thunderstorm; and Clark and Gall (1982) and Smolarkiewicz and Clark (1985) used a 51 km domain with 1000 m grid spacing to simulate New Mexico and Montana thunderstorms, respectively.

4.5 Vertical Grid Structure

The vertical grid structure chosen for this study reflects an attempt to adequately resolve most of the important features of thunderstorm initiation and development with a minimum of computer resources. It was computationally prohibitive to use an extremely high-resolution vertical grid structure required to resolve such important processes as turbulent fluxes, gust fronts, etc. Instead, a vertical grid structure was chosen which resolves the processes thought to be most important and at least allows a gross parameterization of the unresolvable processes.

Banta (1984), Braham and Draginis (1960), Orville (1965a), and others have shown that shallow mountain-valley circulations play a critical role in the development of mountain storms. These flows typically are only a few hundred meters deep.

Properly resolving such circulations would require a vertical grid spacing of 100-200 m. Tripoli (1986) showed that a grid spacing of 500-1000 m is required to adequately resolve gravity waves under conditions similar to those observed over the Magdalena Mountains. Resolving turbulent effects would require a grid spacing on the order of tens of meters.

It is reasonable to expect the actual and simulated thunderstorms to occasionally penetrate the tropopause. To adequately simulate this phenomenon, the model's vertical domain should extend at least several kilometers into the stratosphere. The tropopause on 31 July 1984 was located at approximately 12.4 km. The desired vertical resolution of 100 m would require a computationally prohibitive 160 vertical grid points. In order to facilitate the desired horizontal resolution of 500 m, a vertical resolution of 500 m was chosen. Above the tropopause, the grid is stretched to a maximum spacing of 2000 m at the top to provide the desired extension into the stratosphere. The complete vertical grid structure (for the vertical velocity portion of the staggered grid) is shown in Table 1. Note that the z and Δz values given in Table 1 represent the vertical grid structure over flat terrain with a terrain elevation of zero. In areas of mountainous terrain the actual z and Δz values vary considerably from those shown in Table 1 as a result of the vertical coordinate transformation developed by Gal-Chen and Sommerville (1975a, 1975b).

Several previous studies have employed similar grid structures. For example, Tripoli and Cotton (1986) used a 500 m grid to model an intense, quasi-steady left-moving thunderstorm over mountainous terrain; Smolarkiewicz and Clark (1985) used a 200 m grid to model Montana thunderstorm development; Tripoli (1986) used a variable grid spacing from 250 m to 750 m to model mountain-induced mesoscale convective systems; and Banta (1986) used a 100 m grid spacing to model the evolu-

Table 1: *Model vertical grid structure for vertical velocity grid points.*

HEIGHT (Meters)	ΔZ (Meters)
0	-------
500	500
1000	500
1500	500
2000	500
2500	500
3000	500
3500	500
4000	500
4500	500
5000	500
5500	500
6000	500
6500	500
7000	500
7500	500
8000	500
8500	500
9000	500
9500	500
10000	500
10500	500
11000	500
11500	500
12000	500
12500	500
13000	500
14000	1000

NOTE: *The model vertical grid uses a terrain-following coordinate system similar to that described by Gal-Chen and Sommerville (1975a, 1975b). The grid structure shown above is valid only in areas where the terrain elevation is zero and the terrain is flat. Elsewhere, the transformed Δz values are less than those shown above.*

tion of the boundary layer in mountainous terrain.

4.6 Model Topography

The topography employed in the model for this study was derived from actual 3 arc-second terrain data acquired from the National Cartographic Information Center. The model topography was constructed in the following manner. First, the appropriate data were extracted from the original terrain data set and interpolated to a 33 X 33 km grid (centered on Langmuir Lab) with 0.5 km grid spacing. The data were then smoothed three times using a simple five-point smoother. It was necessary to smooth the terrain field in order to minimize the occurrence of numerical instabilities induced by extremely rough terrain. Around the boundaries of the grid, the topography was flattened to minimize terrain-induced effects at the model's boundaries. Next, to satisfy an internal model requirement that the lowest terrain value be zero, the lowest terrain elevation value in the smoothed field was subtracted from all terrain values in the grid. The resulting terrain grid was used in three-dimensional test simulations. Figure 21 shows the "3-D" model topography.

The model topography used in the two-dimensional simulations for this study was constructed by extracting the appropriate slab of terrain values (y = 0.0 km) from the 33 X 33 km gridded data discussed above. Again the lowest terrain elevation value was subtracted from this subset of data to meet the model requirement. Figure 22 shows the final model topography used in the two-dimensional simulations.

4.7 Initialization

RAMS is initialized with base-state atmospheric temperature, moisture, and wind profiles and base-state soil moisture and temperature profiles. The numerical simulations in this study were all initialized with base-state atmospheric profiles (described in Chapter 5) representative of the state of the atmosphere over the Magdalena Moun-

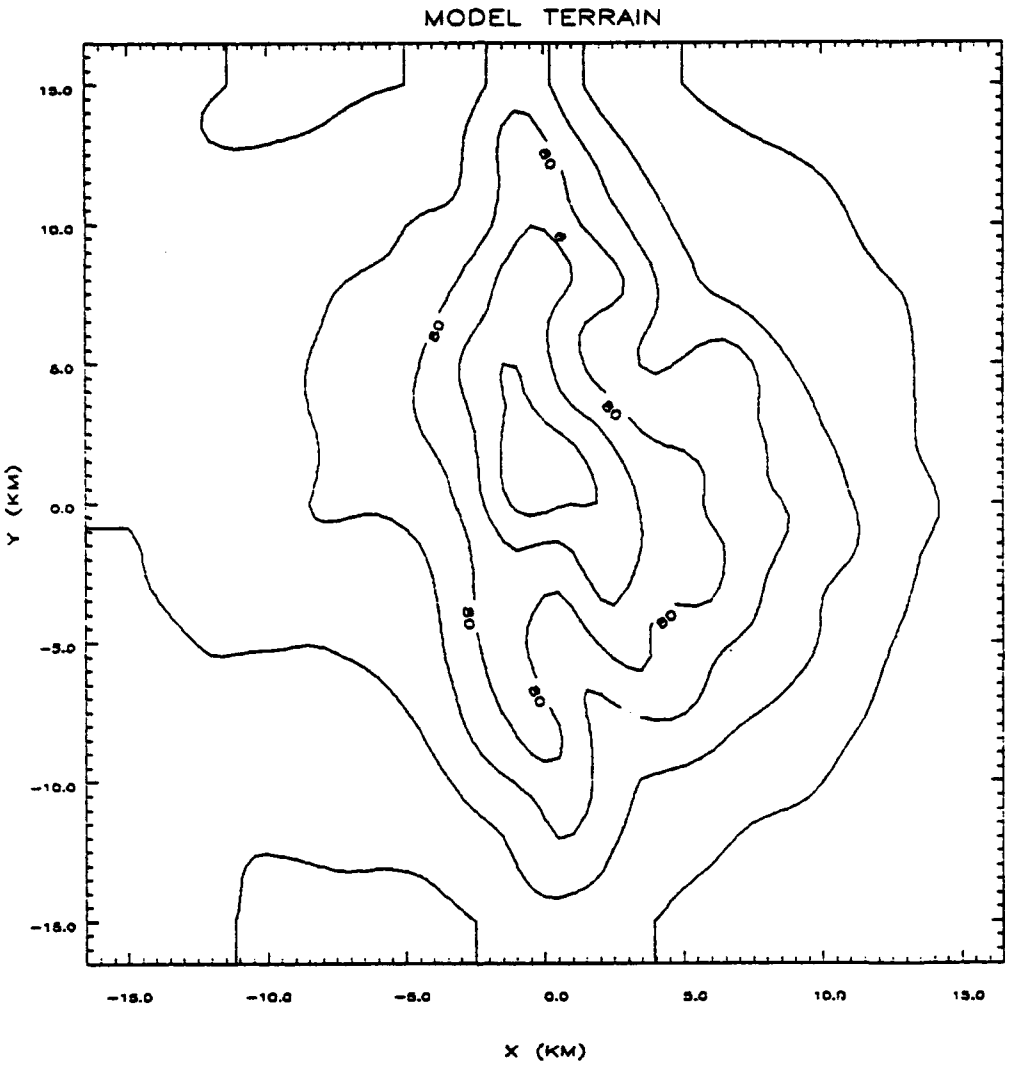

Fig. 21. "Three-dimensional" model terrain elevation data. Terrain elevations are relative to lowest terrain value in grid domain after smoothing as described in text. Terrain elevations are labeled in dekameters and contoured every 20 dekameters. The horizontal and vertical axes are labeled in kilometers. The origin (0,0) is located at Langmuir Laboratory.

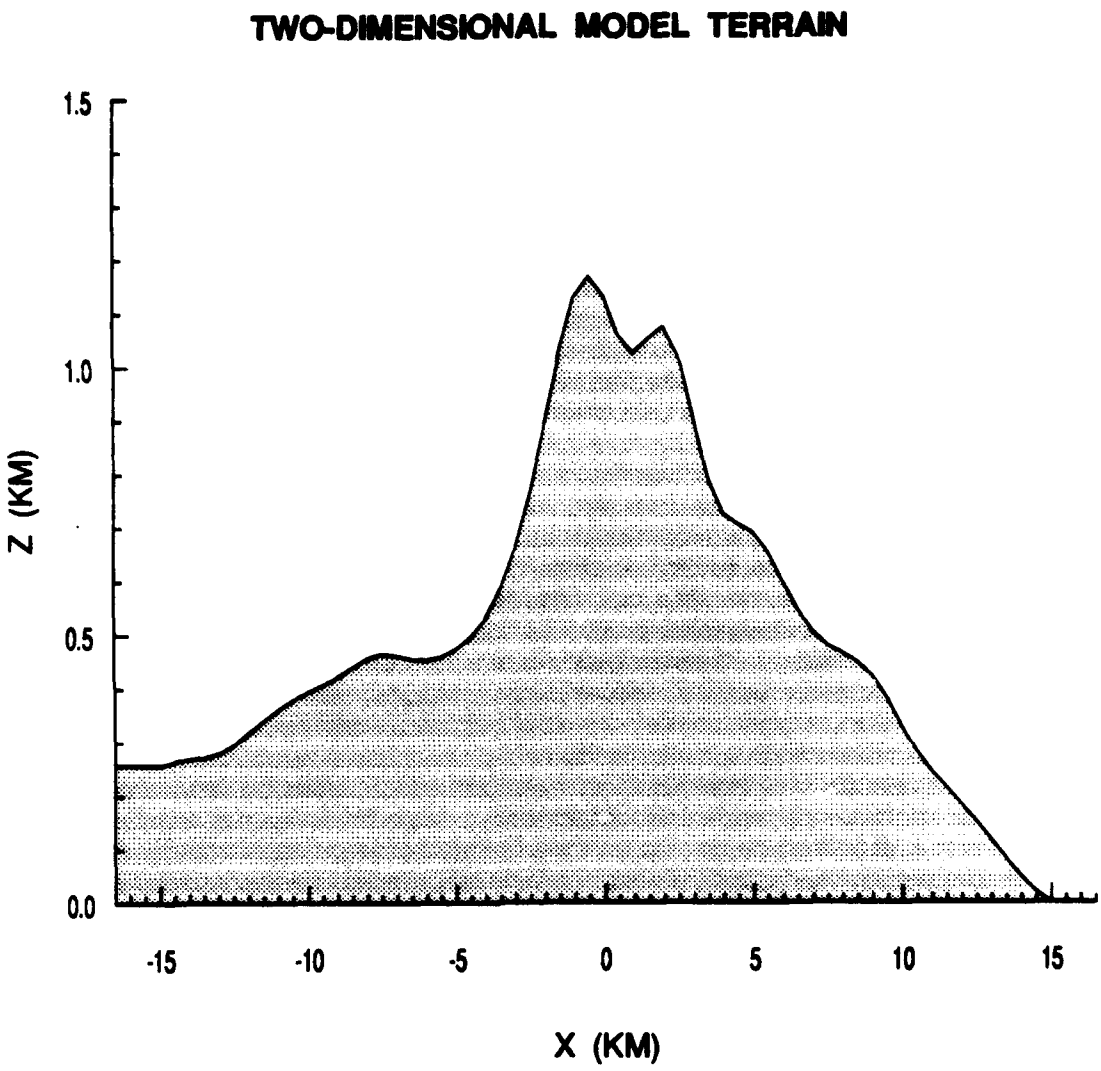

Fig. 22. "Two-dimensional" model terrain elevation data. Terrain elevations are relative to lowest terrain elevation value in slab at y = 0.0 km as described in text. Both axes are labeled in kilometers, with the origin at Langmuir Laboratory.

tains at 0945 MST, 31 July 1984. It was assumed that at initialization time the atmosphere was horizontally homogeneous throughout the model domain. While some horizontal variability certainly existed and probably played a role in the thunderstorm development, it was neglected in this study since it was not possible to determine the exact nature of the variability from the available observational data. The base-state soil moisture and temperature profiles (described in Chapter 5) were likewise assumed to be horizontally homogeneous for the numerical simulations.

For this study, no special initialization procedures were employed. The model was initialized approximately 60 min prior to the expected onset of convection to allow time for model "spin-up." The employment of a simplified base-state wind profile, described later in Chapter 5, combined with the assumption of a nearly dynamically balanced base-state atmosphere permitted the short spin-up time. After an initial 15 min period designed to allow dynamical balancing without external forcing mechanisms, the short-wave radiation package was activated to produce the surface heating crucial to the development of the thunderstorms.

Chapter 5

Experimental Design

As discussed in Chapter 1, the purpose of this study is to determine the important processes involved in the initiation, development, and maintenance of mountain thunderstorms by comparing the results of numerical simulation experiments with Doppler radar observations. This chapter describes the experimental design chosen to achieve this goal. A total of six numerical simulations (one control and five experiments) were conducted with the RAMS to test the effect of differing initial conditions and forcing mechanisms. Section 5.1 completes the description of the basic numerical model configuration chosen for the control simulation. Section 5.2 describes the construction of the base-state atmospheric environmental profiles used to initialize the control simulation and most of the experiments. Finally, section 5.3 outlines the five numerical simulation experiments.

5.1 Control Simulation Configuration

This section completes the description begun in Chapter 4 of the model configuration employed in the control simulation. This configuration formed the basis for all the numerical experiments; changes to the configuration for those experiments are briefly described in section 5.3 and in more detail in later chapters.

The simulation initialization time and location were carefully chosen to properly depict the radiative heating effects on the surface. The control simulation was initialized at 0945 MST and integrated forward in time 9000 s (2.5 hr). The model domain's western edge was placed at 33.975° N, 107.36° W.

The soil model assumes a uniform soil temperature profile throughout the depth of the model. The soil temperature is taken to be the same as the base-state temperature at the lowest level in the atmospheric profile. The base-state soil moisture profile constructed for the control simulation assumed an increasing moisture content with increasing depth beneath the surface. The initial soil moisture profile was specified as a percentage of the soil moisture content at saturation (expressed in terms of volume of water per volume of soil) (Tremback and Kessler, 1985). Table 2 provides the base-state soil moisture profile used to initialize the control simulation. A sandy clay loam soil type was chosen for use in the soil model. This choice is consistent with the soil type typically found in the mountains of the southwestern United States.

Table 2: *Soil model base-state soil moisture profile. Soil moisture given as percentage of saturated soil moisture.*

SOIL MODEL LEVEL (CM)	SOIL MOISTURE (% OF SATURATION)
0	36
1	41
4	48
16	56
32	60

5.2 Atmospheric Base-State Profiles

RAMS requires base-state temperature, moisture, and wind profiles for initialization. This section describes the construction of the atmospheric base-state profiles

used to initialize most of this study's numerical experiments. Modified base-state profiles used to initialize some of the simulation experiments will be discussed as appropriate in later chapters.

The base-state profiles were derived from the observations collected over and near the Magdalena Mountains on the morning of 31 July 1984 (see Chapter 3). Data gaps and unreliable wind information from the morning soundings prevented their use alone to initialize the model. Instead, the two rawinsonde temperature and moisture soundings were combined to construct the base-state temperature and moisture profiles. The alternative wind profiles derived from synthesized Doppler radar wind fields (see section 3.2.4) were used to construct the base-state wind profile.

5.2.1 Temperature And Moisture Profiles

Figures 2 and 3 show the morning radiosonde temperature and moisture soundings available for 31 July 1984 (referred to as the airport and Langmuir soundings respectively). The Langmuir sounding was collected at nearly the simulation initialization time but does not extend down to the valley floor. The airport sounding extends to the valley floor but was collected about 1.5 hr prior to initialization time. Therefore, neither set of observed temperature and moisture data could be used by itself to initialize the model. In constructing the base-state temperature and moisture profiles, the observational data was preserved to the greatest extent possible.

The airport sounding was chosen as the basis for the base-state temperature profile. The later sounding (Langmuir) was not used explicitly because it contained unusually cold temperatures between 550 and 400 mb. At other levels, the two soundings were nearly identical. The airport sounding was used above 780 mb with only minor smoothing. Below 780 mb the observed temperatures were increased slightly to account for the effect of morning heating between the early morning ob-

servation time and the model initialization time. The bottom of the profile was chosen to coincide with the lowest terrain elevation in the model domain. Figure 23 shows the final base-state temperature profile.

Both soundings exhibited basically the same vertical moisture structure, but with widely varying differences in magnitude. Above 660 mb the final base-state profile represents a smoothed average of the two soundings. Below 660 mb the mixing ratio was increased by about 1.5 g kg^{-1} over that in the airport sounding to account for the low-level moistening typically observed in the area in the early morning. This moistening, described by Raymond and Wilkening (1982), is brought on by a weak thermally-driven upslope flow which advects moisture from the lower elevations of the Rio Grande Valley. As with the temperature profile, the bottom of the profile was chosen to coincide with the lowest terrain elevation in the model domain. The final moisture profile (Fig. 23) is similar to the composite thunderstorm profile described by Raymond and Wilkening (1985).

5.2.2 Wind Profiles

Figures 5 and 6 show the two Doppler-derived wind profiles available for 31 July 1984 (referred to as Profiles 1 and 2, respectively). Profile 1 was constructed with data collected nearest the initialization time but extends to only approximately 400 mb. Profile 2 was constructed with data collected well after the initialization time but extends to at least 200 mb. Neither profile provides wind data below the mountain top (approximately 3280 m). Figure 4 shows the Ziegler (personal communication, 1986) estimated wind profile (referred to as Profile 3) that extends from the valley floor to 2000 m above the mountain-top level (approximately 5280 m MSL). Clearly neither set of Doppler-derived wind profiles nor the estimated wind profile could be used alone to initialize the model.

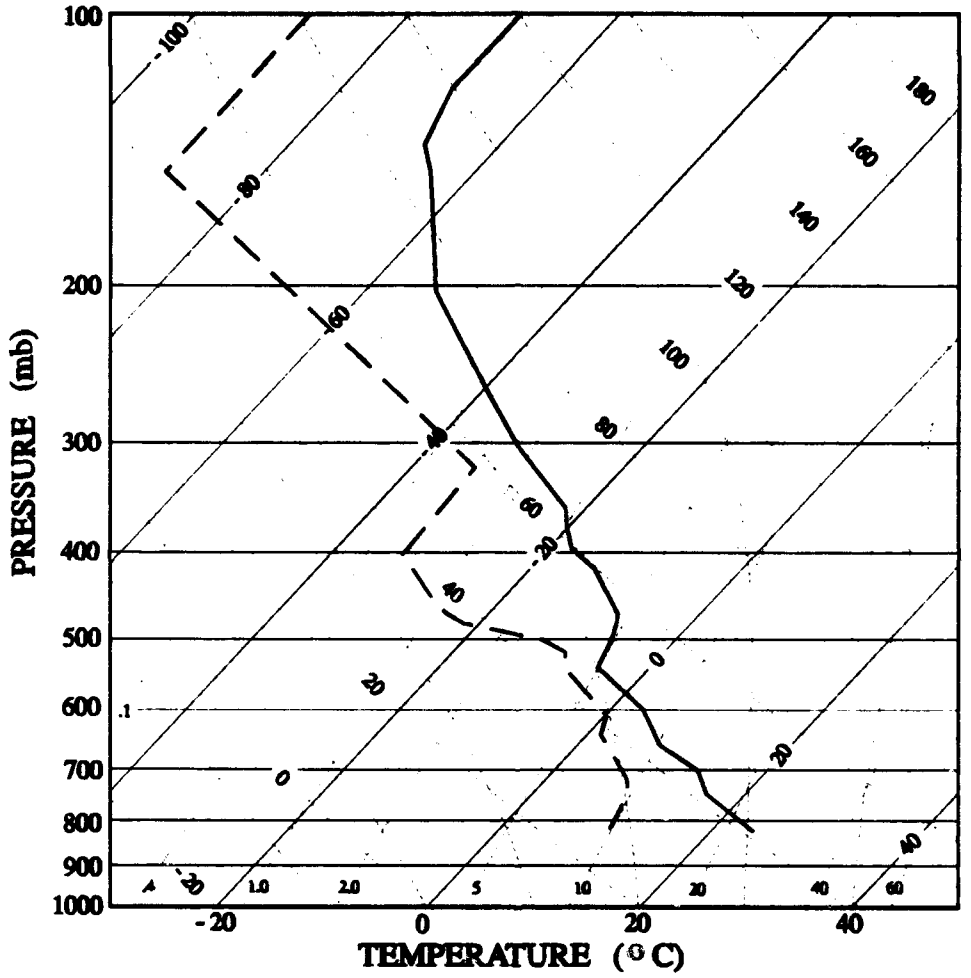

Fig. 23. Skew T, log P plot of base-state thermodynamic profile used to initialize the numerical model. Heavy solid and dashed lines represent sensible and dewpoint temperature profiles, respectively. Skew T, log P diagram labeled as in Fig. 2.

This subsection describes the construction of a preliminary composite wind profile from the three profiles described above. It then describes the modifications made to the preliminary profile to arrive at the base-state wind profile used to initialize the two-dimensional (2-D) numerical simulations.

5.2.2.1 Preliminary Composite Wind Profile

Since Profile 1 contained data collected nearest the initialization time and before significant storm development, it was used wherever possible to construct the preliminary wind profile. Profile 1 was combined with Profile 2 (above 440 mb) and with Profile 3 (below 640 mb) to produce the preliminary profile. Figure 24 shows the three profiles and the smoothed preliminary composite wind profile. The composite wind profile is similar to the composite thunderstorm profile described by Raymond and Wilkening (1985).

5.2.2.2 Base-State Wind Profiles

The preliminary composite wind profile served as the basis for constructing two base-state wind profiles: one a full profile containing both u and v wind components (referred to as the 3-D profile), and the other a profile containing only the u component (referred to as the 2-D profile). Since the 2-D base-state profile was based directly on the 3-D profile, the 3-D profile will be described first.

Above 480 mb the 3-D profile is identical to the preliminary composite profile. Below 740 mb (approximate height of the model mountain top) the wind speed was set to zero. This was done for two reasons. First, the wind profile available for below the mountain top was only estimated--other qualitative observations that day indicated the winds were light and variable below the mountain (Winn, personal communication, 1987). Second, setting the wind speed to zero below the mountain top significantly simplified the model's spin-up phase. Between 740 mb and 480 mb

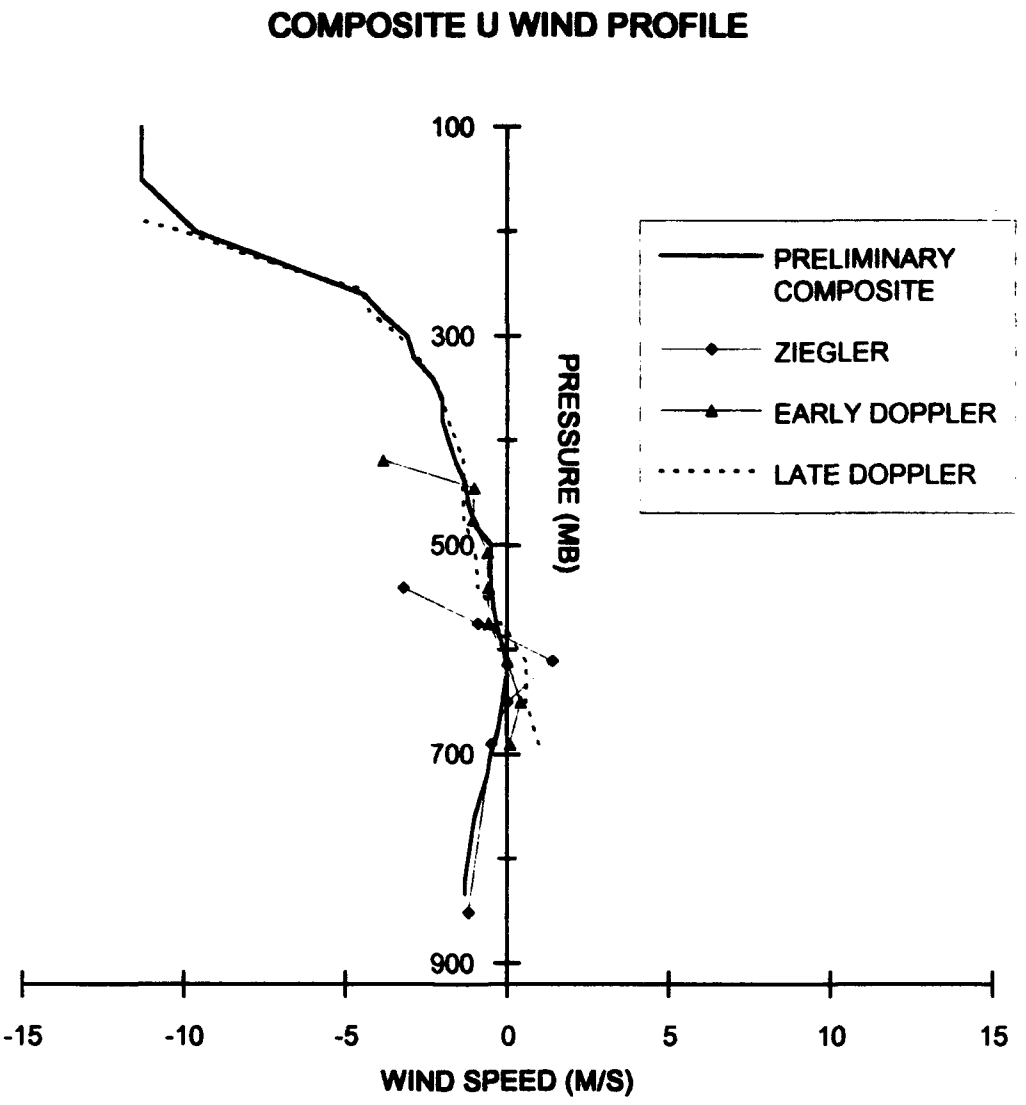

Fig. 24a. Composite vertical profile of u wind component used to construct profile to initialize the numerical model. Heavy solid line represents preliminary composite profile of u wind component. Observed and estimated profiles (shown in Figs. 4, 5, and 6) are shown for reference. Axes labeled as in Fig. 4.

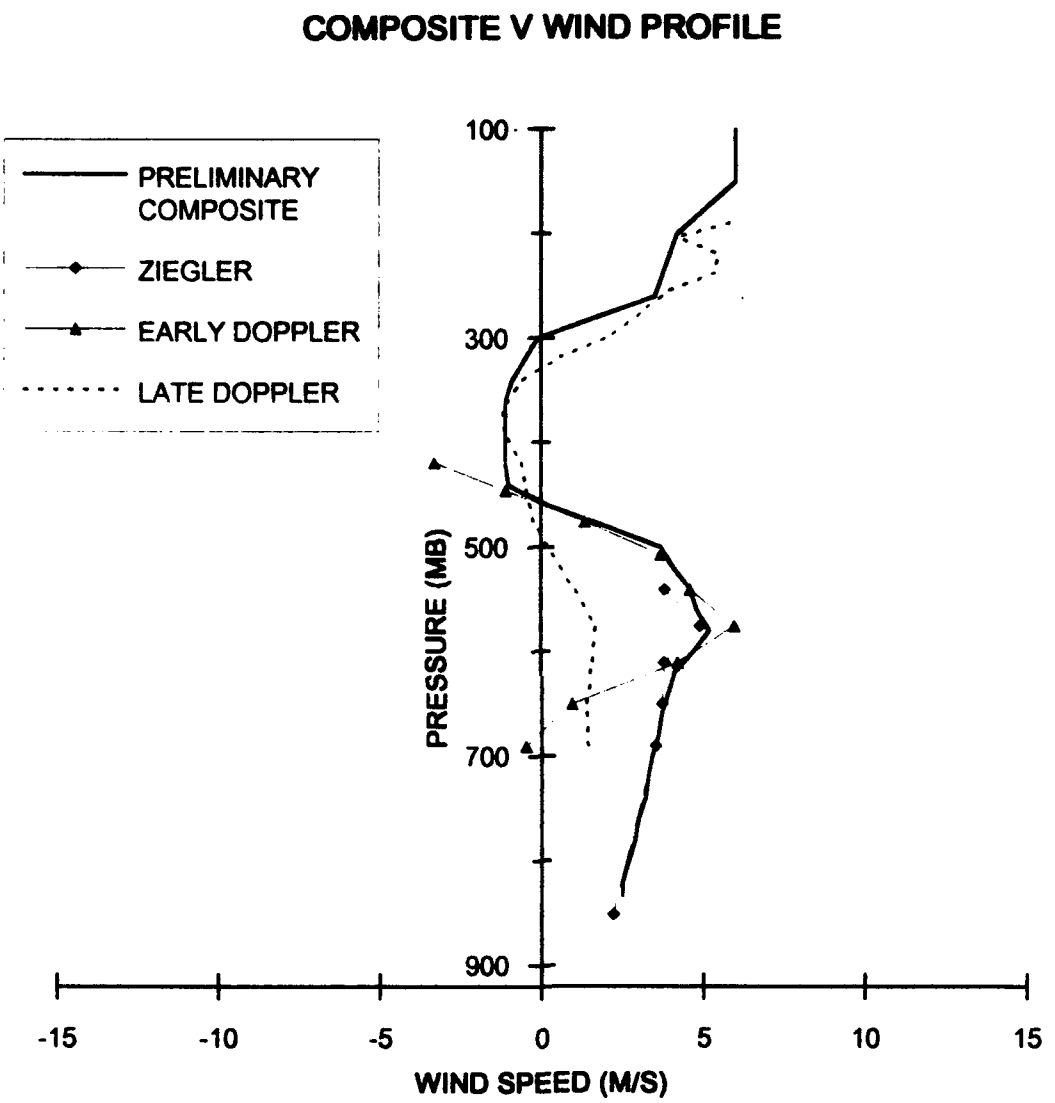

Fig. 24b. Composite vertical profile of v wind component used to construct profile to initialize the numerical model. Heavy solid line represents preliminary composite profile of v wind component. Observed and estimated profiles (shown in Figs. 4, 5, and 6) are shown for reference. Axes labeled as in Fig. 4.

the wind speeds were gradually increased from zero at 740 mb to the full preliminary composite profile speed at 480 mb. Figure 25 shows the preliminary profile and the final 3-D base-state profile.

The construction of the 2-D base-state profile required further manipulation to satisfy the RAMS requirements for 2-D simulations. The version of RAMS employed for this study allows 2-D simulations to be run only in an x-z slab. Thus only the u component of the wind is allowed in such simulations. The 2-D profile was constructed from the 3-D base-state profile by using the magnitude of the total wind at each pressure level as the $-u$ component of the wind. The shape of the mountain and its orientation with respect to the predominant wind flow permitted this approach. The actual wind was predominantly southeasterly (particularly at low-levels) (Figs. 5, 6, and 25) and perpendicular to the mountain slopes. Similar wind *vs*. slope relationships can be produced within the 2-D limitations by using the magnitude of the actual wind as the $-u$ component. The actual wind orientation is even less important in these simulations since the magnitude was set to zero below the mountain top. Figure 26 shows the 2-D base-state wind profile.

5.3 Numerical Experiments

This section describes the five numerical simulation experiments conducted to test the effect of differing initial conditions and forcing mechanisms on the simulated storms. For each experiment, only one such condition or mechanism was varied from the control's configuration. The simulation experiments will be referred to as EXP1 through EXP5 for the rest of this discussion. Table 3 provides a brief overview of all the simulations conducted for this study. The term "standard" as used in the table refers to the profiles or configuration used for the control simulation and described in Chapter 4 and in Sections 5.1 and 5.2. Details of base-state profiles differing from

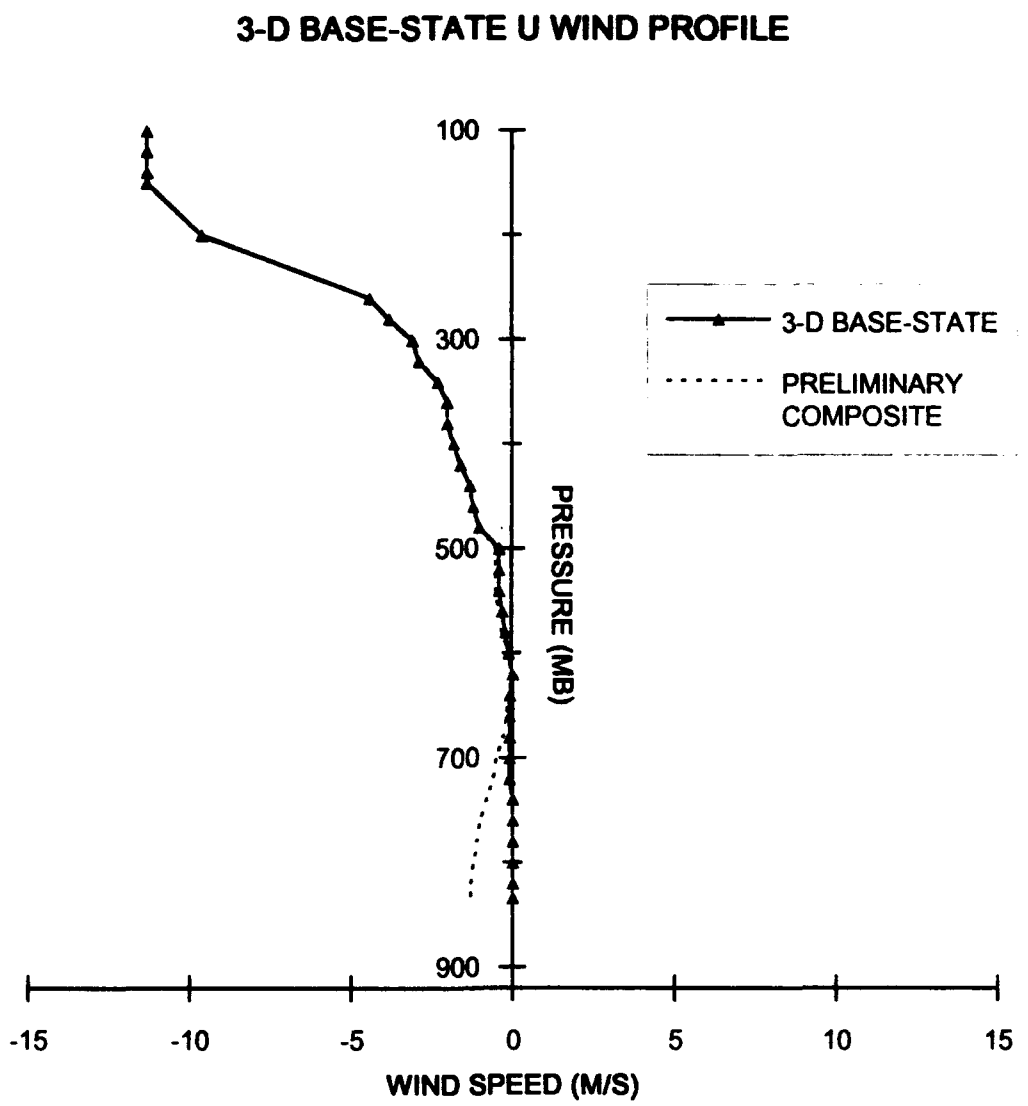

Fig. 25a. Vertical profile of the u wind component of the "three-dimensional" base-state profile (heavy solid line with ticks) used to build final profile for input to the model. The preliminary composite profile shown in Fig. 24a is shown for reference. Axes as labeled in Fig. 4.

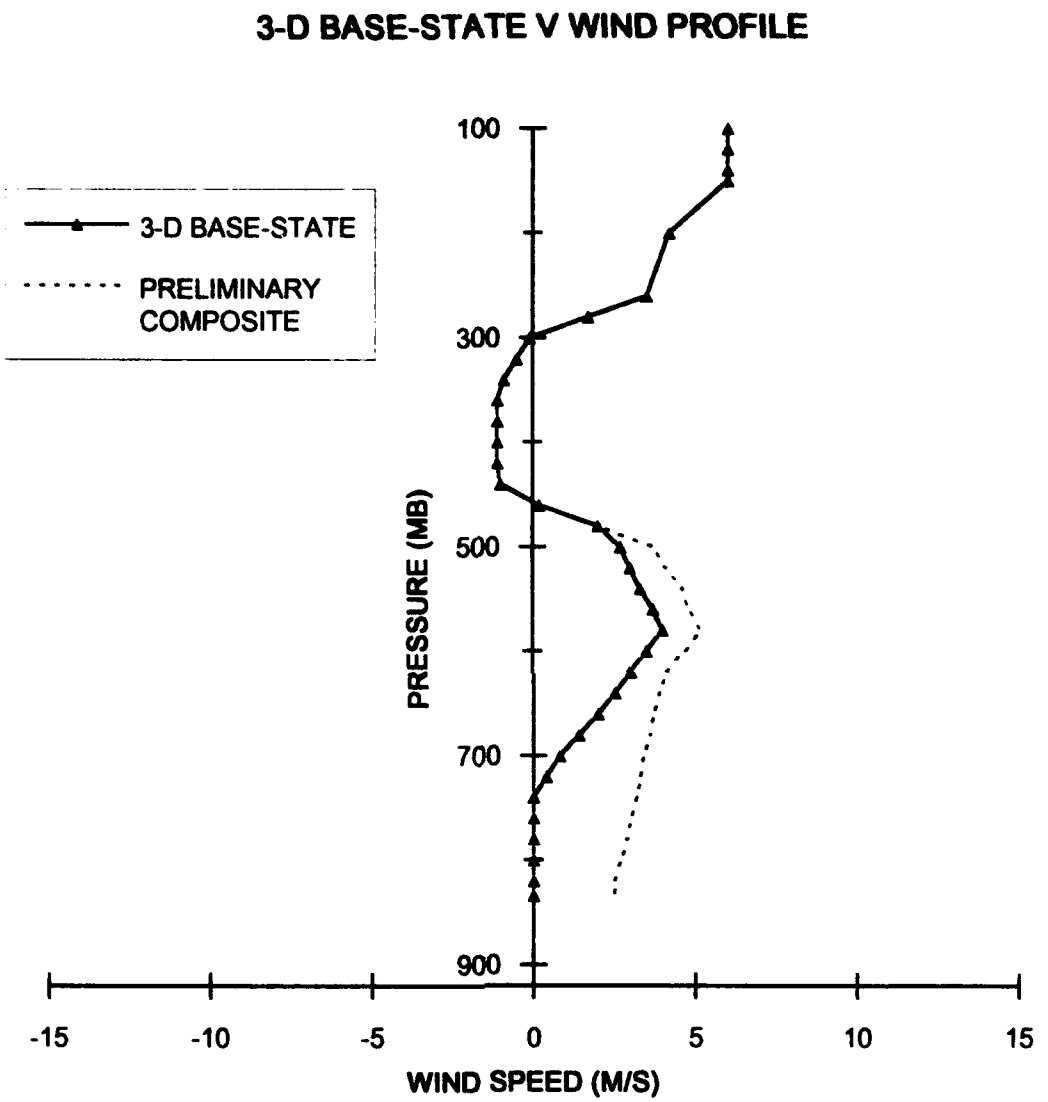

Fig. 25b. Vertical profile of the v wind component of the "three-dimensional" base-state profile (heavy solid line with ticks) used to build final profile for input to the model. The preliminary composite profile shown in Fig. 24b is shown for reference. Axes as labeled in Fig. 4.

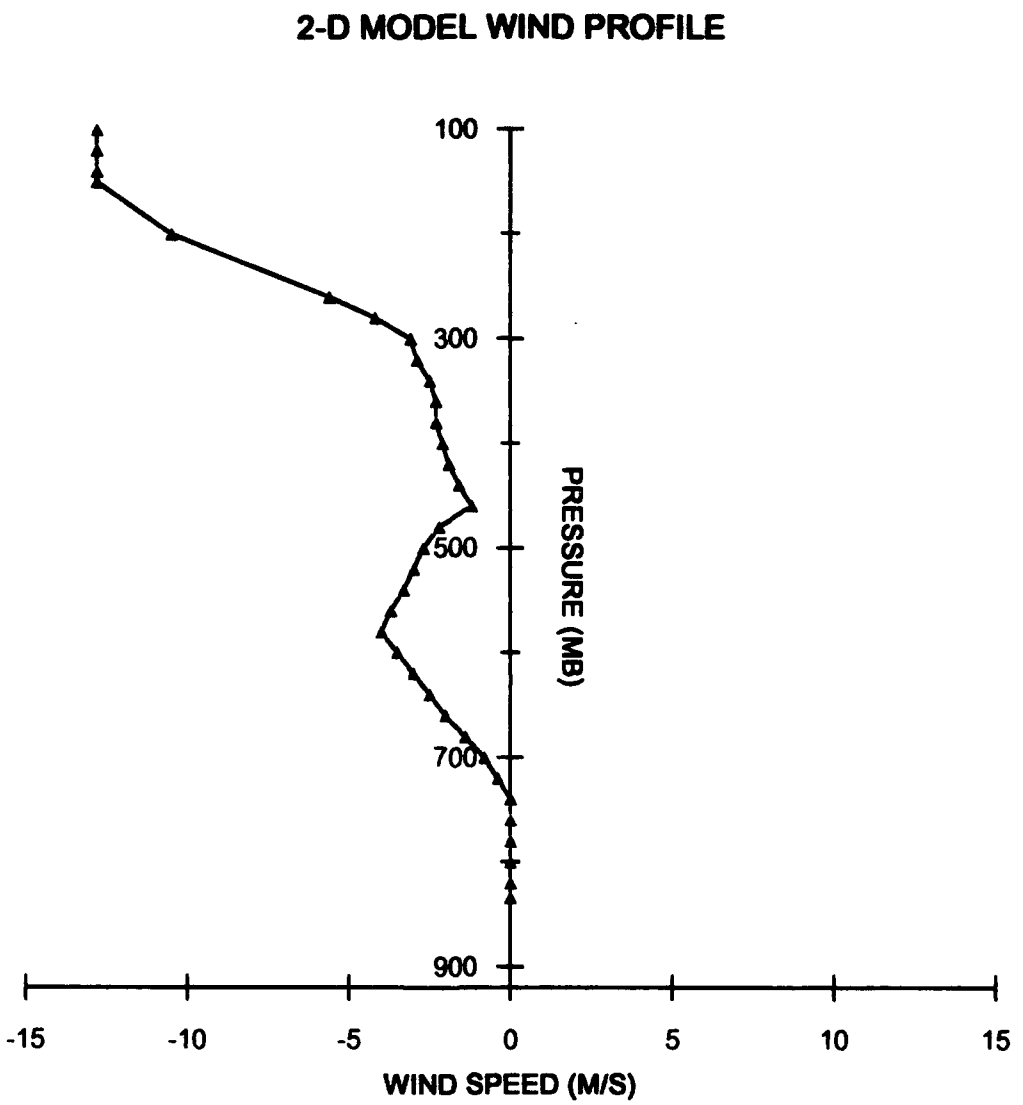

Fig. 26. Vertical wind profile used to initialize the numerical model. Wind speed in this profile equals the magnitude of the total wind in the profiles shown in Fig. 25. Axes labeled as in Fig 4.

Table 3: *Numerical simulation experiment overview. "Standard" refers to condition or process employed in the control simulation.*

SIMULATION NAME	WIND PROFILE	THERMODYNAMIC PROFILE	MICROPHYSICS	SHORT-WAVE RADIATION
CONTROL	STANDARD	STANDARD	STANDARD	STANDARD
EXP1	***CALM***	STANDARD	STANDARD	STANDARD
EXP2	***50% SPEED PROFILE***	STANDARD	STANDARD	STANDARD
EXP3	STANDARD	STANDARD	STANDARD	*NONE*
EXP4	STANDARD	STANDARD	***WARM RAIN MICROPHYSICS***	STANDARD
EXP5	STANDARD	***MOISTENED LOWER LEVELS***	STANDARD	STANDARD

those of the control simulation will be described as appropriate in the following chapters.

EXP1 and EXP2 evaluated the sensitivity of the simulated storms to the initial base-state wind profiles. The intent behind this set of experiments was to isolate the contribution of the environmental wind field to the development of the storms. EXP1 was initialized with calm winds throughout the depth of the atmosphere, while EXP2's initial wind profile contained wind speeds half the magnitude of the control's.

EXP3 and EXP4 tested the sensitivity of the simulations to diabatic heating effects. The purpose of EXP3 was to evaluate the importance of solar heating in storm development. EXP3's simulation was conducted with the RAMS short-wave radiation package deactivated; in effect, "turning off the sun". It is important to note that deactivation of the short-wave radiation package strongly impacts the behavior of the underlying soil model. As in nature, removing the model's solar radiation also cuts off

surface heating and any thermal forcing resulting from such heating. The purpose of EXP4 was to determine the importance of the ice-phase cloud microphysical processes and their associated latent heating effects in storm development. EXP4 was conducted with all the ice-phase microphysical processes deactivated and only the warm rain microphysical parameterizations activated.

The final experiment, EXP5, was conducted to evaluate the effect on the simulated storm of a moistened base-state moisture profile. The base-state moisture profile was moistened by up to 0.5 g kg^{-1} below 720 mb. Section 9.1 describes the profile used for EXP5.

Chapter 6

Analysis And Verification Of The Control Simulation

This chapter describes the results of the control simulation (referred to as the control). Section 6.1 provides a brief analysis of the simulated storm's evolution, and Section 6.2 compares the simulated storm with the 31 July 1984 Doppler radar observations described in Chapter 3. Section 6.3 compares the microphysical evolution of the simulated storm with the results of Lang's (1991) microphysical retrieval study of a similar storm that occurred on 3 August 1984.

Throughout the simulation descriptions which follow in this and later chapters, the following conventions will be employed. First, all time references will be simulation times in seconds unless otherwise noted. Table 4 provides a conversion between simulation times in seconds and hours and actual times with the 0945 MST model initialization time employed for these simulations.

All references ω heights will be based on the model's grid coordinates unless otherwise noted. As discussed in Chapter 4, the model terrain elevations were adjusted so that the lowest terrain elevation in the model grid had a value of zero. Thus, the model's lower boundary is located at approximately 1820 m MSL. All other model grid heights are reduced from actual MSL heights by this same amount. Table 5 provides a conversion between model heights and actual MSL heights.

Finally, for the purposes of the following descriptions, a cell is defined as any relative condensate and/or updraft maximum that exhibits vertical continuity. This definition follows closely that used by Lang (1991) and employed in Chapter 3.

Table 4: *Simulation time to actual time conversion chart.*

SIMULATION TIME (S)	SIMULATION TIME (HR)	ACTUAL TIME (MST)	SIMULATION TIME (S)	SIMULATION TIME (HR)	ACTUAL TIME (MST)
0	0.00	9:45	4680	1.30	11:03
180	0.05	9:48	4860	1.35	11:06
360	0.10	9:51	5040	1.40	11:09
540	0.15	9:54	5220	1.45	11:12
720	0.20	9:57	5400	1.50	11:15
900	0.25	10:00	5580	1.55	11:18
1080	0.30	10:03	5760	1.60	11:21
1260	0.35	10:06	5940	1.65	11:24
1440	0.40	10:09	6120	1.70	11:27
1620	0.45	10:12	6300	1.75	11:30
1800	0.50	10:15	6480	1.80	11:33
1980	0.55	10:18	6660	1.85	11:36
2160	0.60	10:21	6840	1.90	11:39
2340	0.65	10:24	7020	1.95	11:42
2520	0.70	10:27	7200	2.00	11:45
2700	0.75	10:30	7380	2.05	11:48
2880	0.80	10:33	7560	2.10	11:51
3060	0.85	10:36	7740	2.15	11:54
3240	0.90	10:39	7920	2.20	11:57
3420	0.95	10:42	8100	2.25	12:00
3600	1.00	10:45	8280	2.30	12:03
3780	1.05	10:48	8460	2.35	12:06
3960	1.10	10:51	8640	2.40	12:09
4140	1.15	10:54	8820	2.45	12:12
4320	1.20	10:57	9000	2.50	12:15
4500	1.25	11:00			

Table 5: *Model height to actual height conversion.*

MODEL HEIGHT (KM)	ACTUAL HEIGHT (KM MSL)
0.00	1.82
0.25	2.07
0.75	2.57
1.25	3.07
1.75	3.57
2.25	4.07
2.75	4.57
3.25	5.07
3.75	5.57
4.25	6.07
4.75	6.57
5.25	7.07
5.75	7.57
6.25	8.07
6.75	8.57
7.25	9.07
7.75	9.57
8.25	10.07
8.75	10.57
9.25	11.07
9.75	11.57
10.25	12.07
10.75	12.57
11.25	13.07
11.75	13.57
12.25	14.07

6.1 Analysis of Simulated Storm Evolution

Three primary cells developed during the control simulation. The origins of two of the cells can be traced back to the earliest cloud and updraft development in the simulation. The third cell developed primarily as a result of the upslope wind flow induced by circulation of the first two cells.

The first condensate developed at 5760 s over the western slope of the mountain at x = -2.5 km and z = 2.0 km. For the next 9 min, the cloud grew slightly and drifted westward. By 6480 s the cloud had dissipated and was replaced by a new cloud which formed at nearly the same position as the first. Figures 27 and 28 show analyses of total condensate mixing ratio and vertical velocity, respectively, for 6480 s. An analysis of the wind field for this time period showed that the first cloud drifted away from the weak updraft which contributed to its initial development. The updraft remained fixed at approximately its original position and led to the subsequent initiation of the second cloud which quickly developed into a cell. During this same period, a low-level westerly flow of approximately 1.5 m s^{-1} developed below 2.0 km west of the mountain ridge. Further investigation and the results of EXP3 (discussed in Chapter 8) show that this westerly flow appeared to develop as a result of a dynamically induced mountain-wave circulation on the lee side of the mountain. The interaction of this westerly flow with the easterly flow over the mountain created an area of low-level convergence at approximately x = -2.5 km which supported the fixed updraft described above. Figure 29 shows an example of this convergence.

By 6660 s the first cell (denoted hereafter as CC1) was located at x = -2.5 km and z = 2.5 and was approximately 1.0 km deep. A new cell (denoted hereafter as CC2) had developed just over the ridge at x = -1.0 km and z = 2.0 km. These cells continued to develop slowly and drift slowly westward until 7200 s. During this peri-

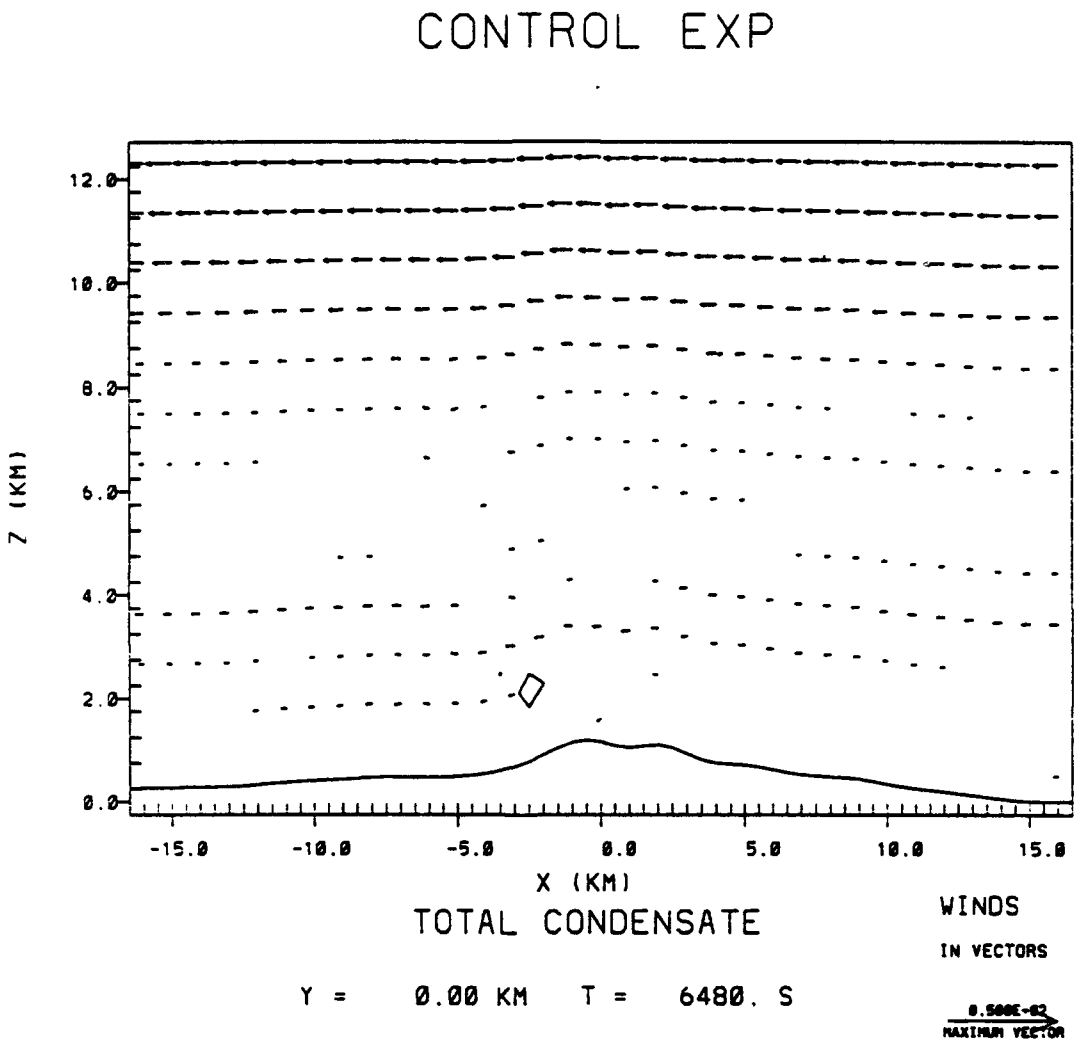

Fig. 27. East-west vertical cross-section of simulated total condensate mixing ratios overlaid with simulated wind vectors for CONTROL simulation at 6480 s. Contours are every 2.0 g kg^{-1} starting at 0.1 g kg^{-1}. Wind vector length shown in lower right-hand corner of figure equals 50 m s^{-1}. Vertical axis is labeled in kilometers above the minimum terrain elevation in the simulation grid (in this case 1.82 km) as described in the text. Horizontal axis is horizontal distance labeled in kilometers. The cross-section shown is located at y = 0.0 km and runs east-west, with the origin at Langmuir Laboratory.

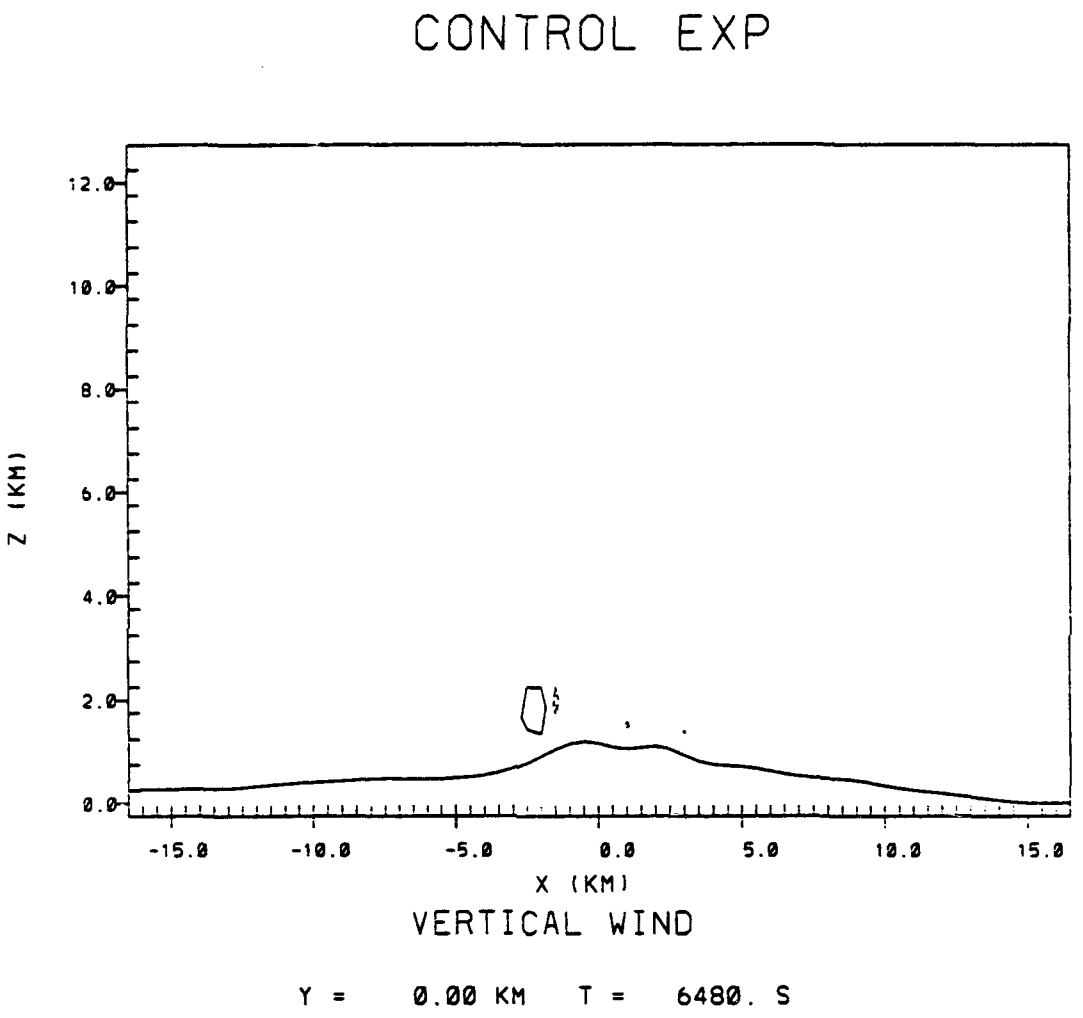

Fig. 28. East-west vertical cross-section of simulated vertical velocity contoured every 3.0 m s^{-1} starting at 1.5 m s^{-1} for CONTROL simulation at 6480 s. Solid (dashed) contours show positive (negative) vertical velocities. Axes labeled as in Fig. 27.

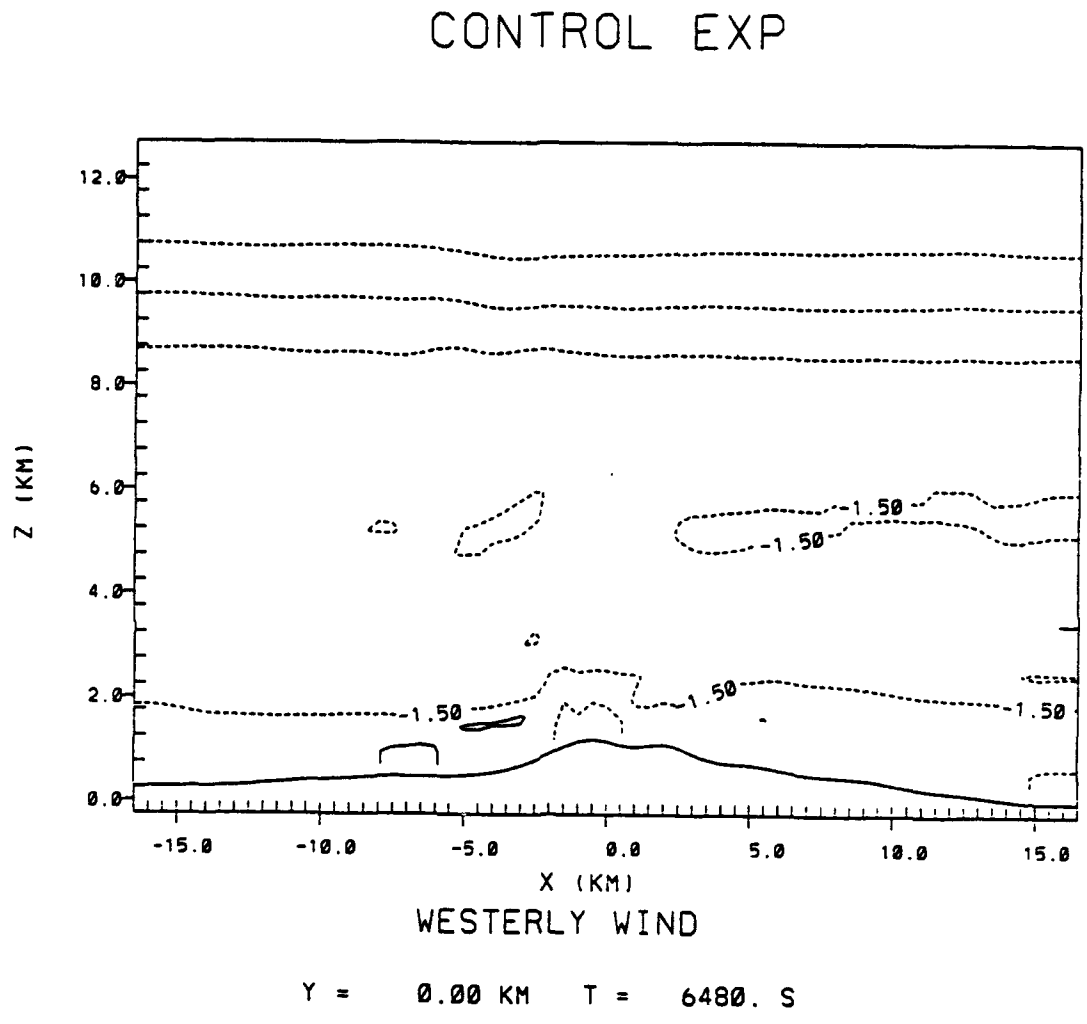

Fig. 29. East-west vertical cross-section of simulated u wind component contoured every 3.0 m s^{-1} starting at 1.5 m s^{-1} for CONTROL simulation at 6480 s. Solid (dashed) contours show westerly (easterly) winds. Axes are labeled as in Fig. 27.

od, the convergent area remained at approximately x = -2.5 km. At the same time, a shallow layer of easterly flow developed beneath the westerly flow, creating a second low-level convergent area at x = -5.0 km (Fig. 30). The updraft associated with CC1 at 6660 s separated into two distinct updrafts after 6840 s. The upper portion of the original updraft drifted westward with the condensate while the lower portion of the updraft remained anchored at approximately x = -2.5 km. CC2's original updraft developed at about 6840 s and moved slightly westward before diminishing after 7200 s. At about this same time, the condensate associated with CC2 moved over the anchored updraft at x = -2.5 km. By 7200 s both major updrafts exceeded 4.5 m s^{-1}. Figures 31 and 32 show analyses of total condensate mixing ratio and vertical velocity, respectively, for a time representative of this period--6840 s.

Between 7200 s and 7560 s, CC2's condensate drifted westward and merged with the lower remnants of CC1's updraft. During this period, both cells' updrafts remained separate and drifted westward. CC2's updraft increased to 6.7 m s^{-1}, while CC1's weakened to about 1.5 m s^{-1} by 7560 s. At 7200 s, a new updraft developed west of CC1 at x = -5.0 km in response to the secondary convergent area at that location. This updraft began to strengthen as CC1 moved into its vicinity. By 7560 s, both CC1's original updraft and the new updraft were approximately the same strength. A relatively strong easterly jet developed west of CC1 at z = 3.75 km near the level of the capping inversion. Several small cloud masses also formed over the ridge between x = 0.0 km and x = 2.0 km and remained very weak with no associated updrafts. The first significant development of rain water, pristine ice crystals, and graupel occurred during this period. Prior to these developments, the condensate consisted almost entirely of cloud water. Rain water first developed at 7100 s in CC1 near z = 3.75 km. By 7380 s, most of the small area of rain had evaporated as it fell

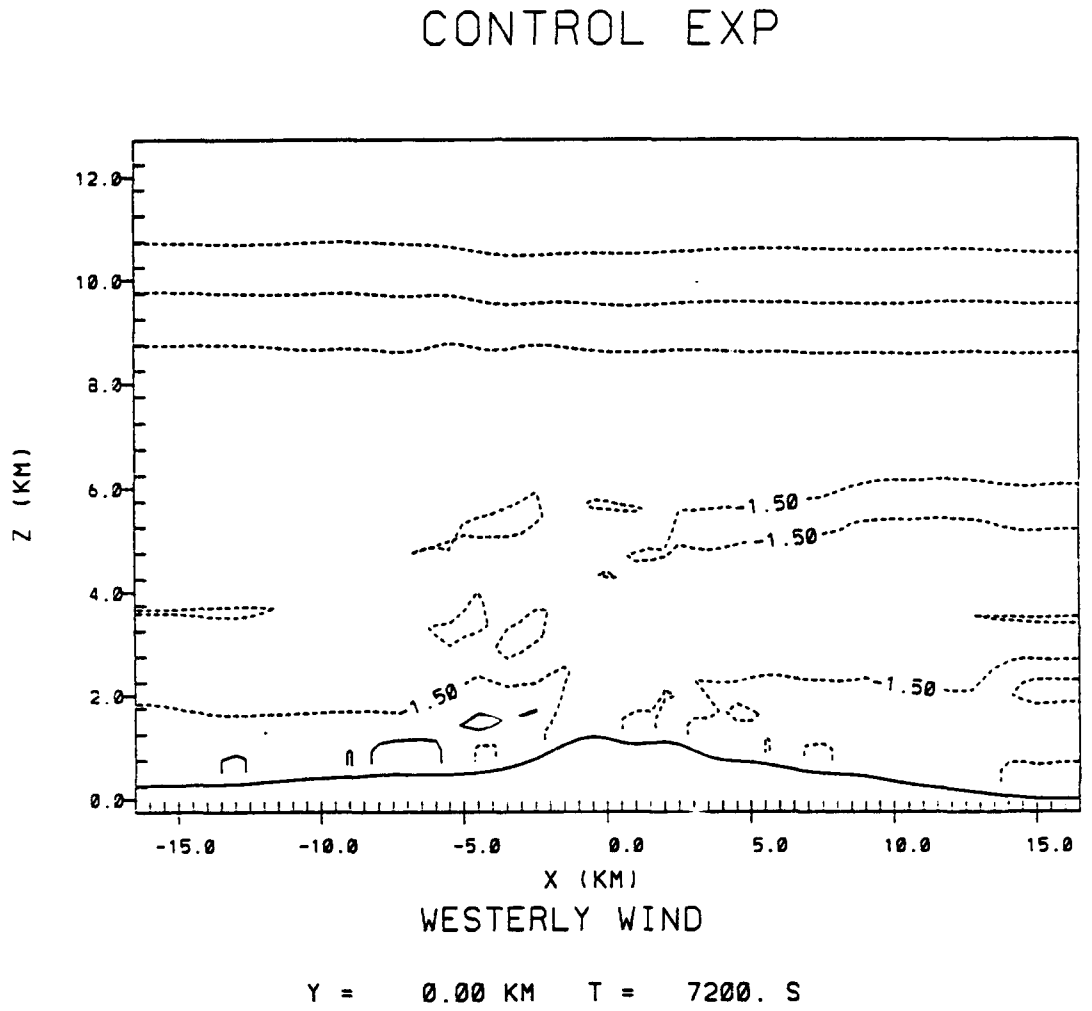

Fig. 30. East-west vertical cross-section of simulated u wind component as in Fig. 29 except for CONTROL simulation at 7200 s.

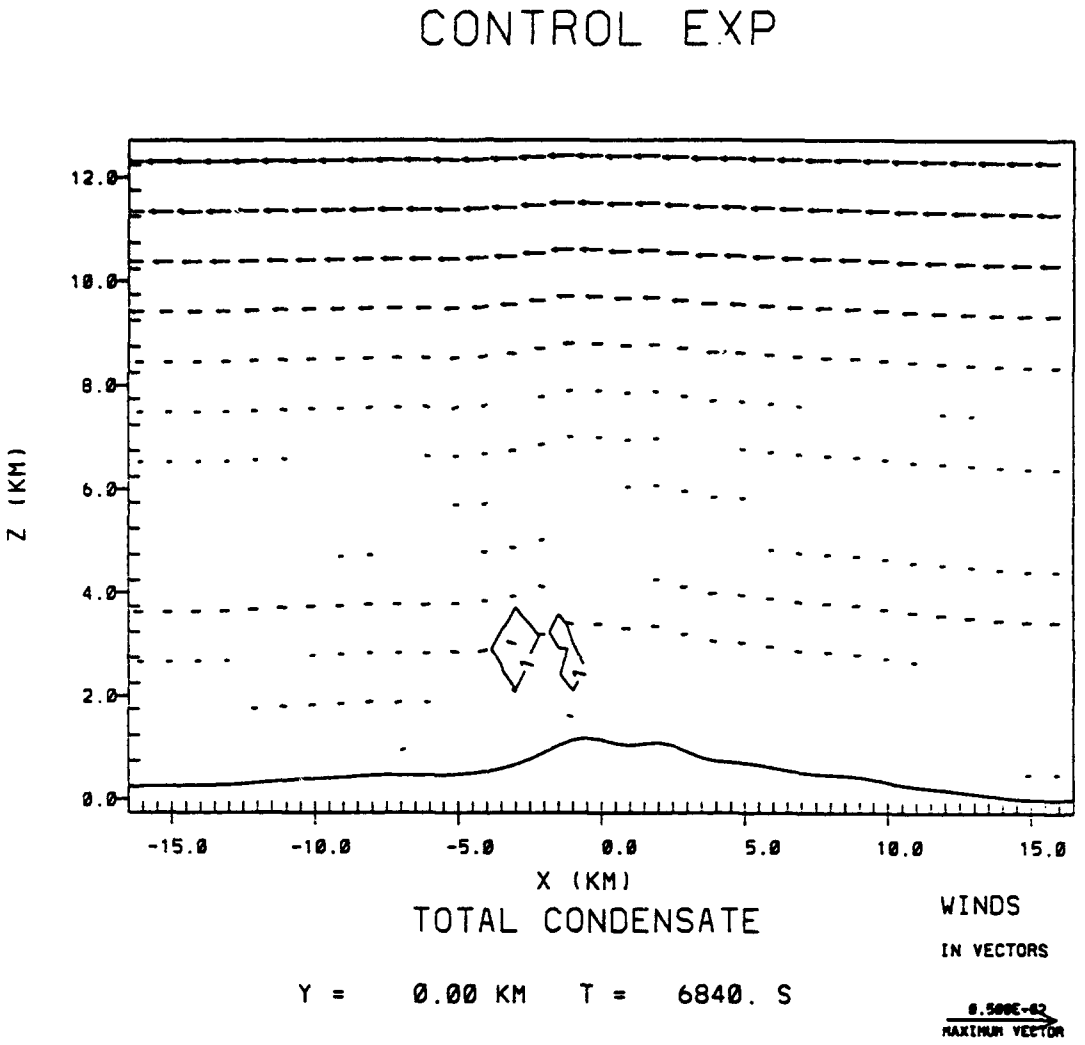

Fig. 31. Analogous to Fig. 27, east-west vertical cross-section of simulated total condensate mixing ratios overlaid with simulated wind vectors for CONTROL simulation at 6840 s. Contour label "1" represents 0.1 g kg^{-1}.

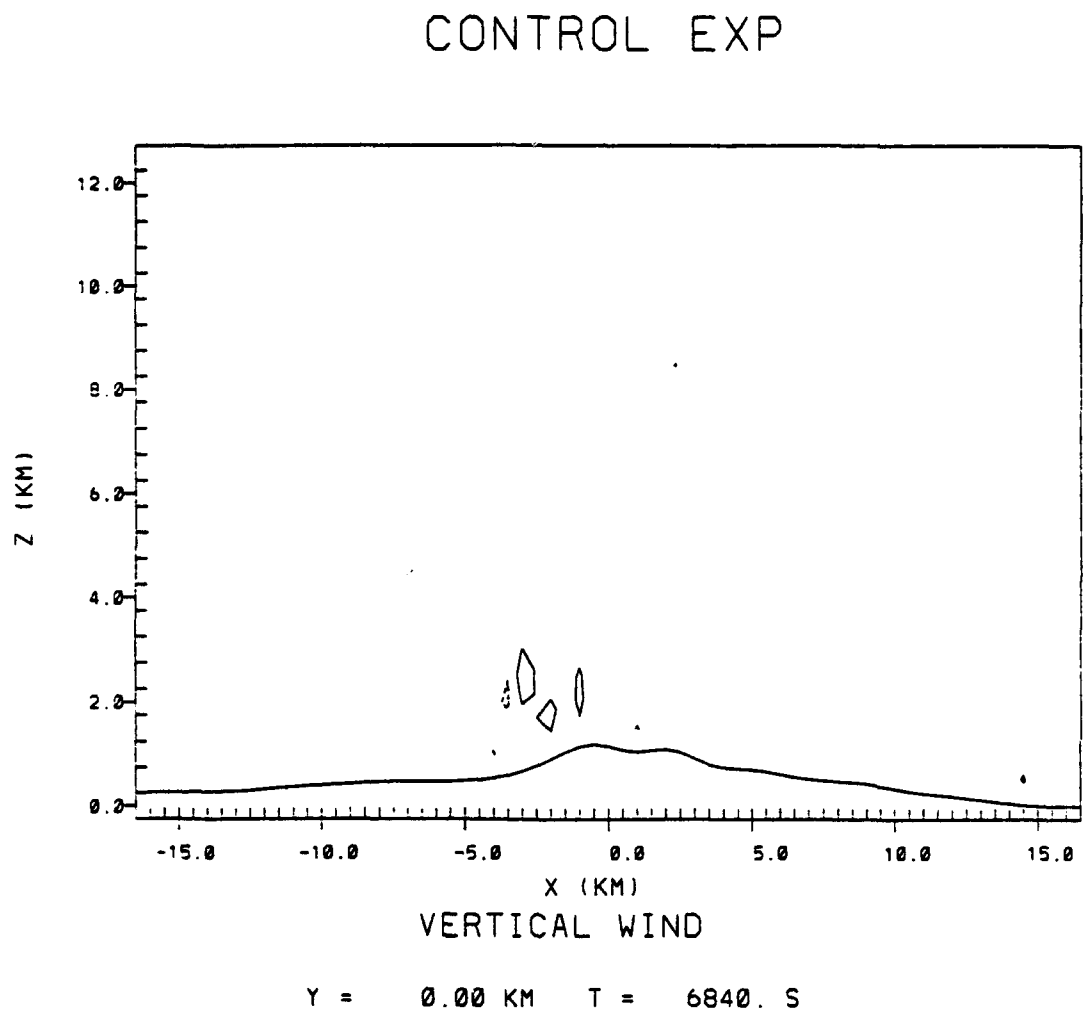

Fig. 32. Analogous to Fig. 28, east-west vertical cross-section of simulated vertical velocity for CONTROL simulation at 6840 s.

out of CC1, and CC1 drifted away. Both pristine ice crystals and graupel developed in CC1 near z = 4.0 km between 7110 and 7290 s. Rain water developed at 7560 s near the center of CC2 between z = 3.25 and 3.75 km. Figures 33 and 34 show analyses of total condensate mixing ratio and vertical velocity, respectively, for 7560 s.

By 7740 s, CC2 had become the dominant cell in the merged storm with maximum total condensate mixing ratios of 3.4 g kg^{-1}. A new cell (denoted hereafter as CC3) developed at x = 0.0 km and z = 1.75 km with a weak updraft. CC3's development appears to have resulted primarily from upslope flow induced by the inflow into CC1 and CC2. CC1's original updraft dissipated by this time and was replaced by the newer updraft at x = -5.0 km which had strengthened to 4.5 m s^{-1}. The secondary area of low-level convergence continued to support CC1's new updraft and also provided support to CC2's updraft. Graupel first developed in CC2 at this time between z = 3.0 and 4.5 km. Ice crystals continued in CC1 and also began to develop in CC2 at this time.

At 7920 s the first precipitation developed as a rain shaft from CC2 between x = -3.0 and -4.0 km. At this time also, CC1 had regenerated significantly while CC2 weakened slightly. Maximum total condensate mixing ratios in both CC1 and CC2 ranged from 2.0 to 3.0 g kg^{-1}. The rapid regeneration of CC1 can be attributed to the rapid strengthening of its new updraft to over 10.0 m s^{-1}. At the same time, another new updraft also developed just to the west of CC1 in response to the low-level convergence which continued near x = -6.0 km. Graupel and rain water redeveloped in CC1 between z = 2.25 and 3.75 km. CC1's total condensate maximum consisted entirely of cloud water, while CC2's maximum consisted of a mixture of ice crystals,

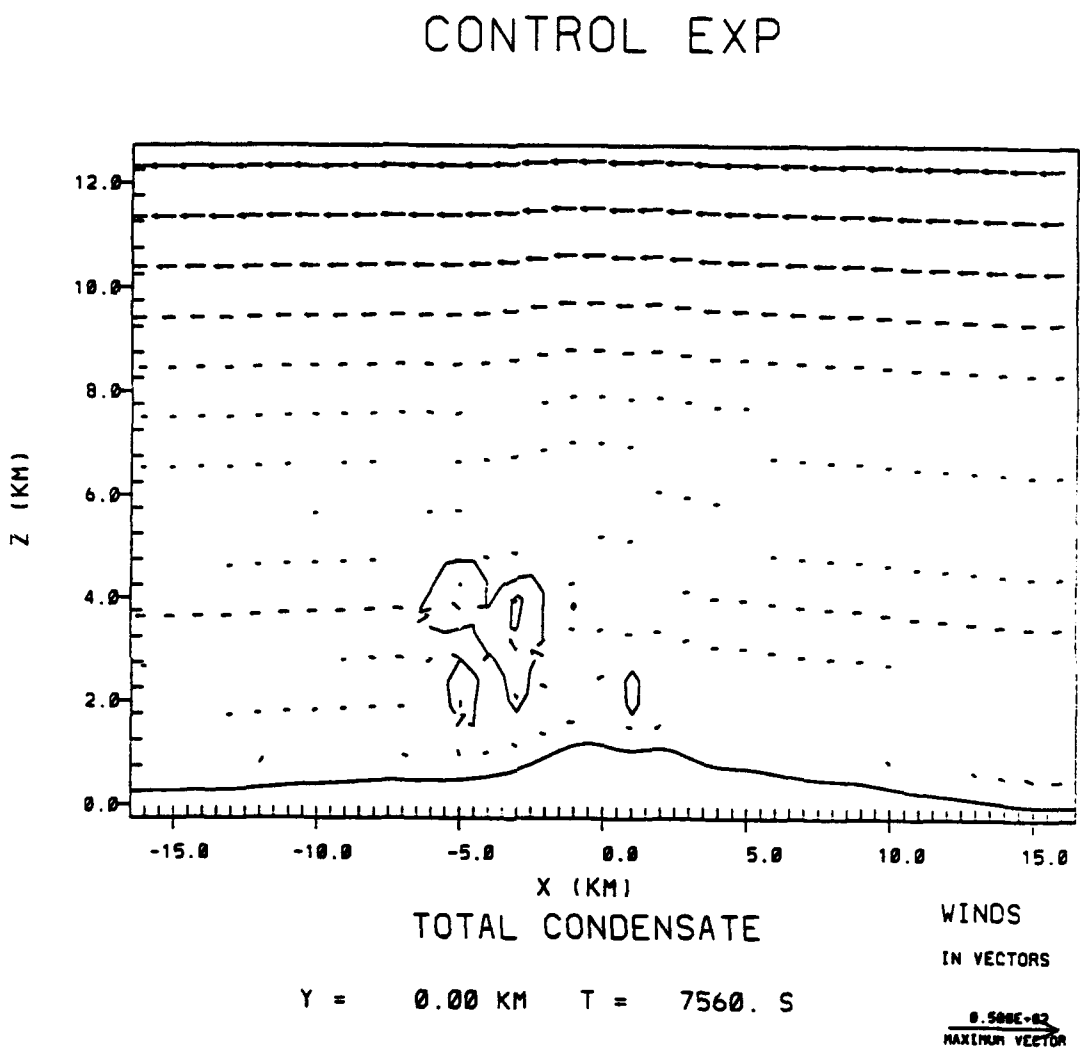

Fig. 33. As in Fig. 27, east-west vertical cross-section of simulated total condensate mixing ratios overlaid with simulated wind vectors for CONTROL simulation at 7560 s. Contour label "1" represents 0.1 g kg^{-1}.

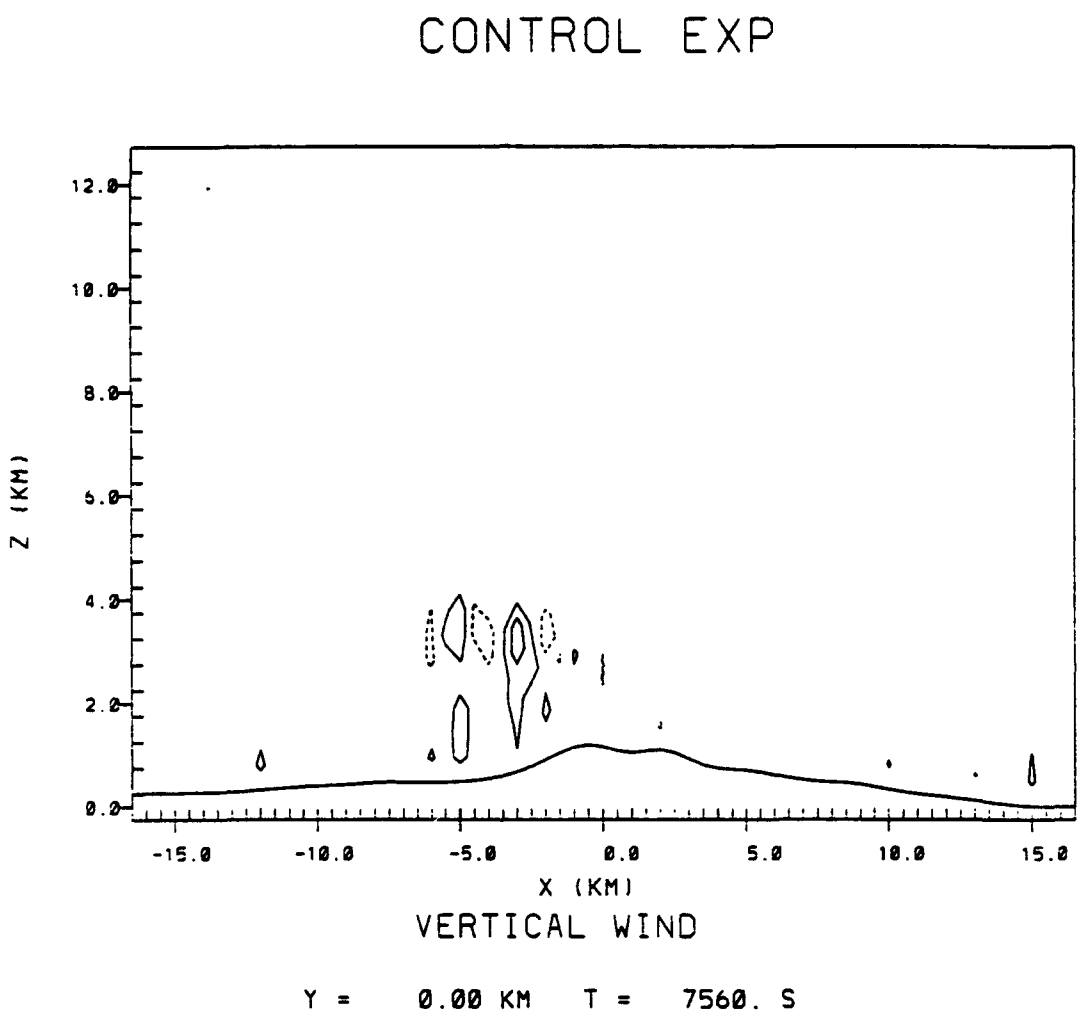

Fig 34. As in Fig. 28, east-west vertical cross-section of simulated vertical velocity for CONTROL simulation at 7560 s.

cloud water, and graupel. Figures 35 and 36 show analyses of total condensate mixing ratio and vertical velocity, respectively, for 7920 s.

CC1 had become the dominant cell at 8100 s with a maximum total condensate mixing ratio exceeding 4.0 g kg^{-1}. By this time both updrafts in the vicinity of CC1 had merged to produce a double maxima updraft. The upper portion of the updraft had strengthened to 13.0 m s^{-1} while the lower portion exceeded 4.5 m s^{-1}. Both portions of the updraft continued to be supported by the low-level convergence near x = -6.0 km. CC2's updraft remained distinct with a maximum strength of over 4.5 m s^{-1}. A significant downdraft of 5.5 m s^{-1} developed at this time between the updrafts associated with CC1 and CC2 and at a height of z = 3.75 km. CC3 remained very weak with several weak updrafts in its vicinity. A new area of rain water developed near CC1's maximum total condensate at z = 4.25 km. CC1's total condensate maximum at this time consisted of a mixture of ice crystals, cloud water, rain water, and graupel. Figures 37 and 38 show analyses of total condensate mixing ratio and vertical velocity, respectively, for 8100 s.

By 8280 s, CC1 was clearly the dominant cell with double maxima in both the total condensate mixing ratio and the vertical velocity fields. Maximum total condensate mixing ratios exceeded 4.0 g kg^{-1} in the upper portion of the cell and 2.0 g kg^{-1} in the lower portion. The cell's condensate reached a maximum height of about 6.0 km. The upper portion of the updraft remained strong at 11.0 m s^{-1} while the lower portion strengthened to over 7.5 m s^{-1}. The low-level convergence continued beneath CC1's updraft while a divergent flow developed at z = 5.25 km near the top of the updraft. As rain began to fall from CC1, the storm's rain shaft increased in size to approximately 2.5 km wide. CC2 remained evident in the total condensate analysis as a turret of condensate on the eastern side of the storm. CC2's updraft diminished

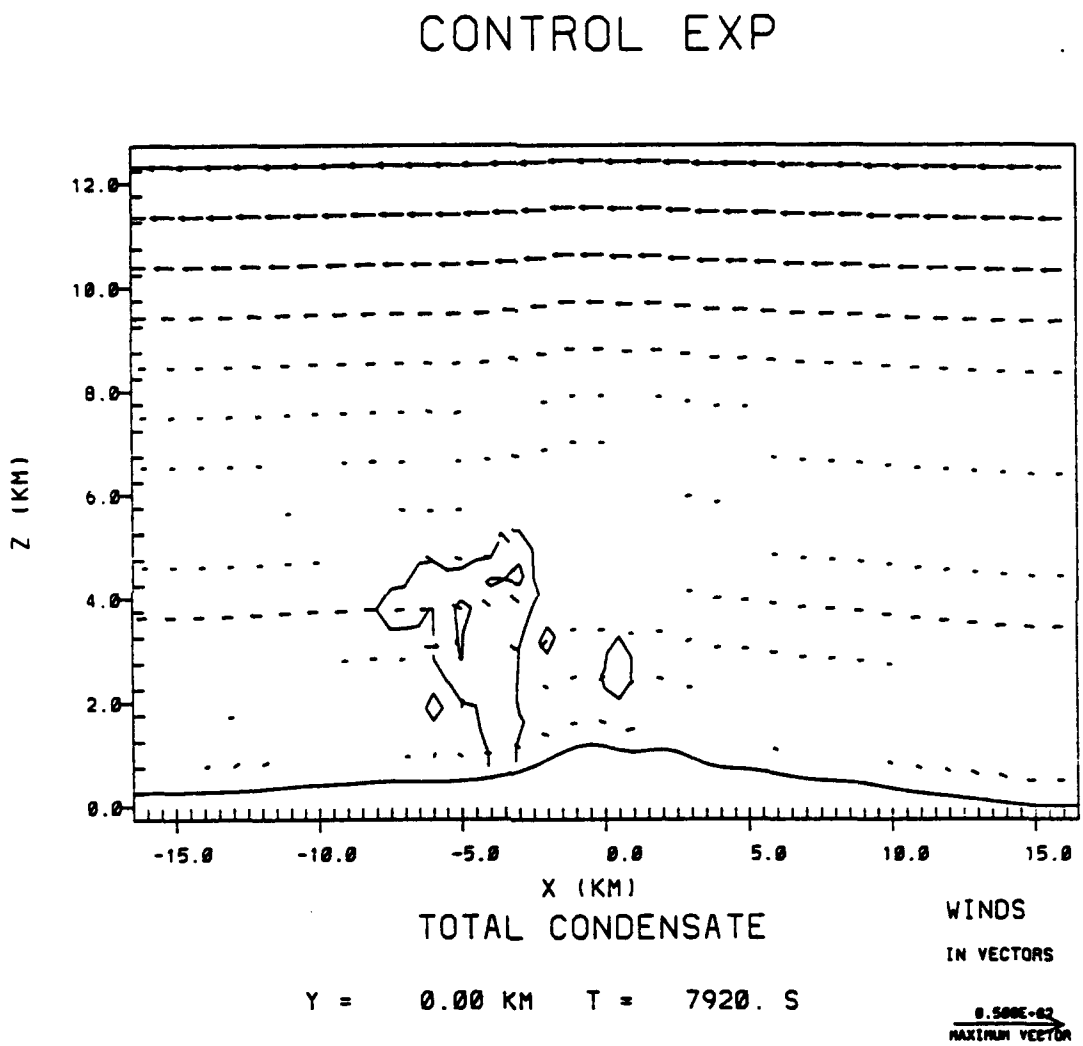

Fig. 35. East-west vertical cross-section of simulated total condensate mixing ratios overlaid with simulated wind vectors, as in Fig. 27, except for CONTROL simulation at 7920 s. Contour label "1" represents 0.1 g kg^{-1}.

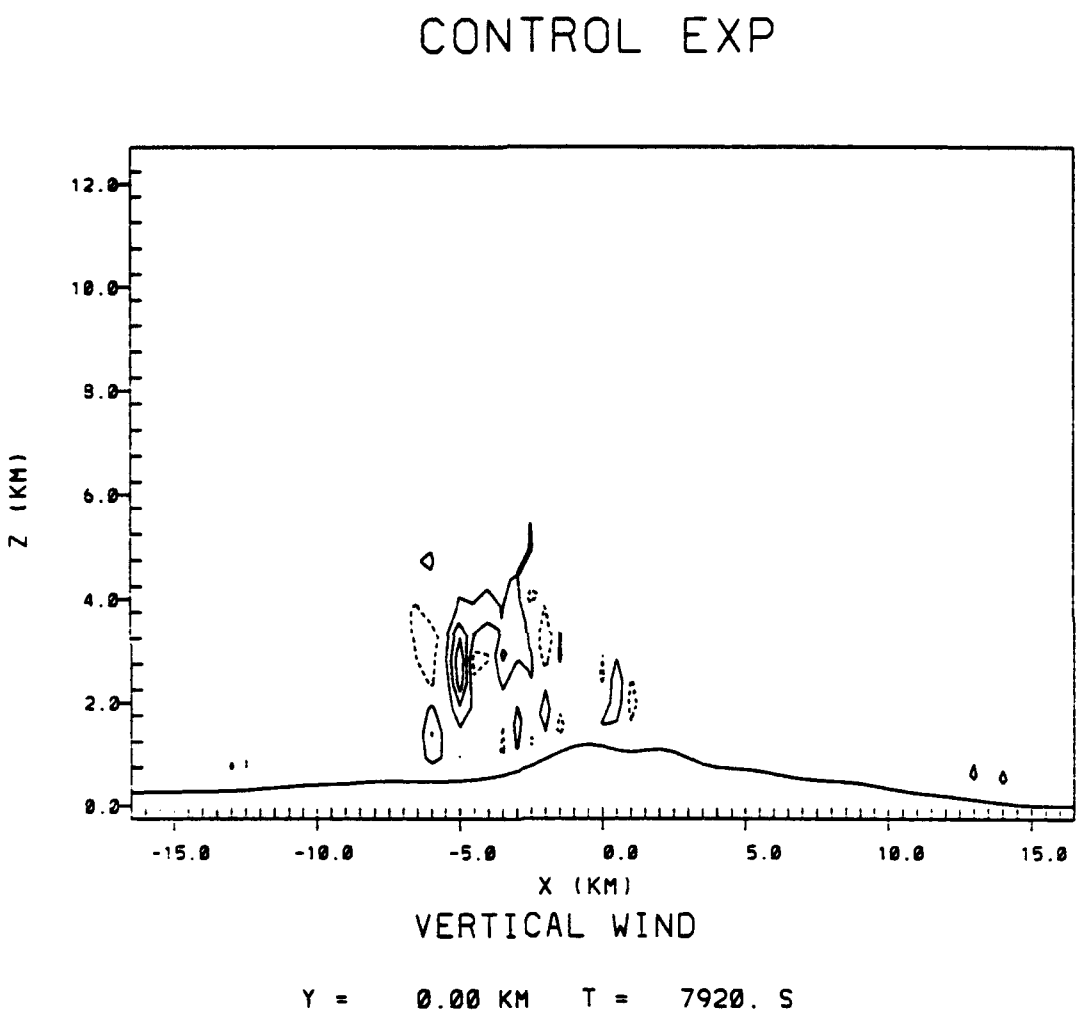

Fig. 36. East-west vertical cross-section of simulated vertical velocity, as in Fig. 28, except for CONTROL simulation at 7920 s.

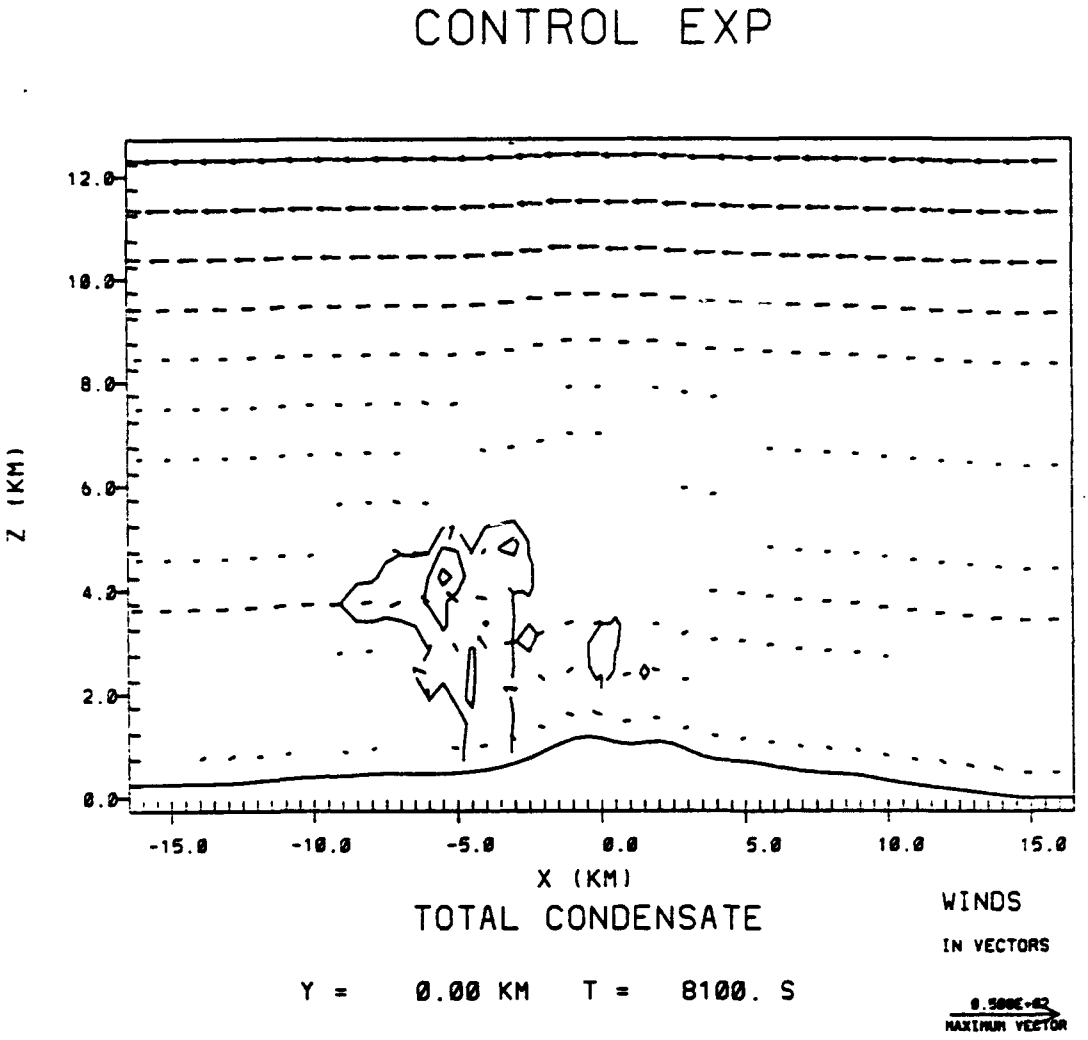

Fig. 37. Analogous to Fig. 27, east-west vertical cross-section of simulated total condensate mixing ratios overlaid with simulated wind vectors for CONTROL simulation at 8100 s. Contour label "1" represents 0.1 g kg^{-1}.

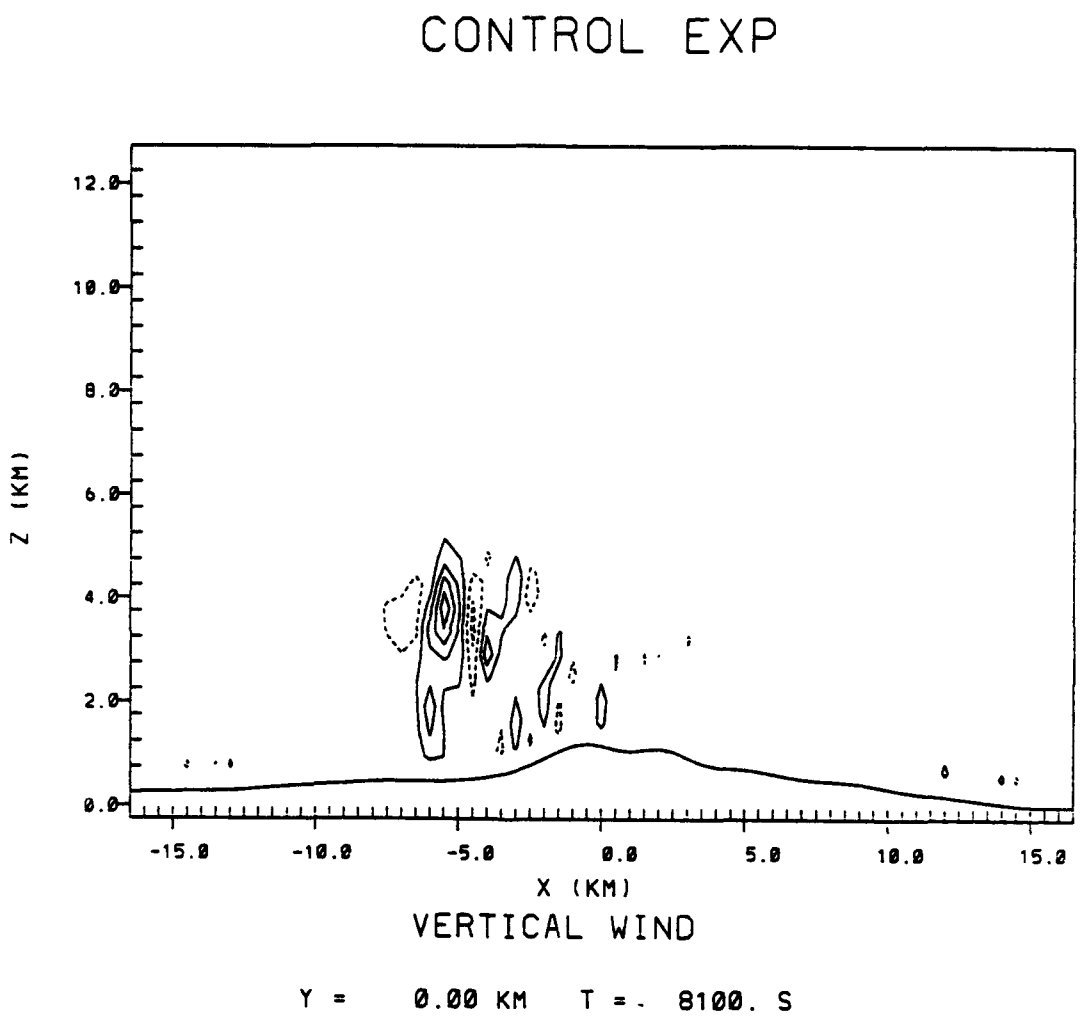

Fig. 38. Analogous to Fig. 28, east-west vertical cross-section of simulated vertical velocity for CONTROL simulation at 8100 s.

considerably in size from the previous analysis. CC3 had increased in size (primarily by building westward), but still contained no significant updrafts. Aggregated snow flakes first developed at this time in CC2. Both CC1 and CC2 contained well-defined graupel shafts. CC3's condensate at this time consisted entirely of cloud water. CC2's area of maximum total condensate consisted primarily of pristine ice crystals but also contained a mixture of graupel, cloud water, and aggregated snow flakes. CC1's maxima on the other hand, consisted primarily of cloud water, with smaller amounts of rain water, graupel, and pristine ice crystals.

At 8460 s, CC1 continued to strengthen with maximum total condensate mixing ratios exceeding 6.0 g kg^{-1} at approximately 6.0 km near the top of the cell. CC1's updraft again contained a double maxima with vertical velocities exceeding 10.5 m s^{-1} and 14.5 m s^{-1} in the upper and lower maxima, respectively. By this time, the area of low-level convergence supporting CC1's updraft had moved slightly westward to x = -7.5 km. This movement resulted from the westward expansion of the cool easterly outflow associated with the precipitation shaft. Meanwhile the divergent flow continued near the top of CC1's updraft at z = 5.75 km. CC1's condensate reached a maximum height of about 7.5 km at this time. CC2 remained distinct as a turret of condensate on the eastern edge of the storm, however, its updraft had weakened to about 1.5 m s^{-1}. At the same time, CC3 had strengthened significantly and moved slightly westward. CC3's maximum total condensate mixing ratios had increased to 2.0 g kg^{-1}, and its updraft developed to a maximum of 4.5 m s^{-1}. Both CC1 and CC2 were dominated by the ice phase at this time. The areas of highest total condensate mixing ratios in both cells consisted primarily of ice crystals, while very little cloud water existed anywhere in the cells. Aggregated snow flakes had also developed by this time in CC1. As expected from the location of the pristine ice crystals, the ag-

gregates were located near the total condensate maxima in both cells. Graupel also continued in both CC1 and CC2. Rain water developed for the first time in CC3.

CC1 continued to dominate the simulation at 8640 s. While CC1's maximum total condensate mixing ratios decreased slightly to 5.9 g kg^{-1}, its updraft continued to exhibit a double maxima with vertical velocities remaining about the same strength as at 8460 s. The low-level convergence at the outflow boundary continued to support CC1's updraft at this time, while the divergence near the top of the updraft continued to increase in height to approximately 6.5 km. The downdraft located just to the east of CC1's updraft strengthened again to 4.5 m s^{-1}. CC1's condensate reached a maximum height of approximately 9.0 km. A new updraft with maximum vertical velocities of 4.5 m s^{-1} developed at this time between the condensate masses associated with CC1 and the remnants of CC2. CC3 continued to strengthen and move slowly westward to about x = -1.0 km. While CC3's total condensate mixing ratios remained virtually unchanged from 8460 s, its updraft increased to a maximum of 7.5 m s^{-1}. A very weak westerly flow, resulting from the precipitation-induced outflow, developed at this time near x = -4.5 km and z = 1.5 km. The interaction of this westerly flow with the prevailing easterly flow at that location produced another area of convergence which helped strengthen CC3's updraft. The ice phase continued to dominate CC1 at this time. The bulk of CC1's condensate, particularly near its maximum, consisted of pristine ice crystals. At the same time, a deep shaft of graupel had developed near the center of the cell. The areas of aggregates continued near the ice crystal maxima in both CC1 and CC2. The bulk of CC3's condensate remained cloud water with smaller amounts of graupel and rain water. Figure 39 shows analyses of total condensate, cloud water, rain water, pristine ice crystals, graupel, and aggre-

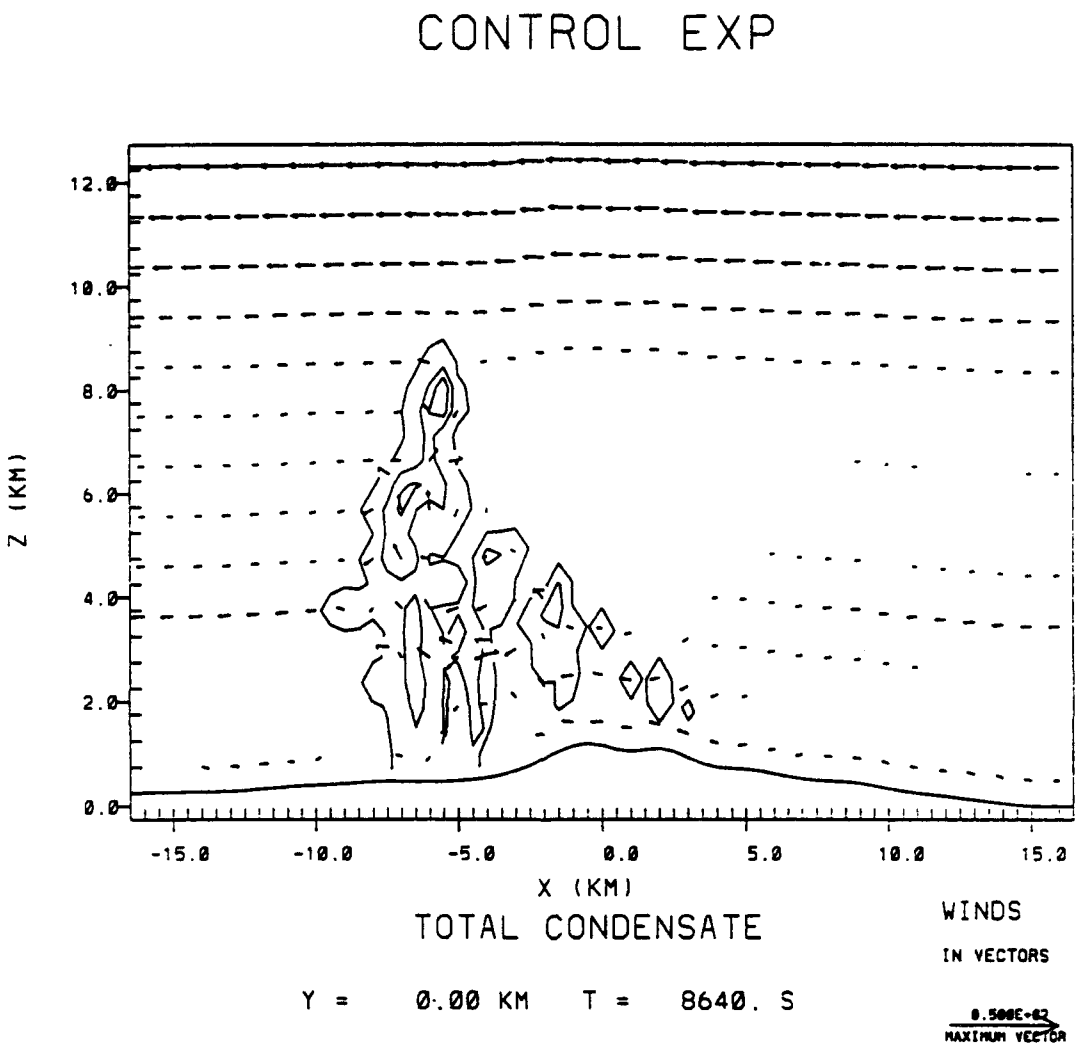

Fig. 39a. East-west vertical cross-section of simulated total condensate mixing ratios overlaid with simulated wind vectors, as in Fig. 27, except for CONTROL simulation at 8640 s. Contour label "1" represents 0.1 g kg^{-1}.

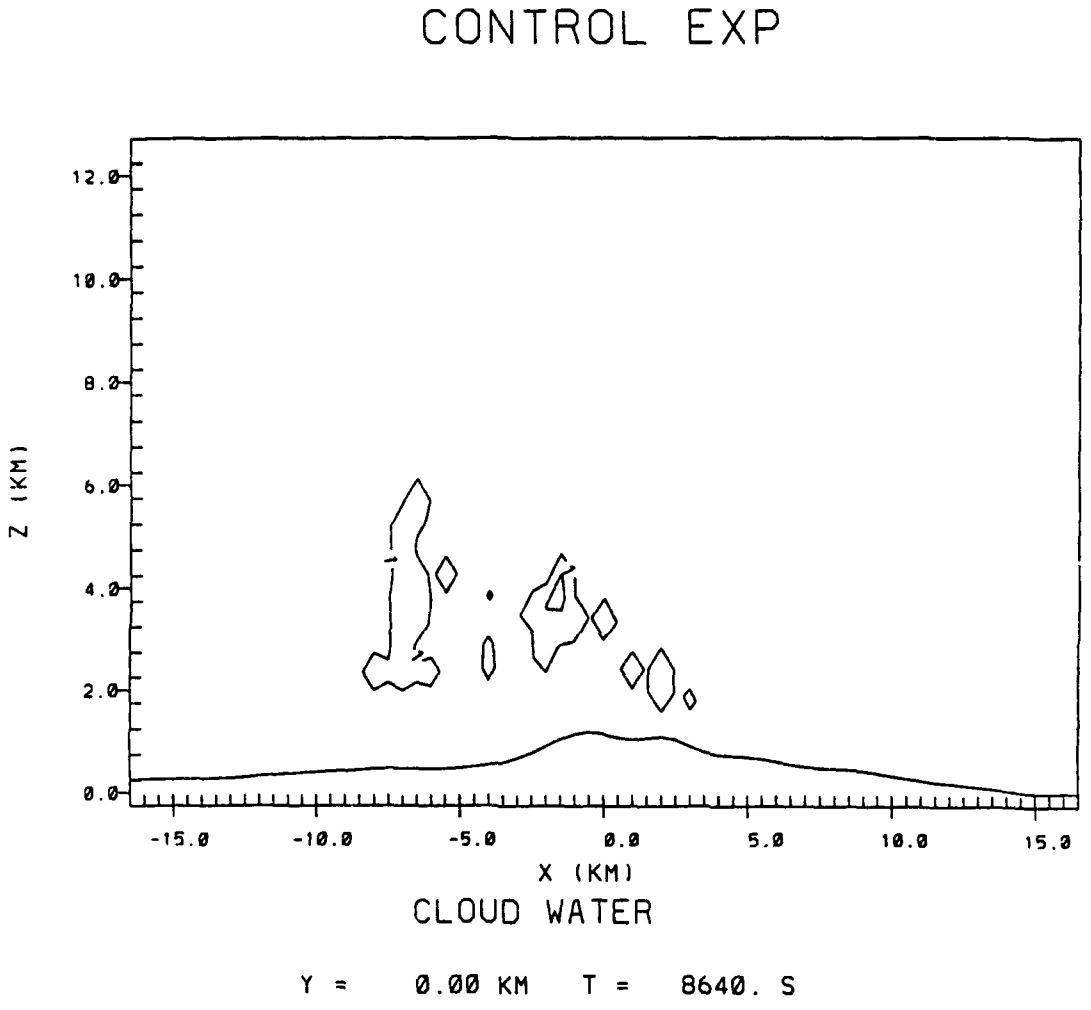

Fig. 39b. East-west vertical cross-section of simulated cloud water mixing ratios contoured every 2.0 g kg^{-1} starting at 0.1 g kg^{-1} for CONTROL simulation at 8640 s. Axes labeled as in Fig. 27. Contour label "1" represents 0.1 g kg^{-1}.

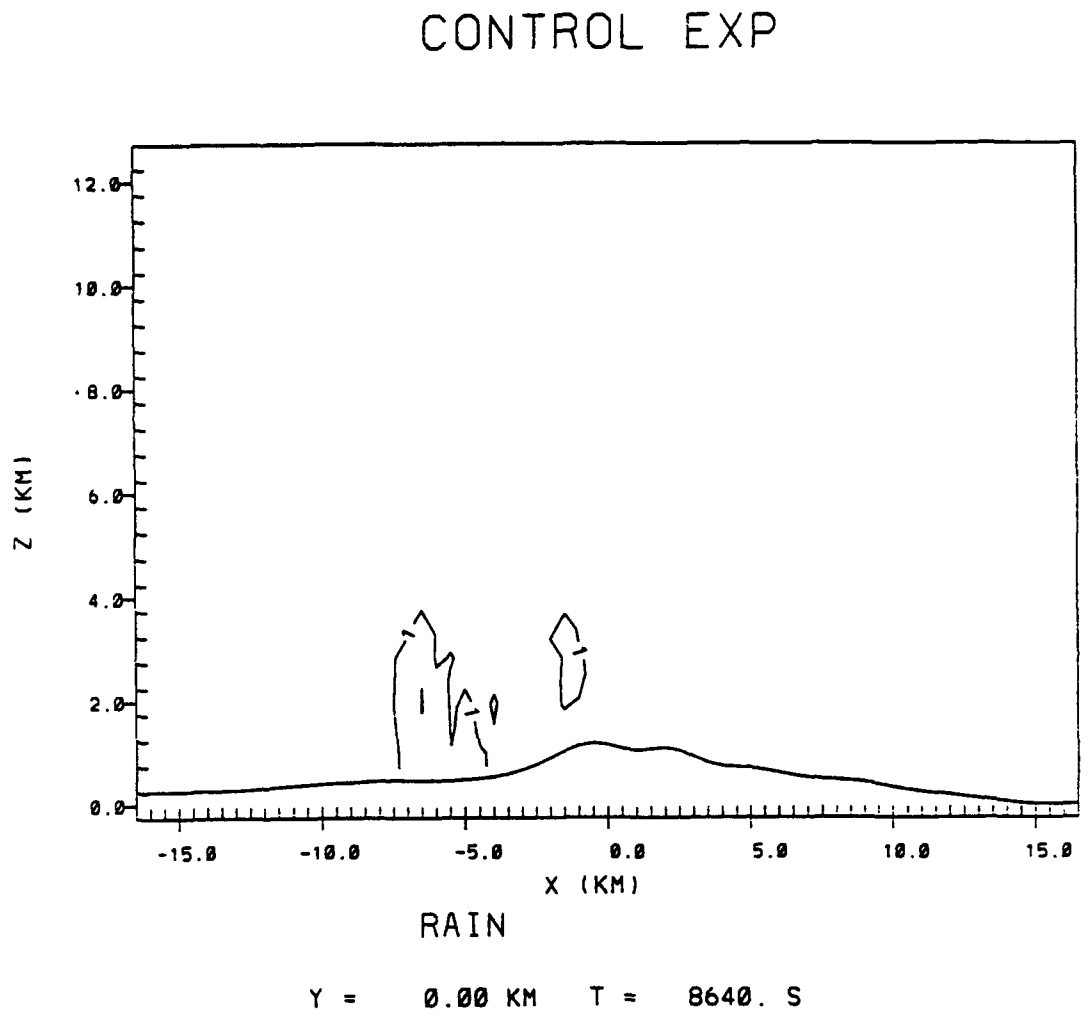

Fig. 39c. Analogous to Fig. 39b, east-west vertical cross-section of simulated rain water mixing ratios for CONTROL simulation at 8640 s. Contour label "1" represents 0.1 g kg^{-1}.

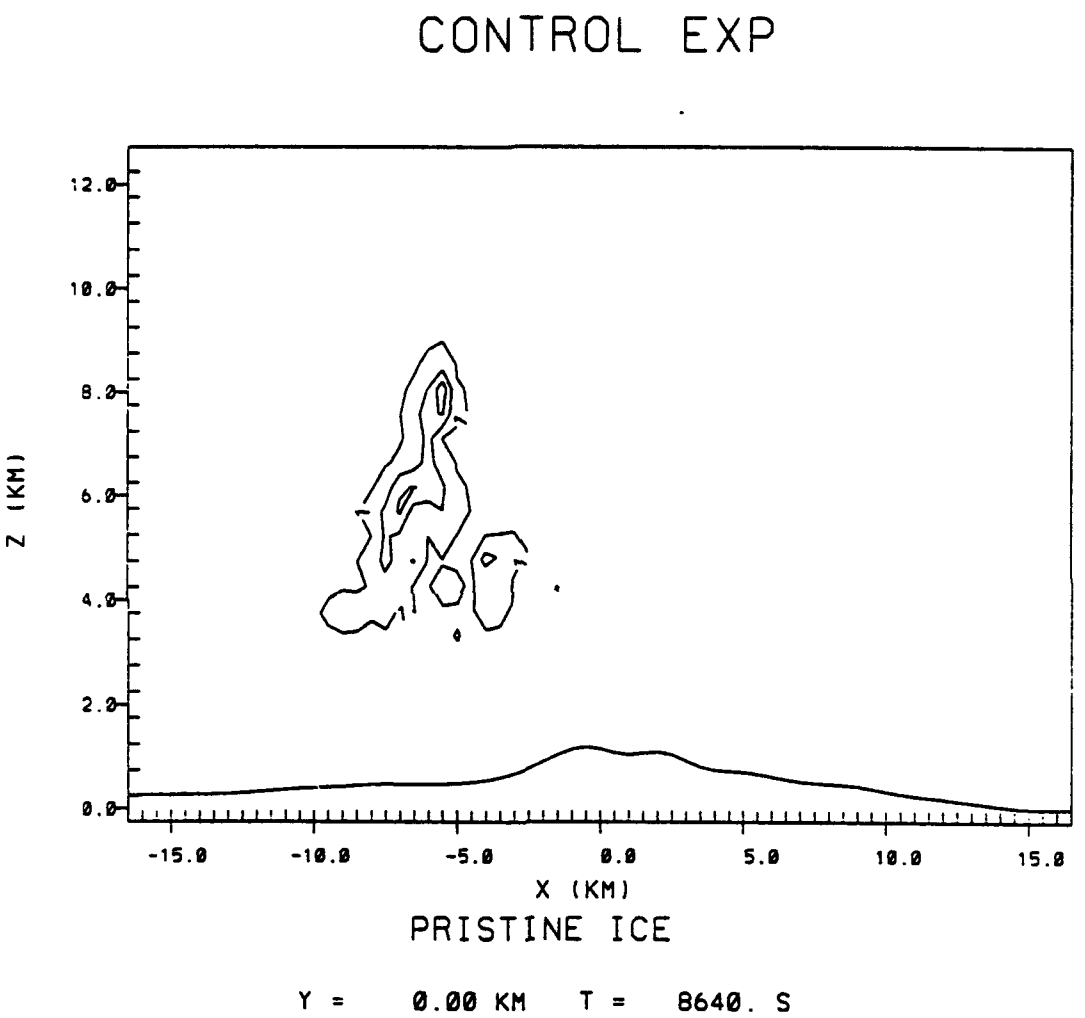

Fig. 39d. Analogous to Fig. 39b, east-west vertical cross-section of simulated pristine ice crystal mixing ratios for CONTROL simulation at 8640 s. Contour label "1" represents 0.1 g kg^{-1}.

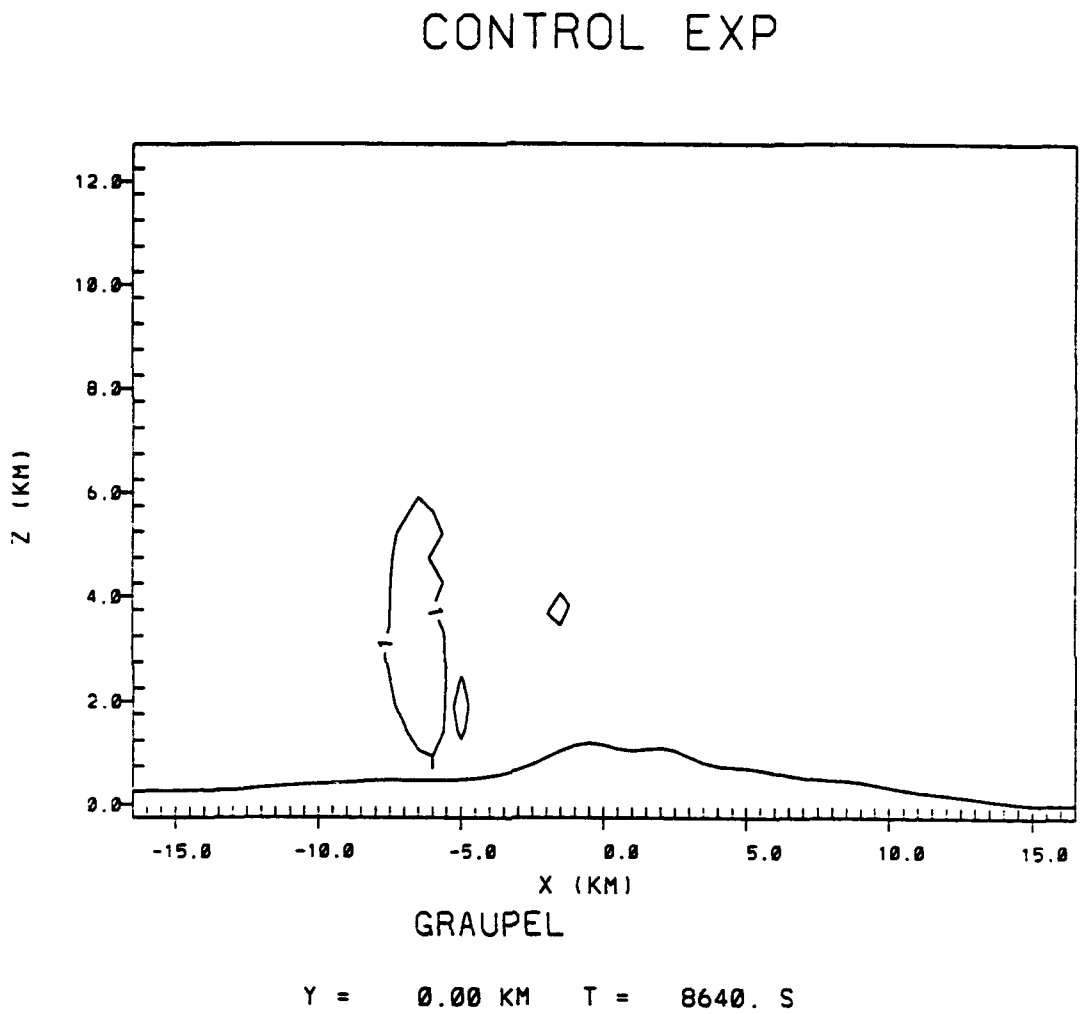

Fig. 39e. Analogous to Fig. 39b, east-west vertical cross-section of simulated graupel mixing ratios for CONTROL simulation at 8640 s. Contour label "1" represents 0.1 g kg^{-1}.

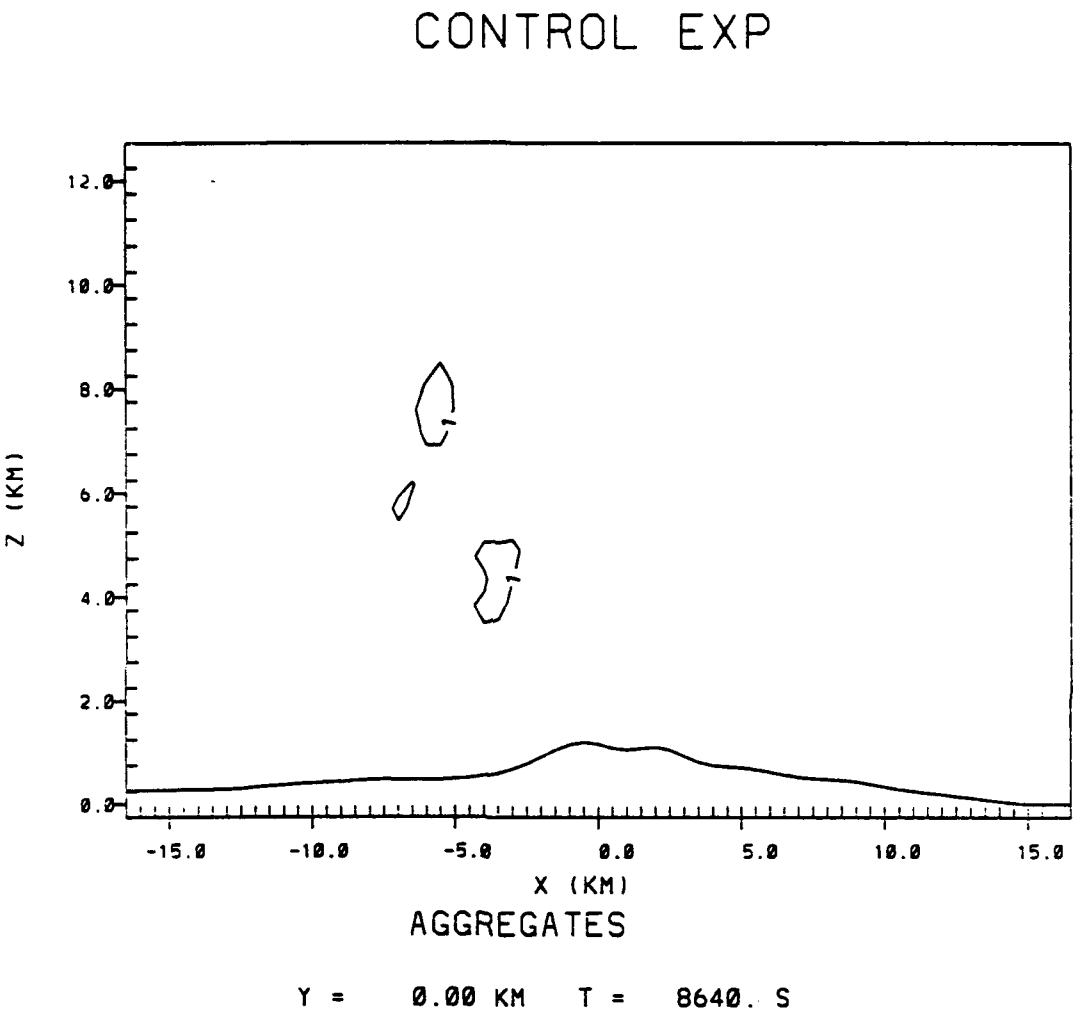

Fig. 39f. Analogous to Fig. 39b, east-west vertical cross-section of simulated aggregated snow flake mixing ratios for CONTROL simulation at 8640 s. Contour label "1" represents 0.1 g kg^{-1}.

gated snow flake mixing ratios, respectively, for 8640 s. Figure 40 shows an analysis of vertical velocity for 8640 s.

By 8820 s CC2 had lost its identity as CC3 moved westward and CC3's condensate merged with CC1. The maximum total condensate mixing ratio exceeded 5.9 g kg^{-1} in both CC1 and CC3, with the highest mixing ratios located above 4.0 km in both cells. CC1's condensate reached a maximum height of 10.25 km, and precipitation first developed from CC3 at this time. CC1's updraft contained several local vertical velocity maxima with the primary maximum of 16.6 m s^{-1} located at 8.0 km near the top of the cell. The precipitation-induced outflow below CC1 continued to create areas of convergence both to the west and east of the main precipitation shaft. The westerly flow portion of the outflow first noted at 8640 s, became better defined by this time. The divergent flow near CC1's updraft extended to nearly z = 8.0 km. The downdraft on the eastern edge of CC1 weakened considerably, while a new downdraft of about 6.2 m s^{-1} formed near the center of the precipitation shaft. CC3's updraft continued at its previous strength of 7.5 m s^{-1}, but the updraft's structure became much less organized. A weak divergent flow developed at 4.75 km near the top of CC3's updraft. The new updraft which had developed between CC1 and CC2 at 8640 s weakened dramatically to 1.5 m s^{-1} as it came under the influence of the downdrafts from CC1 and CC3 as they merged. By this time, the bulk of CC1's condensate consisted of either pristine ice crystals or aggregated snow flakes. Aggregate mixing ratios exceeded 2.0 g kg^{-1}. The graupel shaft continued in CC1, and graupel reached the surface for the first time. CC3's condensate still consisted primarily of cloud water, but pristine ice crystals had developed for the first time. The area of graupel expanded, and rain reached the surface for the first time out of CC3. Figures

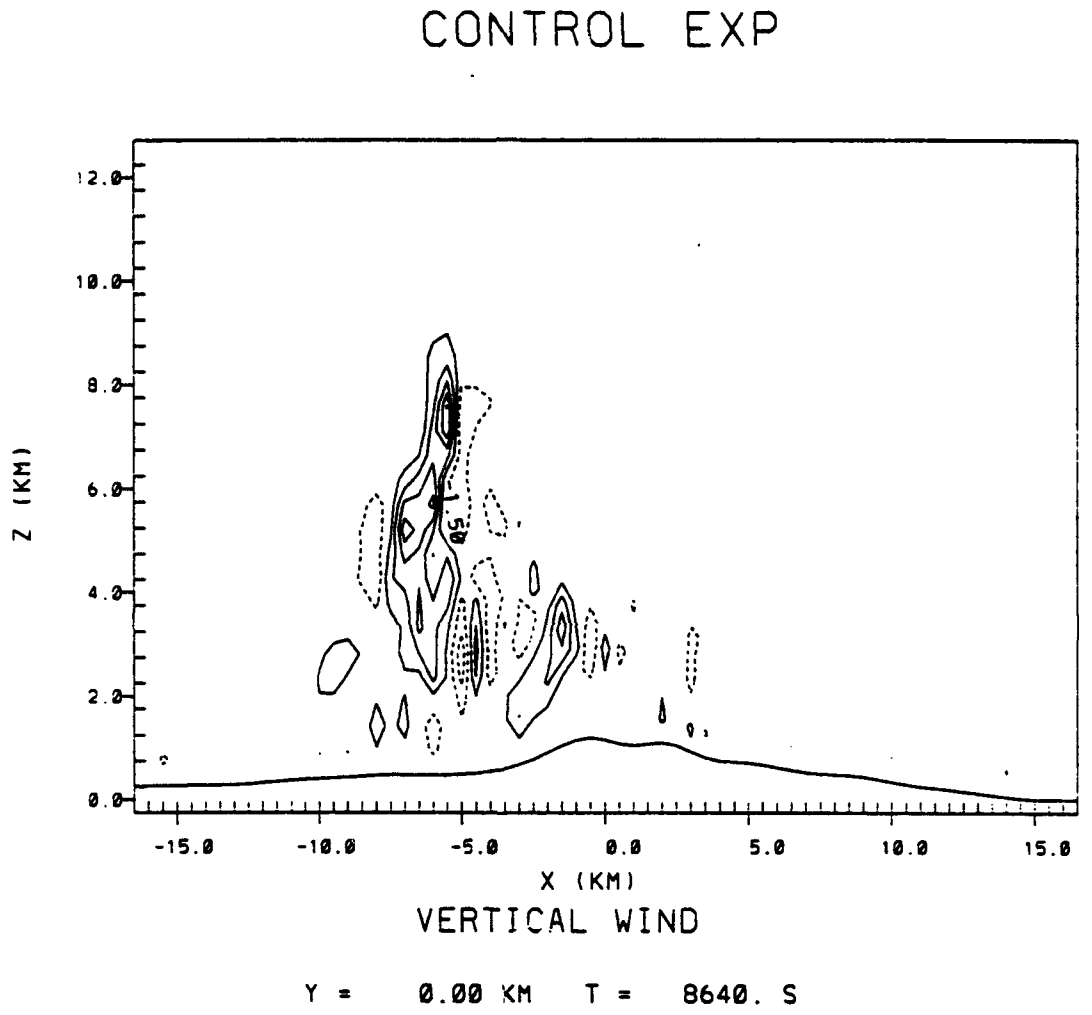

Fig. 40. East-west vertical cross-section of simulated vertical velocity as in Fig. 28, except for CONTROL simulation at 8640 s.

41 and 42 show analyses of total condensate mixing ratio and vertical velocity, respectively, for 8820 s.

At 9000 s, CC1 still dominated the merged storm. The maximum total condensate mixing ratio exceeded 6.0 g kg^{-1} in CC1, while barely reaching 2.0 g kg^{-1} in CC3. CC1's condensate reached a maximum height of 11.0 km. The updraft structure became very complicated as CC1 and CC3 began to interact with each other. CC1's main updraft contained a maximum vertical velocity of over 10.5 m s^{-1}. Meanwhile a secondary updraft core had developed slightly to the east of the original. This core contained a maximum vertical velocity of 7.5 m s^{-1}. At the same time, CC3's updraft had become more organized and strengthened to 10.5 m s^{-1}. By this time the low-level outflow convergence areas were very well defined. The convergent flow on the western side of the outflow spawned the development of several updrafts on the western edge of CC1, while the strong low-level convergence on the eastern side of the outflow supported the strengthening of CC3's updraft. The upper-level divergence near CC1's updraft continued, but became less organized than at previous times. The same basic microphysical structure existed in the cells at this time as reported for the previous time.

6.2 Comparison With Radar Observations

This section presents a comparison of the control simulation results with the Doppler radar storm observations from the 31 July 1984 case. The two-dimensional nature of the numerical simulations conducted for this study naturally limit direct comparisons with storm observations, however, qualitative and some quantitative comparisons can yield a realistic assessment of the simulation's accuracy. Establishing the fidelity of the control simulation represents a crucial first step of this study

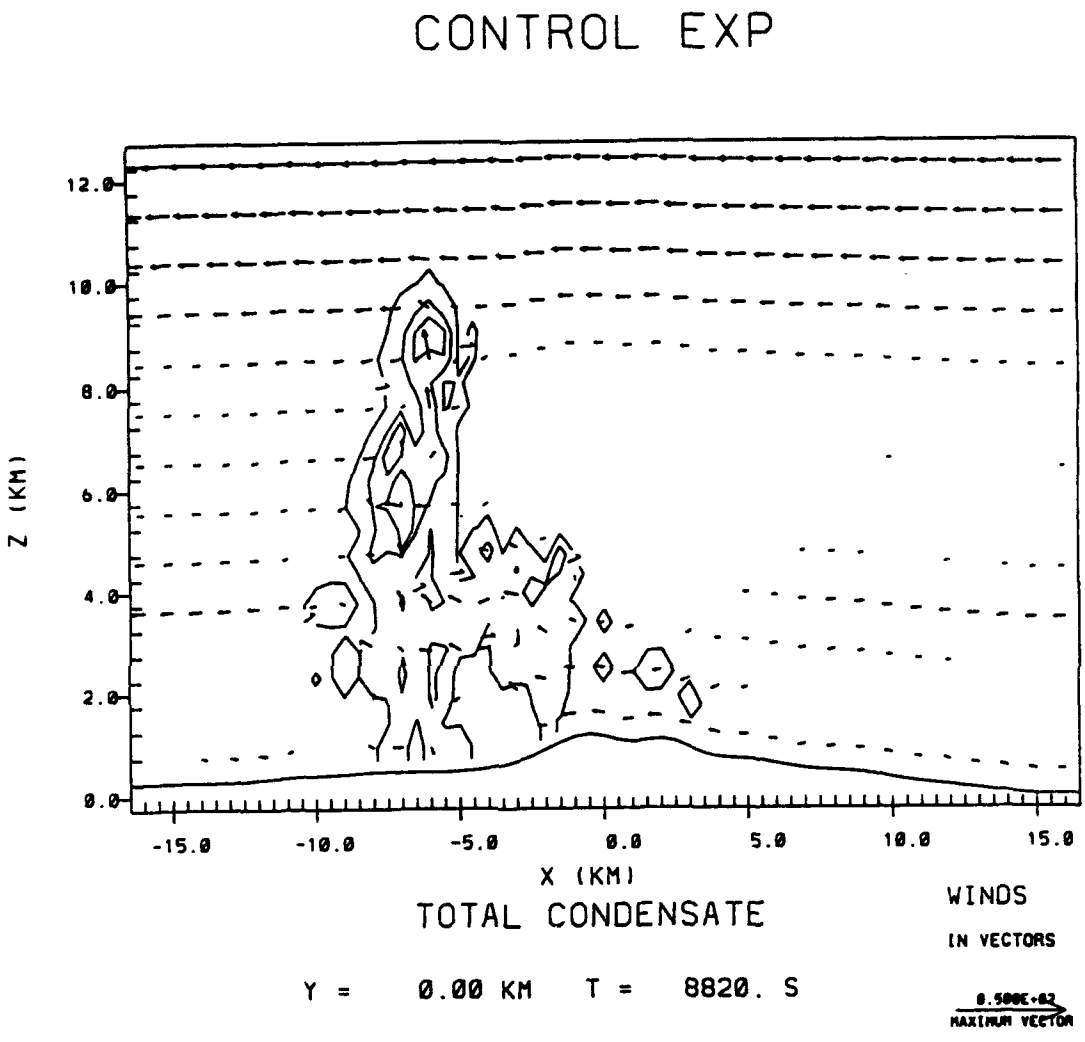

Fig. 41. East-west vertical cross-section of simulated total condensate mixing ratios overlaid with simulated wind vectors, as in Fig. 27, except for CONTROL simulation at 8820 s. Contour label "1" represents 0.1 g kg^{-1}.

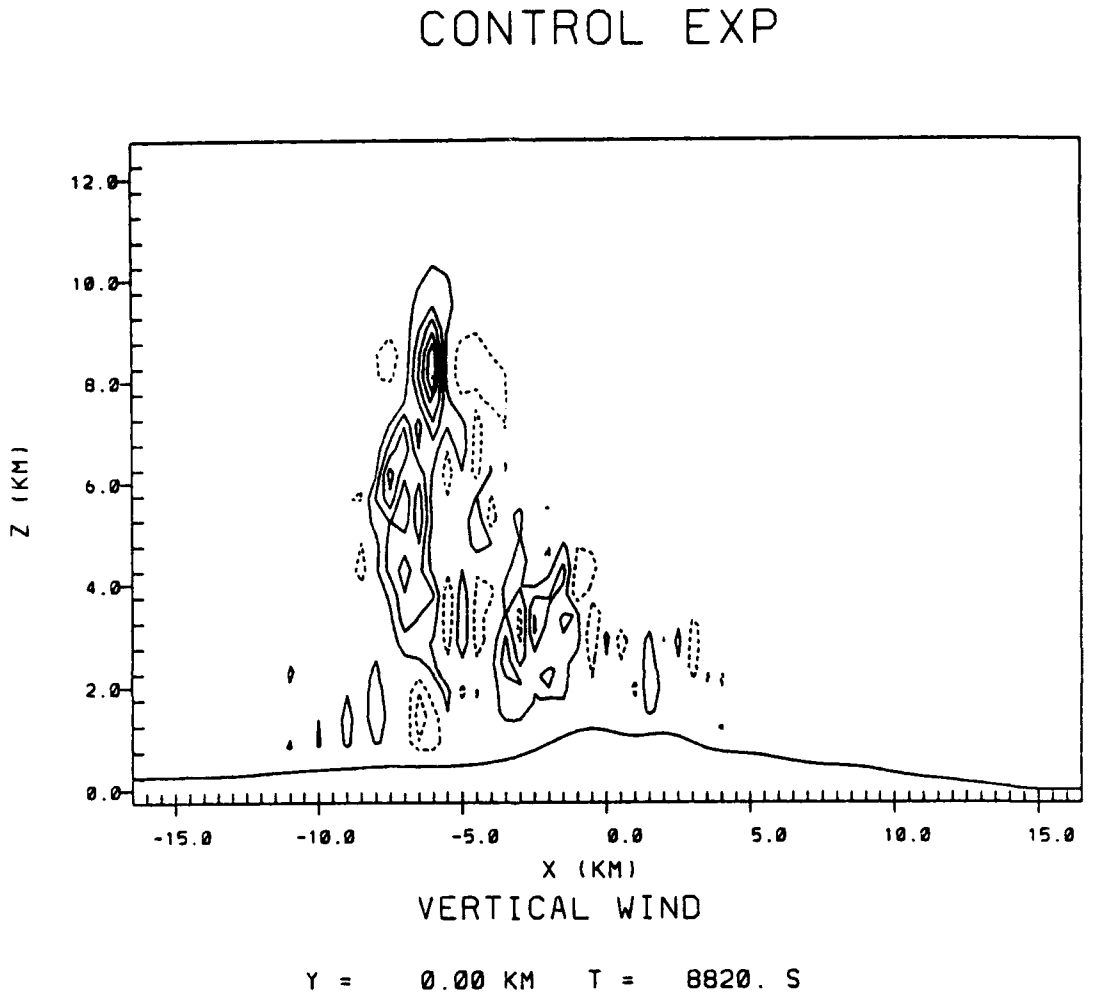

Fig. 42. East-west vertical cross-section of simulated vertical velocity, as in Fig. 27, except for CONTROL simulation at 8820 s.

since the numerical simulation experiments discussed in later chapters will be compared to the control.

Given the limitations imposed by the two-dimensionality of the numerical simulation, the simulation compared very favorably with the Doppler radar observations collected on 31 July 1984. The simulation captured most of the important cell and storm features and characteristics noted in the description of the radar observations in Chapter 3.

6.2.1 General Comparisons

The control simulation captured the multicellular nature of the storms as observed by the radars. Three dominant cells developed in the simulation while seven cells were observed by the radars. Some of this difference can be attributed to the two-dimensional nature of the simulation which naturally decreases the amount of space available for cell development. Second, as described later, the convective development in the simulation lags the observations by between 15 and 40 min. The final four observed cells developed in the last 18 min of the analysis. It is likely that the simulation lag resulted in the simulation ending before further cell development occurred.

The development of low-level convergence areas in the simulation compares reasonably well with that seen in the observations. Since the simulation was conducted in two dimensions, it could not capture the terrain-induced channelling convergence found in the observations. The simulation did show the development of low-level convergence areas in response to the mountain-valley flow as observed in the synthesized wind fields. In both the simulation and in the observations, the low-level convergence areas were crucial to convective initiation. These convergence areas primarily determined the location of initiation. The simulation also reasonably repro-

duced the development of upper-level divergence areas above the strongest cells. For the most part, the simulation's upper-level divergence areas were weaker than those in the synthesized wind fields.

In both the observations and in the simulation, the convective initiation occurred over or very near the ridges. The simulated initiation locations tended to be slightly to the west of the ridge lines while in the observations, the initiation locations generally were either directly over or slightly to the east of the ridge lines. The magnitude of the distance differences between observed and simulation initiation locations was always less than 5.0 km. The two-dimensional nature of the simulation again explains in part the difference in the pattern of initiation locations. As described in Chapter 3, the initiation locations were strongly influenced by the channelling convergence induced by the narrow valleys. These features could not be adequately represented in a two-dimensional simulation. As a result, the simulation's initiation locations are more strongly determined by the thermally-driven mountain-valley flows.

As mentioned previously, the simulation's convective development lagged that observed by the radars by a significant amount of time. The two-dimensional nature of the simulation makes it difficult to determine the exact timing difference. As expected, investigation of individual features yields different timing differences. For example, a comparison of the simulated maximum updrafts and downdrafts with those synthesized from the radar observations (Fig. 43) shows good agreement between the simulation and the observations with a simulation lag time of about 14 min. The simulation's condensate first developed at 1115 (simulation time) and the condensate first extended down to 1.5 km (3.3 km MSL) at 1151 (simulation time). Comparing this time with the observed radar reflectivities of 30 dBZ at 3.3 km MSL at 1116

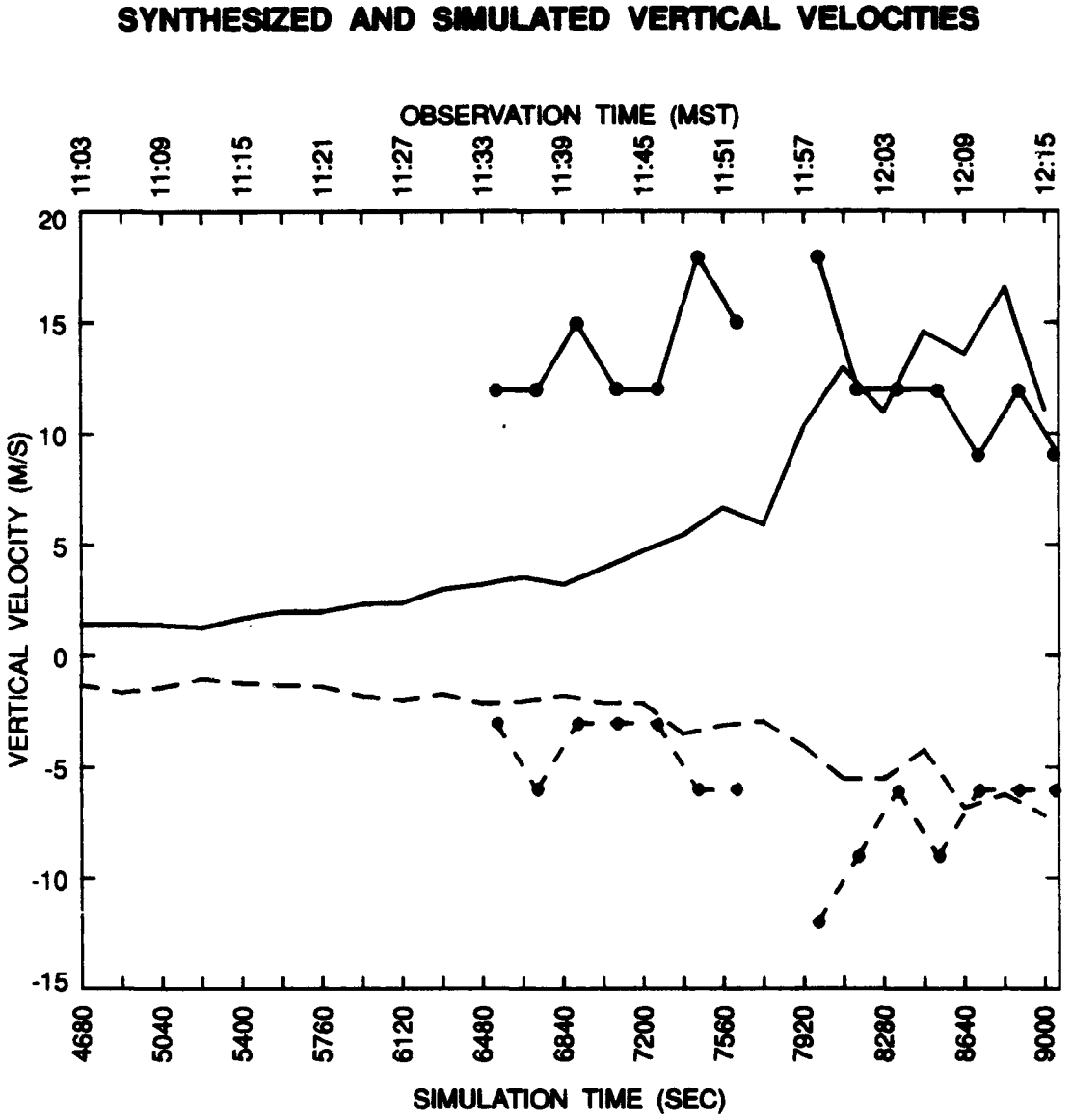

Fig. 43. Time evolution of synthesized (heavy curves with ticks) and CONTROL simulation simulated (light curves without ticks) maximum and minimum vertical velocities. Solid curves show maximum upward vertical velocities (positive w). Dashed curves show maximum downward vertical velocities (negative w). Vertical axis is vertical velocity in m s^{-1}, bottom horizontal axis is simulation time in seconds, and top horizontal axis is observation time in hours and minutes (MST).

MST yields a lag time of at least 35 min. It is important, therefore, to exercise caution when attempting to make one-to-one temporal comparisons between the simulated storms and the observed storms.

The simulated updrafts qualitatively compared quite well with those analyzed from synthesized wind fields. The updrafts in both cases agreed quite well in both horizontal and vertical extent. The width of the simulated updrafts averaged only slightly less than the 2.0 km widths seen in the observations. The simulated updrafts were about 8.0 km deep compared to the 7.0 to 8.0 km depth of the observed updrafts. The comparison of the maximum updrafts (again using Figure 43) shows that, taking into consideration the timing lag discussed above, the maximum strength of the simulated updrafts agrees very well with the observed maximum updrafts. In general, the development of the simulated updrafts also follows quite well that seen in the synthesized wind fields. In both cases cells frequently contained single updrafts with vertical velocities of 12.0 m s^{-1} or less. Also in both cases, early in the convective development, the updrafts are strongest in the low- to mid-levels, and both show a tendency for the updraft maxima to move to the mid- to upper-levels as the cells mature. The simulation showed that some cells developed either multiple updrafts or updrafts with two or more local maxima in the vertical direction. The observed storms also showed a similar phenomenon. The simulated updrafts for the most part are nearly vertical with very little tilt. This contrasts markedly with the observed updrafts which frequently tilted backward (away from the inflow). As observed in the synthesized wind fields, the simulated updrafts developed most often near regions of low-level convergence. The stronger updrafts were associated also with regions of at least weak upper-level divergence.

The simulated downdrafts do not compare nearly as well with observations. A comparison of the horizontal and vertical extent of the simulated downdrafts with the observed shows only a poor correspondence. The simulated downdrafts for the most part are much narrower and shallower than those observed. A comparison of the maximum downdrafts (again using Figure 43) shows agreement between both the simulation and the observations after taking into consideration the simulation's timing lag. The simulation fails to develop the strong downdrafts of over 9.0 m s^{-1} seen in the observations between 1158 and 1201 MST. The simulation also fails to capture the broad areas of strong downdrafts as observed. Instead the simulated downdrafts were usually confined to very narrow regions. The simulated downdrafts were located primarily in low-levels as was predominantly the case with the observations. However, the simulated downdrafts could also be found throughout nearly the entire vertical extent of the model domain.

The analysis of the validity of the simulation's precipitation development is somewhat hindered by the fact that the lowest radar analyses were performed at 3.3 km MSL. Thus it is not possible to determine precisely where or when the precipitation was associated with radar returns at that level. If it is assumed that the precipitation shaft is approximately the size of the radar maximum at the 3.3 km MSL analysis level, then the simulation's precipitation shafts compared very favorably with those observed. In both cases, the precipitation shafts early in the precipitating stage ranged from 1.0 to 1.5 km in diameter and increased to 2.5 to 3.0 km in the latter part of the mature stage. Also in both cases, several precipitation shafts developed. The observations contained more precipitation shafts, and they were farther apart than in the simulation; a discrepancy most likely resulting from the limitations imposed by the two-dimensional nature of the simulation. In both the simulation and in the observa-

tions, the precipitation shafts were located near or directly beneath major updrafts. The separation between precipitation and updrafts was generally greater in the observations than in the simulation.

The simulation's ability to capture the vertical development of cells can be assessed by comparing the height of simulated condensate with the height of radar returns. A comparison of the maximum heights of the simulated condensate with the maximum height of radar returns (Fig. 44) shows a lag of approximately 23 min between the simulated development and the actual development similar to that discussed earlier in this section. Taking this lag into consideration, the simulation captured the rapid increase in maximum radar return height observed between 1146 MST and 1152 MST. Through most of the simulation, the maximum condensate heights remained 2.0 to 3.0 km lower than the observed radar return heights. The simulation indicated a slow steady growth in height to about 5.25 km (7.0 km MSL) followed by a single rapid surge in height to near the absolute maximum seen in the radar data. The rapid development which followed the penetration of the 5.25 km (7.0 km MSL) level appears to result from the favorable moisture and temperature profiles above that level. The relatively strong inversion and the very dry layer which existed below 5.25 km (7.0 km MSL) capped the convective development until late in the simulation. A similar capping phenomenon can be seen in the observed early convective development where no echoes penetrated above 6.5 km MSL until after 1113 MST. The simulation failed to capture the observed double peak in maximum heights seen in Figure 44.

The lifetime of the simulated cells compared very closely with those observed in the radar observations. The longest-lived simulated cell, CC1, existed for 42 min prior to the simulation's termination. This cell likely would have existed for up to

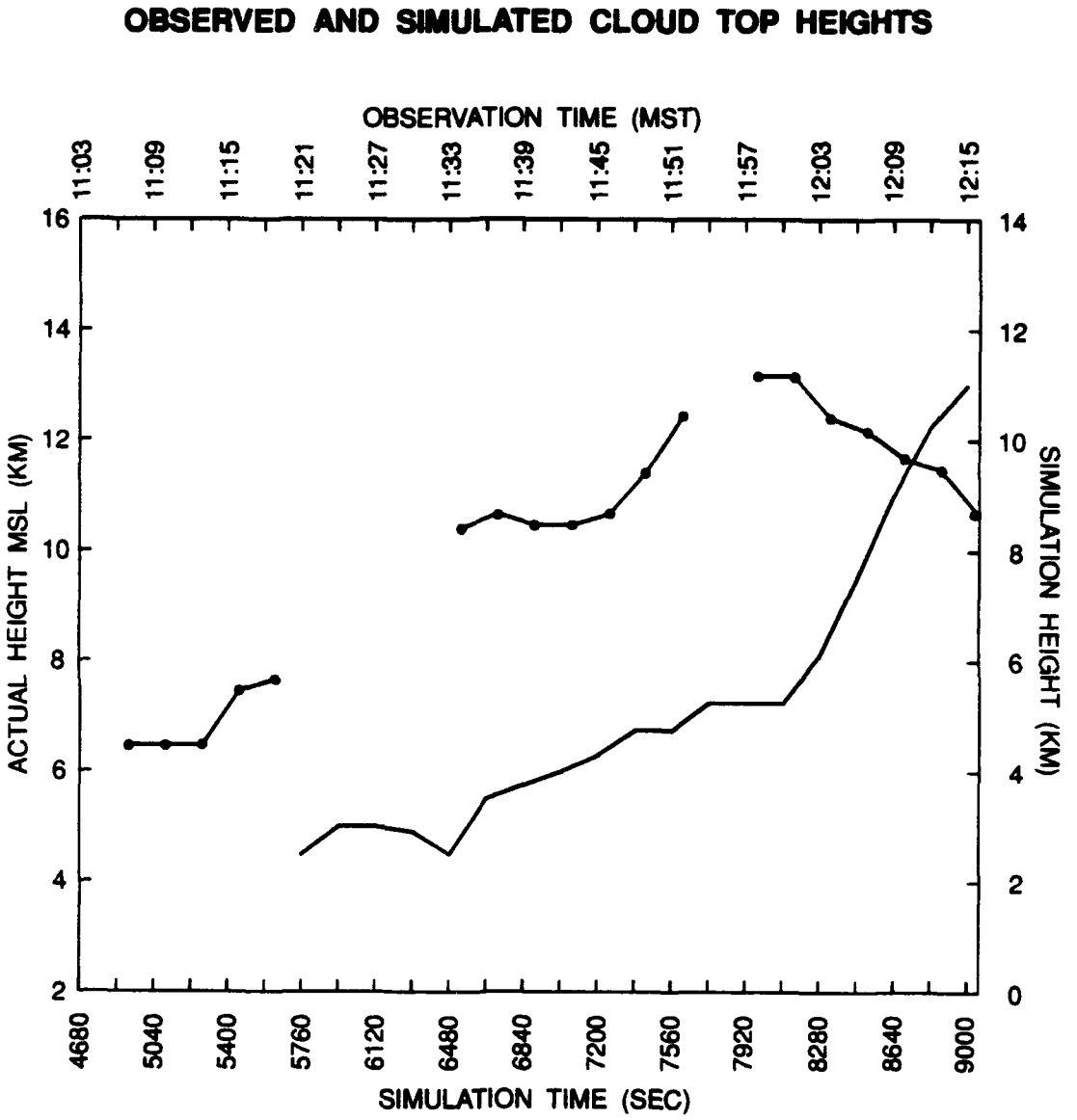

Fig. 44. Time-height cross section showing maximum simulated total condensate height for the CONTROL simulation (plain curve) and maximum height of observed reflectivity (solid curve with ticks). Plain curve shows maximum height of 0.1 g kg^{-1} total condensate mixing ratios. Ticked curve shows maximum height of 10 dBZ radar reflectivities. Right vertical axis is labeled in kilometers above the minimum terrain elevation in the simulation grid (in this case 1.82 km) as described in the text, and left vertical axis is height relative to mean sea level in km. Bottom horizontal axis is simulation time in seconds and top horizontal axis is observation time in hours and minutes MST.

another 10 min had the simulation been extended. CC2 existed for 36 min before being absorbed in CC1. Finally, CC3 existed only 21 min before the simulation ended. This cell was in the early stages of development and likely would have developed for some time had the simulation been extended. These lifetimes compare well with the 20 to 60 min lifetimes seen in the observations. It is likely that had the simulation been extended, the storm would have grown and eventually decayed with the result that the overall storm lifetime also would have compared favorably with the 1.0 to 1.5 hr storm lifetime observed by the radars.

Only one of the simulated cells, CC1, showed the tendency for periodic reintensification seen in the observed cells. In the simulated cell, the cycle of reintensification occurred early in the cell's development between 7200 and 7740 s simulation time. The simulated cell's reintensification period of 9 min agreed well with the observed reintensification periods of 6 to 12 min.

Finally, the simulation captured reasonably well the intercellular relationships seen in the radar data and the synthesized wind fields. The simulation accurately reproduced the alternating intensification between cells described in Chapter 3. CC2 initially developed as the strongest cell in the simulation. Then by 8100 s, CC1 had become the dominant cell. Later, as CC1 began to mature and weaken, CC3 began to intensify. Additionally, the simulation reproduced the observed tendency for intensifying cells to entirely absorb the condensate and circulation of surrounding cells. For example, CC2 was absorbed into CC1 as CC1 and CC3 merged. The simulation to a lesser extent captured the strong observed relationships between the circulations of neighboring cells. Only in a few cases did the divergent outflow at the top of a cell influence or feed the inflow of a neighboring cell. The best example of this occurred between CC3 and CC1 late in the simulation.

6.2.2 Detailed Comparisons

Comparisons of simulation results at selected times throughout the storm development with radar observations and synthesized wind fields provide more detailed insight into the accuracy of the simulation. The comparisons were made using the vertical cross sections of the observed storm cell referred to as C2 in Chapter 3. This cell was chosen because of its proximity to the location of the simulation domain. The comparison times were chosen to account for the simulation's apparent lag time from the observed time as discussed in the previous section. The most rapid cell development occurred in the simulation immediately after penetration of the capping inversion. Unfortunately, the corresponding penetration in nature occurred during the radar data gap between 1119 and 1134 MST. As a result, no comparisons between the simulation and observations could be made for this crucial period in the storm's development.

The first comparison was made using the simulation results at 6840 s (Figs. 31 and 32) and the observations from 1119 MST (Fig. 8). This comparison examines the very early stages of cell development. Both the simulation and the observations show only very weak development occurring at this time. No vertical cross-sections were made from the observations at this time, however, the horizontal cross-sections show only very weak echoes existed above 5.3 km MSL in the vicinity of C2. The simulated cells extended to only 3.75 km (4.5 km MSL). The observed echo and the simulated cell were both approximately 1.5 km wide. The observations at 1119 MST did not support the synthesis of vertical velocities in the vicinity of the echo. The simulated vertical velocities were only 1.5 m s^{-1}.

The next comparison was made using simulation time 8460 s and observations from 1134 MST. This comparison examines the early part of the cell's mature stage.

Figure 45 shows the simulated total condensate and wind fields for 8460 s, and Figure 46 shows the radar reflectivity and synthesized wind fields for 1134 MST. The two figures show many similar features present in both the simulation and in the observations. In both cases, the cell extends to approximately the same MSL height. Both cells contain a relatively strong core of high reflectivity (observed) or total condensate mixing ratio (simulated) located just to the west of the cell's main updraft. Both cases also show low- to mid-level inflow into the eastern side of the cell with relatively strong mid- to upper-level outflow on the western side. Additionally, both cases exhibit a developing weak westerly inflow into the cell at very low levels.

The comparison also shows several marked differences between the simulation and the observations. First, the simulated cell developed several kilometers west of the observed cell. The cause of this difference is not clear, but may be attributed to the lack of three-dimensional forcing effects in the simulation or perhaps an unrealistically strong initial wind profile. Second, the simulation contains a significant total condensate maximum near the top of the cell which does not appear as a maximum in the observed reflectivity field. Further inspection shows the simulated maximum consisted primarily of pristine ice crystals. The lack of a similar upper-level maximum in the observed reflectivity analysis may be attributed to the low radar reflectivity of such ice crystals (Battan, 1973). This phenomena was noted in almost all of the simulations conducted for this study. Third, the simulated cell's updraft was significantly stronger than that observed in C2 (14.6 m s^{-1} *vs.* 9.0 m s^{-1}). Fourth, the simulated cell measured only about 3.5 km across, while the observed cell measured nearly 7.0 km across.

The final comparison was made using simulation time 9000 s and observations from 1152 MST. This comparison examines the latter part of the cell's mature stage.

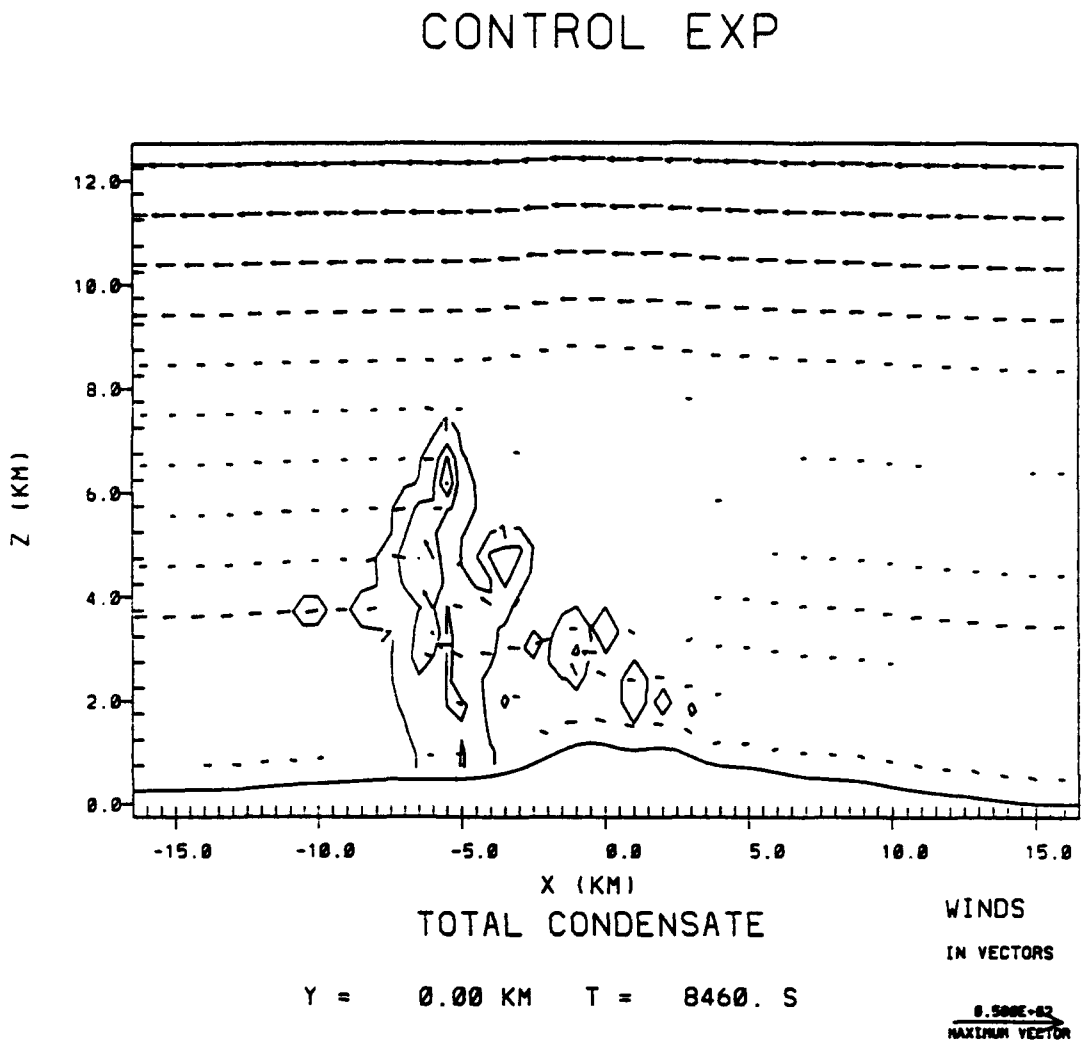

Fig. 45. Analogous to Fig. 27, east-west vertical cross-section of simulated total condensate mixing ratios overlaid with simulated wind vectors for CONTROL simulation at 8460 s. Contour label "1" represents 0.1 g kg^{-1}.

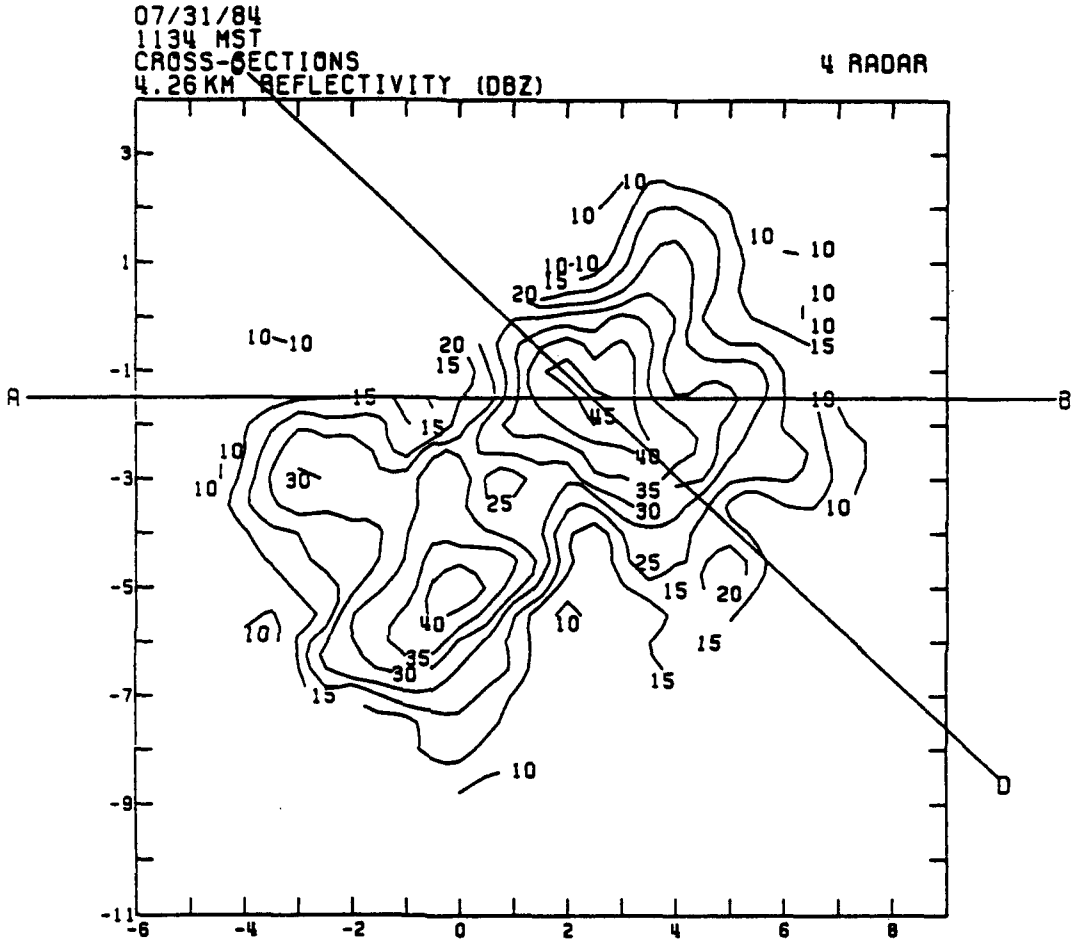

Fig. 46a. Horizontal cross-section of observed radar reflectivities as in Fig. 10a, except at 1134 MST and 4.3 km MSL. Line AB shows location of vertical cross-section in Fig. 46b. Line CD was not used.

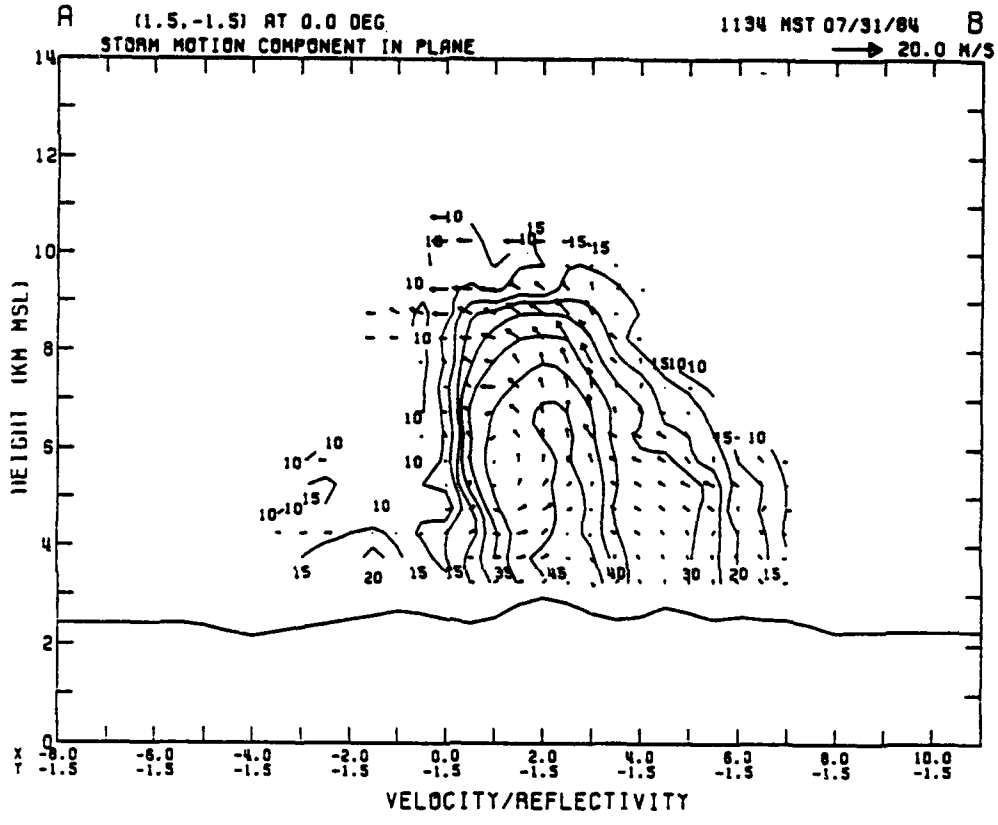

Fig. 46b. As in Fig. 10b, vertical cross-section of observed radar reflectivities and vector velocities at 1134 MST. Cross-section location AB is shown in Fig. 46a.

Figure 47 shows the simulated total condensate and wind fields for 9000 s, and Figure 48 shows the radar reflectivity and synthesized wind fields for 1152 MST. It is important to note that in the previous two comparisons, the single simulated cell (denoted CC1 in earlier discussions) was compared with the observed cell C2, while in this comparison, CC1 corresponds more closely to the observed cell C1. While this change is significant, the qualitative nature of these comparisons still allows an assessment of the simulation's accuracy. The two figures again show many similar features between the simulation and the observations. In both cases, two cells exist in nearly the same configuration. The western cell in both cases extends to nearly the same MSL height. Both western cells contain strong downdrafts associated with the cells' precipitation shafts. In both cases, low-level flow enters the eastern side of the eastern cell, rises through the eastern cell's updraft, exits the western side of the eastern cell, then enters the western cell's updraft to finally exit in the western cell's outflow region. The horizontal dimensions of both simulated cells compared very favorably with those observed. Also in both cases, there are two precipitation shafts with an area between the shaft which contained little or no precipitation.

In addition to the change in cell correspondence described in the previous paragraph, this comparison showed several other major differences between the simulation and the observations. Several of the differences noted in the previous comparison were also noted in this comparison. First, the simulated cells were again located several kilometers west of the observed locations. Second, the western simulated cell again contained a total condensate maximum near the top of the storm with no corresponding reflectivity maximum in the observations. Third, the maximum simulated vertical velocity exceeded that observed in CC1 by over 4.0 m s^{-1}. Finally, the simu-

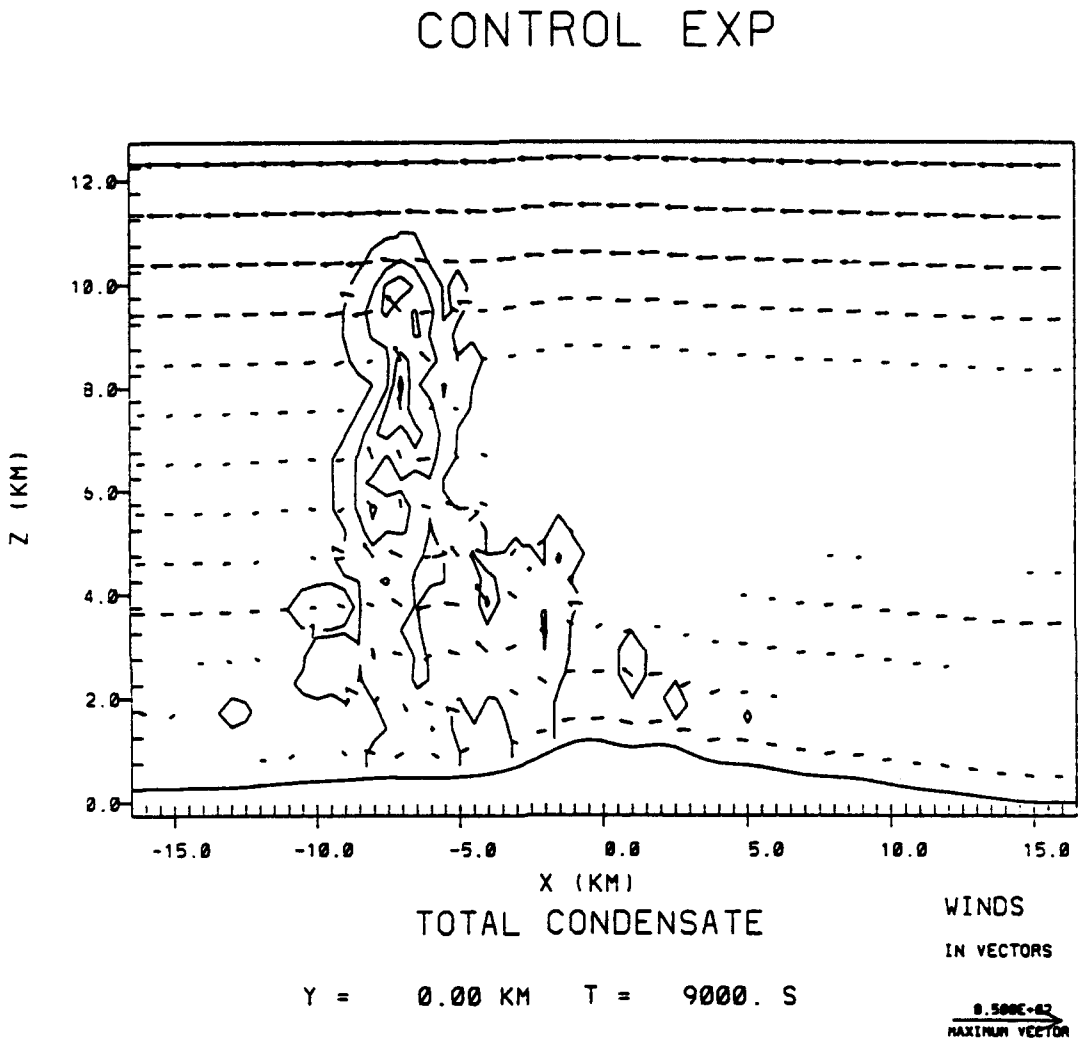

Fig. 47. East-west vertical cross-section of simulated total condensate mixing ratios overlaid with simulated wind vectors, as in Fig. 27, except for CONTROL simulation at 9000 s. Contour label "1" represents 0.1 g kg^{-1}.

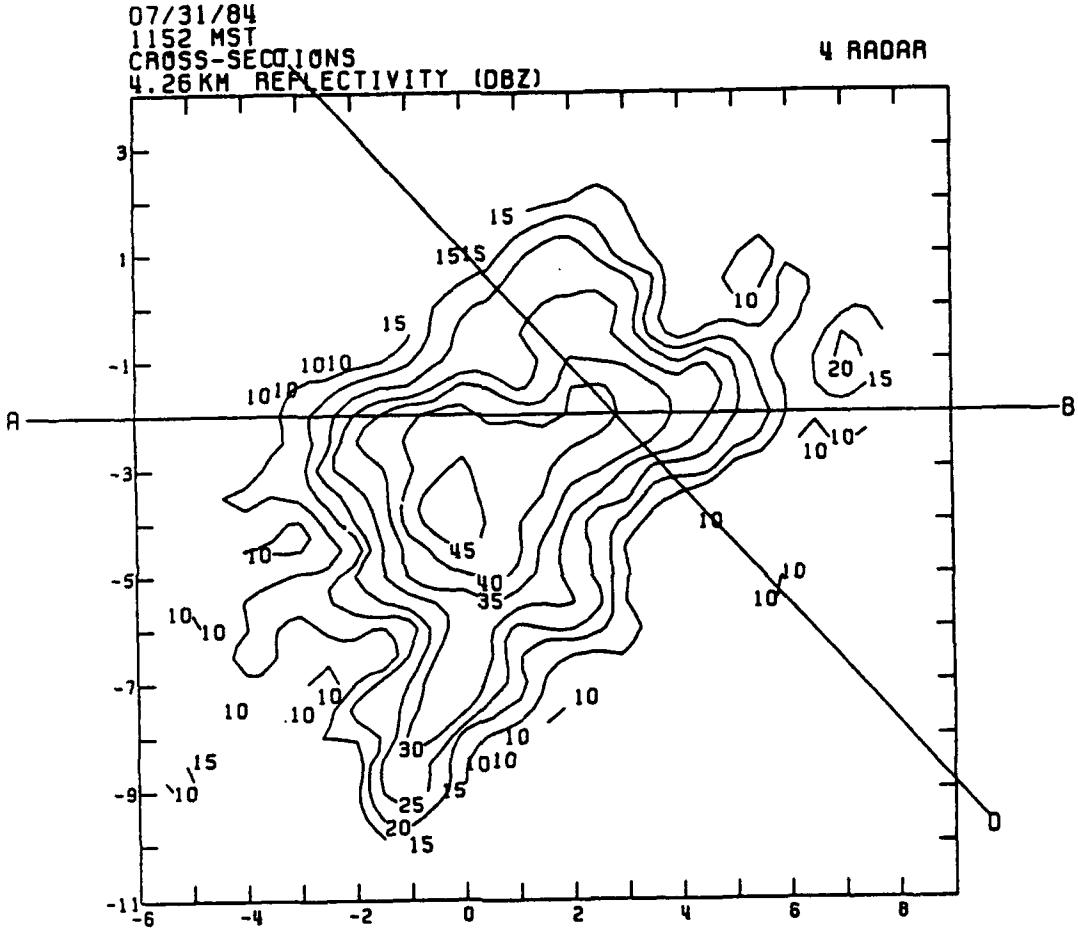

Fig. 48a. Analogous to Fig. 10a, horizontal cross-section of observed radar reflectivities except at 1152 MST and 4.3 km MSL. Line AB shows location of vertical cross-section in Fig. 48b. Line CD was not used.

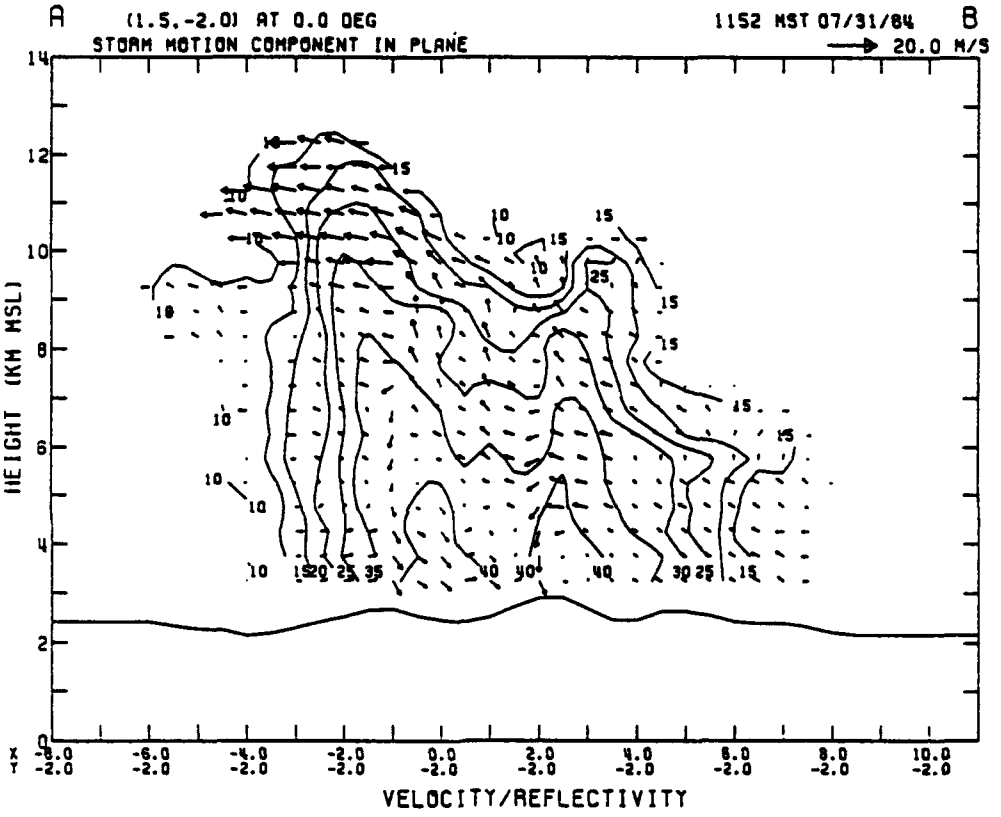

Fig. 48b Analogous to Fig. 10b, vertical cross-section of observed radar reflectivities and vector velocities at 1152 MST. Cross-section location AB is shown in Fig. 48a.

lated eastern cell did not extend nearly as high as the observed eastern cell (5.7 km [7.5 km MSL] *vs.* 10.0 km MSL).

6.3 Comparison With Microphysical Retrievals

The accuracy of the simulated storm's microphysical structure and morphology can be assessed by comparing it with the microphysical structure and morphology retrieved by Lang (1991) from the Doppler radar observations from the 3 August 1984 case. This section presents a brief overview of Lang's (1991) microphysical retrieval results and a comparison of those results with the simulated microphysical results.

Lang's (1991) retrieval showed that the cell development could be divided into two distinct stages: the first phase, in which the cell consisted mostly of liquid cloud and rain water; and the second stage which occurred after penetration of the cell into colder air, in which the ice phases dominated the cell. The maximum retrieved cloud water mixing ratios ranged between 2.5 and 2.7 g kg^{-1} throughout the analysis period. The cloud water existed between 4.3 and 9.3 km MSL. The maximum retrieved rain mixing ratio reached 5.0 g kg^{-1} near the middle of the first phase of development. Lang (1991) reported that the rain mixing ratio maxima in this stage of development existed near the top of the updrafts. Later maxima which occurred in the second stage of development occurred much lower in the analysis domain. The lower elevation rain maxima in the second stage were attributed to the melting of hail/graupel falling from higher levels. Rain water existed between 3.3 and 7.8 km MSL through most of the analysis period and between 3.3 and 5.3 km MSL late in the analysis. The maximum retrieved cloud ice crystal mixing ratio exceeded 3.0 g kg^{-1} about midway through the second phase of development. Cloud ice crystals existed between 7.8 and 11.8 km MSL with the maximum located near 10.0 km MSL. The maximum retrieved hail mixing ratio reached 3.5 g kg^{-1} early in the second phase of development.

The hail existed between 4.3 and 8.3 km MSL during the entire second phase. A distinct double maxima existed in the hail mixing ratio analysis. One maximum was located at 7.3 km MSL while the second was located at 5.3 km MSL. Lang (1991) noted the correspondence of these maxima with the top of the updraft and with the melting level, respectively. Finally, the maximum retrieved snow mixing ratio reached 0.6 g kg^{-1} about mid-way through the second phase. The snow existed between 4.3 and 10.3 km MSL during most of the second phase.

In most respects, the simulated microphysical evolution closely resembled that found by Lang's (1991) microphysical retrievals for the 3 August 1984 case. Examination of the simulated microphysical evolution (Fig. 49) showed that early in the cells' development, the condensate consisted primarily of cloud and rain water. This agrees well with Lang's (1991) observation that warm rain processes dominated the early cell development. As in Lang's (1991) retrievals, as the simulated cells developed and penetrated into the cold air, the ice species rapidly began to dominate the cells' development.

The maximum simulated cloud water mixing ratios generally ranged between 2.5 and 3.0 g kg^{-1} with a few maxima near 4.0 g kg^{-1}. The cloud water was located between 2.0 and 6.1 km (3.8 and 7.9 km MSL). These values and locations agree quite well with those found in the retrieval. The maximum simulated rain water mixing ratio reached 3.1 g kg^{-1} at 8730 s. The rain water existed between the surface and 4.0 km (5.8 km MSL) early in the early precipitating stages of cell development and between the surface and 3.2 km (5.0 km MSL) in the later stages of development. The simulated mixing ratios are about 2.0 g kg^{-1} less than those retrieved. Additionally, the simulated maximum rain water mixing ratio occurred much later in the development than in the retrieval. In fact, in the simulation the rain maximum occurred after

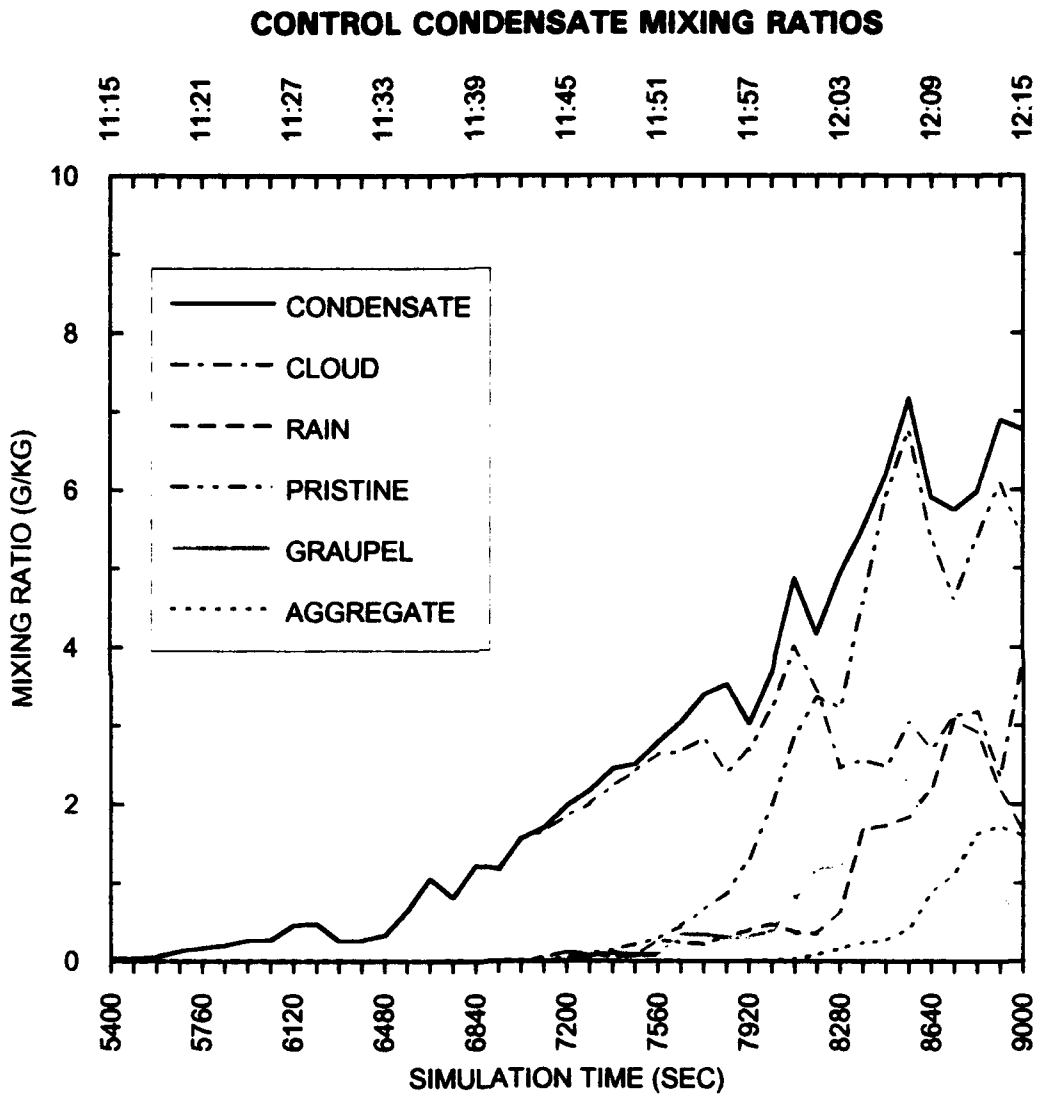

Fig. 49. Time evolution of maximum simulated condensate mixing ratios for the CONTROL simulation. Solid curve shows total condensate mixing ratios, dot-dash curve shows cloud water mixing ratios, dashed curve shows rain water mixing ratios, double dot-dash curve shows pristine ice crystal mixing ratios, shaded curve shows graupel mixing ratios, and dotted curve shows aggregated snow flake mixing ratios. Vertical axis is mixing ratio in grams per kilogram. Horizontal axis is simulation time in seconds (bottom) and in hours and seconds MST (top).

the graupel maximum, while in the retrieval the rain maximum occurred before the graupel maximum. The simulation did show a tendency, similar to that seen in the retrieval, for the rain water maximum to be located near the top of the updraft early in the development, and descend to lower elevations beneath the graupel/hail shaft later in the development.

The maximum simulated pristine ice crystal mixing ratio reached a maximum of 6.8 g kg^{-1} with a typical late simulation value of about 6.0 g kg^{-1}. The ice crystals existed between 3.7 and 11.2 km (5.5 and 13.0 km MSL). The simulated mixing ratios were about twice the magnitude of those found in the retrieval. The ice crystals' location agreed fairly well with those found by Lang (1991). The maximum simulated graupel mixing ratios reached 2.3 g kg^{-1} at 8550 s and near 2.2 km (4.0 km MSL). The graupel/hail existed between the surface and 6.0 km (7.8 km MSL). The simulated mixing ratios agree quite well with those retrieved. The simulation fails to depict the double hail maxima exhibited in the retrieval. In fact, the single simulated graupel/hail maximum is located much lower than the retrieved lower elevation maximum. Additionally, the simulated graupel/hail field extends to the surface while the retrieved hail shafts extend down to only 4.3 km MSL. The maximum simulated aggregated snowflake mixing ratio reached 1.7 g kg^{-1} very late in the simulation. The aggregates existed between 3.2 and 10.7 km (5.0 and 12.5 km MSL). The maximum simulated mixing ratios were about three times the magnitude of those in the retrieval. The location of the aggregates agreed quite well with the retrieval.

The differences between the simulation and the retrieval may be attributed to several factors. First, although the 31 July and 3 August cases were similar, there were certainly differences between them. For example the thermodynamic and wind profiles were certainly different between the two days. Second, the difference in the mi-

crophysical parameterizations between RAMS and the microphysical retrieval model certainly was an important factor in the differing results.

Chapter 7

Sensitivity To Wind Flow

The first two experiments conducted for this study investigated the sensitivity of the simulated storms to the initial base-state wind profiles. In Experiment 1 (EXP1), the simulation was initialized with calm winds throughout the depth of the atmosphere. The next section provides a brief description of the evolution of EXP1's simulated storm. Section 7.2 compares EXP1's results with those of the control. In Experiment 2 (EXP2), the simulation was initialized with a wind profile with wind speeds 50% of those in the control's profile. This simulation developed serious boundary condition instabilities which rendered the simulation useless for the purposes of this study. Section 7.3 provides a brief description of the problems encountered with this simulation.

7.1 Experiment 1 - No Wind Case: Analysis Of Simulated Storm Evolution

Two cells developed directly over the mountain peaks early in the simulation. The cells are denoted hereafter as E1C1 and E1C2 for the western and eastern cells, respectively. Until 6300 s, E1C2 dominated with maximum total condensate mixing ratios of over 4.0 g kg^{-1} and maximum vertical velocities of 11.0 m s^{-1}. Precipitation first developed as a rain shaft out of E1C2 at 6300 s. By 6300 s, both cells already contained some pristine ice crystals. Figures 50 and 51 show analyses of total condensate mixing ratio and vertical velocity, respectively, for 6300 s.

E1C1 strengthened slightly and E1C2 weakened between 6300 and 6660 s. During this period, rain first began reaching the surface from E1C1 and graupel reached

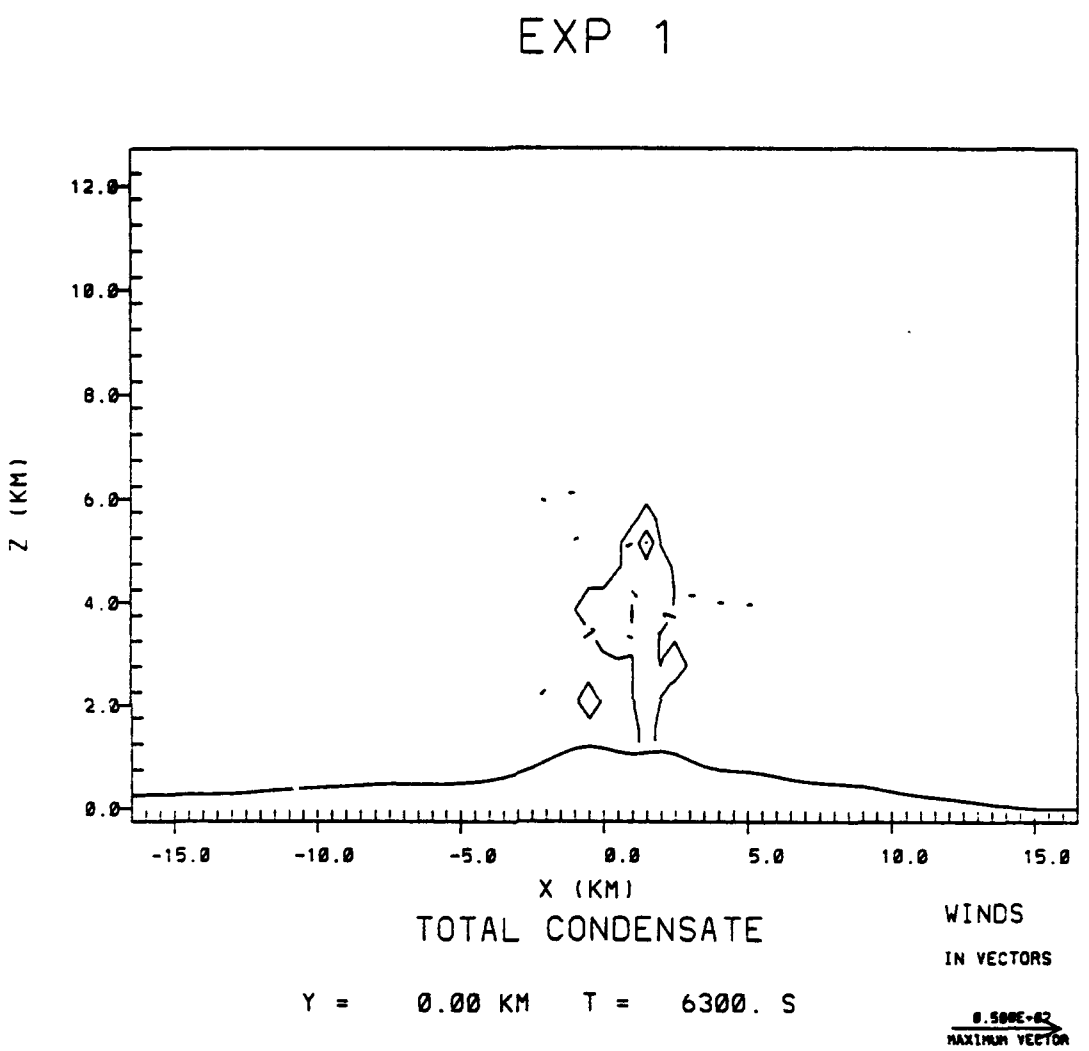

Fig. 50. East-west vertical cross-section of simulated total condensate mixing ratios overlaid with simulated wind vectors for EXP1 simulation at 6300 s. Contours are every 2.0 g kg^{-1} starting at 0.1 g kg^{-1}. Wind vector length shown in lower right-hand corner of figure equals 50 m s^{-1}. Vertical axis is labeled in kilometers above the minimum terrain elevation in the simulation grid (in this case 1.82 km) as described in the text. Horizontal axis is horizontal distance labeled in kilometers. The cross-section shown is located at y = 0.0 km and runs east-west, with the origin at Langmuir Laboratory.

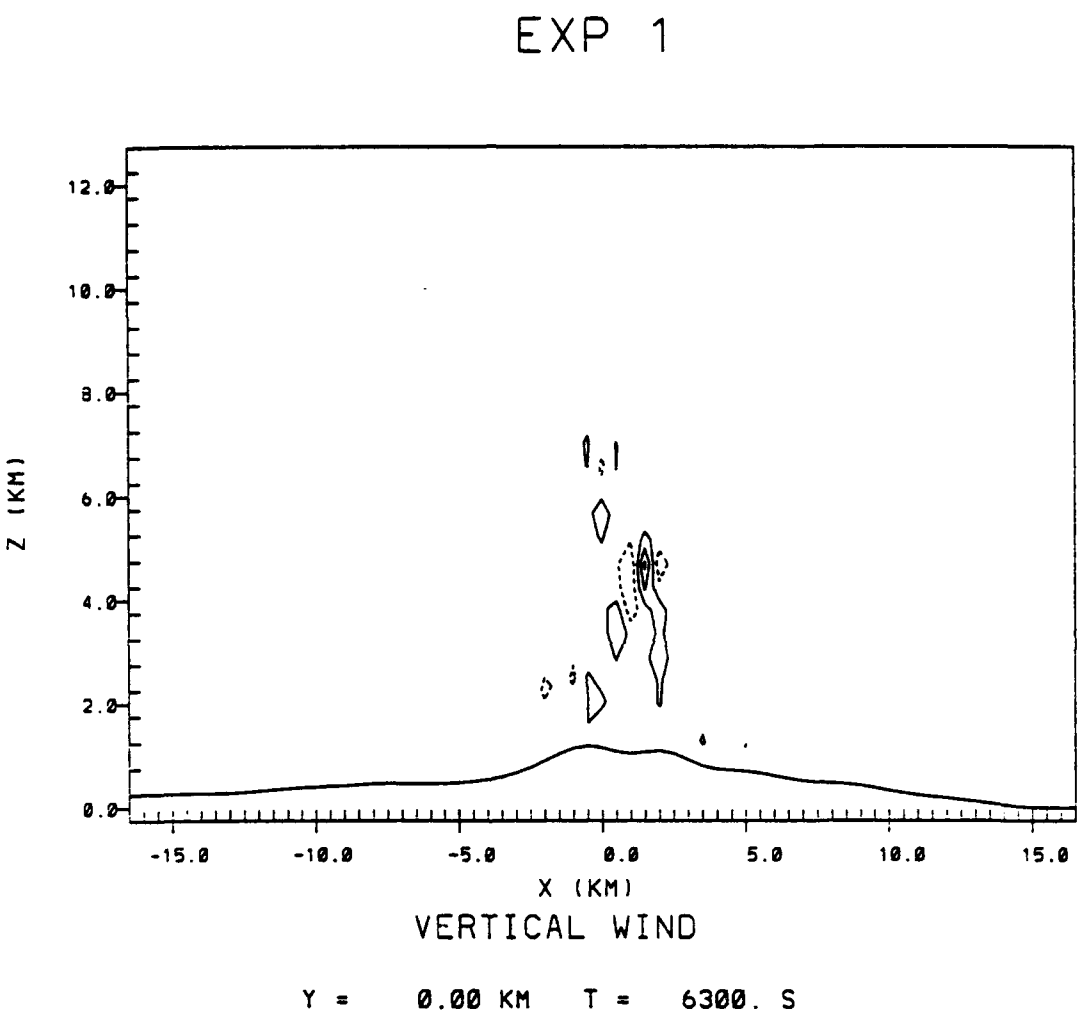

Fig. 51. East-west vertical cross-section of simulated vertical velocity contoured every 3.0 m s^{-1} starting at 1.5 m s^{-1} for EXP1 simulation at 6300 s. Solid (dashed) contours show positive (negative) vertical velocities. Axes labeled as in Fig. 50.

the surface from E1C2 at 6480 s. Maximum total condensate mixing ratios ranged between 3.0 and 3.7 g kg^{-1}, while maximum updrafts decreased to 3.1 m s^{-1} before increasing again in E1C2 to 5.5 m s^{-1}. The cells achieved a maximum height of 6.0 km during this period, and as a result, the ice phase dominated the development as the cells pushed into the colder air at these higher levels.

Between 6660 and 7560 s, both E1C1 and E1C2 continued to develop. The cells exhibited a degree of the oscillatory development individually and between each other as noted in the observations described in Chapter 3 and described by Ziegler *et al.* (1986). During this period, the maximum total condensate mixing ratios reached peaks of 3.6 g kg^{-1} in E1C2 at 6840 s and 4.2 g kg^{-1} in E1C1 at 7290 s. The maximum updrafts during this period reached peaks of 14.0 m s^{-1} in E1C2 at 6840s and 11.5 m s^{-1} in E1C1 at 7290 s. During most of the period, precipitation only fell from E1C2, but by 7380 s, precipitation was falling from both cells. Graupel reached the surface again from E1C2 at 7200 s. Significant pristine ice crystal development also occurred during this period. Figure 52 shows an analysis of total condensate mixing ratio for 7380 s.

Between 7560 and 8190 s further development occurred in both E1C1 and E1C2, and a new cell (hereafter denoted as E1C3) developed just to the east of E1C2. The new cell developed slowly at first, but by 8190 s contained total condensate mixing ratios of over 3.0 g kg^{-1} and updrafts of over 10.0 m s^{-1}. Precipitation first reached the surface from E1C3 between 7920 and 8100 s. Meanwhile E1C1 and E1C2 developed to a maximum height of 8.0 km and contained maximum total condensate mixing ratios of over 4.0 g kg^{-1} and maximum updrafts of up to 11.0 m s^{-1}. During this period, E1C1 also began to build westward slightly. Precipitation fell throughout the period with graupel reaching the surface from E1C1 at 7560 s, from E1C2 at 7740 s,

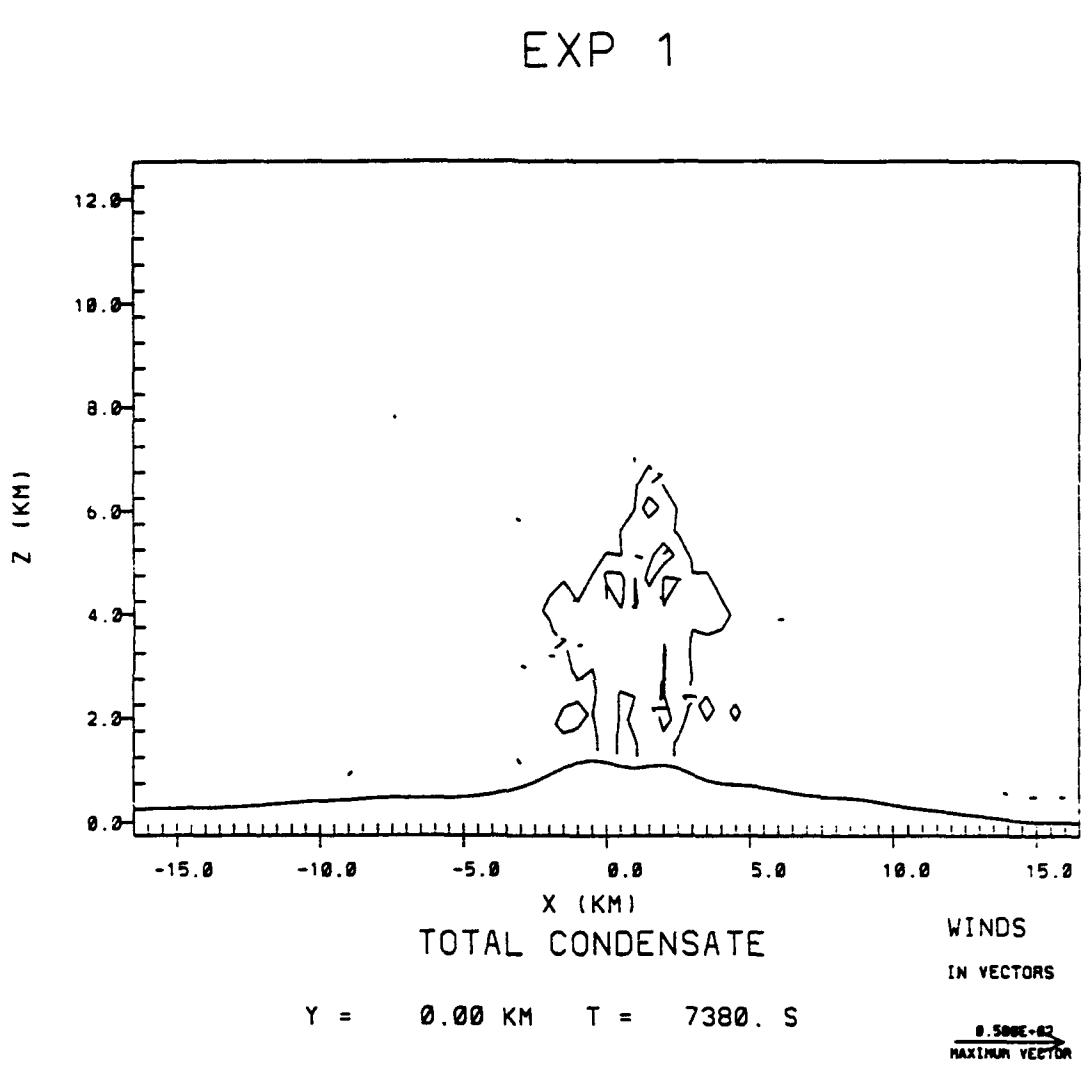

Fig. 52. Analogous to Fig. 50, east-west vertical cross-section of simulated total condensate mixing ratios overlaid with simulated wind vectors for EXP1 simulation at 7380 s. Contour label "1" represents 0.1 g kg^{-1}.

and from E1C2 and E1C3 between 7920 and 8100 s. The ice phases dominated the development during this time with pristine ice crystals and aggregated snow flakes showing maximum mixing ratios of 4.1 and 2.3 g kg^{-1}, respectively. Figures 53 and 54 show analyses of total condensate mixing ratio and vertical velocity, respectively, for 8100 s.

By 8280 s E1C2 had essentially merged with E1C1. At the same time a new cell (hereafter denoted as E1C4) developed near x = -4.0 km. Between 8280 and 9000 s, E1C4 rapidly developed from a small cell to one with a peak maximum total condensate mixing ratio in excess of 4.0 g kg^{-1} and a peak maximum updraft in excess of 15.0 m s^{-1}. During this period, E1C4 consisted primarily of liquid water phases, with ice phases developing near the end of the simulation. The cell began producing rain at the surface by 8820 s. During the same period, E1C1 continued to develop, primarily at the upper levels, where the ice phases were dominant. Maximum total condensate mixing ratios exceeded 4.0 g kg^{-1} through most of this period while the maximum updrafts remained between 7.5 and 10.5 m s^{-1}. The cell reached a maximum height of 10.25 km at 9000 s and produced rain at the surface between 8640 and 9000 s and graupel between 8820 and 9000 s. E1C3 continued its rapid development through the period with maximum total condensate mixing ratios reaching over 6.0 g kg^{-1} and maximum updrafts in excess of 15.0 m s^{-1} with a peak of 19.1 m s^{-1} at 8370 s. This cell consisted of both ice and the liquid water phases. The cell produced rain at the surface throughout the period and graupel after 8460 s. E1C3 developed to reach a maximum height of just under 10.0 km by 9000 s. Over the entire storm, the ice phases continued to dominate during this period with pristine ice crystal mixing ratios reaching a peak of 5.0 g kg^{-1}, aggregated snow flakes a peak of 2.5 g kg^{-1}, and graupel 2.4 g kg^{-1}. At the same time, though, rain and cloud water mix-

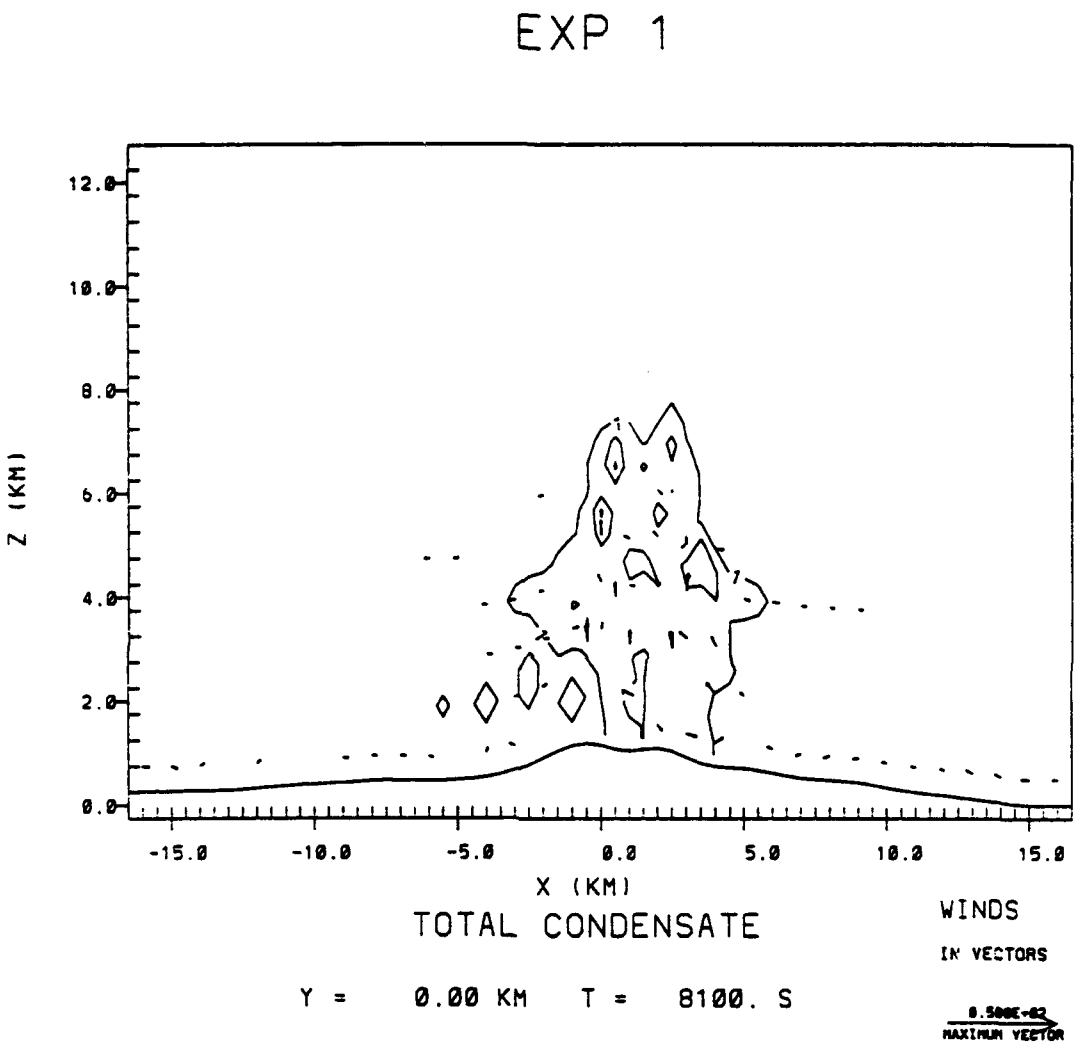

Fig. 53. East-west vertical cross-section of simulated total condensate mixing ratios overlaid with simulated wind vectors, as in Fig. 50, except for EXP1 simulation at 8100 s. Contour label "1" represents 0.1 g kg^{-1}.

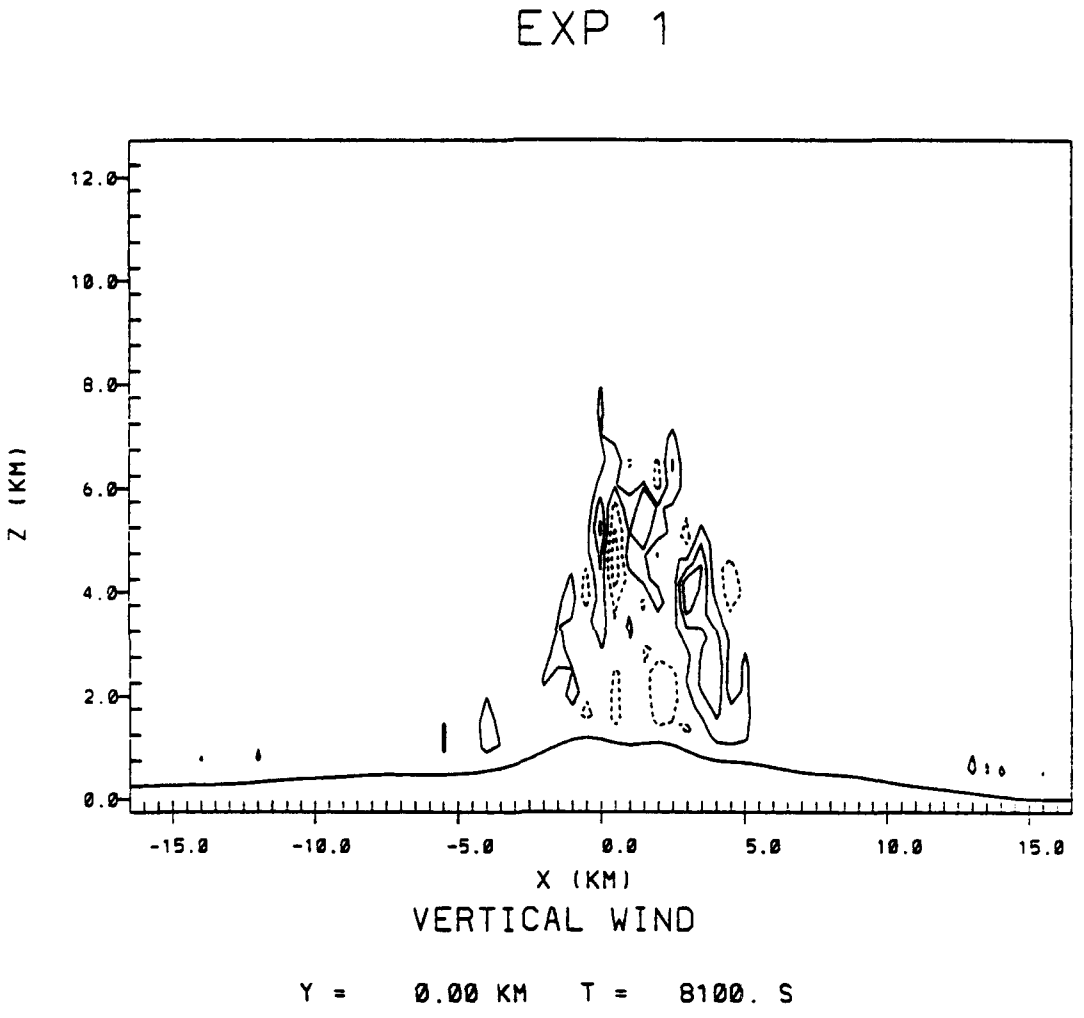

Fig. 54. Analogous to Fig. 51, east-west vertical cross-section of simulated vertical velocity for EXP1 simulation at 8100 s.

ing ratios reached their simulation peaks of 2.5 and 4.2 g kg^{-1}, respectively. A pronounced low-level inflow developed into the storm over this time period also. The low-level flow created convergence areas near the location where E1C4 developed and where E1C3 continued to develop. This low-level convergence continued to support the development of these cells throughout the period. Compensating divergence near the top of the storm also aided continued development. Figures 55 and 56 show analyses of total condensate mixing ratio and vertical velocity, respectively, for a time representative of this period--8820 s.

Figures 57 and 58 show the evolution of the simulation's maximum condensate mixing ratios and upward and downward vertical velocities, respectively.

7.2 Experiment 1 - No Wind Case: Comparison With Control

EXP1's simulated storm showed several similarities to the control simulation's storm, but also exhibited many differences. Qualitatively, the storms appear similar. Both storms contain several cells--four in EXP1 compared with three in the control. Both attained nearly the same maximum heights--10.25 km in EXP1 compared with 11.0 km in the control. Finally, both storms generally look similar in shape.

The storms exhibit some major differences also. First, EXP1's storm is about 3.0 km wider than the control. Second, EXP1's cells appear to have had a more equal chance for development than those in the control. The two major cells in EXP1 grew to about the same height, while in the control, CC1 dominated the vertical development. These two differences may be attributed to the absence of an initial environmental wind flow in EXP1. Compared to the control, EXP1's cells likely experienced less entrainment of drier, less buoyant environmental air. This decreased entrainment allowed the overall storm to grow more in horizontal extent than the control, and also allowed EXP1's eastern cell to grow stronger than the eastern cell in the

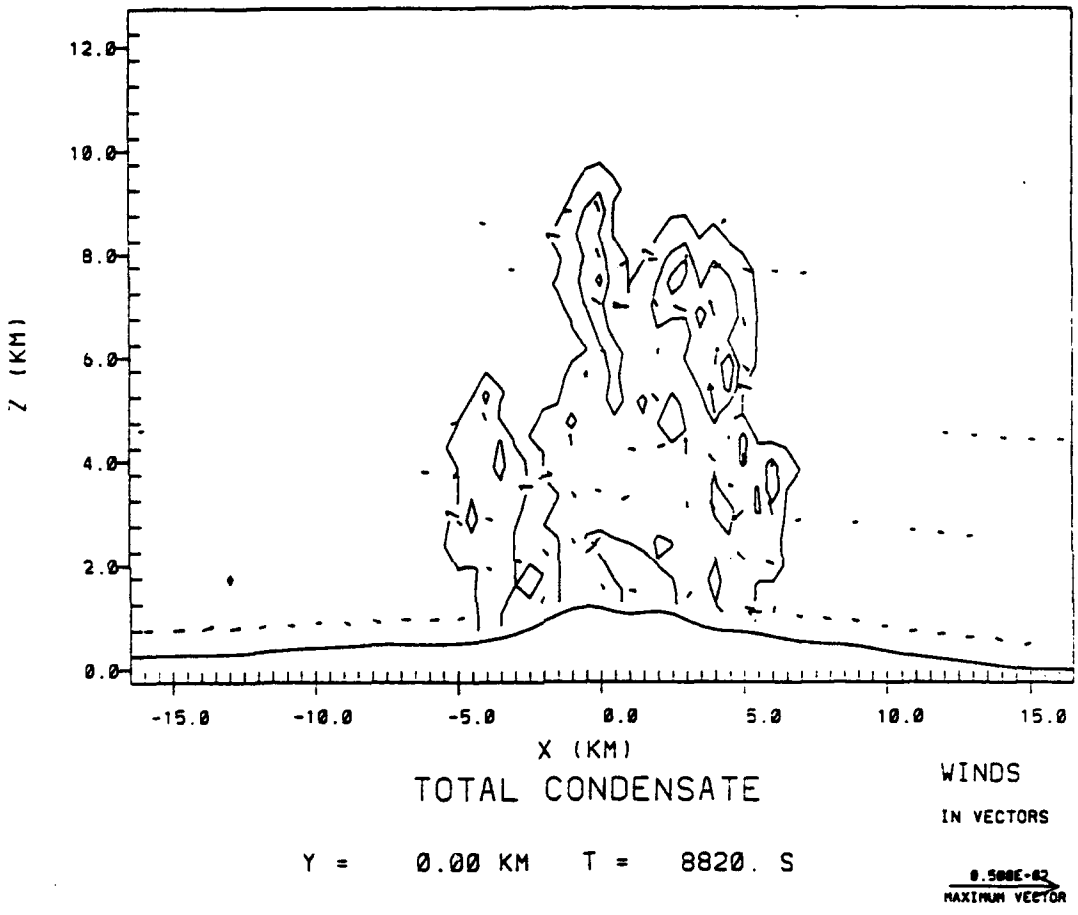

Fig. 55. As in Fig. 50, east-west vertical cross-section of simulated total condensate mixing ratios overlaid with simulated wind vectors for EXP1 simulation at 8820 s. Contour label "1" represents 0.1 g kg^{-1}.

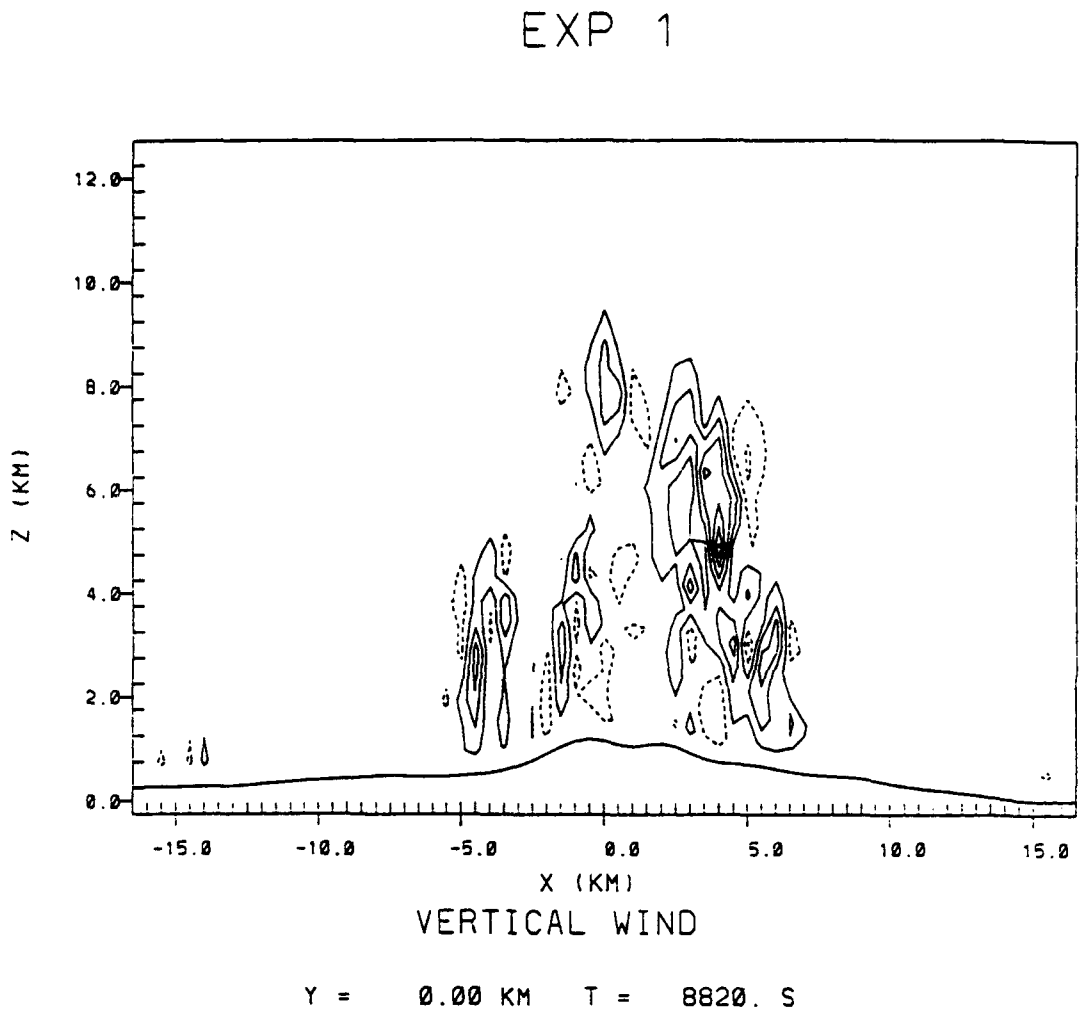

Fig. 56. As in Fig. 51, east-west vertical cross-section of simulated vertical velocity for EXP1 simulation at 8820 s.

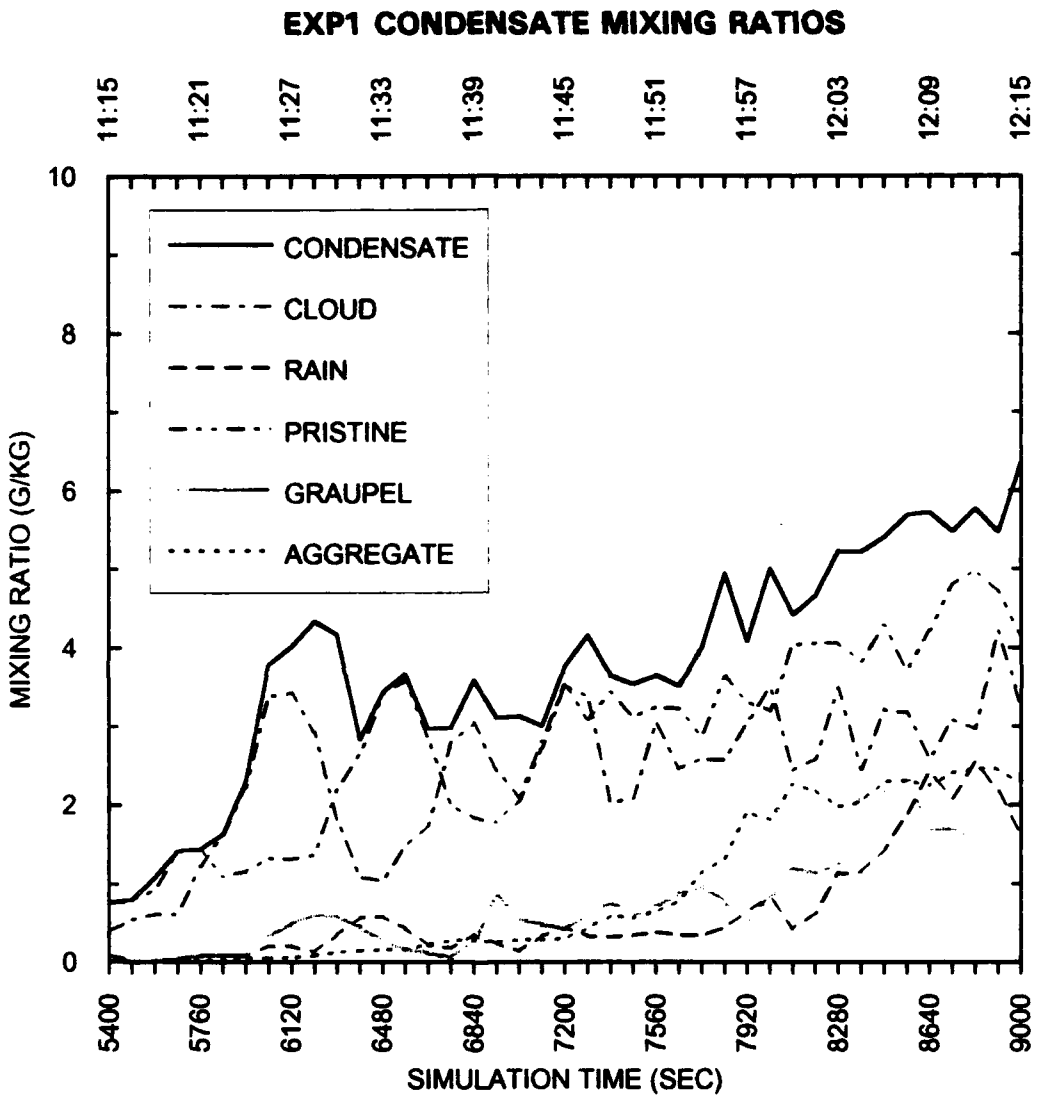

Fig. 57. Time evolution of maximum simulated condensate mixing ratios for the EXP1 simulation. Solid curve shows total condensate mixing ratios, dot-dash curve shows cloud water mixing ratios, dashed curve shows rain water mixing ratios, double dot-dash curve shows pristine ice crystal mixing ratios, shaded curve shows graupel mixing ratios, and dotted curve shows aggregated snow flake mixing ratios. Vertical axis is mixing ratio in grams per kilogram. Horizontal axis is simulation time in seconds (bottom) and in hours and seconds MST (top).

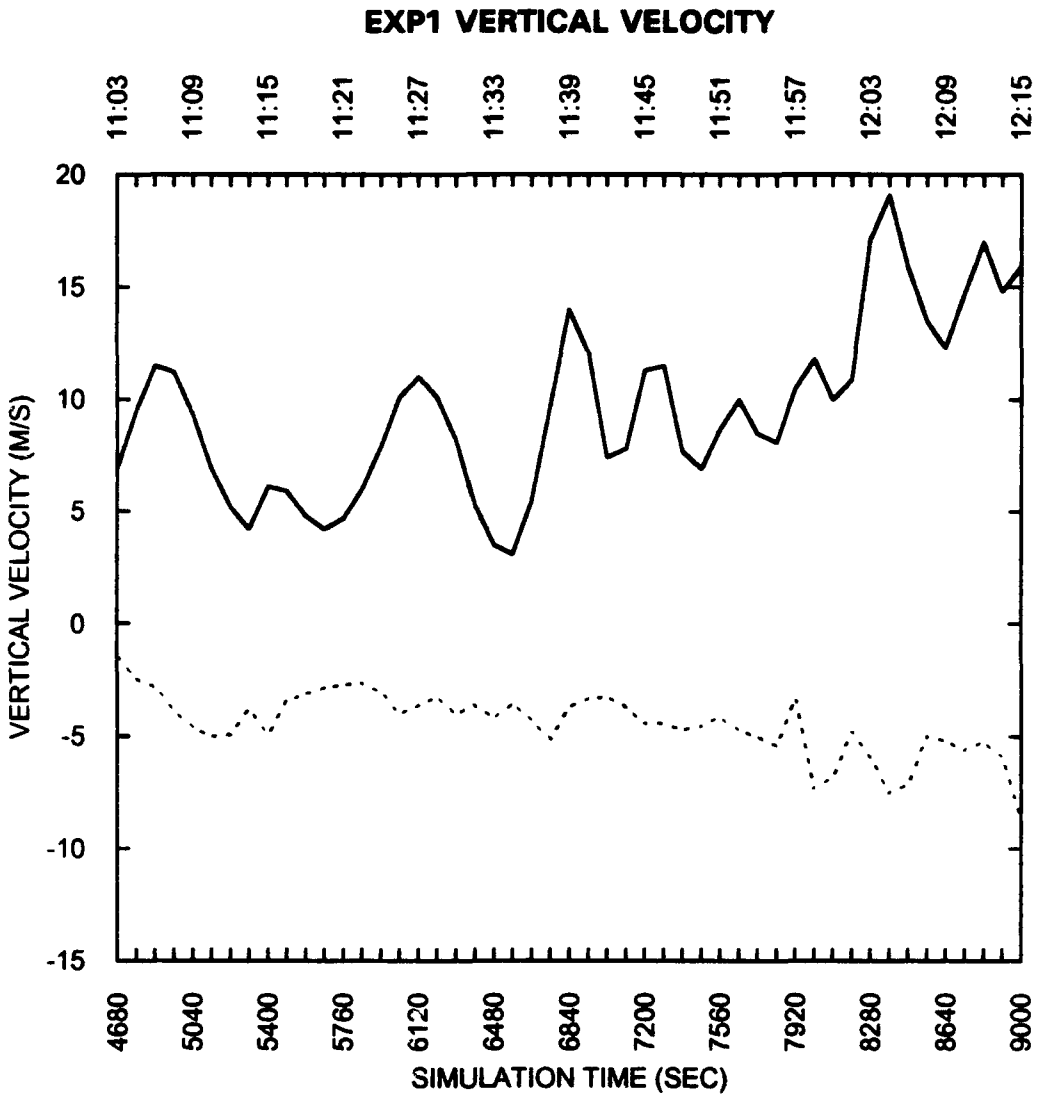

Fig. 58. Time evolution of maximum and minimum simulated vertical velocities for the EXP1 simulation. Solid curve shows maximum upward vertical velocities (positive w). Dashed curve shows maximum downward vertical velocities (negative w). Vertical axis is vertical velocity in m s^{-1}. Horizontal axis is simulation time in seconds (bottom) and in hours and seconds MST (top).

control. Third, the convective initiation occurred much earlier in EXP1 than in the control--4230 s in EXP1 compared to 5670 s in the control. The initial calm winds limited the turbulent transport of heat away from the surface, allowing maximum solar heating and rapid convective development. Fourth, the cells developed between 3.0 and 5.0 km farther east, more directly over the mountain tops, in EXP1 than in the control. Several studies discussed in Chapter 2 (Banta, 1984; Braham and Draginis, 1960; Glass and Carlson, 1963; Orville, 1965b; Barker and Banta, 1985; Banta and Schaaf, 1987; Schaaf *et al.*, 1988) described the tendency for leeside convective development and the mechanisms for such development. In the absence of environmental wind, there is less translation of convective updrafts toward the lee of the mountains (Orville, 1965b). Thus, under calm wind conditions such as EXP1, it is natural to expect the storms to develop closer to the mountains than under windier conditions such as the control. Finally, EXP1's storm developed more steadily and more slowly than the storm in the control. The reason for this difference in development is not entirely clear. The control's more rapid development late in the simulation may be attributed to the relatively strong flow above 6.0 to 8.0 km which served as an "exhaust mechanism" for the developing cell. This flow helped remove heat from the top of the cell and the surrounding environment, keeping the environmental lapse rate favorable for rapid development. The absence of such a flow in EXP1 may have contributed to its slower, more steady development.

Quantitatively, the storms are markedly different in many respects. The maximum total condensate mixing ratio evolution shown in Figure 57 shows a rapid rise in EXP1 between 5850 and 6210 s followed by a steady increase through the rest of the simulation. This development is much different than the extended period of rapid increases in the maximum total condensate mixing ratio seen in the control. Second,

the peak total condensate mixing ratio in EXP1 reached 6.4 g kg^{-1} compared to 7.2 g kg^{-1} in the control. EXP1's pristine ice crystal maximum mixing ratio evolution differed dramatically from that seen in the control. In EXP1, the maximum mixing ratio barely reached 5.0 g kg^{-1}, while in the control, the maximum pristine ice crystal mixing ratio never went below 5.0 g kg^{-1} after 8460 s. The maximum aggregated snow flake and graupel mixing ratios increase earlier and persist longer in EXP1 than in the control. All of the maximum mixing ratio traces in Figure 57 show a large amount of variability not seen in the control. The evolution of maximum updrafts and downdrafts shown in Figure 58 show a similar amount of variability. The maximum updrafts exceeded 5.0 m s^{-1} much earlier in EXP1 than in the control. EXP1's peak updraft exceeded the control's by nearly 3.0 m s^{-1}, while EXP1's peak downdraft exceeded the control's by about 1.0 m s^{-1}. Again, the maximum updrafts and downdrafts indicate a much slower, steadier development in EXP1 than in the control.

The marked differences between EXP1's simulation and the control's precluded any detailed comparison between the two simulations at similar analysis times.

7.3 Experiment 2 - 50% Wind Case

EXP2 was initialized with a wind profile with wind speeds 50% of those in the control's wind profile. This simulation developed serious boundary condition instabilities which ultimately rendered the simulation useless for the purposes of this study.

The simulation started very much like the control. As early as 5400 s, though, the first signs of the boundary problems began to appear. By this time a 4.5 m s^{-1} easterly flow developed near the eastern model boundary at about 2.5 km. A westerly flow of 3.0 m s^{-1} had developed at the same boundary at 0.5 km. This circulation was accompanied by a relatively large negative pressure perturbation (from the base state) in the low levels near the same boundary.

As the simulation progressed, the pressure perturbation and the wind maxima continued to increase in magnitude. Additionally, strong updrafts and downdrafts developed and produced extremely large areas of condensate. The spurious circulations and cells continued to strengthen throughout the simulation. Eventually, the effect of these disturbances destroyed the credibility of the simulation in the rest of the model domain.

The cause of the boundary condition problems observed in this simulation are unclear. The problem most likely resulted from some reflection or excitation of a certain wavelength or wavelengths in the model. It is not obvious why the 50% wind profile produced such disturbances while the stronger winds in the control profile did not. The problem appears to be related to the topography since it occurs in the lower levels. However, the topography should have little effect since the initial wind profiles for both EXP2 and the control had calm winds below the mountain top.

Chapter 8

Sensitivity To Diabatic Heating Effects

The second two experiments conducted for this study investigated the sensitivity of the simulated storms to diabatic heating effects. Section 8.1 describes the results of Experiment 3's (EXP3) simulation. Section 8.2 provides a brief description of the evolution of Experiment 4's (EXP4) simulated storm and a comparison of the results with those of the control.

8.1 Experiment 3 - No Short Wave Radiation Case

In EXP3, the simulation was conducted with the RAMS short-wave radiation package deactivated, effectively "turning off the sun". While no storm developed in this case, the results provide crucial evidence of the importance of the wind flow in focusing the convective initiation.

8.1.1 Analysis Of Simulated Cloud Evolution

No convective development occurred during the simulation, however, a small cloud did develop and persist between 6300 s and 9000 s (Fig. 59). The cloud consisted entirely of cloud water and the maximum mixing ratio never exceeded 0.6 g kg^{-1}. A very weak, but steady, updraft of between 2.5 and 3.4 m s^{-1} supported the small cloud. The updraft developed near a quasi-stationary area of low-level convergence located between x = -2.0 and -3.0 km. The convergence resulted from the interaction of the initial easterly flow with a weak westerly flow below 2.0 km. The westerly flow appears to have developed as result of a dynamically induced mountain-wave circulation, perhaps even a rotor circulation, on the lee side of the mountain.

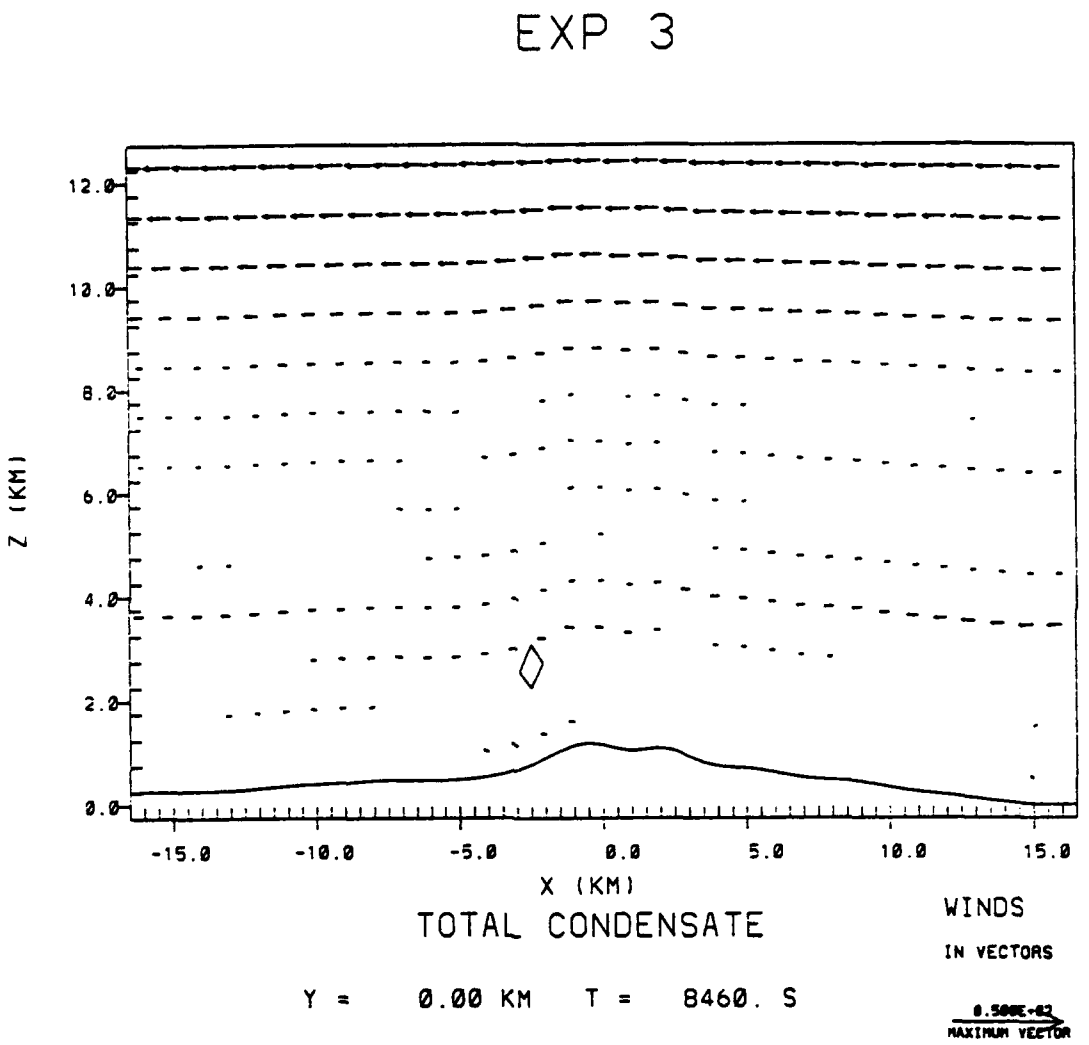

Fig. 59. East-west vertical cross-section of simulated total condensate mixing ratios overlaid with simulated wind vectors for EXP3 simulation at 8460 s. Contours are every 2.0 g kg^{-1} starting at 0.1 g kg^{-1}. Wind vector length shown in lower right-hand corner of figure equals 50 m s^{-1}. Vertical axis is labeled in kilometers above the minimum terrain elevation in the simulation grid (in this case 1.82 km) as described in the text. Horizontal axis is horizontal distance labeled in kilometers. The cross-section shown is located at y = 0.0 km and runs east-west, with the origin at Langmuir Laboratory.

Figure 60 shows an example from 7740 s of the convergence described above. A similar pattern existed well into the simulation to 8460 s.

Both the cloud and the updraft developed between x = -2.0 and -3.0 km, and remained there through the rest of the simulation. The cloud was located at approximately z = 2.75 km. A very small secondary cloud developed just to the east of the first near the end of the simulation.

8.1.2 Comparison With Control

Comparison of the results of EXP3 with those of the control shows several notable similarities. In both cases, the first clouds formed at nearly the same location. The cloud developed slightly higher in EXP3 than in the control. Also in both cases, the cloud and supporting updraft remained nearly stationary for an extended period. In the control, the stationary cloud and updraft remained in place until the convective development began to dominate the circulation in the area. Finally, both EXP3 and the control show the development of the quasi-stationary area of low-level convergence induced by the mountain-wave circulation discussed above. This comparison points out the crucial importance of environmental wind in focusing the convective initiation.

8.2 Experiment 4 - Warm Rain Microphysics Case

EXP4 was conducted with all the ice-phase microphysical processes deactivated and only the warm rain parameterizations activated.

8.2.1 Analysis Of Simulated Storm Evolution

Prior to 7920 s, EXP4's development followed exactly or nearly exactly that described in Chapter 6 for the control and will not be discussed again here. By 7920 s, three cells had developed, E4C1 near x = -5.0 km, E4C2 slightly to the east, and E4C3 near x = 0.0 km. E4C1 dominated the simulated storm with total condensate

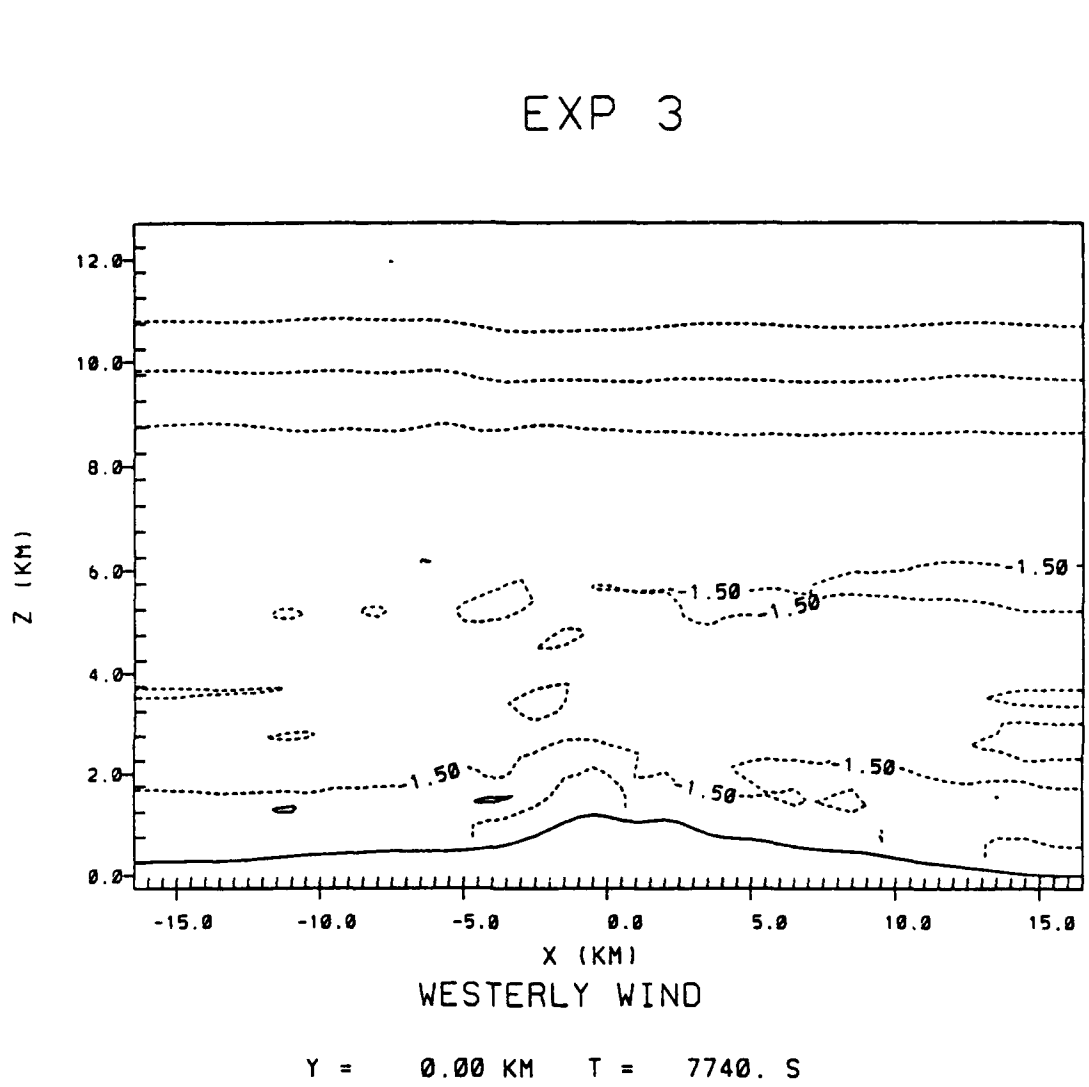

Fig. 60. East-west vertical cross-section of simulated u wind component contoured every 3.0 m s^{-1} starting at 1.5 m s^{-1} for EXP3 simulation at 7740 s. Solid (dashed) contours show westerly (easterly) winds. Axes are labeled as in Fig. 59.

mixing ratios of up to 3.2 g kg^{-1} and updrafts of 10.0 m s^{-1}. E4C2 contained total condensate mixing ratios in excess of 2.0 g kg^{-1} and updrafts in excess of 4.5 m s^{-1}. E4C3 contained low total condensate mixing ratios and weak updrafts of about 1.5 m s^{-1}. The horizontal flow featured an area of low-level convergence near x = -5.5 km. A rain shaft associated with E4C1 and E4C2 developed between x = -3.5 and -4.0 km. The peak rain mixing ratio in the storm reached 0.4 g kg^{-1}. The maximum cloud top at this time reached 5.25 km. Figures 61 and 62 show analyses of total condensate mixing ratio and vertical velocity, respectively, for 7920 s.

At 8100 s, E4C1 continued to dominate the storm with maximum total condensate mixing ratios of 4.8 g kg^{-1} and maximum updrafts of 13.7 m s^{-1}. E4C2 still contained total condensate mixing ratios in excess of 2.0 g kg^{-1} and updrafts of over 7.5 m s^{-1}. A significant downdraft of 5.1 m s^{-1} developed at this time between the updrafts associated with E4C1 and E4C2. E4C3 remained weak with updrafts near 1.5 m s^{-1} and low total condensate mixing ratios. The rain shaft widened to about 1.0 km with a peak storm rain mixing ratio of 1.6 g kg^{-1}. The maximum cloud top reached 5.5 km by this time.

By 8280 s, both E4C1 and E4C2 had weakened slightly. E4C1 continued to dominate with total condensate mixing ratios of 4.8 g kg^{-1} and a maximum updraft of 10.1 m s^{-1}. E4C1's updraft showed a double maxima structure with the upper maximum located near z = 4.5 km and the lower maximum located near z = 2.5 km. E4C2's total condensate mixing ratio remained slightly above 2.0 g kg^{-1} while its updraft weakened to about 4.5 m s^{-1}. Meanwhile E4C3 grew slightly in size, but remained at about the same strength as at previous analysis times. The rain shaft associated with E4C1 and E4C2 widened again, this time to nearly 2.0 km. The

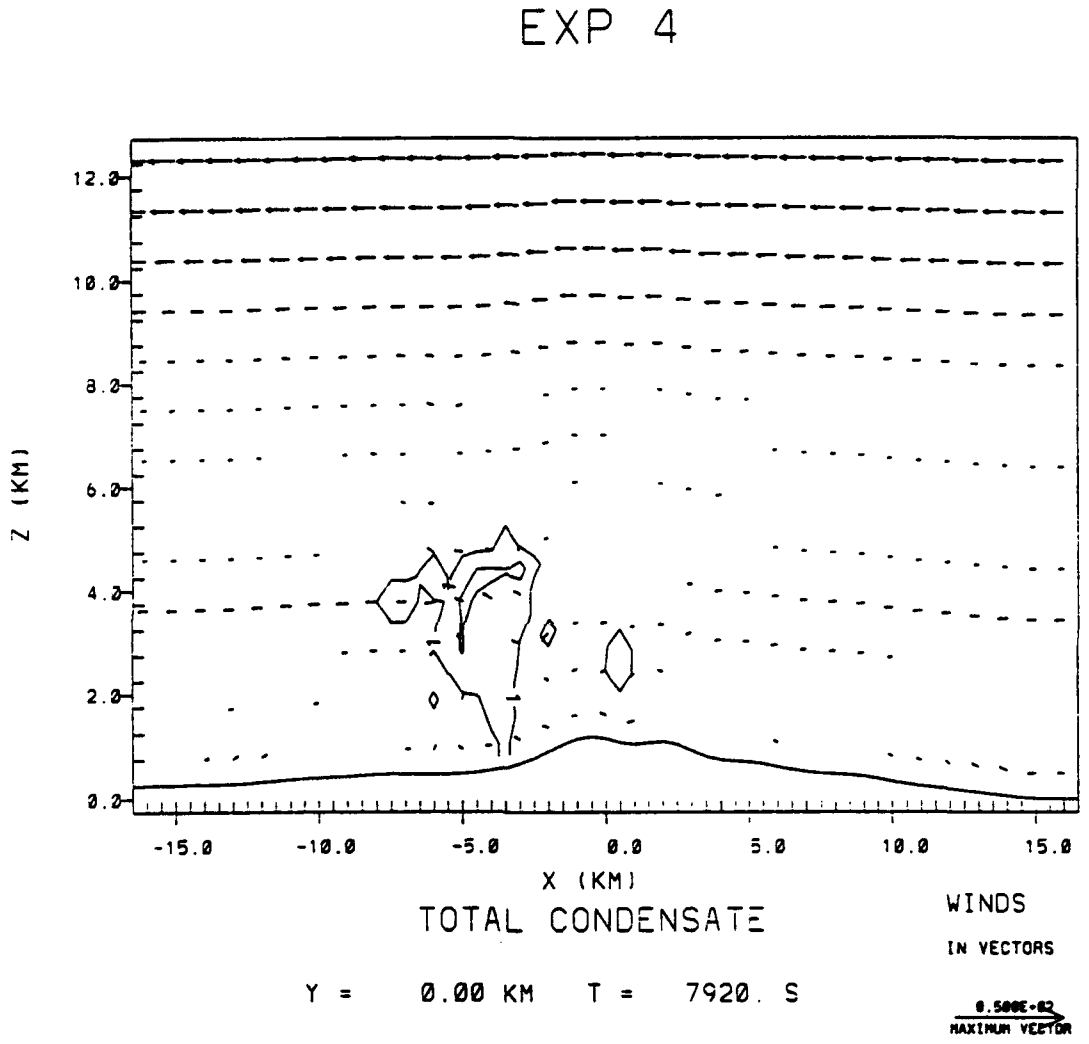

Fig. 61. Analogous to Fig. 59, east-west vertical cross-section of simulated total condensate mixing ratios overlaid with simulated wind vectors for EXP4 simulation at 7920 s.

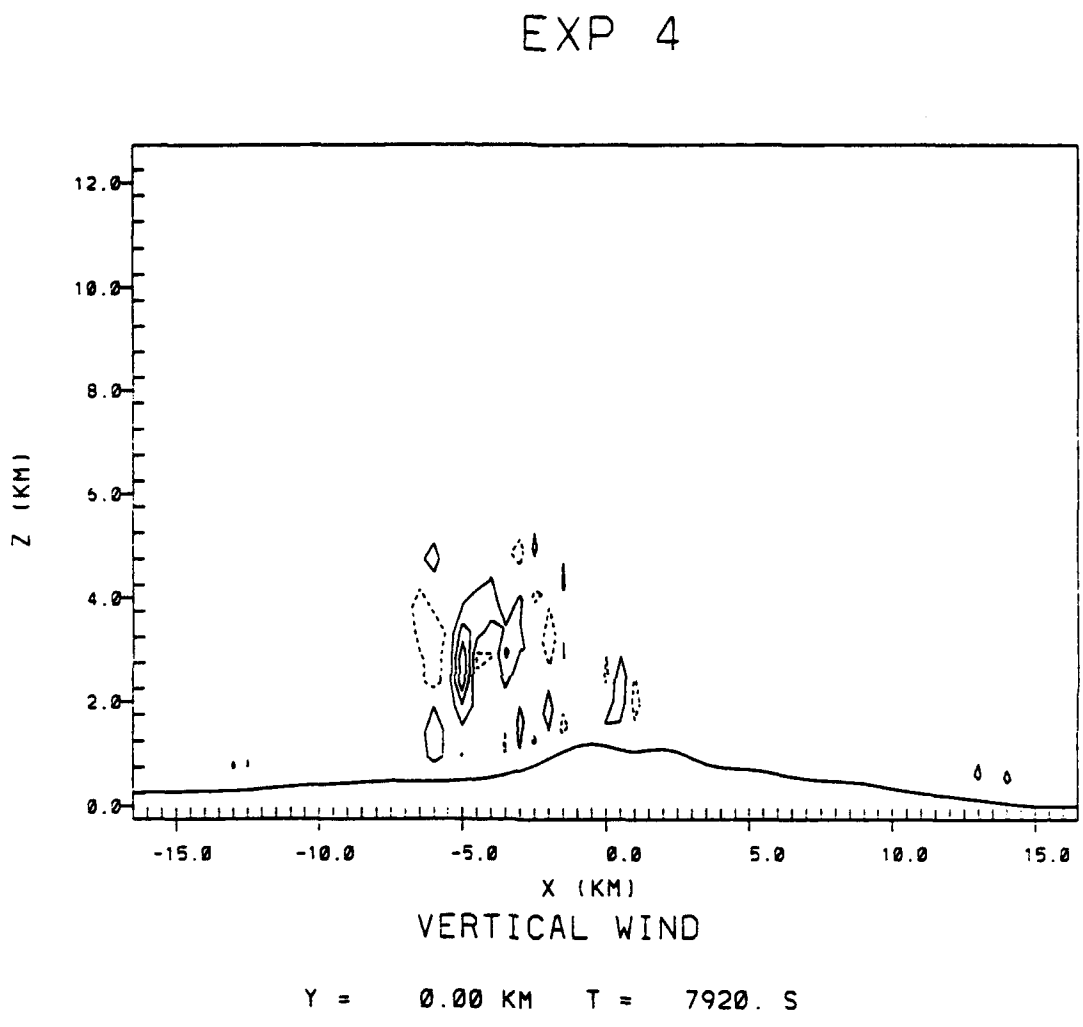

Fig. 62. East-west vertical cross-section of simulated vertical velocity contoured every 3.0 m s^{-1} starting at 1.5 m s^{-1} for EXP4 simulation at 7920 s. Solid (dashed) contours show positive (negative) vertical velocities. Axes labeled as in Fig. 59.

maximum storm rain mixing ratio reached 1.9 g kg^{-1} in E4C1, and the maximum cloud top reached 6.25 km.

At 8460 s E4C1 clearly dominated the storm. The cell contained a double maxima in the total condensate mixing ratio. The upper maximum was located at about 5.5 km and contained mixing ratios in excess of 4.0 g kg^{-1}. The lower maximum was located near 4.0 km and contained mixing ratios of 5.5 g kg^{-1}. The updraft associated with E4C1 increased to 11.8 m s^{-1}. Meanwhile, E4C2 continued to weaken with maximum total condensate mixing ratios dropping below 2.0 g kg^{-1} and maximum updrafts only reaching 1.5 m s^{-1}. At the same time, E4C3 developed significantly over previous analyses with total condensate mixing ratios exceeding 2.0 g kg^{-1} and maximum updrafts exceeding 4.5 m s^{-1}. The maximum rain mixing ratio in the storm reached 3.5 g kg^{-1} in E4C1. The rain shaft widened to 2.5 km, and the maximum cloud height reached 6.5 km. Figures 63 and 64 show analyses of total condensate mixing ratio and vertical velocity, respectively, for 8460 s.

The simulation at 8640 s showed that E4C1 continued to dominate the storm. Its maximum total condensate mixing ratio remained nearly steady at 5.4 g kg^{-1}, and its maximum updraft strengthened to 13.0 m s^{-1}. E4C2 remained relatively weak with total condensate mixing ratios barely exceeding 2.0 g kg^{-1} and maximum updrafts of 4.5 m s^{-1}. E4C3 remained at about the same strength as at the previous analysis time, but grew in size. At this time, a strong mid-level flow out of E4C3, through E4C2, and into E4C1 matured. The rain shaft continued to widen at this time to 3.0 km. The shaft began to show signs of a split between E4C1 and E4C2. The maximum rain mixing ratio at this time reached 4.4 g kg^{-1} in E4C1, while the maximum cloud height remained at 6.5 km.

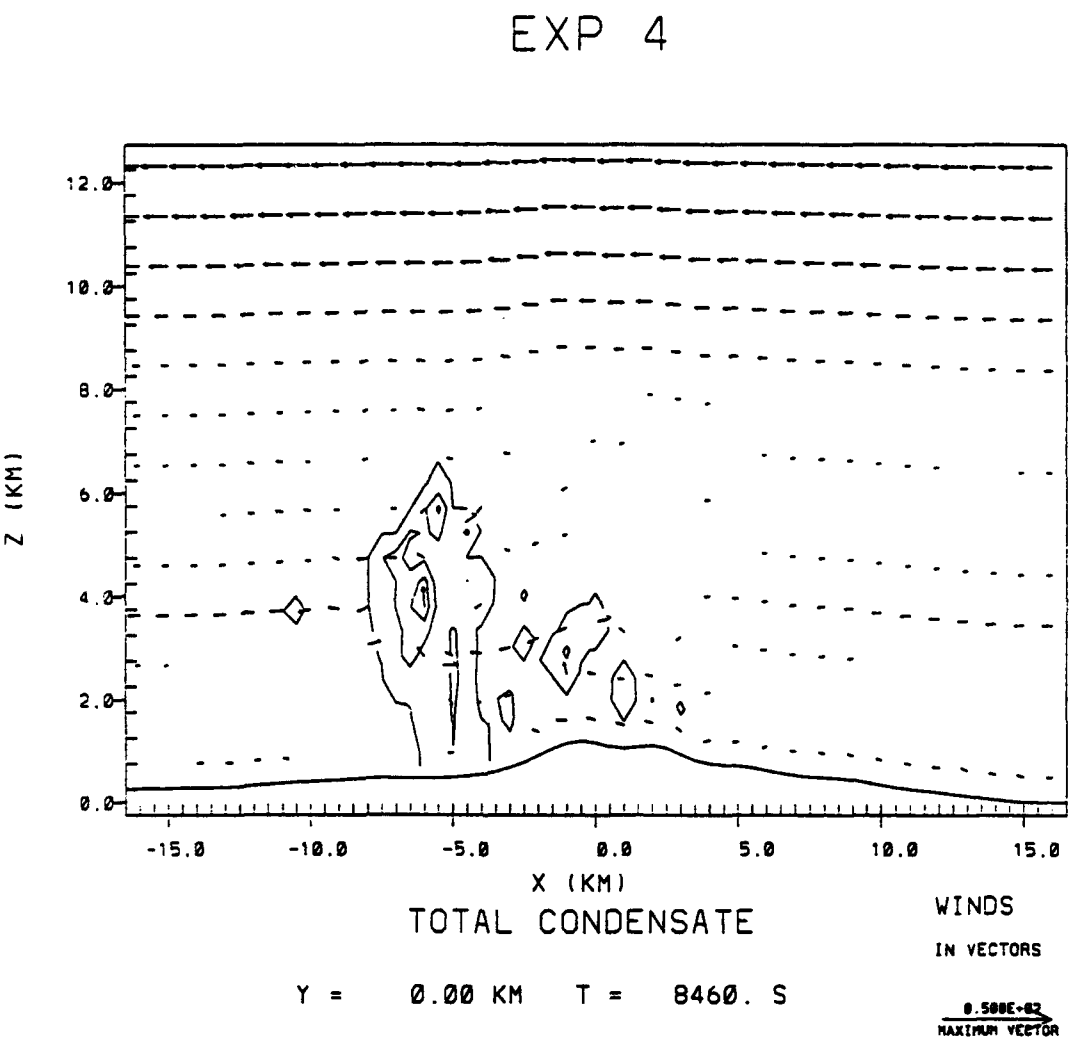

Fig. 63. Analogous to Fig. 59, east-west vertical cross-section of simulated total condensate mixing ratios overlaid with simulated wind vectors for EXP4 simulation at 8460 s. Contour label "1" represents 0.1 g kg^{-1}.

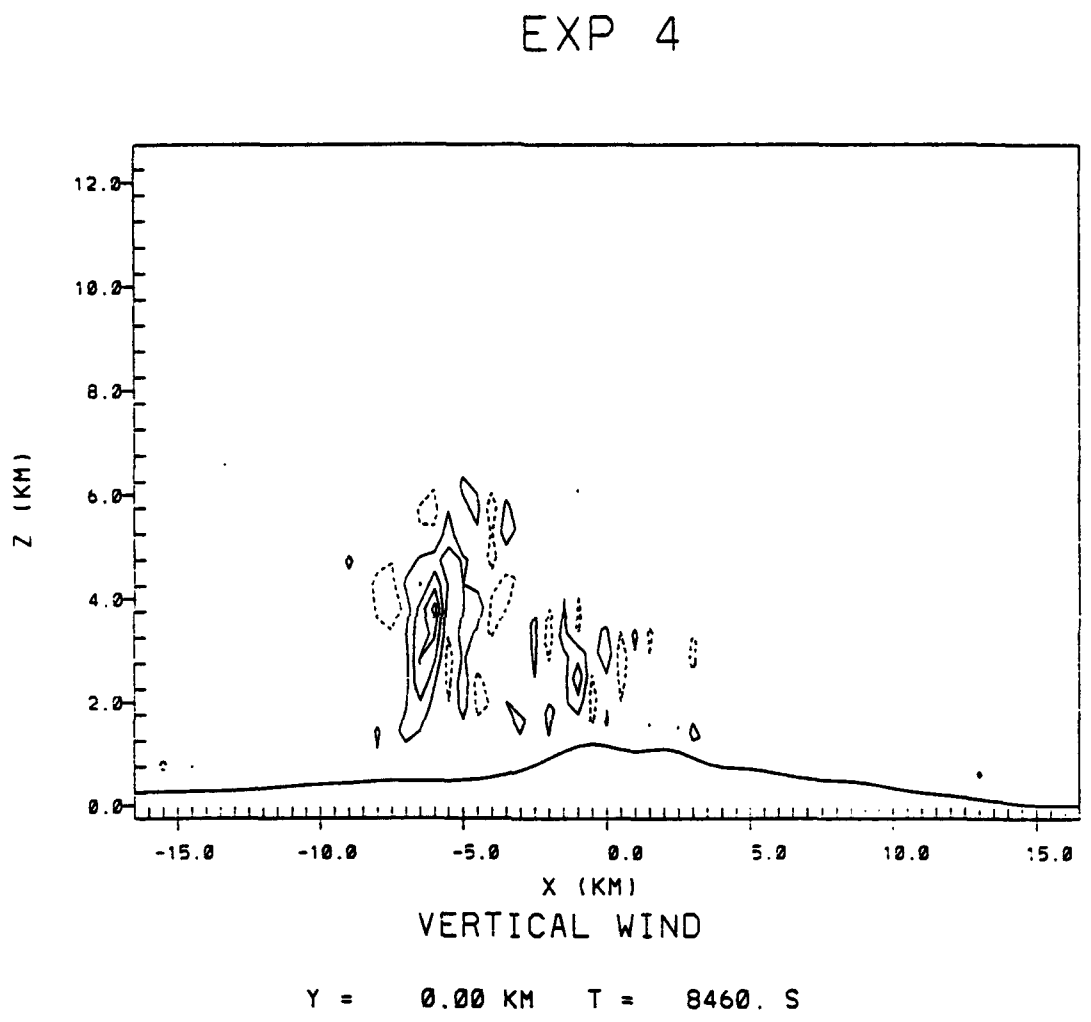

Fig. 64. Analogous to Fig. 62, east-west vertical cross-section of simulated vertical velocity for EXP4 simulation at 8460 s.

At 8820 s, the condensate from all three cells joined to form a single storm dominated by E4C1. The cell's updraft contained double maxima in both the total condensate mixing ratio field and the updraft. The maximum total condensate mixing ratio exceeded 4.0 g kg^{-1}, and the maximum updraft reached 9.2 m s^{-1}. E4C2 showed little change in strength from the previous analysis time. A strong downdraft of 5.7 m s^{-1} developed between the updrafts associated with E4C1 and E4C2. E4C3 remained at about the same strength as in the previous analysis. The rain shaft associated with E4C1 and E4C2 widened to 3.5 km with a split between E4C1 and E4C2. The maximum rain mixing ratio decreased to 3.7 g kg^{-1}. The maximum cloud height increased at this time to 7.0 km.

By 9000 s, E4C1 still dominated the storm with a maximum total condensate mixing ratio of 4.9 g kg^{-1} and a maximum updraft of 10.2 m s^{-1}. Both of these maxima were located very near the top of the storm at elevations above 6.0 km. E4C2 became nearly absorbed in E4C1 and E4C3 at this time. E4C3 contained two updrafts with the strongest exceeding 4.5 m s^{-1}. The maximum total condensate mixing ratio in E4C3 exceeded 4.0 g kg^{-1}. Rain fell out of all three cells at this time, with a maximum rain mixing ratio of 3.1 g kg^{-1}. The maximum cloud height reached 7.5 km. Figures 65 and 66 show analyses of total condensate mixing ratio and vertical velocity, respectively, for 9000 s.

Figures 67 and 68 show the evolution of the simulation's maximum condensate mixing ratios and upward and downward vertical velocities, respectively.

8.2.2 Comparison With Control

In general, the results of EXP4's simulation were similar to those of the control--especially given the marked difference in the microphysical parameterizations used. Prior to 7920 s, EXP4's simulation nearly reproduced exactly that seen in the control.

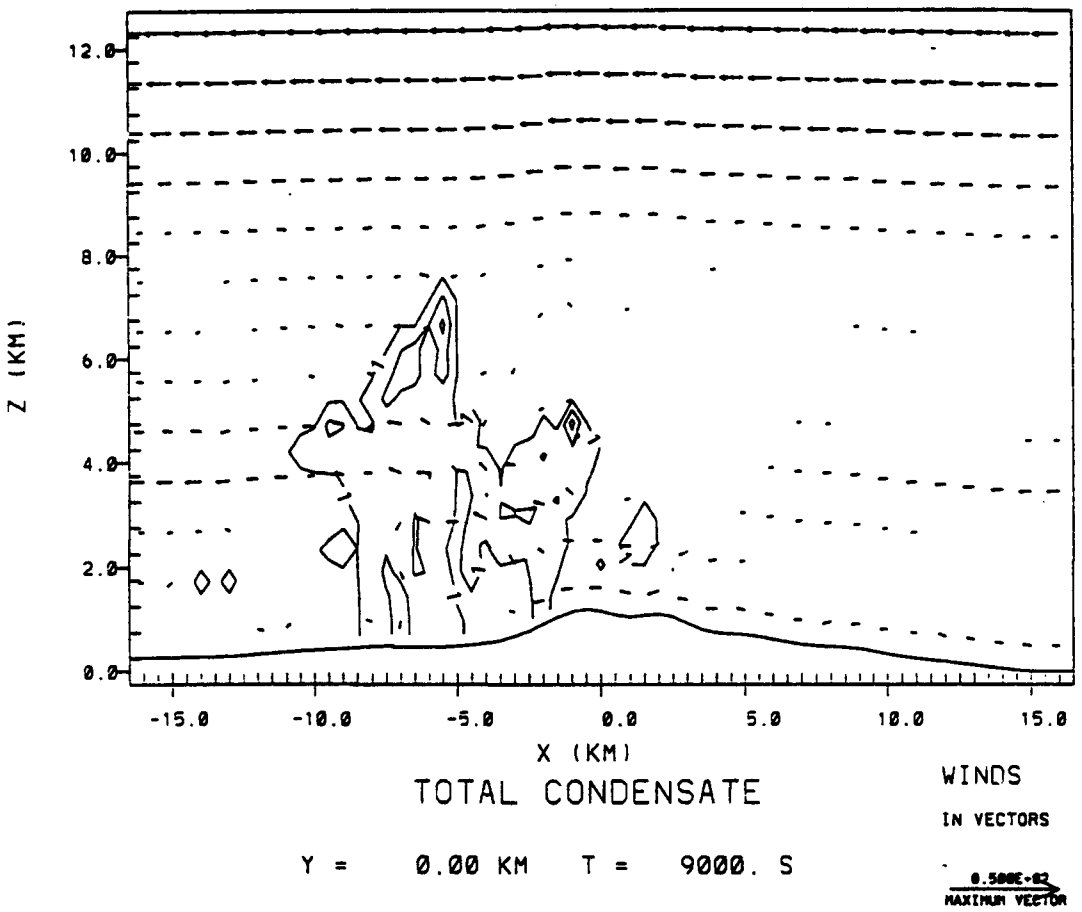

Fig. 65. Analogous to Fig. 59, east-west vertical cross-section of simulated total condensate mixing ratios overlaid with simulated wind vectors for EXP4 simulation at 9000 s. Contour label "1" represents 0.1 g kg^{-1}.

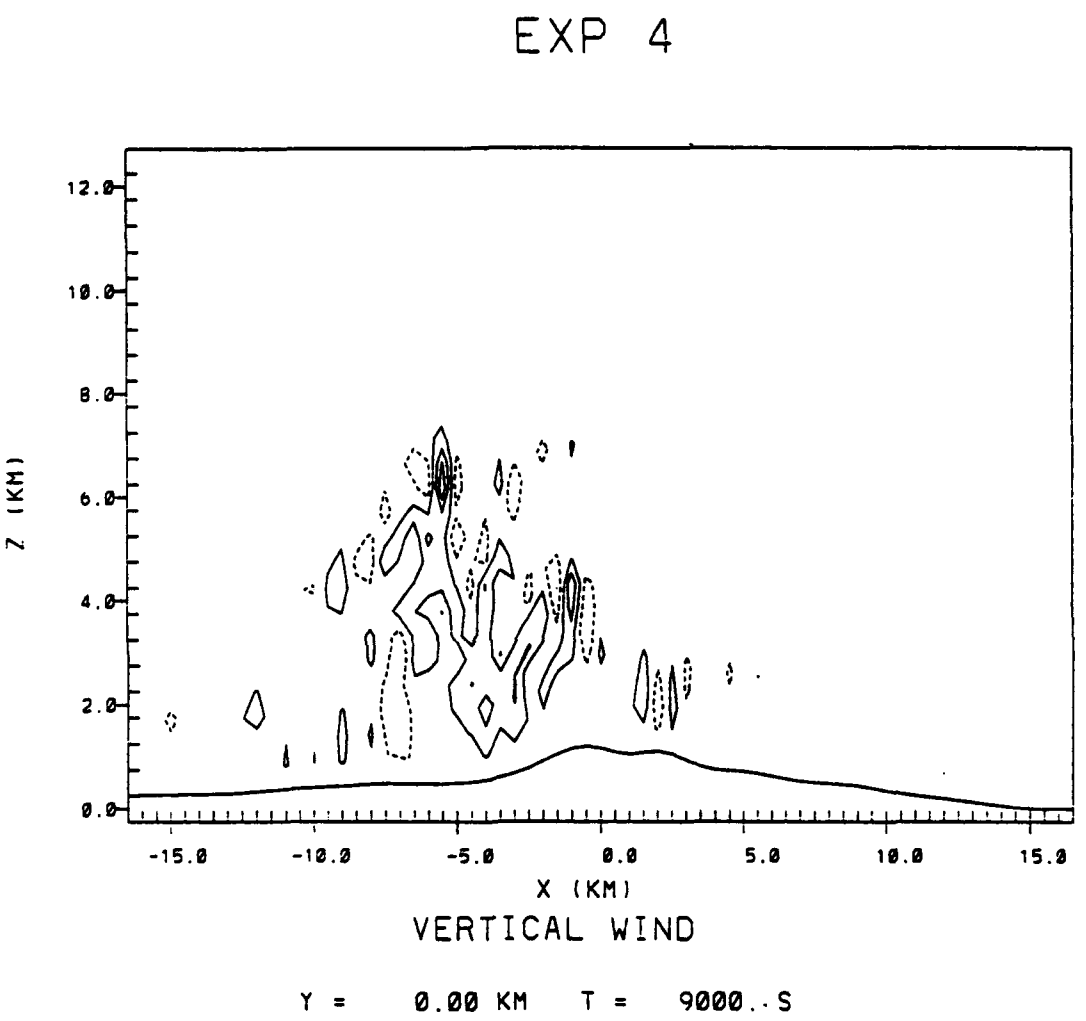

Fig. 66. Analogous to Fig. 62, east-west vertical cross-section of simulated vertical velocity for EXP4 simulation at 9000 s.

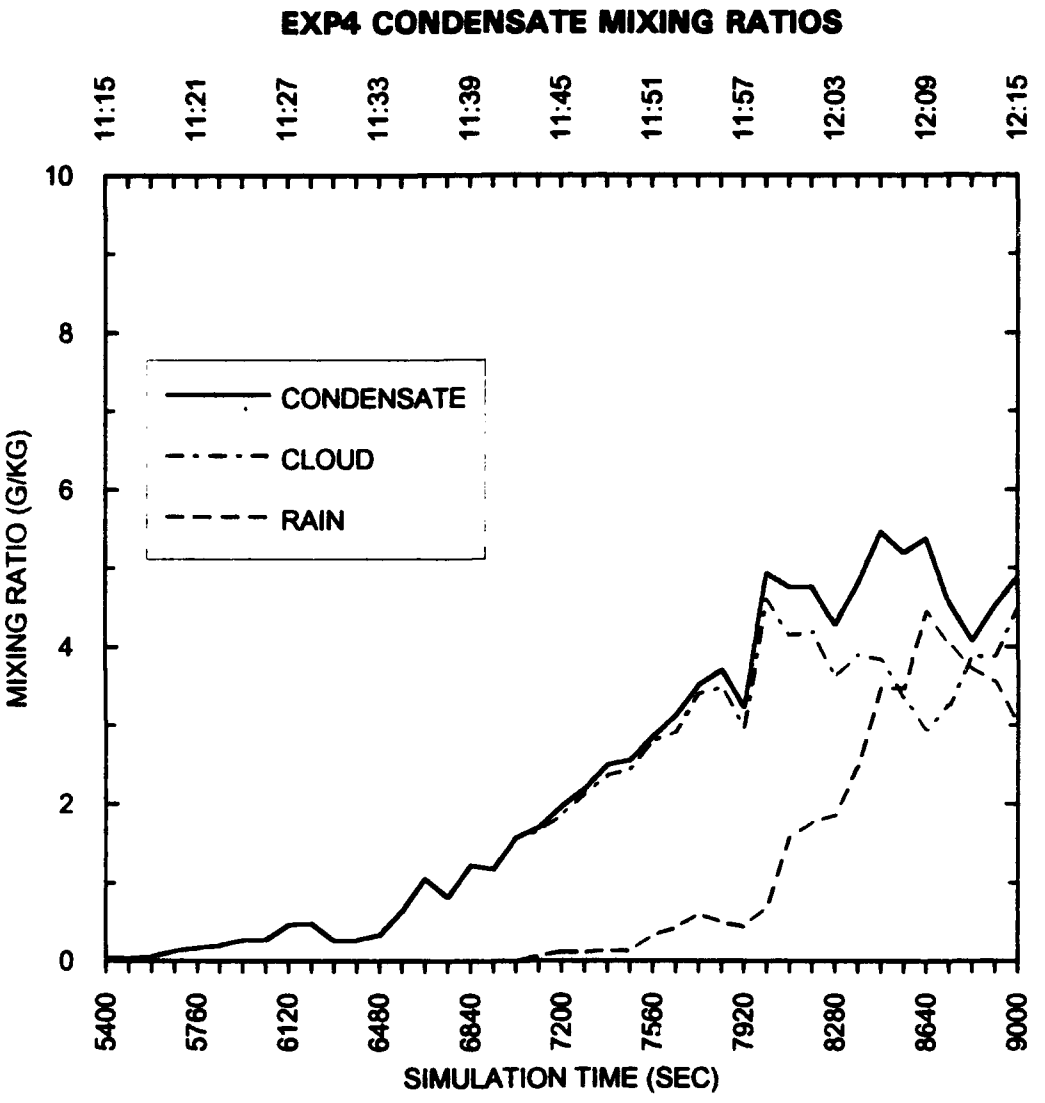

Fig. 67. Time evolution of maximum simulated condensate mixing ratios for the EXP4 simulation. Solid curve shows total condensate mixing ratios, dot-dash curve shows cloud water mixing ratios, dashed curve shows rain water mixing ratios, double dot-dash curve shows pristine ice crystal mixing ratios, shaded curve shows graupel mixing ratios, and dotted curve shows aggregated snow flake mixing ratios. Vertical axis is mixing ratio in grams per kilogram. Horizontal axis is simulation time in seconds (bottom) and in hours and seconds MST (top).

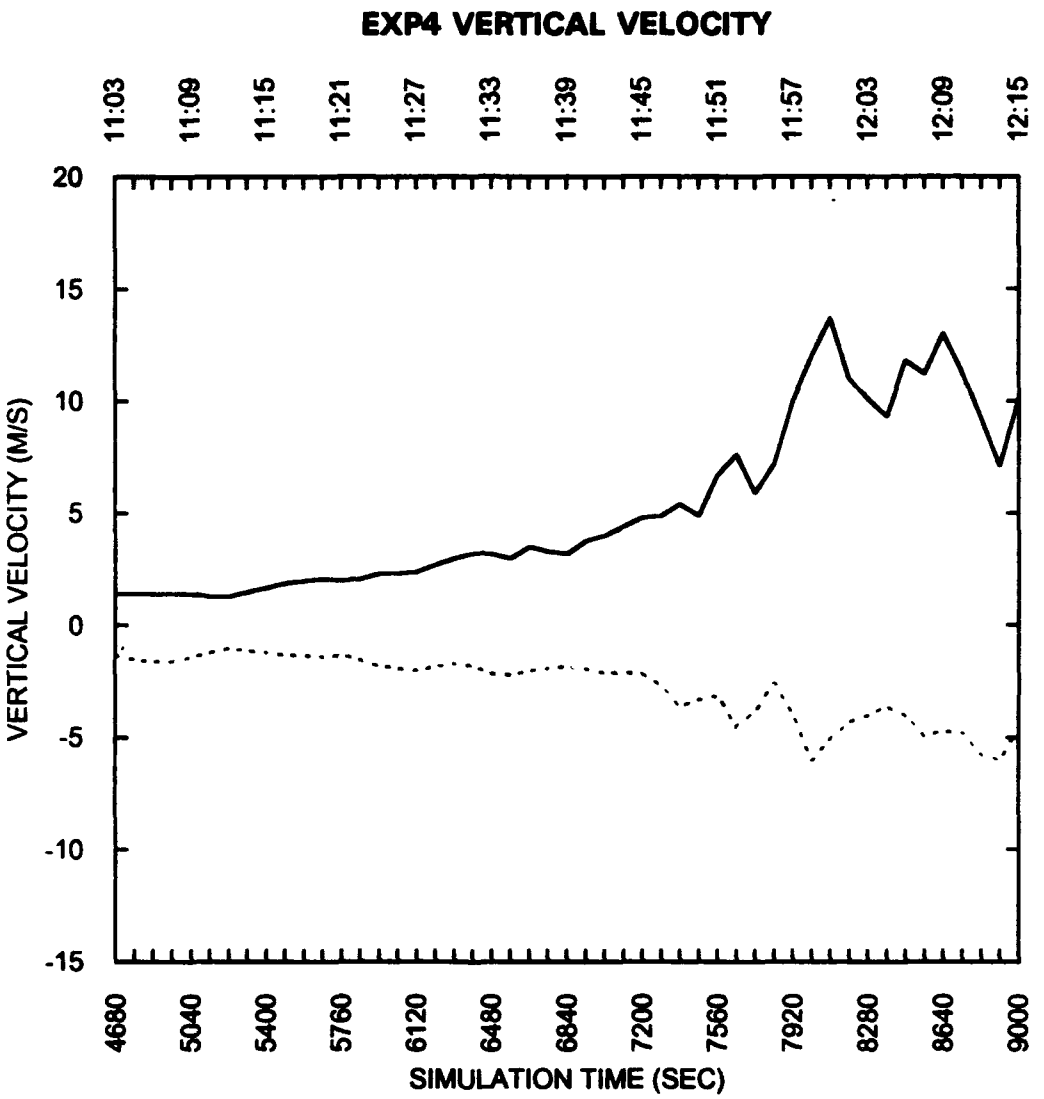

Fig. 68. Time evolution of maximum and minimum simulated vertical velocities for the EXP4 simulation. Solid curve shows maximum upward vertical velocities (positive w). Dashed curve shows maximum downward vertical velocities (negative w). Vertical axis is vertical velocity in m s^{-1}. Horizontal axis is simulation time in seconds (bottom) and in hours and seconds MST (top).

After that time, the two simulations began to differ substantially, but they still generally corresponded quite well. A comparison of EXP4's condensate mixing ratio evolution (Fig. 67) with the control's evolution (Fig. 49) shows nearly perfect agreement in the timing of total condensate mixing ratio maxima and minima. Naturally, the values do not agree quantitatively, but the degree of qualitative agreement is remarkable. A similar comparison of the vertical velocity evolution (Fig. 68 for EXP4 and Fig. 43 for the control) shows good agreement prior to about 8280 s. After that time, the correspondence between the two simulations deteriorates with the control's maximum updrafts and downdrafts exceeding the strength seen in EXP4.

A more detailed comparison of the simulations shows similar results. Prior to 7920 s, very little, if any, distinction could be made between the two simulations. After that time, several of EXP4's storm characteristics were weaker or less significant than the control's. First, EXP4's maximum cloud heights evolved from nearly the same height as the control's at 7920 s, to 1.0 km lower than the control's at 8460 s, to 2.5 km lower at 8640 s, to 3.5 km lower at 8820 s, and finally to 4.5 km lower than the control's at 9000 s. During this time period, the ice phases dominated the development of the storm in the control. In EXP4, the ice phases were not permitted and thus the development was retarded significantly. Second, the maximum updrafts in EXP4 were sometimes 5.0 to 7.0 m s^{-1} weaker than in the control. Similarly, EXP4's total condensate mixing ratios in many cases were up to 2.0 g kg^{-1} less than in the control. Again, most of these differences can be attributed to the lack of the ice phases in the simulation. The latent heat release associated with the ice phases accounted for the most rapid development of the cells in the control during this time period. Throughout the precipitating phase of EXP4's simulation, the rain shafts were always narrower and weaker than those observed in the control. This, too, can

be attributed to the lack of the ice phases. The rain shafts in the control were very strongly influenced by the presence of graupel shafts aloft above the rain shafts. Without the graupel in EXP4, the rain production process did not proceed as efficiently as it did in the control. EXP4's simulated cells did not exhibit the strong total condensate mixing ratio maxima found near the top of the control simulation's cells. The maxima in the control were a direct result of maxima in the ice phases' mixing ratios, and thus were not a factor in EXP4's simulation. Finally, both E4C2 and E4C3 were noticeably less significant in EXP4 than their counterparts in the control simulation.

Chapter 9

Sensitivity To Initial Moisture Profile

The final experiment conducted for this study investigated the sensitivity of the simulated storm to the initial base-state moisture profile. Section 9.1 provides a brief description of the modified moisture profile used to initialize EXP5. Section 9.2 briefly describes the evolution of EXP5's simulated storm, and Section 9.3 compares EXP5's results with those of the control.

9.1 Experiment 5 - Moistened Lower Levels Case

EXP5 was designed to test the sensitivity of the simulated storm development to the initial atmospheric moisture profile. As briefly described in Chapter 5, EXP5's initial moisture profile was constructed to produce a profile with a higher moisture content in the lower atmosphere. For this case the initial mixing ratio was increased in the lowest model levels by 0.5 g kg^{-1} over that in the control's base-state moisture profile. The amount of increase over the control was gradually reduced to zero at 720 mb. Above 720 mb, EXP5's initial moisture profile and the control's were identical. Figure 69 shows EXP5's moisture profile superimposed over the control's.

9.2 Analysis Of Simulated Storm Evolution

By 6840 s, two cells, E5C1 near x = -3.0 km and E5C2 near x = -1.0 km, had developed. E5C1 contained a maximum updraft of 5.4 m s^{-1} and a maximum total condensate mixing ratio of 2.2 g kg^{-1}. The cells' development prior to this time followed that of the control with EXP5's development occurring slightly more rapidly than the control's. For example, by 6840 s, the control's maximum updraft and total

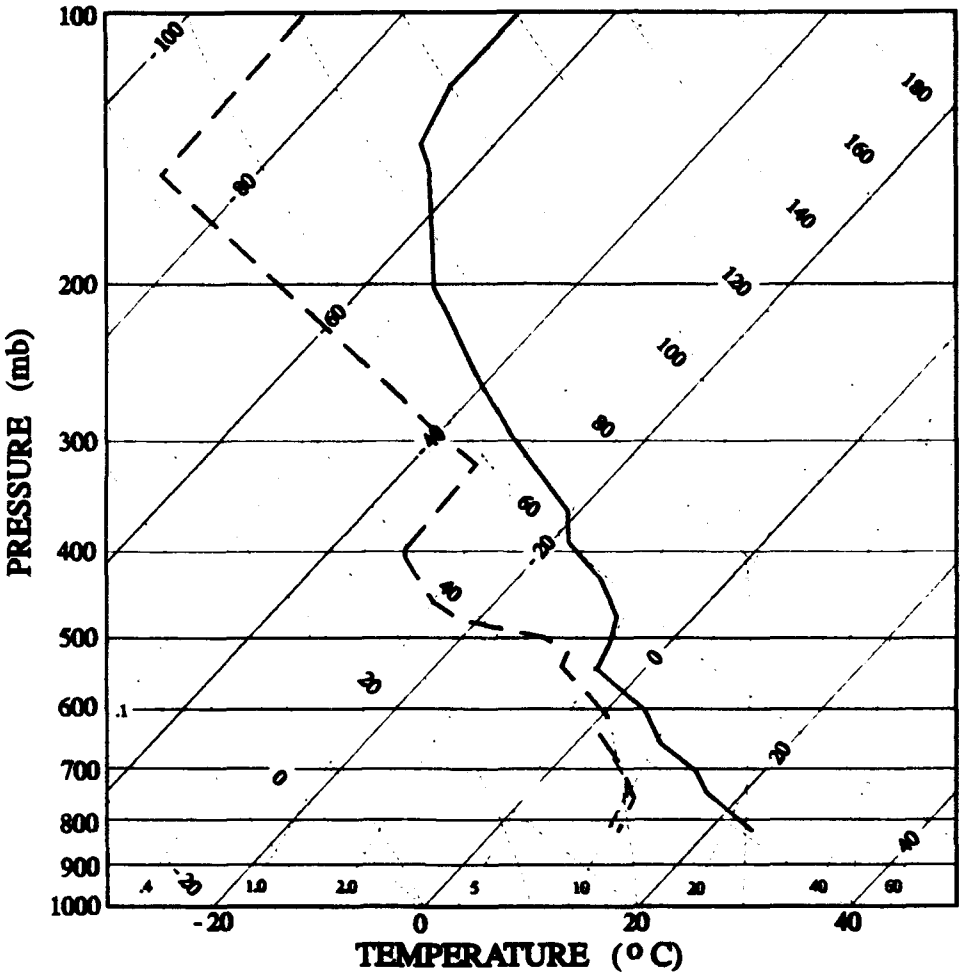

Fig. 69. Skew T, log P plot of modified base-state moisture profile used to initialize the numerical model for the EXP5 simulation. Heavy solid and dashed lines represent sensible and dewpoint temperature profiles, respectively. Light dashed line shows original base-state moisture profile for reference. Skew T, log P diagram labeled as in Fig. 2.

condensate mixing ratio reached only 3.2 m s^{-1} and 1.2 g kg^{-1}, respectively, compared with EXP5's 5.4 m s^{-1} and 2.2 g kg^{-1}. Figures 70 and 71 show analyses of total condensate mixing ratio and vertical velocity, respectively, for 6840 s.

Between 6840 and 7380 s, the storm matured significantly with E5C1 dominating the storm until 7200 s and E5C2 dominating late in the period. The cells exhibited a degree of the oscillatory development individually and between each other as noted in the observations described in Chapter 3 and described by Ziegler *et al.* (1986). E5C1 dominated the storm until 7200 s with maximum updrafts reaching 6.2 m s^{-1} at 7020 s and maximum total condensate mixing ratios reaching 2.6 g kg^{-1} at the same time. These values diminished quickly to about 1.5 m s^{-1} and less than 2.0 g kg^{-1} by 7380 s. A new updraft of about 1.5 m s^{-1} developed in association with E5C1 after 7200 s near x = -5.0 km. By 7380 s, cloud water, pristine ice crystals, rain, and graupel had developed in E5C1. As E5C1 was weakening late in the period, E5C2 strengthened significantly to contain peak updrafts of 5.5 m s^{-1} and total condensate mixing ratios of 2.4 g kg^{-1}. At 7380 s, a new cell (denoted hereafter as E5C3) developed near x = 1.0 km. Figures 72 and 73 show analyses of total condensate mixing ratio and vertical velocity, respectively, for 7380 s. During this period, two areas of low-level convergence developed: one near x = -3.0 km and the other near x = -5.0 km (Fig. 74). The convergence resulted from the interaction of wind flow patterns similar to those described in the analysis of the control simulation's evolution.

E5C3 had developed quite rapidly by 7560 s. The cell contained maximum updrafts of 10.4 m s^{-1} and a peak total condensate mixing ratio of over 2.0 g kg^{-1}. By this time, cloud water, pristine ice crystals, graupel, and rain water had developed in the cell. E5C2 remained relatively unchanged from the previous analysis time with maximum updrafts of over 4.5 m s^{-1} and maximum total condensate mixing ratios of

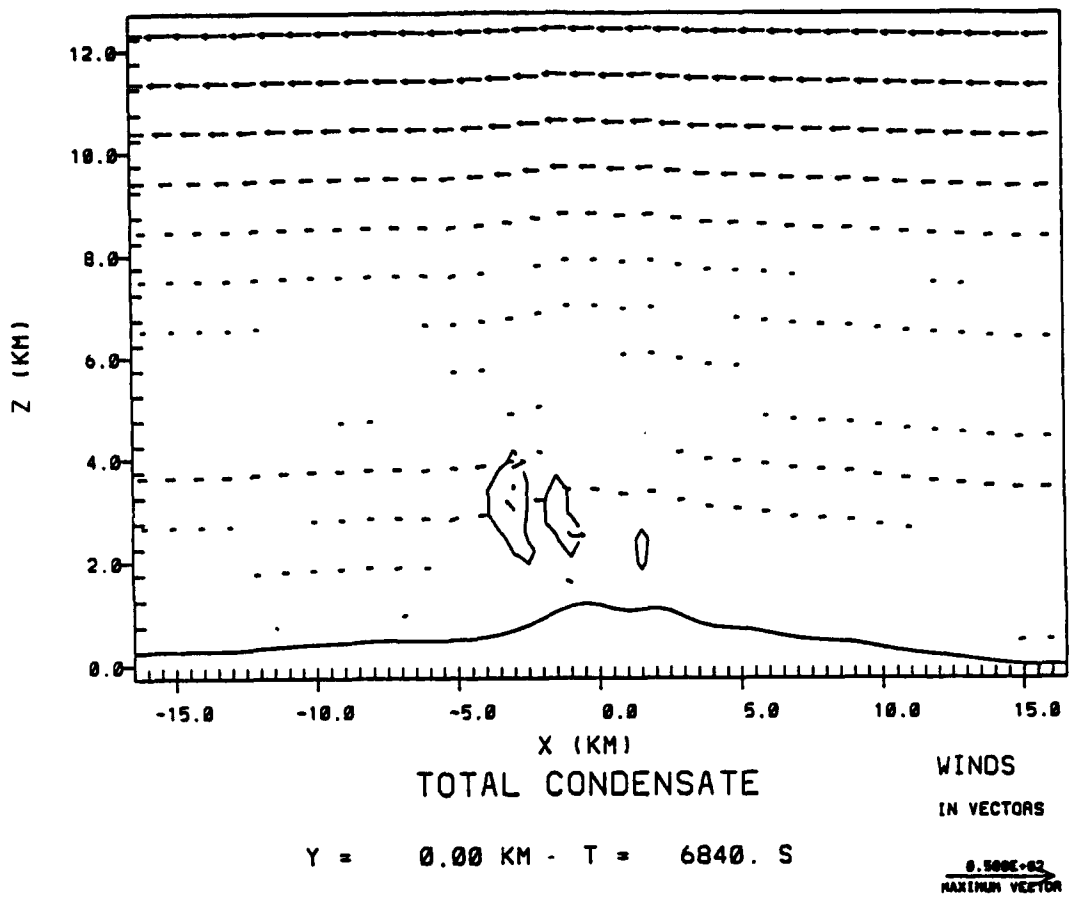

Fig. 70. East-west vertical cross-section of simulated total condensate mixing ratios overlaid with simulated wind vectors for EXP5 simulation at 6840 s. Contours are every 2.0 g kg^{-1} starting at 0.1 g kg^{-1}. Wind vector length shown in lower right-hand corner of figure equals 50 m s^{-1}. Vertical axis is labeled in kilometers above the minimum terrain elevation in the simulation grid (in this case 1.82 km) as described in the text. Horizontal axis is horizontal distance labeled in kilometers. The cross-section shown is located at y = 0.0 km and runs east-west, with the origin at Langmuir Laboratory.

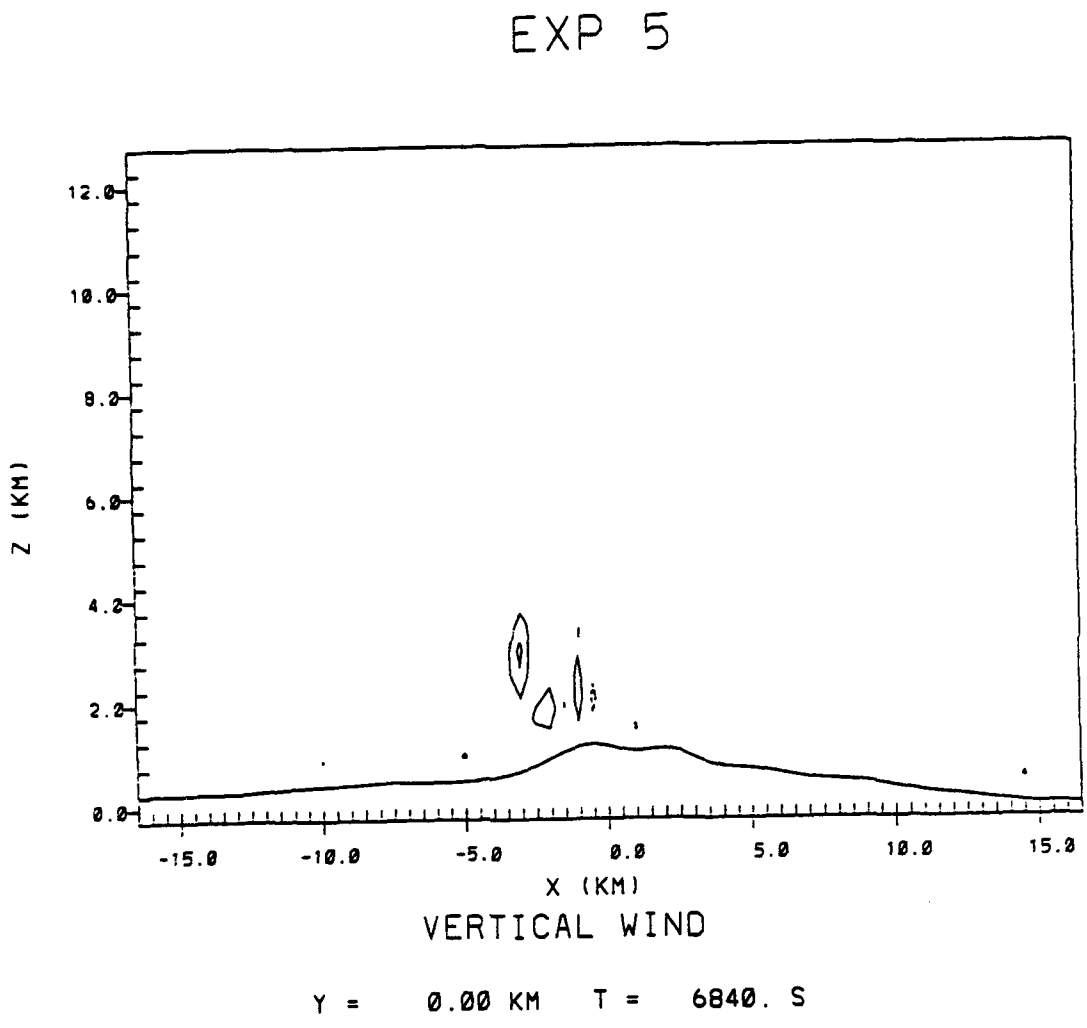

Fig. 71. East-west vertical cross-section of simulated vertical velocity contoured every 3.0 m s^{-1} starting at 1.5 m s^{-1} for EXP5 simulation at 6840 s. Solid (dashed) contours show positive (negative) vertical velocities. Axes labeled as in Fig. 70.

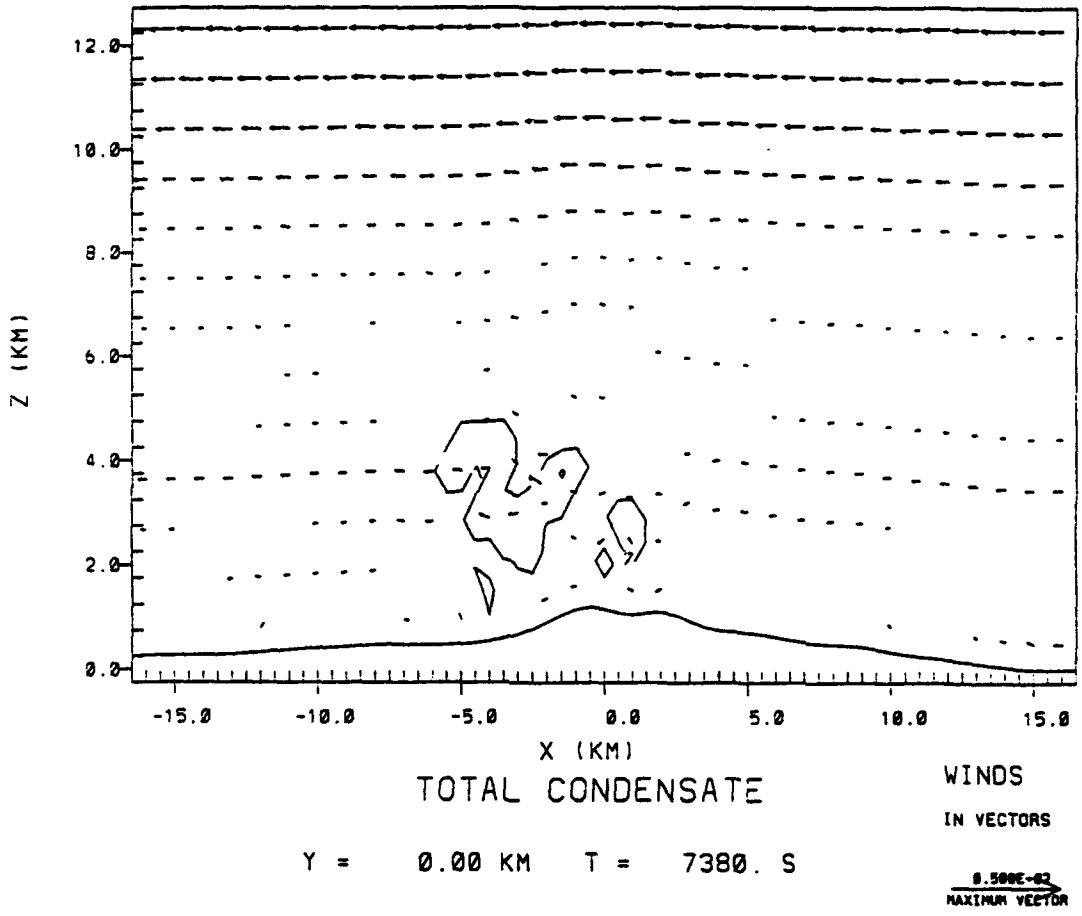

Fig. 72. Analogous to Fig. 70, east-west vertical cross-section of simulated total condensate mixing ratios overlaid with simulated wind vectors for EXP5 simulation at 7380 s. Contour label "1" represents 0.1 g kg^{-1}.

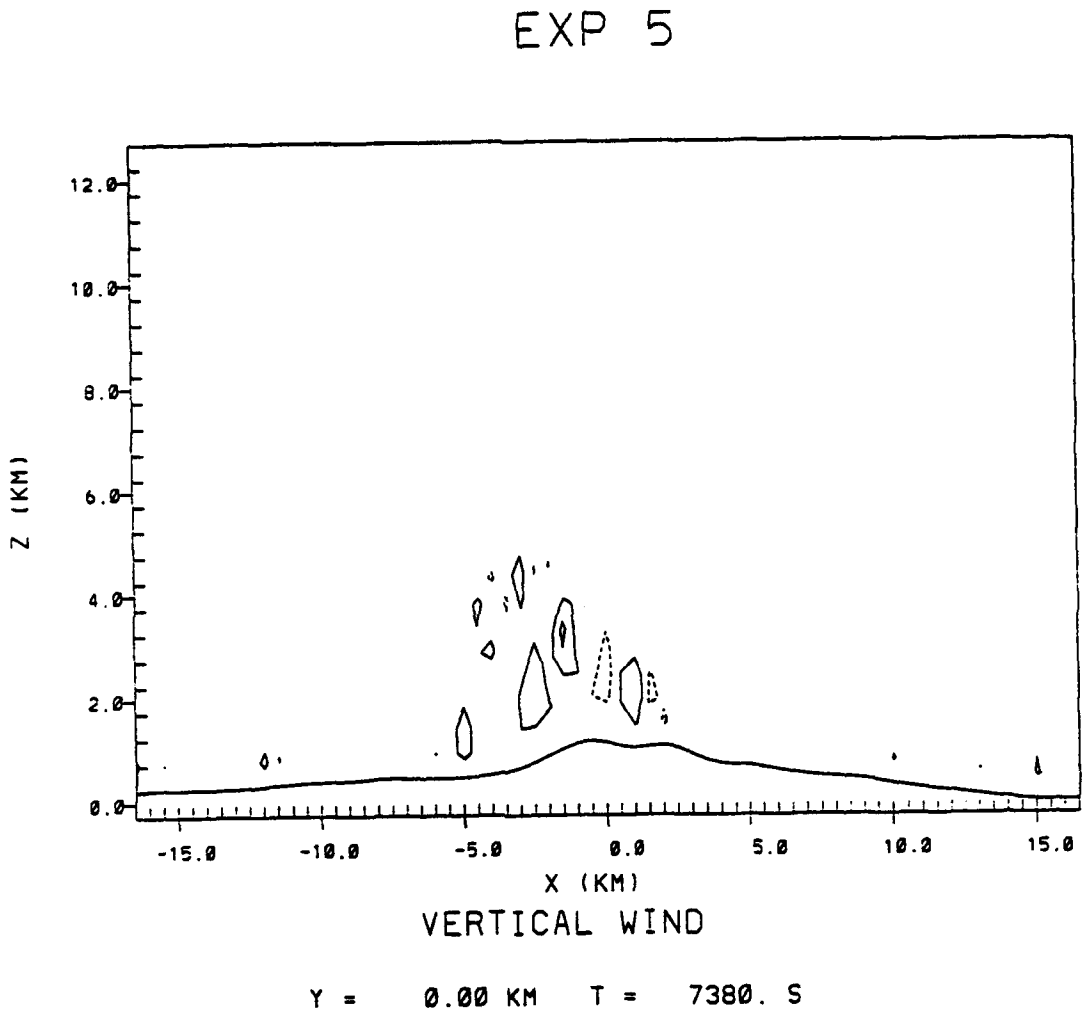

Fig. 73. Analogous to Fig. 71, east-west vertical cross-section of simulated vertical velocity for EXP5 simulation at 7380 s.

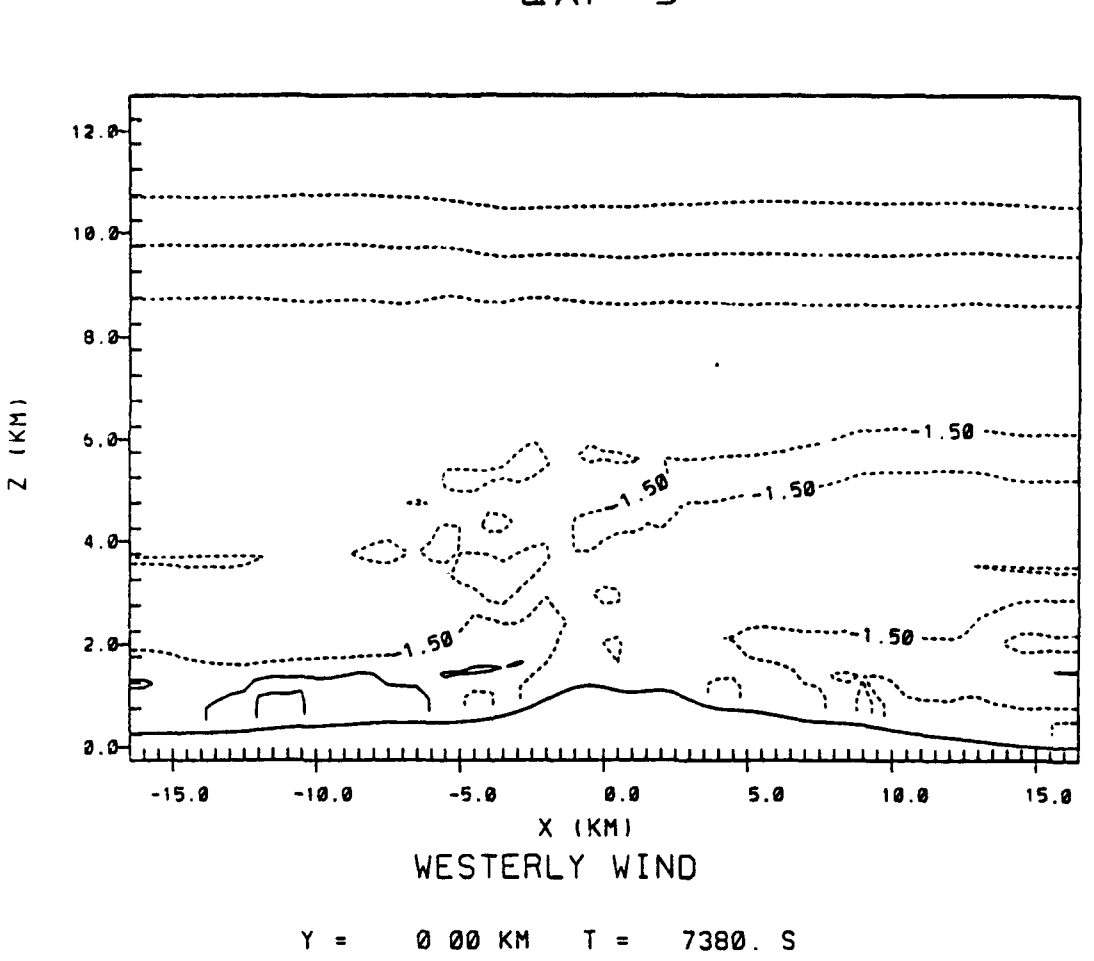

Fig. 74. East-west vertical cross-section of simulated u wind component contoured every 3.0 m s^{-1} starting at 1.5 m s^{-1} for EXP5 simulation at 7380 s. Solid (dashed) contours show westerly (easterly) winds. Axes are labeled as in Fig. 70.

3.0 g kg^{-1}. E5C1 remained weak with only very weak updrafts and maximum total condensate mixing ratios of less than 2.0 g kg^{-1}.

By 7740 s, E5C2 clearly dominated the storm with maximum updrafts of 11.8 m s^{-1} and peak total condensate mixing ratios of 4.3 g kg^{-1}. Graupel developed for the first time in E5C2 at this time. E5C2 also contained a relatively strong downdraft of 4.5 m s^{-1}. At the same time, E5C3 weakened slightly with a maximum updraft of 7.5 m s^{-1} and maximum total condensate mixing ratios of over 2.0 g kg^{-1}. This cell also contained a downdraft in excess of 4.5 m s^{-1}. E5C1 strengthened slightly to include maximum total condensate mixing ratios of over 2.0 g kg^{-1}.

At 7920 s, E5C3 dominated the storm with a maximum total condensate mixing ratio of 4.4 g kg^{-1}. The cell's updraft contained a double maxima with the upper maximum (located near 4.0 km) reaching 11.2 m s^{-1} and the lower maximum (located near 3.0 km) reaching over 4.5 m s^{-1}. The cell also contained a downdraft of 4.7 m s^{-1}. The first precipitation reached the surface at this time as a rain shaft from E5C3. E5C2 weakened from the previous analysis time as its updraft split into two maxima. The upper maximum, located near 4.0 km, exceeded 7.5 m s^{-1}, while the lower maximum, located near 3.0 km, exceeded 4.5 m s^{-1}. The cell's maximum total condensate still exceeded 2.0 g kg^{-1}. E5C1 remained very weak with updrafts still near 1.5 m s^{-1} and maximum total condensate mixing ratios dropping below 2.0 g kg^{-1}. Figures 75 and 76 show analyses of total condensate mixing ratio and vertical velocity, respectively, for 7920 s.

By 8100 s, E5C1 showed signs of reintensification while E5C3 weakened dramatically. E5C3 contained maximum updrafts of over 4.5 m s^{-1} and maximum total condensate mixing ratios of 3.9 g kg^{-1}. Rain continued to fall out of this cell. E5C2 maintained its earlier strength with a maximum updraft in excess of 4.5 m s^{-1} and

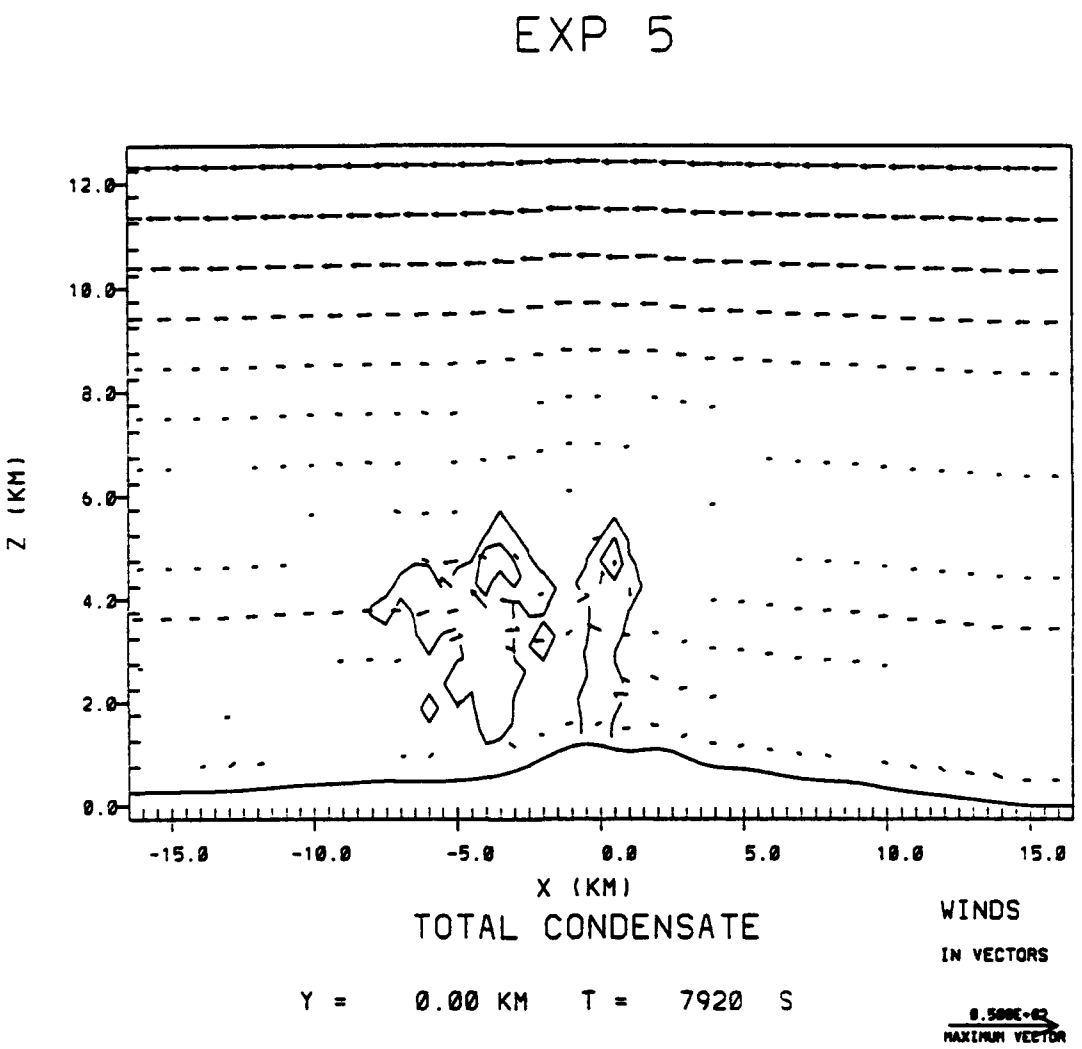

Fig. 75. East-west vertical cross-section of simulated total condensate mixing ratios overlaid with simulated wind vectors, as in Fig. 70, except for EXP5 simulation at 7920 s. Contour label "1" represents 0.1 g kg^{-1}.

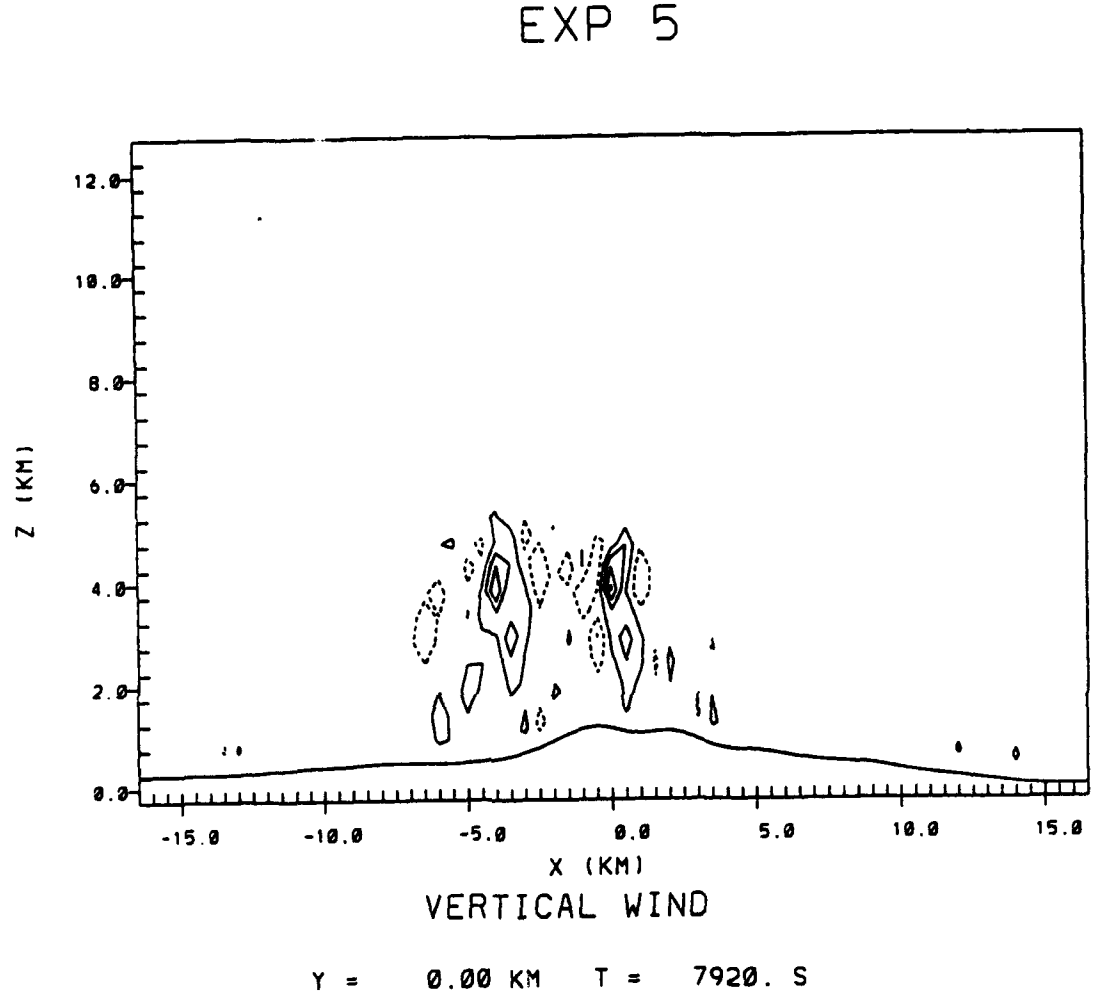

Fig. 76. East-west vertical cross-section of simulated vertical velocity as in Fig. 71. except for EXP5 simulation at 7920 s.

maximum total condensate mixing ratios of over 2.0 g kg^{-1}. The first precipitation developed out of E5C2 at this time as a rain shaft. Meanwhile, E5C1's maximum updraft increased to 7.5 m s^{-1} while its maximum total condensate mixing ratio remained below 2.0 g kg^{-1}. The maximum cloud top reached 6.0 km at this time. The ice phases began to dominate at this time as E5C2 pushed into the colder air at these higher levels. E5C1's intensification at this time resulted from the intensification of the low-level convergence near x = -5.5 km. This intensification was accompanied by a gradual weakening of the convergent area near x = -3.0 km (Fig. 77).

E5C1 continued to develop rapidly at 8280 s with maximum updrafts of 12.2 m s^{-1} and maximum total condensate mixing ratios exceeding 2.0 g kg^{-1}. The first precipitation from E5C1 developed as a rain shaft at this time. Also, the first graupel developed in the cell at this time. All of E5C1's condensate became very closely merged with that of E5C2 at this time. E5C2's strength remained nearly steady with peak updrafts in excess of 4.5 m s^{-1} and a maximum total condensate mixing ratio of 4.4 g kg^{-1}. The condensate maximum occurred near the top of the cell and consisted primarily of pristine ice crystals. The first aggregated snow flakes of the simulation developed near this maximum at this time. Rain continued to fall from E5C3, but its maximum updraft decreased to just over 1.5 m s^{-1} while its maximum total condensate mixing ratio dropped below 2.0 g kg^{-1}. At the same time, graupel from the cell nearly reached the surface and some weak development of aggregated snow flakes occurred near the top of the cell.

By 8460 s, E5C1's updraft dominated the storm with a maximum value of 14.8 m s^{-1}. The cell's maximum total condensate mixing ratio continued to remain above 2.0 g kg^{-1}. E5C2 contained a double maxima updraft with the upper maximum exceeding 7.5 m s^{-1} and the lower maximum exceeding 4.5 m s^{-1}. The cell's maximum

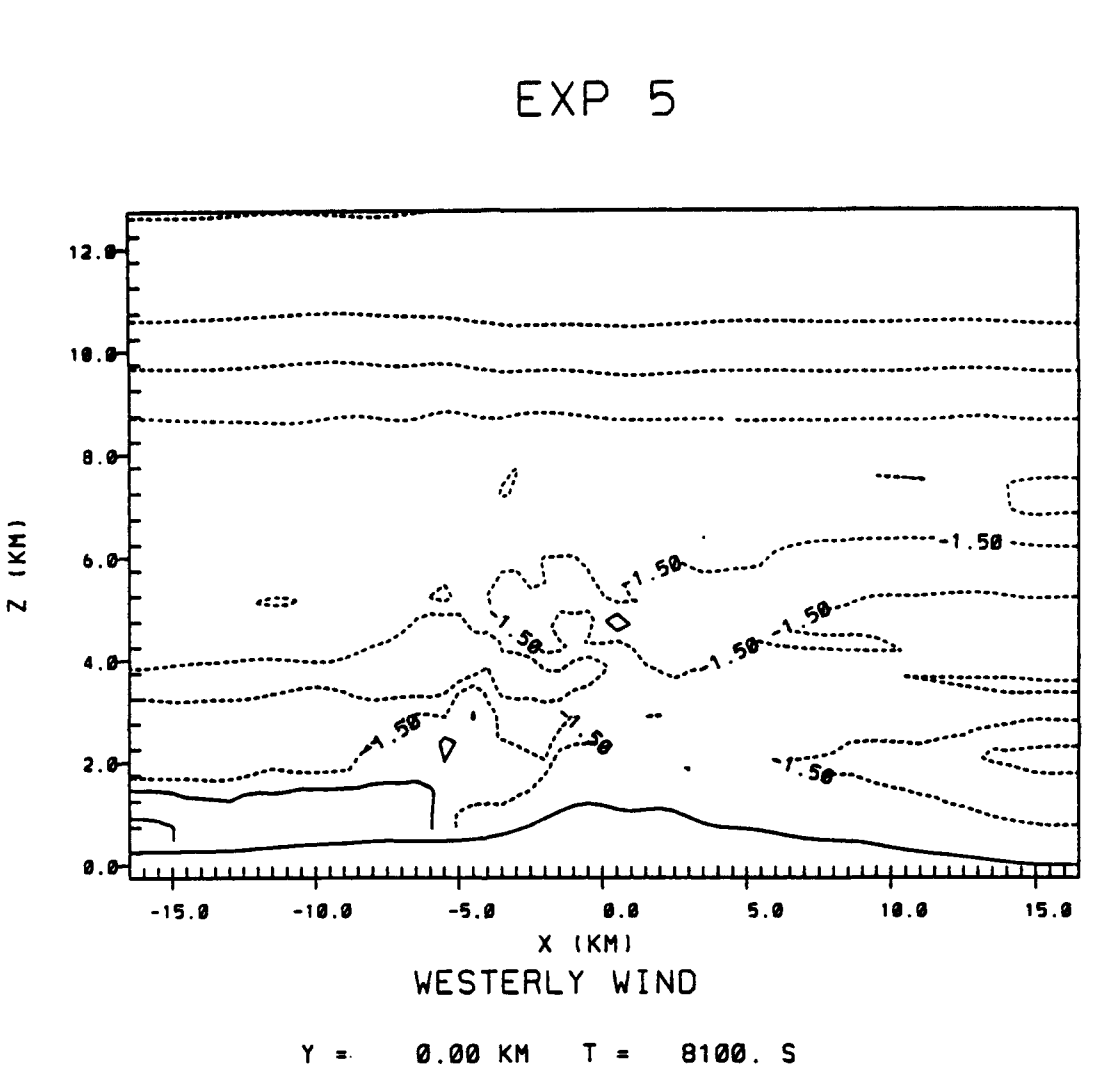

Fig. 77. East-west vertical cross-section of simulated u wind component as in Fig. 74 except for EXP5 simulation at 8100 s.

total condensate mixing ratio reached 5.3 g kg^{-1}. At this time, the cell contained some rain water which did not reach the surface. A relatively strong downdraft of 4.5 m s^{-1} developed between the updrafts associated with E5C1 and E5C2. E5C3 continued to dissipate with only very weak updrafts aloft and a small amount of condensate--mainly pristine ice crystals. A new cell developed at this time (denoted hereafter as E5C4) near x = 2.5 km. The new cell contained a maximum updraft of over 4.5 m s^{-1}, but maximum total condensate mixing ratios did not exceed 2.0 g kg^{-1}.

E5C1 clearly dominated the storm by 8640 s with a maximum updraft of 16.3 m s^{-1} and peak total condensate mixing ratios of 4.7 g kg^{-1}. E5C1 developed its own distinct rain shaft at this time. E5C2 continued to exhibit a double maxima updraft with the lower maximum reaching over 7.5 m s^{-1} while the upper maximum exceeded 4.5 m s^{-1}. The cell's maximum total condensate mixing ratio exceeded 4.0 g kg^{-1}. For the purposes of this discussion E5C3 had dissipated by this time. E5C4 remained at about the same strength as at the previous analysis time with maximum updrafts of over 4.5 m s^{-1} and maximum total condensate mixing ratios of less than 2.0 g kg^{-1}. Rain water developed in the cell at this time, but did not reach the surface. Figures 78 and 79 show analyses of total condensate mixing ratio and vertical velocity, respectively, for 8640 s. The horizontal wind analysis showed an area of strong upper-level divergence over the area of low-level convergence associated with E5C1.

E5C1 continued to dominate the simulation at 8820 s with a large updraft containing several maxima. The absolute maximum had decreased slightly to 12.6 m s^{-1}. The cell contained a double maxima in the total condensate mixing ratio with the upper maximum reaching 6.8 g kg^{-1} and the lower maximum reaching over 4.0 g kg^{-1}. Aggregated snow flakes developed and the graupel shaft reached the surface for the first time in E5C1 at this time. E5C2 remained at about the same strength as the pre-

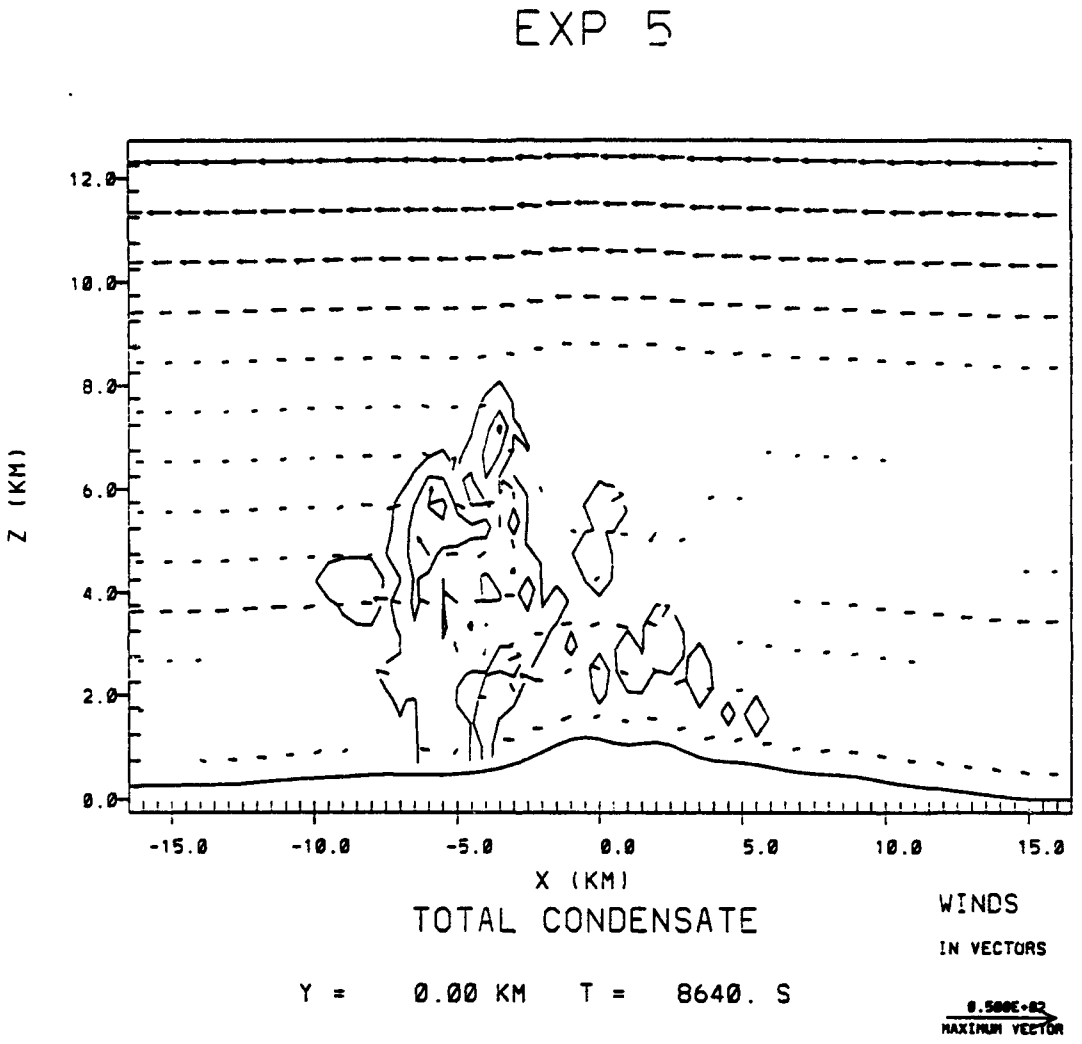

Fig. 78. Analogous to Fig. 70, east-west vertical cross-section of simulated total condensate mixing ratios overlaid with simulated wind vectors for EXP5 simulation at 8640 s. Contour label "1" represents 0.1 g kg^{-1}.

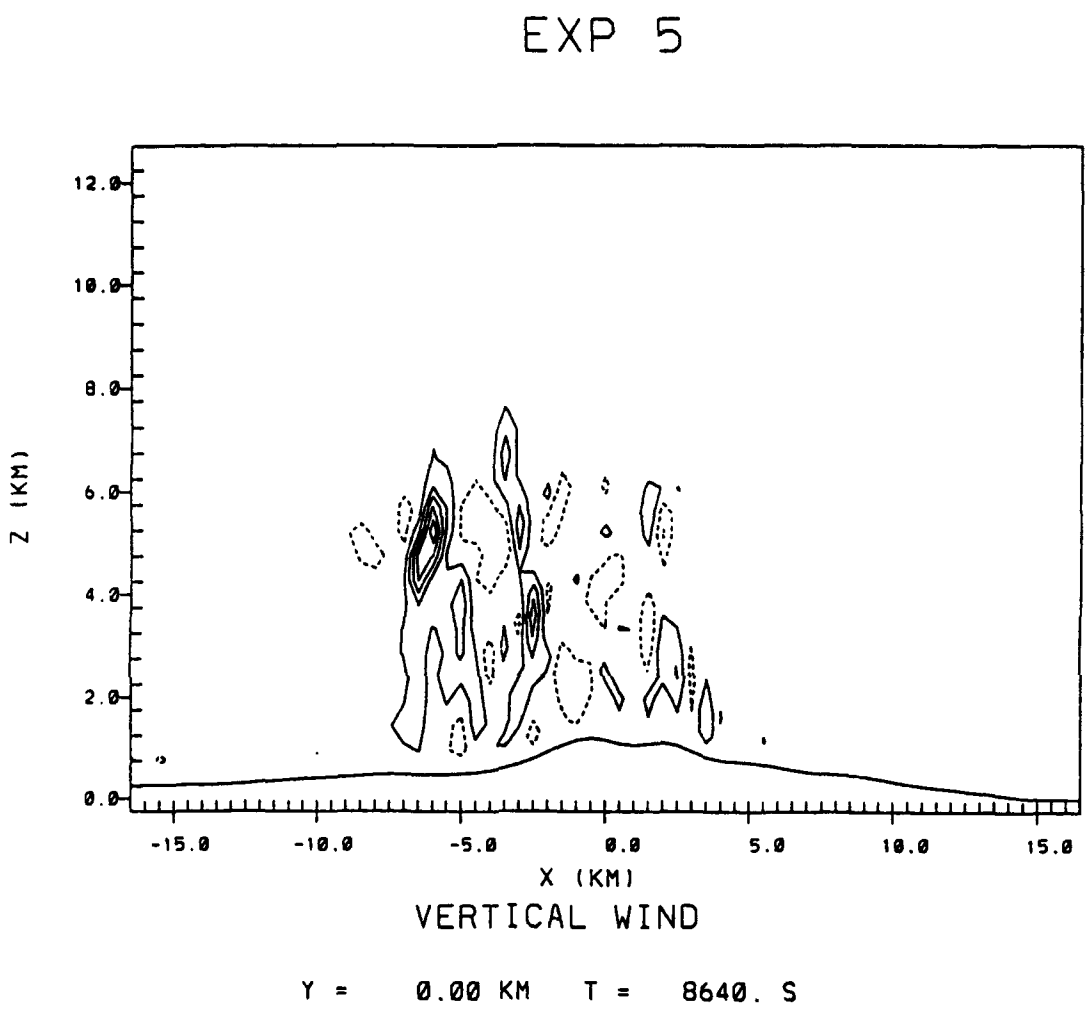

Fig. 79. Analogous to Fig. 71, east-west vertical cross-section of simulated vertical velocity for EXP5 simulation at 8640 s.

vious analysis time with peak updrafts of over 7.5 m s^{-1}. The cell contained several total condensate mixing ratio maxima with most of them over 4.0 g kg^{-1}. E5C4 continued to intensify with peak updrafts reaching over 7.5 m s^{-1} and maximum total condensate mixing ratios of over 2.0 g kg^{-1}. Pristine ice crystals and graupel developed in E5C4 at this time.

By the end of the simulation at 9000 s, E5C1 continued to dominate the storm. The cell contained several updraft maxima with the strongest peaking at 14.6 m s^{-1}. The maximum total condensate mixing ratio reached 7.1 g kg^{-1} near the top of the cell. The aggregated snow flake mixing ratio increased to over 2.0 g kg^{-1} for the first time. E5C2 weakened slightly with a maximum updraft continuing to exceed 7.5 m s^{-1}, but with the maximum total condensate mixing ratio dropping to just over 2.0 g kg^{-1}. E5C4 remained at about the same strength as before with updrafts in excess of 4.5 m s^{-1} and maximum total condensate mixing ratios of over 2.0 g kg^{-1}.

Figures 80 and 81 show the evolution of the simulation's maximum condensate mixing ratios and upward and downward vertical velocities, respectively.

9.3 Comparison With Control

Given the relatively small change in the initial moisture profile, the results of EXP5's simulation differed dramatically from those of the control. EXP5's simulation produced four cells compared to three cells in the control. The first three cells to develop in EXP5 developed in generally the same locations as their counterparts in the control. The development of these cells differed dramatically from those in the control. While the western-most cell (E5C1 in EXP5 and CC1 in the control) ultimately dominated the simulation in both cases, in EXP5, this domination was preceded by strong development of E5C2 and E5C3. In fact, the rapid development of E5C3 seemed to retard for a time the development of the two cells to its west. The

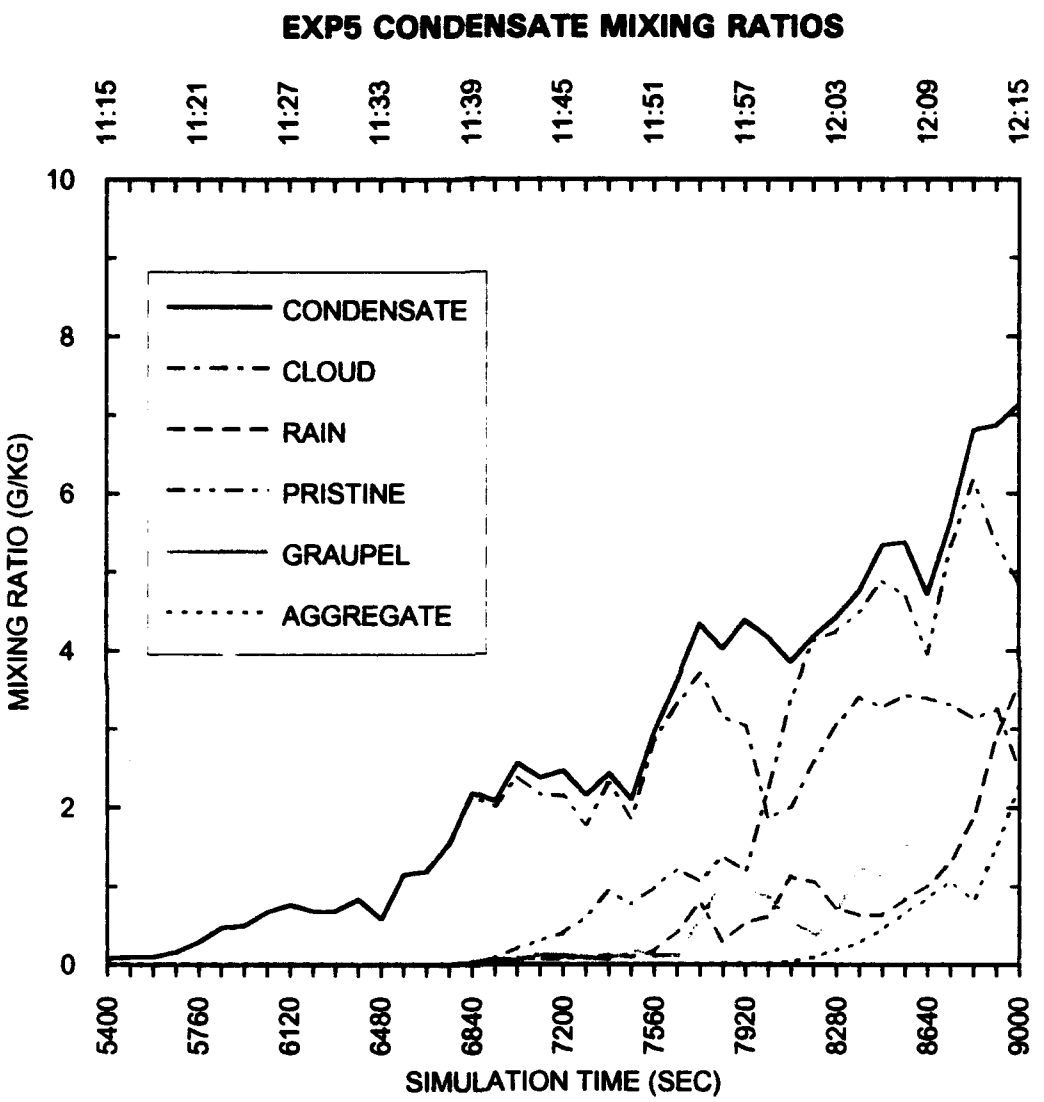

Fig. 80. Time evolution of maximum simulated condensate mixing ratios for the EXP5 simulation. Solid curve shows total condensate mixing ratios, dot-dash curve shows cloud water mixing ratios, dashed curve shows rain water mixing ratios, double dot-dash curve shows pristine ice crystal mixing ratios, shaded curve shows graupel mixing ratios, and dotted curve shows aggregated snow flake mixing ratios. Vertical axis is mixing ratio in grams per kilogram. Horizontal axis is simulation time in seconds (bottom) and in hours and seconds MST (top).

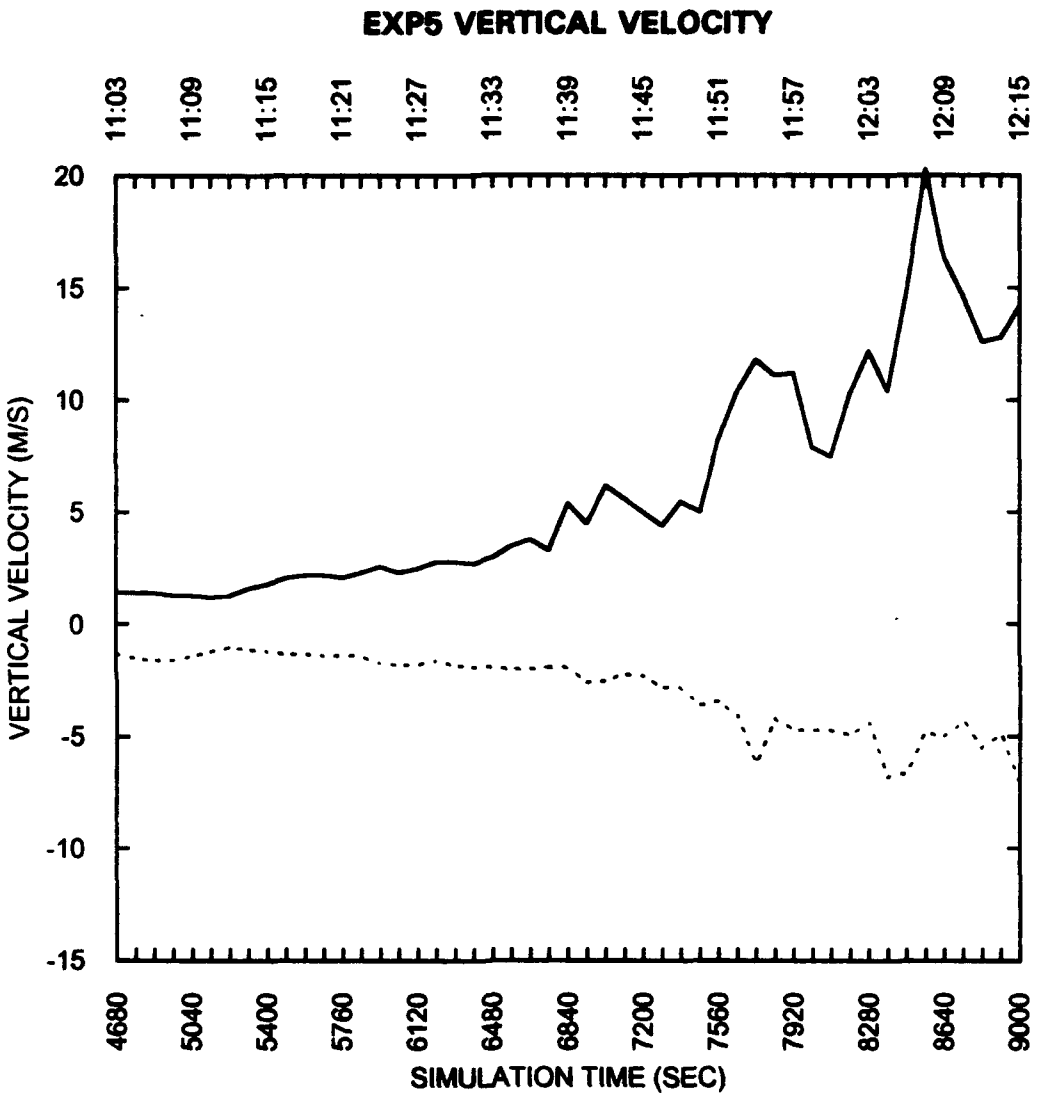

Fig. 81. Time evolution of maximum and minimum simulated vertical velocities for the EXP5 simulation. Solid curve shows maximum upward vertical velocities (positive w). Dashed curve shows maximum downward vertical velocities (negative w). Vertical axis is vertical velocity in m s^{-1}. Horizontal axis is simulation time in seconds (bottom) and in hours and seconds MST (top).

circulation and cool downdrafts associated with E5C3 inhibited the flow of warm, moist air into the cells to its west, thus slowing their development. E5C2 maintained its strength much longer into the simulation than its counterpart cell in the control.

A comparison of EXP5's maximum condensate ratio evolution (Fig. 80) with the control's evolution (Fig. 49) shows several differences. First, EXP5's development appears steadier, and did not reach its absolute maximum total condensate mixing ratio until the end of the simulation. The early development (before 8280 s) produced higher total condensate mixing ratios in EXP5 than in the control. Second, EXP5's rain water mixing ratios were slightly higher early in the simulation and then lagged those of the control by up to 1.0 g kg^{-1} later in the simulation. EXP5's peak graupel mixing ratios were higher much earlier than in the control. The pristine ice crystal mixing ratios in both cases followed about the same development pattern with a rapid increases between 7920 s and 8280 s.

A similar comparison of the vertical velocity evolution (Fig. 81 for EXP5 and Fig. 43 for the control) shows general agreement in the upward trend of updraft strength. The comparison shows little correspondence between the timing of the maxima and minima in the updrafts of both simulations. The absolute maximum for EXP5 was about 4.0 m s^{-1} greater than in the control. A comparison of the downdraft time series shows generally good agreement between both simulations.

A more detailed comparison of the simulations shows similar results. Prior to 7560 s, the simulations in both EXP5 and in the control were very similar. The differences were minor with EXP5's updrafts slightly stronger than the control's and the maximum total condensate mixing ratio in EXP5 reaching peaks about 0.5 g kg^{-1} greater than the control's between 6840 and 7560 s. Between 7560 and 7920 s, E5C3 developed very rapidly and even began producing precipitation. The corresponding

cell in the control, CC3, showed only very weak development during this period. EXP5's two western cells, E5C1 and E5C2, still were not producing precipitation by 7920 s, while the merged storm in the control was producing precipitation by this time. Between 8100 and 8460 s, as E5C3 diminished, the pattern of the merged storm in EXP5 appeared very similar to that in the control. The major difference during this period was that in EXP5, the dominant cell was E5C2, the eastern cell, while in the control, the dominant cell was CC1, the western cell. The updrafts and maximum total condensate mixing ratios for the two simulations agreed reasonably well during this period. During the period from 8640 to 9000 s, the maximum cloud tops in EXP5 were consistently lower than those in the control. The difference ranged from 0.75 km at 8640 s to 1.75 km at 8820 s. Also during this time, both E5C1 and E5C2 attained approximately the same height while in the control, CC1 grew to much higher levels than did CC2.

Chapter 10

Conclusions

This research examined the initiation, development, and maintenance of a small mountain thunderstorm using numerical simulations. The storm considered in this study occurred on 31 July 1984 and is typical of the many storms which form each summer in and around the Magdalena Mountains of central New Mexico. As a result of their frequency and relatively fixed location, the storms have been studied extensively for at least the past 15 years. The current study examines the 31 July 1984 storm using the two-dimensional, non-hydrostatic cloud model configuration of the Colorado State University Regional Atmospheric Modeling System (Tripoli and Cotton, 1982, 1986; Cotton *et al.*, 1982, 1986; Tripoli, 1986). The study also employs the multiple Doppler analyses performed by Lang (personal communication, 1992) following the technique of Ray *et al.* (1981) and described in detail by Lang (1991) as well as the three-dimensional microphysical retrieval performed by Lang (1991) for a similar storm that occurred on 3 August 1984.

The numerical model was used to isolate the processes and initial conditions most important in the initiation, development, and maintenance of these types of storms. A total of six simulations were conducted--one control and five experiments. The results of the control simulation were compared with Doppler analyses and with Lang's (1991) retrieval to assess the validity of the simulation and its usefulness in studying the storm. The experiments were conducted to test the sensitivity of the simulated storms to initial wind profile, the lack of solar heating, restriction to warm rain

processes, and the initial moisture profile. The results of these simulations were compared with the control's results.

Analyses of the Doppler radar observations and synthesized wind fields provided the basis for evaluating the accuracy of the control numerical simulation. The analyses showed that early cell development occurred directly over or slightly east of the ridge lines. Convective initiation was favored in these locations by upslope flow through convergent valleys located on the eastern and southeastern slopes of the mountain. As the storm developed, circulations from existing cells affected the initiation locations of new cells. For example, several short-lived cells developed along the outflow boundaries from older cells, and in some cases the low-level flow induced by the existing cells enhanced or created upslope and/or convergent flows which in turn helped focus new cell development.

The observed storms generally had lifetimes of 1.0 to 1.5 hr with individual cell lifetimes ranging from 20 to 60 min. Many of the cells exhibited periodic intensification and weakening with a period of 6 to 12 min. Radar returns from the strongest cells exceeded 50 dBZ several times, but maximum returns from most cells ranged from 30 to 40 dBZ. Most cells never extended higher than 10.0 km MSL, however, the strongest cells frequently extended to over 12.0 km MSL. Most cells contained single updrafts approximately 2.0 km wide with maximum vertical velocities of 12.0 m s^{-1} or less, however, the strongest updrafts reached 18.0 m s^{-1}. At least one cell contained multiple low-level updrafts which merged into a single updraft at mid-levels. Mature cells contained downdrafts with large areal coverages and maximum vertical velocities frequently exceeding 6.0 m s^{-1} with an absolute maximum of 12.0 m s^{-1}. During one cell's mature stage, the interaction between the updraft and the downdraft appeared to be symbiotic in a manner similar to that often observed in

long-lived severe storms. In this case, the precipitation and its associated downdraft were located behind and below the updraft (relative to the low-level inflow) and thus did not interfere with the inflow or the updraft.

A strong interrelationship existed between all the cells in the analysis domain. In the mature stage, the outflow from downdrafts appeared in some cases to enhance low-level convergence that either focused the development of new cells or helped sustain existing cells. In several instances the updrafts of two or more cells merged into one updraft at upper-levels. Often the updraft of a newer cell developed in the low- to mid-levels and fed into a higher-level updraft associated with an older cell. The periodic intensification noted above appeared to alternate among the cells. In other words, when one cell intensified, the others weakened slightly. Finally, the observations showed several cases where older or weaker cells were overtaken and absorbed by newer and/or stronger cells.

Comparison of the evolution of the control's simulated storm with observations and with Lang's (1991) microphysical retrieval show that the simulation accurately captured the major features observed by the radars and accurately depicted the microphysical evolution of the storm cells. In fact, given the limitations imposed by the use of a single initialization sounding and the two-dimensional nature of the simulation, the simulation performed above expectations. The simulation accurately depicted the development of a multi-cellular storm with horizontal and vertical dimensions very similar to those observed. The simulation captured low-level inflow and convergence regions as well as upper-level outflow regions. In general, the strength of the simulated cells was close to that observed by the radars. The imposed limitations did, however, introduce several discrepancies between the simulation and the observations. These included an initial delay in convective development of about

20-30 min from that observed; more rapid development than observed; slightly stronger updrafts and weaker, less-organized downdrafts than observed; a tendency for development farther west than observed; and the development of an upper-level total condensate mixing ratio maximum with no corresponding maximum in the radar reflectivity fields.

The simulated microphysical evolution compared favorably with that described by Lang (1991). In particular, the simulation accurately depicted the importance of warm rain processes early in the cell development and the subsequent rapid increase in the importance of the ice phase processes. The simulation also differed from the retrieval results in several areas. The simulated mixing ratios of ice crystals and aggregated snow flakes were much higher than those retrieved, while the simulated rain mixing ratios were much lower than those retrieved. Additionally, the maximum simulated rain mixing ratio occurred after the graupel maximum, while in the retrieval, the rain maximum occurred first.

The first two experiments tested the sensitivity of the simulated storm to the initial wind profile. The first experiment, EXP1, used an initial wind profile consisting of calm winds throughout the depth of the atmosphere. Comparison of the results of this simulation with those of the control shows that the initial wind profile plays an important role in the initiation and evolution of the simulated storms. The simulated cells in EXP1 developed directly over the ridge lines instead of to the west of the ridges as in the control. The location of cell development in EXP1 is more consistent with the observed cell development than is the control. EXP1's storm cells developed earlier, but grew at a slower, steadier pace than the control's. EXP1's initially calm winds limited the turbulent transfer of heat away from the surface, allowing maximum solar heating and rapid convective development. The control's more rapid growth may be

attributed to a relatively strong flow at mid- to upper-levels which served as an "exhaust mechanism" for the developing cells. EXP1's storm contained two cells of nearly equal strength and height through most of the development period. The reason for this difference from the control was not clear. Finally, EXP1's microphysical and vertical velocity evolution showed a much greater variability than that seen in the control.

The results of EXP1 showed that the initial wind profile strongly influences the rate of development of all cells and may even inhibit the development of some cells. The wind profile also exerts influence over the microphysical evolution and vertical velocity evolution of the storm. Finally, the initial wind profile plays a significant role in the convective initiation location.

The second experiment, EXP2, was initialized with a wind profile containing wind speeds 50% of those in the control. This simulation developed serious boundary condition instabilities which rendered the simulation useless for the purposes of this study.

The third experiment, EXP3, was conducted with the model's short-wave radiation package deactivated to test the effect on the simulated storm of a "no sun" scenario. In this simulation, very small, non-convective clouds form at nearly the same locations as the initial clouds in the control--slightly west of the ridge. A weak, but steady, updraft supported the clouds. The updraft developed near a nearly stationary area of low-level convergence which resulted from interaction of the predominantly easterly flow with a weak westerly flow near the surface. The westerly flow developed as a result of a dynamically induced mountain wave circulation on the lee side of the mountain. The results of this simulation show that solar heating plays the most important role in the development of these mountain thunderstorms. The results of

this experiment combined with those of EXP1 also show that the environmental wind field plays a crucial role in determining the convective initiation locations.

The fourth experiment, EXP4, tested the sensitivity of the simulated storm to a restriction to warm rain microphysical processes. In this experiment all the model's ice phase microphysical parameterizations were deactivated. The results from early in this simulation agreed very well with those of the control. Later in the simulation EXP4's results showed the simulated storm contained weaker updrafts and lower total condensate mixing ratios. Additionally, the cells did not extend as high as those in the control. EXP4's rain shafts were much weaker than in the control, and the total condensate mixing ratio maxima noted near the cell tops in the control were much weaker in EXP4. The good early agreement between the results of this experiment and those of the control confirm the importance of warm rain processes in the storm's early development. The growing differences between the two simulations show that as the storm matured, the ice phases became increasingly important to the evolution of the storm's development. Indeed, the absence of the ice phase processes and their associated latent heat release processes in EXP4 prevented the storm from reaching the strengths achieved in the control. The lack of the efficient precipitation-producing mechanisms associated with the ice phases prevented the rain shafts in EXP4 from reaching the strengths achieved in the control. This experiment demonstrated the importance of the ice phases in the development of these mountain storms--particularly in their middle to late stages of development.

The final experiment, EXP5, tested the sensitivity of the simulated storms to the initial base-state moisture profile. The initial moisture profile in this case was moistened by up to 0.5 g kg^{-1} in the lowest 1.0 km. This simulated storm generally followed that of the control, however, one of the very minor cells in the control

dominated EXP5's simulation for a time. In general EXP5's simulated storm developed at a steadier pace than the control and eventually contained stronger updrafts and higher graupel mixing ratios than the control. EXP5's cells did not reach the same heights as the control's, and as in EXP1, two cells developed to nearly the same strength. This experiment clearly shows the importance of low-level moisture to the evolution of these mountain storms. In particular, the moisture profile seemed to influence the ability of some cells to develop beyond cumulus stages. Additional low-level moisture contributes to stronger updrafts and slightly higher condensate mixing ratios, but interestingly does not increase the height of the cells. The lower cloud heights may be attributed to the increase in the number of larger cells. The increased competition among the larger cells may prevent any of them from reaching the heights seen in the control.

In summary, the results of the numerical simulations showed the following conditions and processes to be most important (in descending order) to the development and maintenance of the mountain storms under study here: solar heating, ice phase microphysical processes, environmental wind profile, and low-level moisture profile. The environmental wind profile was the single most important factor in the convective initiation location.

The most obvious limitation of the simulations conducted for this study was their two-dimensional nature. This limitation prevented a detailed quantitative analysis of the validity of the control simulation compared with the Doppler analyses. It also prevented the simulation from capturing the channelling of the wind flow up the various valleys in the Magdalena Mountains. The observations demonstrate the importance of this phenomenon in focusing the convective initiation and in contributing to the maintenance of the storm development.

Future studies of this nature should attempt to overcome these limitations by employing fully three-dimensional simulations. The three-dimensional simulations should also be conducted with larger domains so as to further minimize the boundary condition effects on the areas of interest such as those noted in EXP2. Future studies should also attempt to employ higher resolution grid systems in both the horizontal and vertical directions. A higher resolution grid system will naturally require a higher resolution input terrain field. Such high resolution grids will minimize the need for extensive parameterizations of processes so important to the development of these small storms.

Comparison of numerical simulation results with Doppler analyses would be markedly simplified with the employment of a technique to synthesize radar reflectivities based on the simulated microphysical storm structure. Finally, the accuracy of three-dimensional simulations could be improved with improved initial conditions. This study used a single profile to initialize the simulation. A complex four-dimensional data assimilation system using all available data including Doppler radar observations and perhaps retrieved microphysical parameters could provide the model with a significantly more realistic representation of the base-state atmosphere. With further model developments, such high-quality analyses could provide information required to "nudge" the simulation as it is progressing toward a more realistic solution.

REFERENCES

Anderson, C.E., 1960: A study of the pulsating growth of cumulus clouds. *Geophysical Research Papers*, No. 72, Air Force Cambridge Research Laboratories, 136 pp.

Bader, D.C. and T.B. McKee, 1983: Dynamical model simulation of the morning boundary layer development in deep mountain valleys. *J. Clim. Appl. Meteor.*, **22**, 341-351.

Bader, D.C. and T.B. McKee, 1985: Effects of shear, stability and valley characteristics on the destruction of temperature inversions. *J. Clim. Appl. Meteor.*, **24**, 822-832.

Bader, D.C., T.B. McKee, and G.J. Tripoli, 1987: Mesoscale boundary layer evolution over complex terrain. Part I: Numerical simulation of the diurnal cycle. *J. Atmos. Sci.*, **44**, 2823-2838.

Banta, R.M., 1983: A boundary-layer-scale model of mountain upslope flow. *Preprints*, Sixth Conference on Numerical Weather Prediction, Omaha, American Meteorological Society, Boston, 328-334.

Banta, R.M., 1984: Daytime boundary-layer evolution over mountainous terrain. Part I: Observation of the dry circulations. *Mon. Wea. Rev.*, **112**, 340-356.

Banta, R.M., 1986: Daytime boundary-layer evolution over mountainous terrain. Part II: Numerical studies of upslope flow duration. *Mon. Wea. Rev.*, **114**, 1112-1130.

Banta, R.M. and C.B. Schaaf, 1987: Thunderstorm genesis zones in the Colorado Rocky Mountains as determined by traceback of geosynchronous satellite images. *Mon. Wea. Rev.*, **115**, 463-476.

Barker, C.L. and R.M. Banta, 1985: Preferred regions of thunderstorm initiation over the Colorado Rockies. *Preprints*, 14th Conference on Severe Local Storms, Indianapolis, Indiana, American Meteorological Society, Boston, 17-20.

Battan, Louis J., 1973: *Radar Observation of the Atmosphere*. University of Chicago Press, Chicago, IL, 324 pp.

Braham, R.R. and M. Draginis, 1960: Roots of orographic cumuli. *J. Meteor.*, **17**, 214-226.

Browning, K.A., J.C. Fankhauser, J.-P. Chalon, P.J. Eccles, R.G. Strauch, F.H. Merrem, D.J. Musil, E.L. May, and W.R. Sand, 1976: Structure of an evolving hailstorm, Part V: Synthesis and implications for hail growth and hail suppression. *Mon. Wea. Rev.*, **104**, 603-610.

Chen, C. and W.R. Cotton, 1983: A one-dimensional simulation of the stratocumulus-capped mixed layer. *Boundary-Layer Meteorol.*, **25**, 289-321.

Clark, T.L., 1977: A small scale dynamic model using a terrain-following coordinate transformation. *J. Comp. Physics*, **24**, 186-215.

Clark, T.L. and R. Gall, 1982: Three-dimensional numerical model simulations of airflow over mountainous terrain: A comparison with observations. *Mon. Wea. Rev.*, **110**, 766-791.

Cotton, W.R., M.A. Stephens, T. Nehrkorn, and G.J. Tripoli, 1982: The Colorado State University three-dimensional cloud/mesoscale model--1982. Part II: An ice phase parameterization. *J. Rech. Atmos.*, **16**, 295-320.

Cotton, W.R. and G.J. Tripoli, 1978: Cumulus convection in shear flow--Three-dimensional numerical experiments. *J. Atmos. Sci.*, **35**, 1503-1521.

Cotton, W.R., G.J. Tripoli, R.M. Rauber, and E.A. Mulvihill, 1986: Numerical simulation of the effects of varying ice crystal nucleation rates and aggregation processes on orographic snowfall. *J. Clim. Appl. Meteor.*, **25**, 1658-1680.

Defant, F., 1951: Local winds. *Compendium of Meteorology*, T.M. Malone, Ed., American Meteorological Society, 655-672.

Durran, D.R., 1981: The effects of moisture on mountain lee waves. Ph. D. Dissertation, Massachusetts Institute of Technology and National Center for Atmospheric Research, Cooperative Thesis No. 65, 142 pp.

Dye, J.E., B.M. Ruiz, J.J. Jones, W.P. Winn, W. Williams, J.W. Bullock, B.A. Miller, and D.J. Younkin, 1987: The onset of electrification in New Mexico thunderstorms. *Preprints*, 23rd Conference on Radar Meteorology, Snowmass, CO, American Meteorological Society, 153-156.

Gal-Chen, T. and R.C.J. Somerville, 1975a: On the use of a coordinate transformation for the solution of the Navier-Stokes equations. *J. Comp. Physics*, **17**, 209-228.

Gal-Chen, T. and R.C.J. Somerville, 1975b: Numerical solution of the Navier-Stokes equations with topography. *J. Comp. Physics*, **17**, 276-310.

Glass, M. and T.N. Carlson, 1963: The growth characteristics of small cumulus clouds. *J. Atmos. Sci.*, **20**, 397-406.

Hill, G.E., 1974: Factors controlling the size and spacing of cumulus clouds as revealed by numerical experiments. *J. Atmos. Sci.*, **31**, 646-673.

Joss, J. and D. Waldvogel, 1970: Raindrop size distributions and Doppler velocities. *Preprints*, 14th Conference on Radar Meteorology, Tuscon, AZ, American Meteorological Society, 153-156.

Kessler, E. III, 1969: On the Distribution and Continuity of Water Substance in Atmospheric Motions. *Meteorological Monographs*, No. 32, American Meteorological Society, Boston, 84 pp.

Klemp, J.B. and R.B. Wilhelmson, 1978a: The simulation of three-dimensional convective storm dynamics. *J. Atmos. Sci.*, **35**, 1070-1096.

Klemp, J.B. and R.B. Wilhelmson, 1978b: Simulations of right- and left-moving storms produced through storm splitting. *J. Atmos. Sci.*, **35**, 1097-1110.

Lang, S.E., 1991: Retrieving microphysical variables in a small mountain thunderstorm. M. S. Thesis, Florida State University, Tallahassee, FL, 269 pp.

Lilly, D.K., 1962: On the numerical simulation of buoyant convection. *Tellus*, **14**, 148-172.

Liu, J.Y. and H.D. Orville, 1969: Numerical modeling of precipitation and cloud shadow effects on mountain-induced cumuli. *J. Atmos. Sci.*, **26**, 1283-1298.

Louis, J.-F., 1979: A parametric model of vertical eddy fluxes in the atmosphere. *Boundary-Layer Meteorol.*, **17**, 187-202.

Manton, M.J. and W.R. Cotton, 1977: Parameterization of the atmospheric surface layer. *J. Atmos. Sci.*, **34**, 331-334.

McCumber, M.C. and R.A. Pielke, 1981: Simulation of the effects of surface fluxes of heat and moisture in a mesoscale numerical model. 1. Soil layer. *J. Geophys. Res.*, **86**, 9929-9938.

McCutchan, M.H. and D.G. Fox, 1986: Effect of elevation and aspect on wind, temperature, and humidity. *J. Clim. Appl. Meteor.*, **25**, 1996-2013.

Ogura, Y., 1962: Convection of isolated masses of buoyant fluid: a numerical calculation. *J. Atmos. Sci.*, **19**, 492-502.

Orville, H.D., 1964: On mountain upslope winds. *J. Atmos. Sci.*, **21**, 622-633.

Orville, H.D., 1965a: A numerical study of the initiation of cumulus clouds over mountainous terrain. *J. Atmos. Sci.*, **22**, 684-699.

Orville, H.D., 1965b: A photogrammetric study of the initiation of cumulus clouds over mountainous terrain. *J. Atmos. Sci.*, **22**, 700-709.

Orville, H.D., 1968: Ambient wind effects on the initiation and development of cumulus clouds over mountains. *J. Atmos. Sci.*, **25**, 385-403.

Paegle J., W.G. Zdunkowski, and R.M. Welch, 1976: Implicit differencing of predictive equations of the boundary layer. *Mon. Wea. Rev.*, **104**, 1321-1324.

Ray, P.S., C.L. Ziegler, W. Bumgarner, and R.J. Serafin, 1980: Single- and multiple-Doppler radar observations of tornadic storms. *Mon. Wea. Rev.*, **108**, 1607-1625.

Raymond, D.J. and M. Wilkening, 1980: Mountain-induced convections under fair weather conditions. *J. Atmos. Sci.*, **37**, 2693-2706.

Raymond, D.J. and M. Wilkening, 1982: Flow and mixing in New Mexico mountain cumuli. *J. Atmos. Sci.*, **39**, 2211-2228.

Raymond, D.J. and M. Wilkening, 1985: Characteristics of mountain-induced thunderstorms and cumulus congestus clouds from budget measurements. *J. Atmos. Sci.*, **42**, 773-783.

Schaaf, C.B., J. Wurman, and R.M. Banta, 1988: Thunderstorm-producing terrain features. *Bull. Amer. Meteor. Soc.*, **69**, 272-277.

Schlesinger, R.E., 1975: A three-dimensional numerical model of an isolated deep convective cloud: Preliminary results. *J. Atmos. Sci.*, **32**, 934-957.

Schlesinger, R.E., 1978: A three-dimensional numerical model of an isolated thunderstorm: Part I. Comparative experiments for variable ambient wind shear. *J. Atmos. Sci.*, **35**, 690-713.

Scorer, R.S., 1958: *Natural Aerodynamics*. Pergamon Press, New York, NY, 312 pp.

Scorer, R.S. and F.H. Ludlam, 1953: Bubble theory of penetrative convection. *Quart. J. Roy. Meteor. Soc.*, **79**, 94-103.

Smolarkiewicz, P.K. and T.L. Clark, 1985: Numerical simulation of the evolution of a three-dimensional field of cumulus clouds. Part I: Model description comparison with observations and sensitivity studies. *J. Atmos. Sci.*, **42**, 502-522.

Srivastava, R.C., 1967: A study of the effect of precipitation on cumulus dynamics. *J. Atmos. Sci.*, **24**, 36-44.

Tapp, M.C. and P.W. White, 1976: A non-hydrostatic mesoscale model. *Quart. J. Roy. Meteor. Soc.*, **102**, 277-296.

Todd, C.J., 1964: Aircraft traverses in a growing mountain cumulus cloud. *J. Atmos. Sci.*, **21**, 529-538.

Toth, J.J. and R.H. Johnson, 1985: Summer surface flow characteristics over northeast Colorado. *Mon. Wea. Rev.*, **113**, 1458-1469.

Tremback, C.J. and R. Kessler, 1985: A surface temperature an moisture parameterization for use in mesoscale numerical models. *Preprints*, Seventh Conference on Numerical Weather Prediction, Montreal, Canada, American Meteorological Society, 355-358.

Tremback, C.J., G.J. Tripoli, and W.R. Cotton, 1985: A regional scale atmospheric numerical model including explicit moist physics and a hydrostatic time-split scheme. *Preprints*, Seventh Conference on Numerical Weather Prediction, Montreal, Canada, American Meteorological Society, 433-434.

Tripoli, G.J., 1986: A numerical investigation of an orogenic meso-scale convective system. Ph. D. Dissertation, Atmos. Sci. Paper No. 401, Colorado State University, Ft. Collins, CO, 290 pp.

Tripoli, G.J. and W.R. Cotton, 1980: A numerical investigation of several factors contributing to the observed variable intensity of deep convection over south Florida. *J. Appl. Meteor.*, **19**, 1037-1063.

Tripoli, G.J. and W.R. Cotton, 1981: The use of ice-liquid water potential temperature as a thermodynamic variable in deep atmospheric models. *Mon. Wea. Rev.*, **109**, 1094-1102.

Tripoli, G.J. and W.R. Cotton, 1982: The Colorado State University three-dimensional cloud/mesoscale model--1982. Part I: General theoretical framework and sensitivity experiments. *J. Rech. Atmos.*, **16**, 185-219.

Tripoli, G.J. and W.R. Cotton, 1986: An intense, quasi-steady thunderstorm over mountainous terrain, Part IV: Three-dimensional numerical simulation. *J. Atmos. Sci.*, **43**, 894-912.

Tripoli, G.J., P.J. Flatau, and W.R. Cotton, 1988: Generalized microphysics scheme for use in mesoscale/cloud models. *Preprints*, 10th International Cloud Physics Conference, 15-20 August 1988, Bad Homburg, FRG.

Turner, J.S., 1962: The "starting plume" in neutral surroundings. *J. Fluid Mech.*, **13**, 356-368.

Winn, W.P., G.W. Schweda, and C.B. Moore, 1974: Measurements of electric fields in thunderclouds. *J. Geophys. Res.*, **79**, 1761-1767.

Ziegler, C.L., P.S. Ray, and D.R. MacGorman, 1986: Relations of kinematics, microphysics, and electrification in an isolated mountain thunderstorm. *J. Atmos. Sci.*, **43**, 2098-2114.

BIOGRAPHICAL SKETCH

Mark Edwin Raffensberger was born on 9 January 1961 in York, Pennsylvania. Mark graduated in June of 1979 from Dallastown Area High School in Dallastown, Pennsylvania. From 1979 to 1983 he attended the Pennsylvania State University campuses in York and State College, Pennsylvania and graduated with a Bachelor of Science degree in meteorology in May of 1983. After completing Officer Training School in November of 1983, Mark was commissioned in the United States Air Force and assigned to Hill Air Force Base in Utah where he served as Staff Meteorologist for the Utah Test and Training Range. He began his graduate work in the Air Force Institute of Technology Civilian Institutions program at Florida State University in the fall of 1986. After completing his coursework in 1988, he was transferred to Air Weather Service Headquarters at Scott Air Force Base, Illinois, where he managed Air Force weather research and development programs while simultaneously completing his thesis requirements for graduate school.

Mark has co-authored a paper presented in 1989 at the 24th Conference on Radar Meteorology in Tallahassee, Florida based on material from his master's thesis. He will continue his work in numerical modeling in the Simulations and Techniques branch at the United States Air Force Environmental Technical Applications Center at Scott Air Force Base, Illinois, where he was transferred in August of 1993.